Doctoral Dissertation

Isoscalar and isovector spin-*M1* transitions from the even-even, $N = Z$ nuclei across the *sd*-shell region

sd 殻領域に渡る $N = Z$ 偶々原子核からの
アイソスカラー・アイソベクター型スピン-*M1* 遷移の研究

Hiroaki MATSUBARA

August, 2010

Department of Physics
Graduate School of Science
Osaka University

Abstract

The isoscalar (IS) and the isovector (IV) spin-$M1$ transition strengths were systematically measured for the study of the 1^+ ($M1$) transitions that are mediated by "σ" and "$\sigma\tau$" operators, respectively. The cross sections of the (p, p') reaction using 295 MeV proton beam were measured in the range of the scattering angle of $0-14^\circ$. The experiment was performed at the RCNP by using the Grand Raiden spectrometer applying the dispersion matching technique for high energy resolution. The target nuclei of ^{12}C, ^{16}O, ^{20}Ne, ^{24}Mg, ^{28}Si, ^{32}S, ^{36}Ar, and ^{40}Ca, the $N = Z$ and even-even nuclei in the *sd*-shell region, were measured for the systematic study. These nuclei allowed us to separately observe the pure IS and the IV spin-$M1$ transition because their ground states are $T = 0$. The gas target system was newly developed to employ neon and argon gas, and the elemental sulfur was successfully used as a target with charged particle irradiation for the first time.

The $J^\pi$and T assignments for the low-lying discrete states were performed by the angular distribution of the differential cross section based on the distorted wave Born approximation (DWBA) calculation. The spin-$M1$ transition strengths were derived from the cross section at 0° using the unit cross sections. The unit cross sections were determined from the β-decay and the γ-decay experiments in literature.

The quenching factors, the strength ratio of the experiment to the shell model calculation accumulated up to $E_x = 16$ MeV, were systematically 1.0 and 0.6 for the IS and the IV transitions, respectively. The IV 1^+ quenching factors were found to be consistent with the GT quenching factors that were derived from the shell model calculation. The difference of the quenching factors between the IS and the IV 1^+ transitions was supposed to originate from the different contribution of the $2p2h$ configuration mixing into the high excitation energy region in each transition. Such difference in the $2p2h$ configuration mixing has not been considered in theory.

Abstract

”σ” と ”$\sigma\tau$” の遷移演算子によって引き起こされる 1^+ の原子核遷移を調べるために我々はアイソスカラー・アイソベクター型のスピン $M1$ 遷移強度を系統的に測定した。295 MeV に加速した陽子ビームを用いて (p, p') 反応の微分散乱断面積を 0〜14° の散乱角度範囲内で測定した。実験は RCNP 施設においてグランドライデンスペクトロメーターを用いて行われ、エネルギー高分解能測定のために分散整合の手法が執られた。 sd 殻領域に渡る全ての $N = Z$ の偶々核である ^{12}C, ^{16}O, ^{20}Ne, ^{24}Mg, ^{28}Si, ^{32}S, ^{36}Ar, ^{40}Ca の原子核に対して系統的な研究を行った。これらは $T = 0$ の原子核であるので、純粋なアイソスカラー・アイソベクター型のスピン $M1$ 遷移強度の測定を可能にしてくれる唯一の原子核である。本研究の 0 度高分解能測定に適している、自己保持型の単体硫黄標的やネオン・アルゴン用のガス標的システムを新たに開発した。

励起エネルギースペクトルで観測された低励起なピークそれぞれに対して、歪曲波ボルン近似（DWBA）計算に基づく微分断面積の角度分布の形よりスピンパリティとアイソスピンを決定した。0 度の微分断面積の値から単位断面積の比例性を用いてスピン $M1$ 遷移強度を求めている。ここでこの単位断面積は β 崩壊や γ 崩壊の既存のデータから求められている。

励起エネルギー 16 MeV までの積算値の遷移強度に関する実験と殻模型計算の比をクエンチング因子と定義すると、質量数に関わらず系統的に IS 遷移では 1.0、IV 遷移では 0.6 という結果になった。この IV 1^+ 遷移のクエンチング因子は GT 遷移での殻模型計算から得たクエンチング因子の結果と一致している。この IS と IV 1^+ 遷移でのクエンチング因子の違いは、$2p2h$ 励起の配位混合の影響がそれぞれの遷移で異なっていることに起因すると考えられる。このような $2p2h$ 励起の配位混合の IS、IV 遷移での違いは理論的にはこれまで全く考えられてこなかった。

Contents

List of Figures

List of Tables

Chapter 1

Introduction

1.1 Electro-magnetic monents and nuclear structure

Nuclear structure has been studied in the light of electromagnetic properties of the nucleus both experimentally and theoretically over the past decades. The interaction of the nucleus with external electromagnetic field is expressed by the operators of electric as well as magnetic multipole moments. The static multipole moments are represented in terms of the diagonal matrix elements of the operators and the transition amplitudes between the states by the off-diagonal elements.

The electric multipole moments involve the charge distribution and its motion in the nuclei. The electric monopole ($E0$) transition has suggested the presence of nuclear oscillation of " breathing mode " and the electric dipole ($E1$) resonance observed in the photo-absorption experiment has provided the signature of a collective dipole oscillation of the protons relative to the neutrons. Furthermore, the electric quadrupole ($E2$) moment have provided the decisive proof for the spheroid deformation of nuclear shape and the quadrupole oscillations of the nucleus, as a whole, to allow the establishment of the concept on the collective motion of the nucleons inside the nucleus.

The magnetic multipole moments, on the other hand, represents the interaction of the current density inside the nucleus with the electromagnetic field. Since the current density involves two different contributions due to orbital motions and intrinsic spins of the nucleons inside the nucleus, the situation becomes somewhat complicated compared with the case of electric moments. For the odd mass nucleus, however, the magnetic dipole ($M1$) moment, the lowest order moment, has served as a good probe for the single particle characters of the last odd nucleon in the nucleus, thus strongly stimulating the development of the shell model *i.e.*, the particle picture of the nuclear structure.

The simple shell model, however, has been unable to correctly explain the observed values of the magnetic dipole moments of odd nuclei as well as the hindered $M1$ transition rates between the nuclear states. These have been discussed phenomenologically in terms

of the quenching of the nucleon spin gyromagnetic factor (g_s), as compared to the free nucleon value. The improvements of the theory have been considered by taking into account the configuration mixings (or core polarization) in the nuclear states. Since, however, only a limited amount of experimental data have been available to separate the contributions of the nucleon orbital motions and the intrinsic spins to the current density in the nucleus, the thorough understanding of the situation with the $M1$ moment is still an open problem in nuclear physics and awaits further experimental information. The present study follows this line and especially aims to provide the systematic information on the spin contributions to the $M1$ moment.

1.2 "Quenching problem" of magnetic dipole moment

One of the interest subjects is the "quenching problem" in the magnetic dipole moment *i.e.*, reduction of the values of the matrix elements related to the $M1$ operator. Before going into details of the problem, it would be of value to describe the form of the M1 moment operator briefly.

1.2.1 Operator of magnetic dipole moment

The $M1$ moment operator $\hat{O}(M1)$ is represented by the sum of the contributions of protons and neutrons in the nucleus, and rewritten into the sum of isoscalar and isovector moments in the isospin formalism, as follows.

$$\hat{O}(M1) = \left[\sum_{k=1}^{Z}\left({g_l}^{\pi}\mathbf{l}_k + {g_s}^{\pi}\mathbf{s}_k\right) + \sum_{k=Z+1}^{A}\left({g_l}^{\nu}\mathbf{l}_k + {g_s}^{\nu}\mathbf{s}_k\right)\right]\mu_N \tag{1.1}$$

$$= \left[\sum_{k=1}^{A}\left\{\left({g_l}^{IS}\mathbf{l}_k + {g_s}^{IS}\frac{\sigma_k}{2}\right) + \left({g_l}^{IV}\mathbf{l}_k + {g_s}^{IV}\frac{\sigma_k}{2}\right)\tau_z(k)\right\}\right]\mu_N, \tag{1.2}$$

where μ_N denotes the nuclear magneton, g's are the gyromagnetic factors (g-factors) for the protons or neutrons denoted by the superscripts π or ν. The suffixes IS and IV denote isoscalar and isovector quantities, respectively, in the isospin representation. The vectors $\mathbf{l}_k$, $\mathbf{s}_k$, and σ_k denote the orbital angular momentum, spin and Pauli spin operators acting on the k-th nucleon. The operator $\tau_z(k)$ is the third component of the isospin operator τ acting on the k-th nucleon and the eigen value is $+1$ for neutrons and -1 for protons. The values of the g-factors for the free nucleons are ${g_l}^{\pi} = 1$, ${g_l}^{\nu} = 0$, ${g_s}^{\pi} = 5.586$, and ${g_s}^{\nu} = -3.826$, giving ${g_l}^{IS}$, ${g_s}^{IS}$, ${g_l}^{IV}$, and ${g_s}^{IV}$ to be 0.5, 0.880, -0.5, -4.706, respectively.

Each term of the isoscalar (IS) and the isovector (IV) components may be seen to be composed of the two terms of orbital part and spin part. Leaving out the gyromagnetic ratios and a constant, the matrix element of the $M1$ operator is thus given by the sum

of the four reduced matrix elements of IS orbital, IS spin, IV orbital and IV spin parts, symbolically expressed by $M(l)$, $M(\sigma)$, $M(l\tau)$ and $M(\sigma\tau)$, respectively, hereafter.

1.2.2 Static magnetic moment and Gammow-Teller transition rate

As mentioned above, the static magnetic moments of the ground states of odd nuclei have not been reproduced correctly by the single particle model. The experimental values have been known to fall in the range between the single particle predictions for the particles in the orbits of $l \pm 1/2$ (Schmidt value). This fact has strongly suggested the presence of configuration mixings in the ground states to reduce the matrix elements of $M(\sigma)$ and $M(\sigma\tau)$, and has been discussed in terms of g_s-quenching. The deviation of the magnetic moment from the Schmidt value, however, is rather complicated because of the combined contributions of the four components mentioned above. The separation of the contributions of the different components is expected to provide precious information for the nuclear structure.

In the past decade, there bas been experimentally observed another quenching problem in the Gammow-Teller (GT) transitions of ΔS=1, ΔL=0, and ΔT=1. The GT transition is considered to be caused by the operator proportional to $\sigma\tau$. The summed GT strengths in the GT giant resonance of up to $E_x \sim 20$ MeV in the (p, n) reactions have been observed to be ∼50% [1] of the model independent prediction of the Ikeda sum rule [2], nearly irrespective of the mass number, as shown in Fig 1.1. The quenching problem has been solved by extending the measuring region in terms of excitation energy. The detailed strength measurements by the (p, n) and (n, p) reactions up to $E_x = 50$ MeV [3] have revealed that a significant amount of the GT strength, ∼40% of the sum rule, distributes in the continuum region, showing a presence of the $2p2h$ configuration coupling to the $1p1h$ state. Thus, the quenching phenomena observed in the region of low excitation energy reflect the strength distribution at the region of high excitation energy.

1.2.3 Quenching phenomena in spin-flip transition operator

Since the GT transition operator is analogous to the last term in Eq. (1.2) for the $M1$ transition, it is of considerable interest to explore the IV spin part (mediated by $\sigma\tau$ operator) of the $M1$ strength systematically, for comparison with the behavior of the GT transition strength. It is also of interest to study how differently the IS and the IV spin parts (mediated by σ and $\sigma\tau$ operators, respectively) behave in the nuclear chart since they are mediated by the spin-flip operators.

How does the present theory predict the IS and the IV spin-flip transitions? The shell model calculation shows the similar strength distributions and the similar quenching

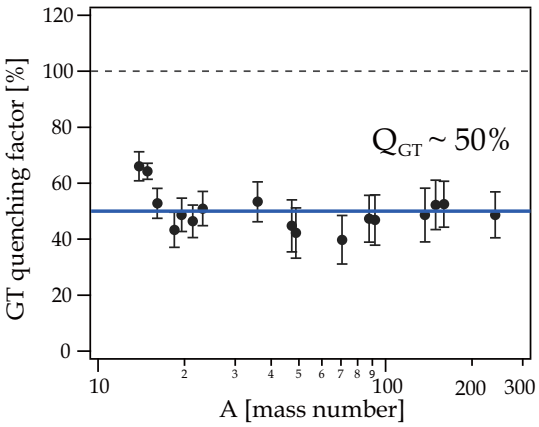

Figure 1.1: GT quenching factor observed in (p, n) reactions [1]. The quenching factor is defined as the strength ratio of experimental to the theoretical ones.

degree for the IS and IV spin-$M1$ transitions. In one meson exchanging model, however, pseudo-scalar mesons of η and π correlates with a nucleon for the IS and IV spin-$M1$ transitions, respectively. Since their masses and coupling constants are not identical, different quenching phenomena and different strength distributions may be to be observed in the IS and IV spin-$M1$ excitations.

Unfortunately, the IS spin-flip transition is much weaker than the IV one *i.e*, the IS transition strength is as weak as 3.5% and ∼10% of the IV one in electro-magnetic interactions and hadronic interactions, respectively. Since few experimental data of the IS spin-$M1$ transition have been observed owing to the weakness of the transition, new measurements which allow us to study the IS and IV spin-$M1$ transition strength distributions are required.

1.3 Measurement of spin-$M1$ transition strength

1.3.1 Definition of spin-$M1$ strength

Following the convention of Edmonds [4], the IS and IV spin-$M1$ transition strengths can be defined as

$$B(M1)_{\sigma} = \frac{1}{2J_i+1}\frac{3}{4\pi}\left|\frac{g_s^{IS}}{2}M(\sigma)\right|^2 {\mu_N}^2 \tag{1.3}$$

$$B(M1)_{\sigma\tau} = \frac{1}{2J_i+1}\frac{3}{4\pi}\left|\frac{g_s^{IV}}{2}M(\sigma\tau_z)\right|^2 {\mu_N}^2, \tag{1.4}$$

respectively. The details of the formalism are described in Appendix A.

1.3.2 Proton inelastic scattering at small angles for spin-$M1$ excitation

The proton inelastic scattering at small scattering angles is supposed to be the best probe for the study of the IS and IV spin-$M1$ transition strength because the probe is believed to excite only spin parts in the $M1$ transition and the response for the IS transition by the hadronic interaction is stronger than that by the electro-magnetic interaction. The spin part of the $M1$ transition couples the central component of the interaction. For the unnatural parity transition, *e.g.*, $M1$ transition, the effective interaction by the calculation shows that the central component increases but the spin-orbit and tensor components decreases at the region of the small momentum transfer, as shown in Fig. 1.2. The sensitivity ratio for the IS and IV transitions in the hadronic scattering at the region of the inter mediated energy for incident proton is estimated to be $|V_\sigma/V_{\sigma\tau}| \sim 0.1$ as shown in Fig. 1.3, while that in the electromagnetic interaction is $\left|{g_s}^{IS}/{g_s}^{IV}\right|^2 = 0.035$. Thus, the proton inelastic scattering at the region of small scattering angles is essential for the observation of the IS and IV spin-$M1$ transitions.

The nucleon-nucleon (NN) interaction between an incident particle and a target nucleon can be described as [5, 6]

$$\begin{aligned} V_{12} &= V_0 + V_\sigma(\vec{\sigma_1}\cdot\vec{\sigma_2}) + V_{LS}(\vec{L}\cdot\vec{S}) + V_T S_{12} \\ &\quad +\vec{\tau_1}\cdot\vec{\tau_2}\left(V_\tau + V_{\sigma\tau}(\vec{\sigma_1}\cdot\vec{\sigma_2}) + V_{LS\tau}(\vec{L}\cdot\vec{S}) + V_{T\tau}S_{12}\right), \end{aligned} \tag{1.5}$$

where the suffixes "1" and "2" refer to the incident particle and the target nucleon, respectively. The total spin operator and the relative angular momentum are defined as $\vec{S} \equiv \vec{s_1} + \vec{s_2}$ and $\vec{L} \equiv (\vec{r_1} - \vec{r_2}) \times (\vec{p_1} - \vec{p_2})$. The two-body tensor operator is defined as $S_{12} \equiv 3(\vec{\sigma_1}\cdot\vec{r})(\vec{\sigma_1}\cdot\vec{r})/r^2 - (\vec{\sigma_1}\cdot\vec{\sigma_2})$. In the direct nuclear reaction, the V_σ and $V_{\sigma\tau}$ terms are responsible for the IS and IV spin-$M1$ excitations, respectively. The energy dependences of the t-matrix amplitudes of terms, V_0, V_σ, V_τ, and $V_{\sigma\tau}$, are shown in Fig. 1.3. The V_0 term contribution reaches a minimum at 300 MeV of the proton beam energy. Since, therefore, the distortion effects in the (p, p') reaction are expected to be minimum at 300 MeV, the reaction at 300 MeV proton beam would make the best probe for the study of the spin-$M1$ transitions. The distorted wave Born approximation (DWBA) calculation would provide a good description of nucleon-nucleus scattering owing to the dominance of the one-step process in the intermediated energy region.

1.3.3 Pure IS spin-$M1$ transition

It is usually hard to experimentally extract the IS spin-$M1$ transition strength because the IS transition is mixed with the IV one and the observed transition strength is exhausted mainly by the IV transition because of the weakness of the IS excitation. However, there

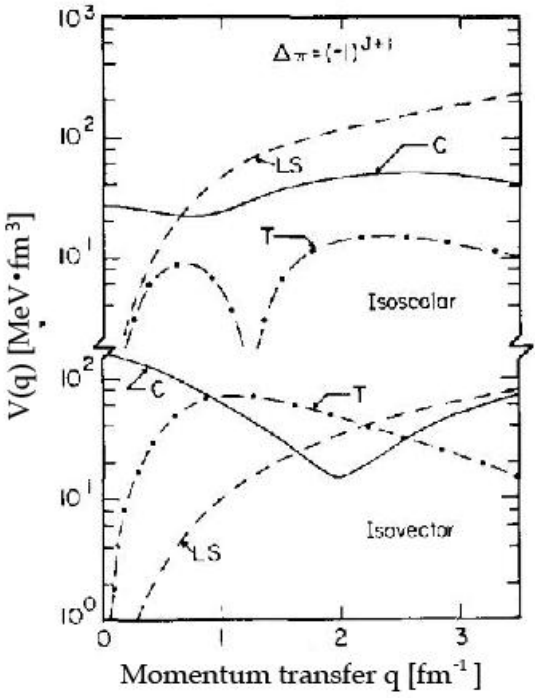

Figure 1.2: Nucleon-nucleon interaction at $E_p = 135$ MeV for unnatural parity transition, taken from Ref. [14]. The decomposition of the complete interaction is shown as a function of momentum transfer. The symbols C, LS, and T denote central, spin-orbit, and tensor, respectively.

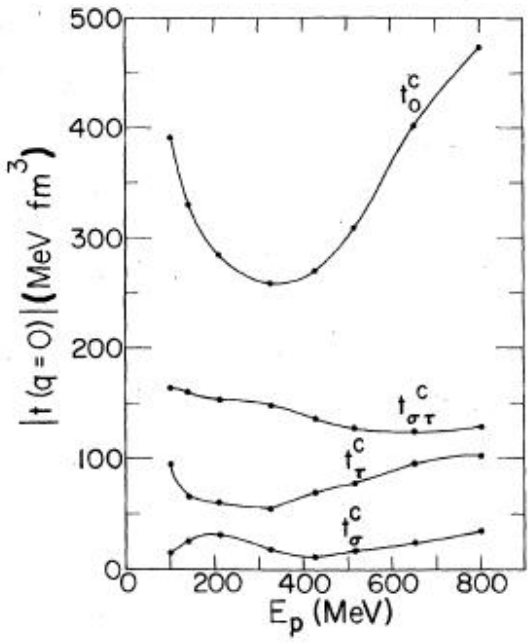

Figure 1.3: Energy dependence of the t-matrix amplitudes in the central component of the interaction, taken from Refs. [5, 6].

is the only one case where the IS spin-$M1$ transition are purely observed. Figure 1.4 schematically shows the $T_0 \to T_0$ and $T_0 \to T_0 + 1$ transitions in the $T_0 \neq 0$ nucleus (left) and the $T_0 = 0$ nucleus (right). The pure IS transition occurs only in the $T_0 = 0$ nucleus although the pure IV transition occurs in any nucleus. This leads to that only the $N = Z$ nucleus allows us to observe the pure IS transition. Furthermore, if we consider the proton scattering on the J^π=0^+ target, the transitions leading to the 1^+ final states are of pure $M1$ character. Therefore, the $N = Z$ and even-even nucleus is a good target for the study of the $M1$ strengths with clean separation of the IS and IV characters. Only the target nuclei of ^{4}He, ^{12}C, ^{16}O, ^{20}Ne, ^{24}Mg, ^{28}Si, ^{32}S, ^{36}Ar, and ^{40}Ca allows us to observe the pure IS and IV transitions separately.

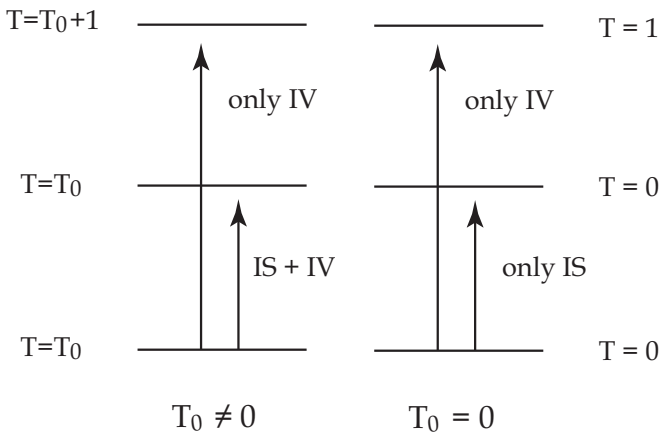

Figure 1.4: Schematic diagram of isospin structure in the $T_0 \neq 0$ nucleus and the $T_0 = 0$ nucleus.

1.3.4 1^+ and T assignment

In an excitation energy spectrum of the (p, p') reaction, many kinds of transitions are observed because the (p, p') reaction does not have any selectivity to the nuclear excitations leading to the states of different spin-parity (J^π) and isospin (T). Thus, it is of considerable importance to make the J^π and T assignments correctly for the excited states.

There are typically three methods of the assignments *i.e.*, a model independent method [7] by the use of polarization transfer observables [8, 9], a method to estimate T by comparing the results of different reactions with different isospin selectivity and a method based on the empirical dependence of the angular distribution shape of the reaction yield on J^π and T. In the present study, we adopted the last method for the simplicity of the measurement.

It is to be noted that the DWBA calculation gives a good description of the (p, p') reaction at 300 MeV because of the dominance of one step process at this energy. Therefore, the J^π (especially 1^+) and T assignments can be performed with the aid of DWBA, after the careful preparation of the parameters involved and the examination for the reproducibility of the angular distributions of the yields for the states of known J^π (especially 1^+) and T. The detailed procedure of the assignment will be presented in Sec. 6.3.

1.3.5 Optical model potential parameter

The optical model potential parameters are employed in the DWBA calculation to describe the distortion effect in the nuclear reaction. It has been found that the parameters are sensitive to the calculation [10]. Thus, the parameters are expected to be experimentally determined. The optical potential parameters can be derived from the elastic scattering

cross section and the analyzing power observed in elastic scattering measurement using a polarized proton beam. For this reason, we also performed the elastic scattering measurements on each nucleus and the optical model analysis. The detail of the analysis will be given in Chapter. 5.

1.3.6 Derivation of spin-$M1$ strength

Similarly to the case of the GT transition, the reduced spin-$M1$ strength $B(M1)_{spin}$ ("*spin*" denotes σ or $\sigma\tau$) can be derived from the measured yield of the (p,p) reaction in the following way;

$$\frac{d\sigma_{M1}}{d\Omega}(0^\circ) = \hat{\sigma}_{M1} F(q,\omega) B(M1)_{spin}, \tag{1.6}$$

where the left side is the experimental spin-$M1$ differential cross section. The $F(q,\omega)$ in the right side is the kinematic factor for the momentum and energy transfers q and ω, defined as the ratio of the cross section value at finite (q,ω) to that at $(q=0,\omega=0)$. The factor $\hat{\sigma}_{M1}$ is a proportionality constant called "unit cross section". The kinematic factor $F(q,\omega)$ becomes unity as q approaches zero, namely when the measurement is made at very forward angles. The unit cross sections for the IS and IV transitions are to be determined experimentally by using the measured yields for the transitions of known isospin properties.

1.3.7 High energy-resolution (p,p') measurement at 0°

Summarizing the descriptions in the preceding sections, it is to be stressed that the (p,p') reactions at 300 MeV on even-even target nuclei would provide a key information to untangle the mysterious problem on the $M1$ quenching phenomenon. The 0° measurements are of especial importance in deriving the spin-$M1$ transition strengths.

In order to make such information available, the most important would be to realize high energy-resolution as well as low-background measurements for the scattered protons. The high energy resolution will considerably help the correct J^π and T assignments by resolving the mixed transitions with different multipole orders and will also remove the difficulty of causing errors in the strength derivations as seen in ^{28}Si(Sec. 1.4). For this purpose, careful dispersion matching between the beam line and the proton spectrometer is indispensable. For reducing the background, the careful handling of the beam is important to prevent the beam halo from occurring. The halo, if any, will cause a huge amount of background particles to mask the proton spectrum at 0°, thereby making the measurement impossible.

1.4 Previous study on spin-$M1$ quenching

The spin-$M1$ transition rate has been systematically measured for the nuclei in the *sd*-shell region by the (p, p') reactions [11, 12]. The experiments have been performed using a 201 MeV proton beam from the Orsay synchrocyclotron. The observed transition rates have been compared with shell model predictions in the full *sd*-space [13] in the form of quenching factor, which is defined as the ratio of the sum of the reduced spin-$M1$ transition probabilities $B(M1)$ observed in a nucleus to the sum of those predicted by the shell model. In the shell model calculations, the free g_s-factor values have been assumed. The quenching factors reported are plotted in the left panel of Fig. 1.5 against mass number A. From this figure, the authors of Ref. [12] have claimed that almost no quenching is present in the *sd*-shell nuclei because the $M1$ quenching factors are scattered from unity. However, there are two problems to be considered before reaching the conclusion of the $M1$ quenching. Firstly, the IS and IV spin-$M1$ transition strengths have not been decomposed except for the cases of ^{28}Si and ^{32}S. Because the transition operators for the IS and the IV spin-$M1$ transitions are not identical, it is essential to observe the IS and IV excitations separately for the study of the $M1$ quenching and the strength distribution. Secondly, the IV quenching factors for ^{28}Si and ^{32}S have not been consistent with the GT quenching factors observed in the (p, n) reaction at $E_p = 135$ MeV [15, 16], where not the model independent sum rule but the shell model prediction in the full *sd*-shell has been applied for the GT quenching factor. The observed GT quenching factors with the shell model calculation have been systematically 0.6 for ^{20}Ne, ^{24}Mg, ^{28}Si, and ^{32}S as shown in the right panel of Fig. 1.5. This does not imply that the relationship in terms of isospin symmetry is present between the IV spin-$M1$ and the GT transitions. Since the quenching phenomena have been observed in the static magnetic moments mainly based on the IV spin part, it may be natural that the IV spin-$M1$ transition strength has also quenching phenomena. Therefore, the IS and IV spin-$M1$ transition strengths are considerably required to be systematically measured for the $M1$ quenching factors.

1.5 Outline of this thesis

In this thesis, the IS and IV spin-$M1$ excitations were precisely and systematically measured for ^{12}C, ^{16}O, ^{20}Ne, ^{24}Mg, ^{28}Si, ^{32}S, ^{36}Ar, and ^{40}Ca. This is the first systematic measurement of the IS and IV spin-$M1$ transition strengths at 0°. The (p, p') measurements at 0° and at small scattering angles with high energy resolution were performed using a 300 MeV proton beam from the RCNP RING cyclotron. The unit cross section were reliably determined by using the known data of the β-decay, the γ-decay, and the (^{3}He,t) experiments.

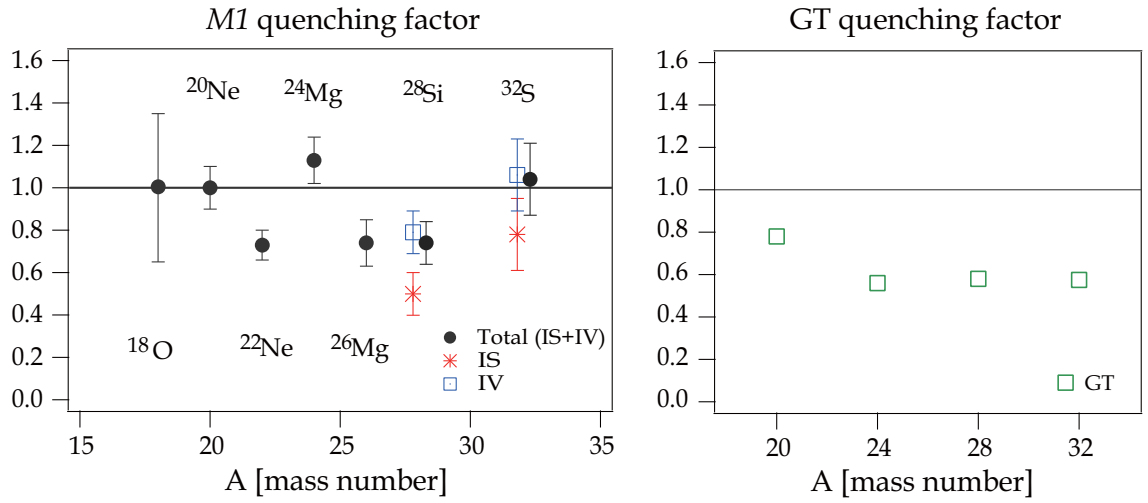

Figure 1.5: The $M1$ (left) and GT (rigth) quenching factors observed in the (p, p') reaction at E_p=201 MeV [12] and the (p, n) reaction at E_p=135 MeV [15, 16], respectively. The quenching factor is defined as the total strength ratio of the observed transitions in a nucleus to the full *sd*-shell model prediction with the free g_s-factors. The model independent sum rule is not employed for the GT quenching factor.

The experimental setup and conditions are given in Chapter 2. The preparation and the development of the targets are described in Chapter 3. The analysis for the proton inelastic scattering data taken by using unpolarized proton beam together with proton elastic scattering data taken by using polarized proton beam are presented in Chapter 4 and Chapter 5, respectively. The 1^+ and T assignment and the conversion to $B(M1)_\sigma$ and $B(M1)_{\sigma\tau}$ values using unit cross sections are described in Chapter 6. The comparison of the experimental spin-$M1$ transition strengths with theoretical calculations is discussed in Chapter 7. Finally, the summary of this thesis is presented in Chapter 8.

The formalisms of $M1$ transition operator and IS- and IV-spin-$M1$ transition strengths are given in Appendix A. The experimental excitation energy spectra are shown in Appendix B. The observed angular distributions of differential cross section for the final discrete states in each target are presented in Appendix C. The experimental numerical data of elastic scattering are summarized in Appendix D. The spin-$M1$ transition strengths of $B(M1)_\sigma$ and $B(M1)_{\sigma\tau}$ are tabulated and compared with the previous results in Appendix E. The performance of the analyzer target is reported in Appendix F.

Chapter 2

Experimental setup

For the high energy resolution experiment at 0°, the following conditions must be satisfied as

- halo-free beam
- dispersive beam
- thin and large target.

It is hard to perform inelastic scattering measurements at 0° because particles to be detected in the measurement are scattered to the identical direction to the primary beam. Their separation in terms of momentum must be performed certainly for the measurement. If the beam has a halo-component, a huge number of extra scattering originated from the beam line or at the target folder is produced. Since the momentum of those extra scattering is supposed to be uniform, they make the measurement impossible because of their tremendous number noise events. Thus, high quality beam without halo-component is required for the inelastic scattering measurement at 0°. The (p, p') experiments at 0° have been realized by employing finely tuned beam [8, 9, 19]. For high energy resolution, careful dispersion matching [21, 22] between the beam line [23] and the spectrometer is required. The combination of the two noble techniques for the measurement at 0° with high energy resolution have been realized recently [20]. The requirement for targets to be used in the experiment is described in Chap. 3. Thus, the measurement for the sophisticated study of the $M1$ quenching by the (p, p') reaction at 0° is feasible at the at the Research Center for Nuclear Physics (RCNP), Osaka University, Japan.

The high energy-resolution (p, p') measurements at small scattering angles including 0° were performed at the Research Center for Nuclear Physics (RCNP), Osaka University, Japan. The layout of the RCNP facility is illustrated in Fig. 2.1. The coupled cyclotrons, the $K = 140$ MeV Azimuthally Varying Field (AVF) cyclotron and the $K = 400$ MeV RING cyclotron, were used to accelerate protons up to 295 MeV. The beam was transported onto the target placed in the scattering chamber of a magnetic spectrometer

Grand Raiden (GR) [24] through the WS beam line [23]. Large Acceptance Spectrometer (LAS) was simultaneously used to monitor the beam height at the target position, which provided essential information for the reconstruction of scattering angles (see Secs. 4.3 and 4.4).

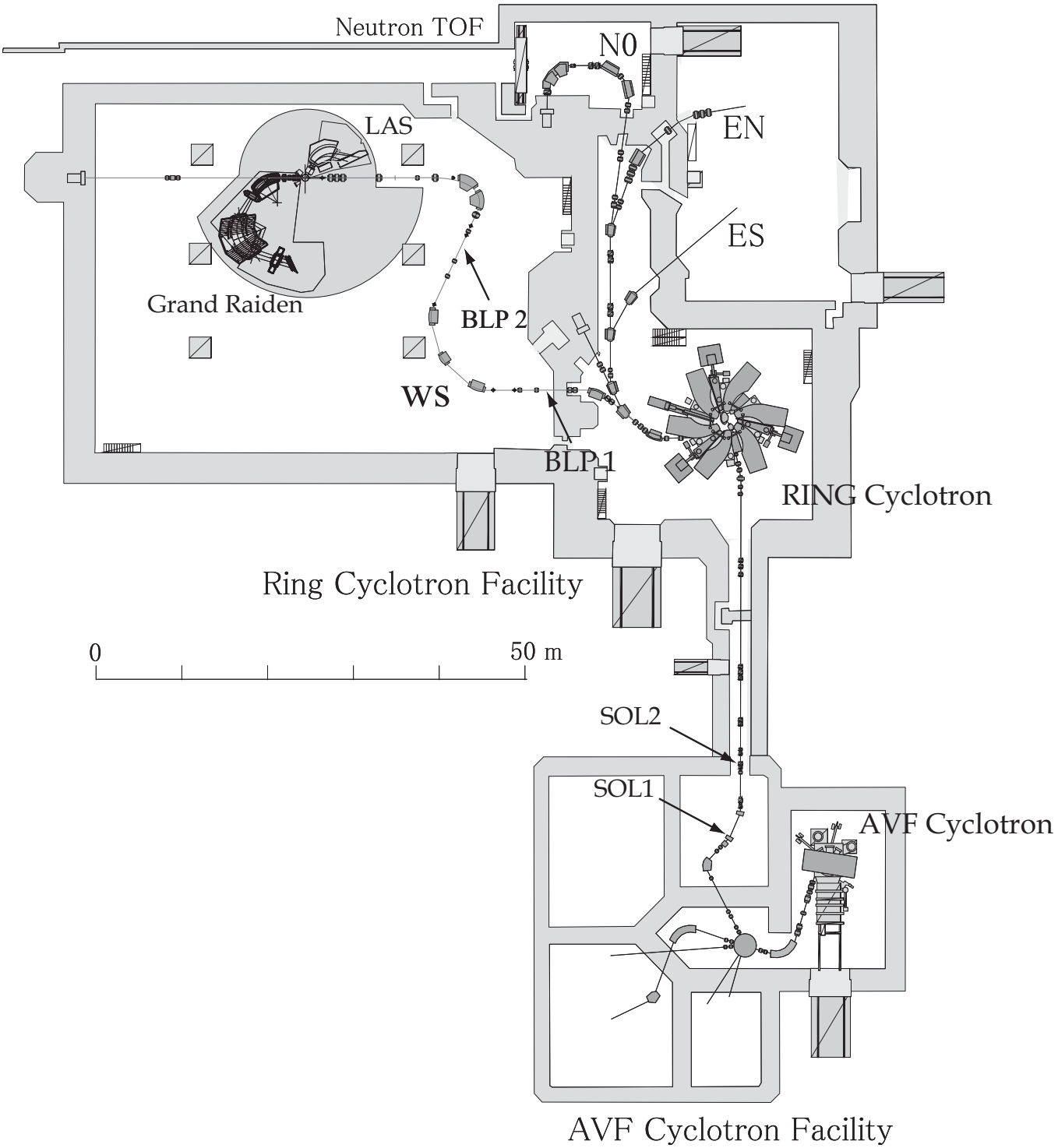

Figure 2.1: The layout of the RCNP cyclotron facility.

2.1 Experimental setup

2.1.1 Ion source

Unpolarized and polarized proton beams were provided by the Electron Cyclotron Resonance (ECR) ion source NEOMAFIOS [25], and the High Intensity Polarized Ion Source HIPIS [26], respectively. The unpolarized proton beam was employed for the inelastic scattering measurement and the polarized proton beam was employed for the elastic scattering measurement. For the HIPIS, the proton polarization state was toggled between the normal and the reverse states in every second to cancel out the geometrical asymmetries of the experimental apparatus. A typical beam intensity was 2−10 nA on the target position.

2.1.2 Beam Line Polarimeter (BLP)

The Beam Line Polarimeters (BLP1 and BLP2 in Fig. 2.1) were used to monitor the beam polarization of polarized protons in the elastic scattering measurement. The two BLP's were placed in the WS beam line. Each BLP consisted of four plastic scintillation detectors arranged to form two pairs as shown in Fig. 2.2 in the horizontal plane to measure the asymmetry of the *pp* elastic scattering. Each pair of the detectors (R−R' or L−L') counted scattered protons and the recoiled protons from an analyzer target in coincidence. For this purpose, the scintillation counters were placed at 17.0° and 70.5° in laboratory frame.

During the elastic scattering measurement, the BLP's monitored the asymmetry of *pp* scattering in the horizontal plane. A polyethylene (CH_2) sheet with an areal density of 8.4 mg/cm^2 and an aramid film ($C_{14}O_2N_2H_3$, made by Asahi-kasei Co. Ltd.) with an areal density of 5.0 mg/cm^2 (50 μm-thick) were used for the analyzer targets. Since the analyzing power of the polyethylene target for 295 MeV protons has been known [27], that of the aramid was determined by comparing the experimental asymmetries for the two targets as described in App. F. The analyzer targets were continuously placed in the beam line during the experiment.

The BLP's were also used to monitor the beam transmission (beam loss) in the beam line and the charge collection in a Faraday cup during the inelastic scattering measurements employing the unpolarized proton beams. The targets were periodically inserted in for 1 s and removed out of the beam for 10 s. Data by the detector system of the GR and the LAS were taken only when the analyzer targets were moved out of the beam position. The aramid film with an areal density of 5 mg/cm^2 was used as a target. The polyethylene film was not adequate to be used as the BLP target for this purpose because the thickness was found to change during the irradiation. The stability of the target

thickness is discussed in App. F.

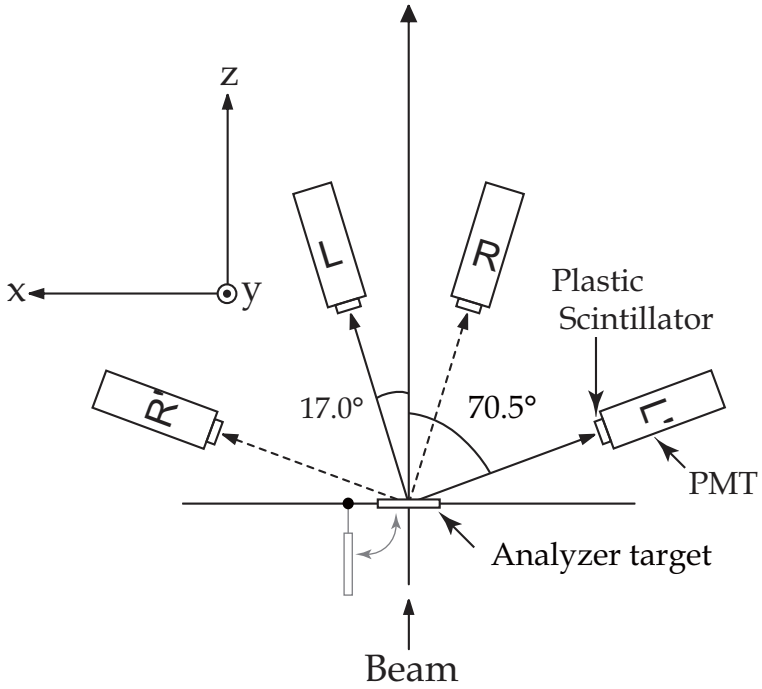

Figure 2.2: Configuration of the BLP.

2.1.3 Configuration for 0 degrees measurement

Figure 2.3 shows the experimental setup of the spectrometers in the 0° measurement. The two spectrometers, the Grand Raiden (GR) spectrometer [24] and the Large Acceptance Spectrometer (LAS) [30], were employed. The GR spectrometer was placed at 0° for the proton inelastic scattering measurement. The LAS measured quasi-free scattering protons to monitor the beam position at the target in the vertical direction. The LAS was placed at $\theta_{lab} = 60°$, the most forward angle when the GR spectrometer was placed at 0°, throughout the experiment.

The experimental setup of the downstream of the GR spectrometer in the 0°measurement is shown in Fig. 2.4. The beam ducts were connected to the 0° Faraday Cup (0° FC) from the exit of the GR spectrometer. This setup was used only in the 0° measurement. The 0° FC was placed at 12 m downstream of the focal plane detectors of the GR spectrometer. Lead, iron, and concrete blocks were piled to surround the 0° FC, shielding γ-ray and neutrons from flying to the detectors. The distance of 12 m and the shield for the 0° FC were indispensable to suppress background events originated from the FC in the 0° measurement. For precise charge collection of the beam by the 0° FC, an electron sweeper to bend away electrons which come from the upstream side by a magnetic field was placed at the entrance, inside the concrete block.

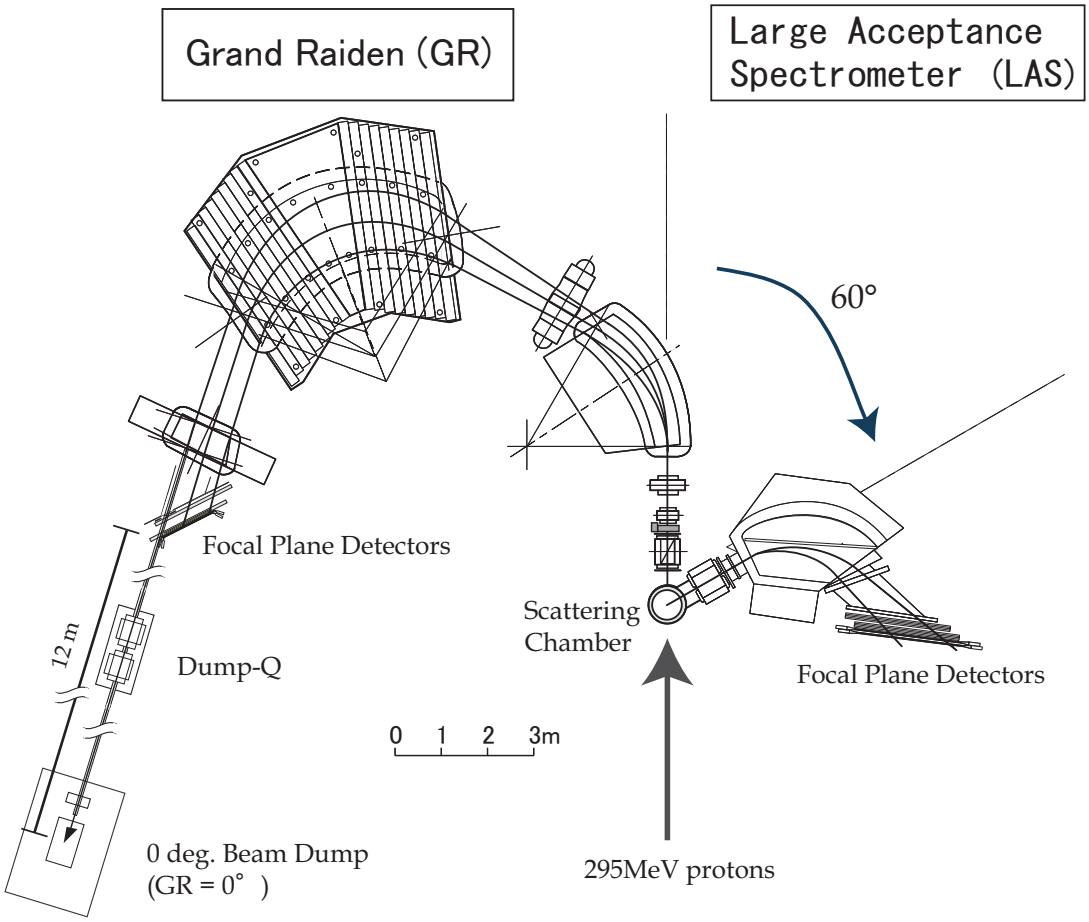

Figure 2.3: The arrangement of the GR spectrometer and the LAS for the inelastic scattering measurement at 0°.

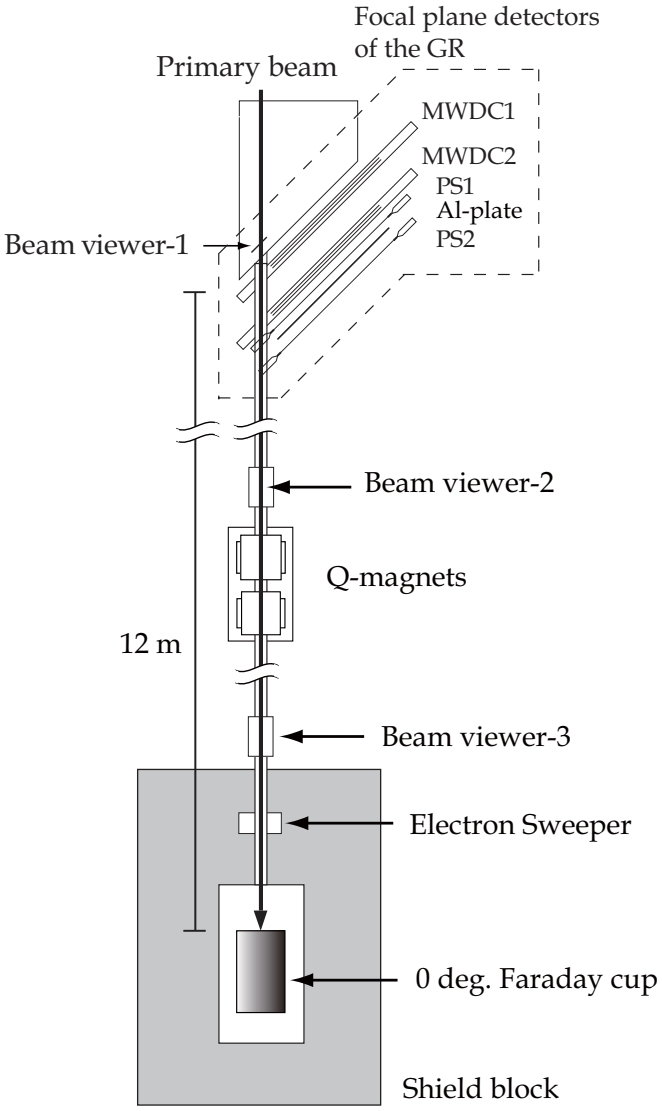

Figure 2.4: The experimental setup of the downstream of the GR in the 0°measurement. The primary beam was stopped in the 0° Faraday cup placed 12 m downstream from the detector system to reduce background events.

2.1.4 Grand Raiden spectrometer (GR)

The spectrometer GR has been designed for high resolution measurement. Its configuration is abbreviated to QSQDMDD; three Dipole magnets (D1, D2 and DSR), two Quadrupole magnets (Q1 and Q2), a Sextupole magnet (SX) and a Multipole magnet (MP) as shown in Fig. 2.5. The specifications of the GR spectrometer are summarized in Table 2.1. One of the remarkable characteristic is in its high momentum resolution of $p/\Delta p = 3.7 \times 10^4$. The GR was placed at 0, 2.5, 4.5, 6, 8, 10, 12, and 14° in the inelastic scattering measurement to observe angular distribution of the differential cross section for the J^π and T assignments. In the elastic scattering measurement, the GR spectrometer was placed at 6, 9, 12, 15, 18, 21, 24, 27, and 30°.

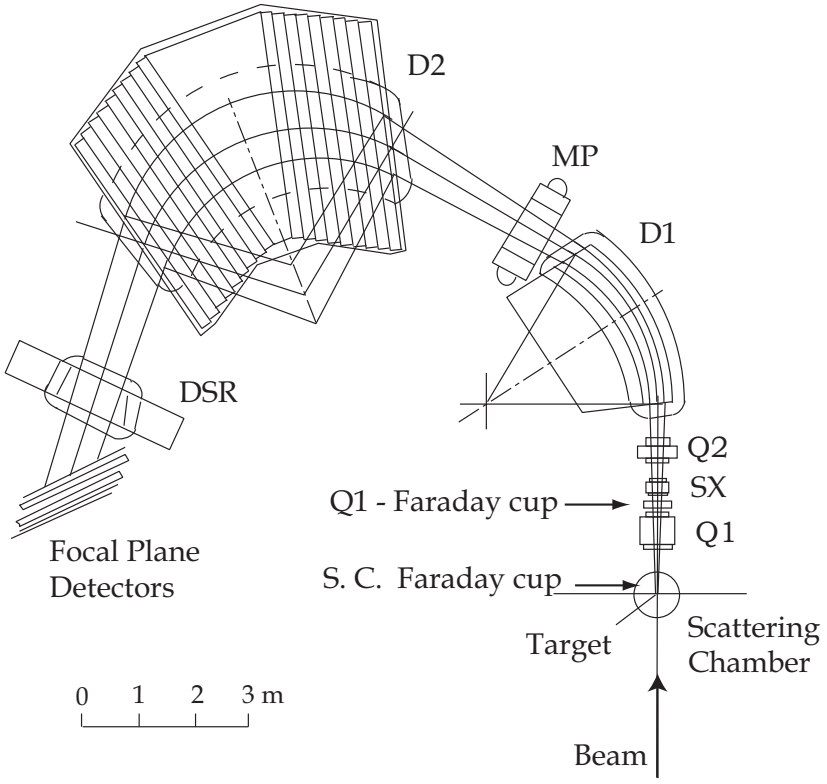

Figure 2.5: The high resolution spectrometer Grand Raiden (GR) spectrometer. The locations of the Faraday cup (FC) in the scattering chamber (SCFC) and that at the exit of Q1 magnet (Q1FC) are indicated by the arrows.

The focal plane detector system [28] of the GR is shown in Fig. 2.6. The system consisted of two multi-wire drift chambers (MWDC1 and MWDC2) and two plastic scintillation counters (PS1 and PS2).

The MWDC's were used to determine positions and angles of the momentum analyzed particle. The specifications of the MWDC are summarized in Table 2.2. Each MWDC had two anode wire planes (X and U). The tilting angle of the U plane wires was 48.19°

Table 2.1: The specifications of the GR spectrometer and the LAS at the RCNP.

	Grand Raiden (GR)	Large Acceptance Spectrometer (LAS)
Configuration	QSQDMDD	QD
Mean orbit radius	3m	1.75m
Total deflection angle	162°	70°
Tilting angle of focal line	45°	57°
Maximum magnetic rigidity	5.4 T·m	3.2 T·m
Vertical magnification	5.98	-7.3
Horizontal magnification	-0.417	-0.4
Momentum range	5 %	30 %
Momentum resolution	37076	4980
Acceptance of horizontal angle	±20 mr	±60 mr
Acceptance of vertical angle	±70 mr	±100 mr

relative to the vertical X plane wires. A high voltage of -5.6 kV was applied to the cathode planes of the MWDC's. A voltage of -0.3 kV was applied to the potential wires. A gas mixture of argon (70%), iso-butane (30%), and iso-propyl-alcohol (vapor pressure at 2 ℃) was used. Signals from the anode wire were pre-amplified and discriminated by the LeCroy 2735DC cards. Time information was obtained by using the LeCroy 3377 Time to Digital Converters (TDC's). See Sec. 4.2 for reconstruction of particle trajectory.

The PS's gave information on energy loss for particle identification and trigger signals for the data acquisition system. The scintillation light was detected by the photomultiplier tubes (PMT's) on both sides of each PS. Signals from the PMT's were digitized by the LeCroy FERA and FERET system. See Secs. 4.1 and 2.2 for the particle identification and the trigger system, respectively. An aluminium plate with a thickness of 10 mm (or 5 mm) was placed between the PS1 and the PS2 to reduce background due to Compton scattered electrons by background γ-rays. The aluminium plate, however, decreases the trigger efficiency because a few percent of true events of protons may be scattered out. To save them, the trigger efficiency using the aluminium plate has been calibrated by using the triplet scintillation counters employing the 295 MeV proton beams [29]. The trigger efficiency is summarized in Table 2.3, and they were used to deduce absolute cross sections as τ in Eq. 4.14 (Sec. 4.7).

2.1.5 Large Acceptance Spectrometer (LAS)

The LAS [30] is a QD type spectrometer with a large acceptance in terms of momentum of $\delta p/p = 30\%$ and a solid angle of 20 msr. The configuration of the LAS is illustrated in Fig. 2.7. The specifications of the LAS are summarized in Table 2.1. The LAS was placed at 60° throughout the experiment to monitor the beam position in the vertical direction

Table 2.2: The specifications of the MWDC of the GR spectrometer.

Wire configuration	X(0°=vertical), U(48.2°)
Active area	$1150^{w} \times 120^{H}$ mm
Number of sense wires	192 (X), 208 (U)
Cathode-anode gap	10 mm
Anode wire spacing	2 mm
Sense wire spacing	6 mm (X),4 mm (U)
Sense wires	20μmϕ gold-plated tungsten wire
Potential wires	50μmϕ beryllium-copper wire
Cathode	10μm carbon-aramid film
Cathode voltage	-5.6 kV
Potential-wire voltage	-0.3 kV
Gas mixture	Argon(70%) + Iso-butane(30%)
	+ Iso-propyl-alcohol(vapor pressure at 2 ℃)
Gas seal	12.5 μm aramid film
Pre-amplifier	LeCroy 2735DC
TDC	LeCroy 3377

Table 2.3: The trigger efficiency in using the aluminium plate [29]. The efficiency is used as τ in Eq. 4.14 to deduce an absolute cross section.

Aluminiumu	τ
5 mm	0.984(1)
10 mm	0.978(1)

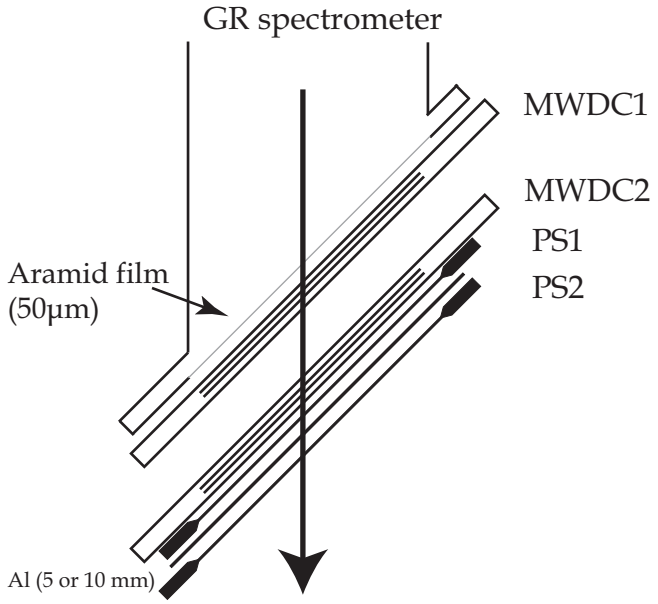

Figure 2.6: The focal plane detector system of the GR.

at the target by mainly measuring the quasi-free scattered protons from the target. The angle of 60° was the most forward angle when the GR was placed at 0°.

The focal plane detector system of the LAS [31] consisted of two MWDC's and two planes of plastic scintillator counters (PS1 and PS2) as shown in Fig. 2.8. The specifications of the MWDC's of the LAS are summarized in Table 2.4. Each MWDC had three anode wire planes (X, U, and V). The tilting angle of the U (V) plane wires was 31° (−31°) relative to the vertical X plane ones. Voltages of −5.3 kV and −0.3 kV were applied to the cathode plane of the MWDC 's and to the potential wires in the U and V planes, respectively. The X plane was not used. The same gas mixture with the GR MWPC's was employed.

Each of PS1 and PS2 consisted of three scintillation counters of 196 × 15 × 0.6 cm^3 to cover the whole area of the focal plane of the LAS. Only the middle counters of the PS1 and the PS2, however, were used for the present experiment since scattered protons from the target were collimated in ±69 mrad (horizontal) and ±6.9 mrad (vertical) by the slit (Sec. 2.1.6) and a large acceptance of the LAS was not required. The signals from the PS1 and the PS2 were used to trigger the circuit of the LAS detector (see Sec. 2.2).

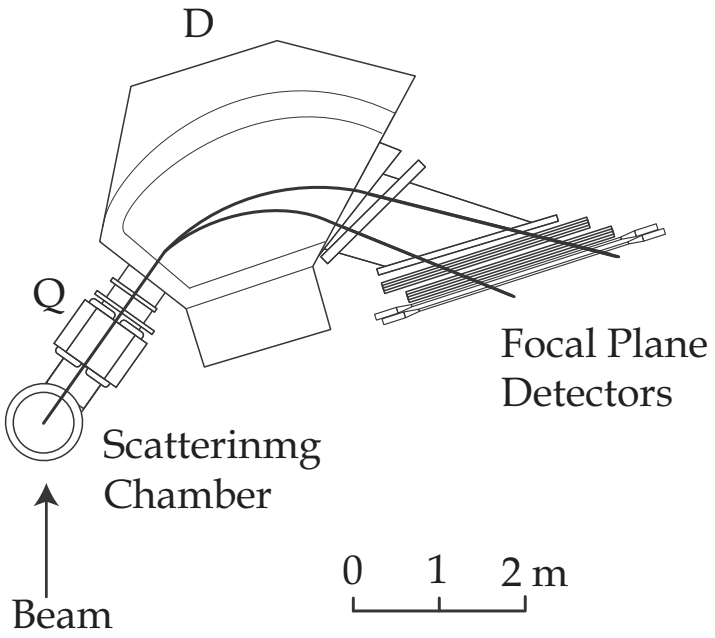

Figure 2.7: The configuration of the LAS.

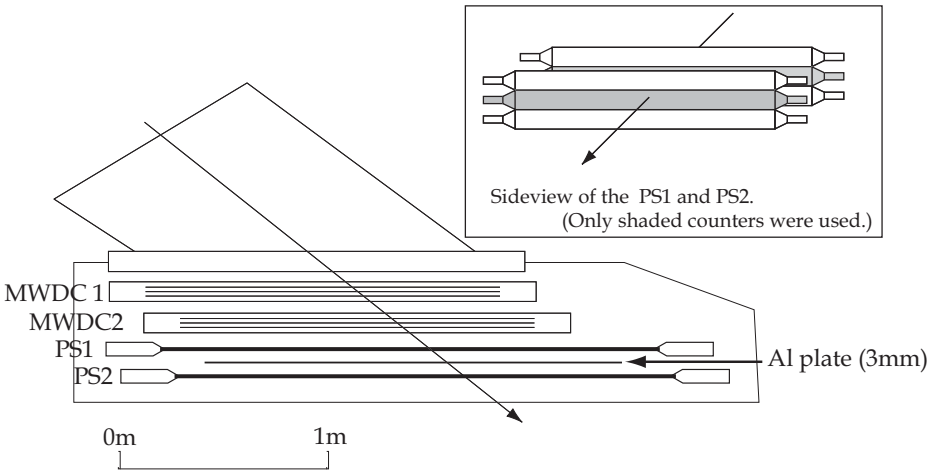

Figure 2.8: The focal plane detector system of the LAS. The PS1 (PS2) consisted of three scintillation counters. Only the middle ones were used because particles scattered from the target were collimated in ±69 mrad (horizontal) and ±6.9 mrad (vertical).

Table 2.4: The specifications of the MWDC's of the LAS.

Wire configuration	X(0°=vertical), U(−31°) , V(+31°)
Active area	$1700^{w} \times 350^{H}$ mm
Number of sense wires	272 (X), 256 (U, V)
Cathode-anode gap	10 mm
Anode wire spacing	2 mm (X), 2.33 mm (U,V)
Sense wire spacing	6 mm (X), 7 mm (U,V)
Sense wires	20μmϕ gold-plated tungsten wire
Potential wires	50μmϕ beryllium-copper wire
Cathode	10μm carbon-aramid film
Cathode voltage	−5.3 kV
Potential-wire voltage	−0.3 kV
Gas mixture	argon(70%) + iso-butane(30%)
	+ iso-propyl-alcohol(vapor pressure at 2 ℃)
Gas seal	25 μm aramid film
Pre-amplifier	LeCroy 2735DC
TDC	LeCroy 3377

2.1.6 Faraday cups and slits

Faraday cups

The primary beam after passing the target was stopped by a Faraday cup (FC). Three kinds of FC's were used depending on the angle of the GR. Their positions are shown in Figs. 2.3 and 2.5. The 0° FC was used in the measurement at 0°. The Q1FC [32] placed at the exit of the first Q1 magnet was used for the measurements at 2.5° and 4.5°. For the inelastic scattering measurement at 6−14° and the elastic scattering measurement at 6−30°, the primary beam was stopped by the SCFC in the scattering chamber.

The charge collection due to the beam transmission to the 0° and the Q1 FC's was compared to that of the SCFC because the absolute efficiency for the charge collection by the SCFC has been calibrated [29]. The efficiency of the SCFC has been $0.986(8) \times Q$, where Q is the beam charges read by the SCFC. The efficiency value 0.986(8) is expressed as ϵ in Eq. 4.14. The ratio of the total events counted by the BLP to the charges collected was measured for each FC. The ratio of the 0° FC (Q1FC) becomes larger than that of the SCFC if a charge collection is not perfect due to an incomplete beam transmission to 0° FC (Q1FC). The measurement for the ratio was performed in two different ways. **Method 1**: with placing a BLP target in the beam, the ratio was periodically measured for the 0° FC (Q1FC) and the SCFC. **Method 2**: with periodically moving a BLP target in and out of beam, the ratio was measured during the inelastic scattering measurement for 10 s in every 99 s. In the first 10 s, the ratio was measured inserting the BLP target, and the inelastic scattering was measured with removing the BLP target in the left time. The ratio of each FC was averaged through the experiment in the Method 2. In each method, an aramid film was used as the BLP target (see Sec. 2.1.2 and Chap. F) and a target was set in the scattering chamber. The deviations of the ratio of the 0° FC (Q1FC) from that of the SCFC in each experiment are shown in the Fig. 2.9. The experiments were held five times in total. In the last one, the measurement at 0° was not carried out. The method 2 was performed in the third and the fourth experiments. The result of the two methods was consistent within error bars. It was found that the charge collection in the 0° FC and the Q1FC should be corrected. because their deviations were not zero. The fact that the deviation value was not zero indicated the beam loss in the beam line.

As summarized in Table 2.5, the relative efficiency due to the charge collection and the beam loss in the experiment measured by the 0°FC and the Q1FC was 1.032(3) and 1.008(4), respectively. These values were used as c_{rel} in Eq. 4.14 for the correction between the FC's. The standard deviation was taken as the errors. Only for the 0° measurement in the third experiment, the efficiency of 1.061(8) was used because the deviation originated mainly from not the charge collection of the FC but the beam loss depending on the beam transportation.

The method 2 was intended also to monitor a change of the beam transmission (the beam loss in the beam line) to each FC during the experiment. The trend of the beam transmission is shown in Fig. 2.10 by normalizing the vertical axis. The difference of the event rates between the BLP1 and the BLP2 is due to an areal density of the BLP target. It is clear that the beam transmission to each FC was stable throughout the experiment. The correction between the FC's, however, was found to be applied because the averaged values for the 0°FC and the Q1FC were slightly higher than that for the SCFC. The correction for the FC's is summarized in Table 2.5.

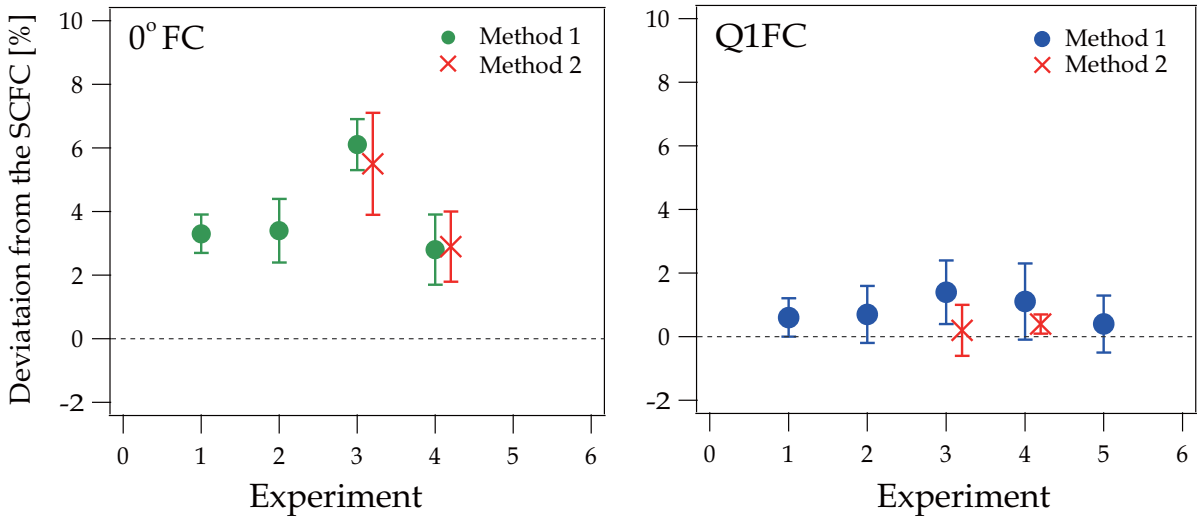

Figure 2.9: The deviation of the charge collection and the beam loss measured by the 0°FC (Q1FC) from that of the SCFC in each experiment.

Table 2.5: The relative efficiency of the charge collection and the beam transmission compared to that of the SCFC. See the text for the method 1 and 2.

FC	c_{rel}
0°FC	1.032(3)
	1.061(8)[1]
Q1FC	1.008(4)

[1]For the third experiment.

Slits

For the inelastic scattering measurement at small angles (0°, 2.5°, and 4.5°), no slit was placed at the entrance of the GR in order to reduce extra scattering in the beam line. For

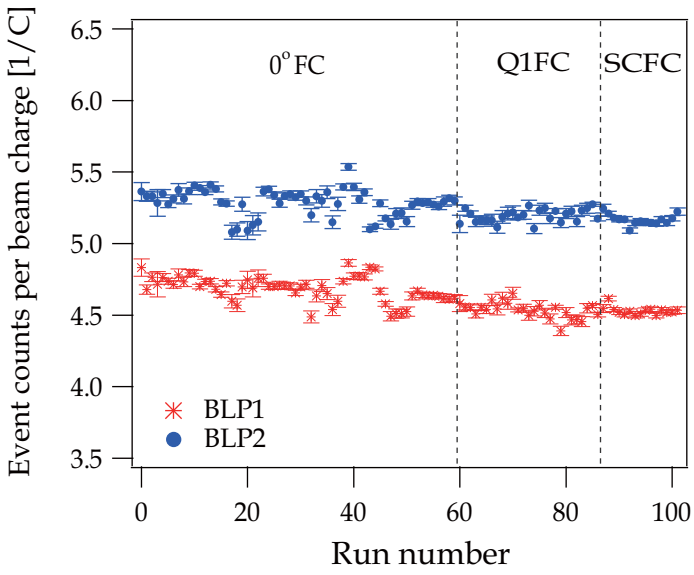

Figure 2.10: The trend of the beam transmission measured in the method 2. Event rates taken by the BLP per beam charge measured each FC are plotted. The vertical axis is normalized. The transmission was stable throughout the experiment. The averaged values in the 0° FC and the Q1FC are shown in Fig. 2.9 with the normalization by that of the SCFC.

---

the inelastic and elastic scattering measurement at more than 6°, a slit with an acceptance of ±20 mrad (horizontal) and ±30 mrad (vertical) was used.

A slit with a taper [33] was set at the entrance of the LAS, where was 580 mm downstream of the target. The slit determined the opening angle of the LAS to be ±69 mrad (horizontal) and ±6.9 mrad (vertical).

2.2 Trigger and data acquisition system

The schematic diagram of the trigger circuits for the GR and the LAS detector systems is shown in Fig. 2.11. Charge signals generated in the PS's were obtained from the left (-L) and the right (-R) PMT's. A PMT output was divided into two signals; one was sent to a FERA (Fast Encoding and Readout ADC (analog-to-digital converter)) module for pulse height measurement and the other was discriminated by a CFD (Constant Fraction Discriminator). A CFD output was further divided into two signals. One was transmitted to a FERET (Fast Encoding and Readout TDC system consisting of TFC's (time to FERA converter) and FERA's for time-of-flight information. The other signal was sent to a Mean Timer circuit, to generate a coincidence signal of the two PMT-outputs at the both ends of the same scintillator. The trigger system was constructed by using LeCroy 2366 Universal Logic Module (ULM) of the field programmable gate-array (FPGA) chips [34]. The trigger

system received signals from the output of the Mean Timer and then internally generated the trigger signal for the GR (LAS) data acquisition system. A typical trigger rate of the GR detectors was 3 kHz in the 0° measurement.

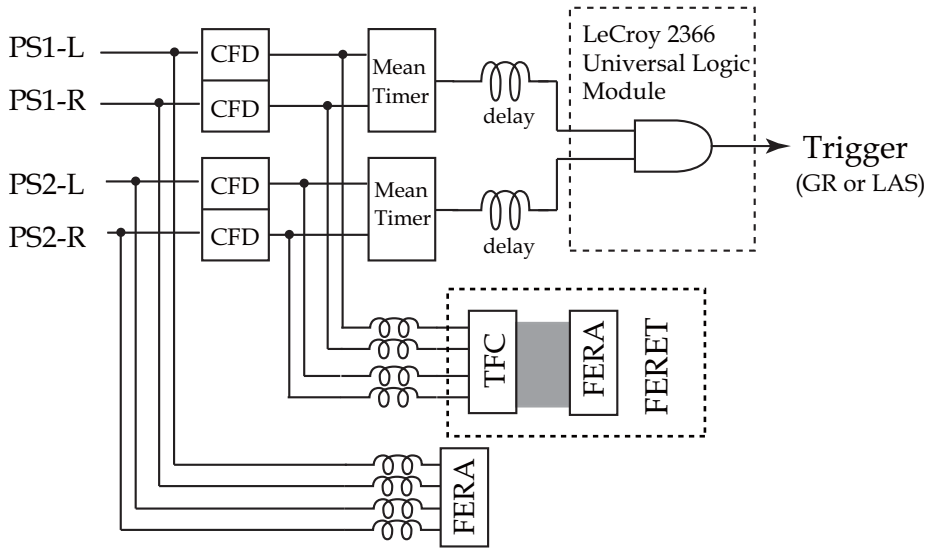

Figure 2.11: Schematic diagram of the trigger circuit of the GR (LAS) detector system.

The block diagram of the data acquisition (DAQ) system [35] for the focal plane detectors in the GR spectrometer or the LAS is illustrated in Fig. 2.12. Data taken in the present experiment consisted of electron drift time from the MWDC's and charge and timing signals from the PS's. For the consistency of data flow, an event header, an event number, and input register words were added to every event by the Flow Controlling Event Tagger (FCET) [36]. The digitized data from each detector were transferred in parallel via an ECL bus to a high speed memory module (HSM) in the VME crate (Lecroy 1191 Dual Port Memory) without any management by a software. To reduce dead time to be caused by the data transfer, a pair of the HSM's were used as a double buffer. The typical live time fraction of the DAQ system was 90% for the GR detectors in the 0° measurement. The data stored in the HSM's were moved via a gigabit Ethernet to an IBM RS/6000SP (later replaced to an IBM eServer p5 595) work station. The data were finally stored in the 480 GByte local hard disk of the work station. The event building and online data analysis were also performed on this computer.

2.3 Beam tuning

A single turn extraction from the accelerators is indispensable for the (p, p') experiment at 0° with high energy-resolution [20]. In this section, a beam tuning after the beam entering in the WS hall is described. The following procedure required 1−1.5 days typically in

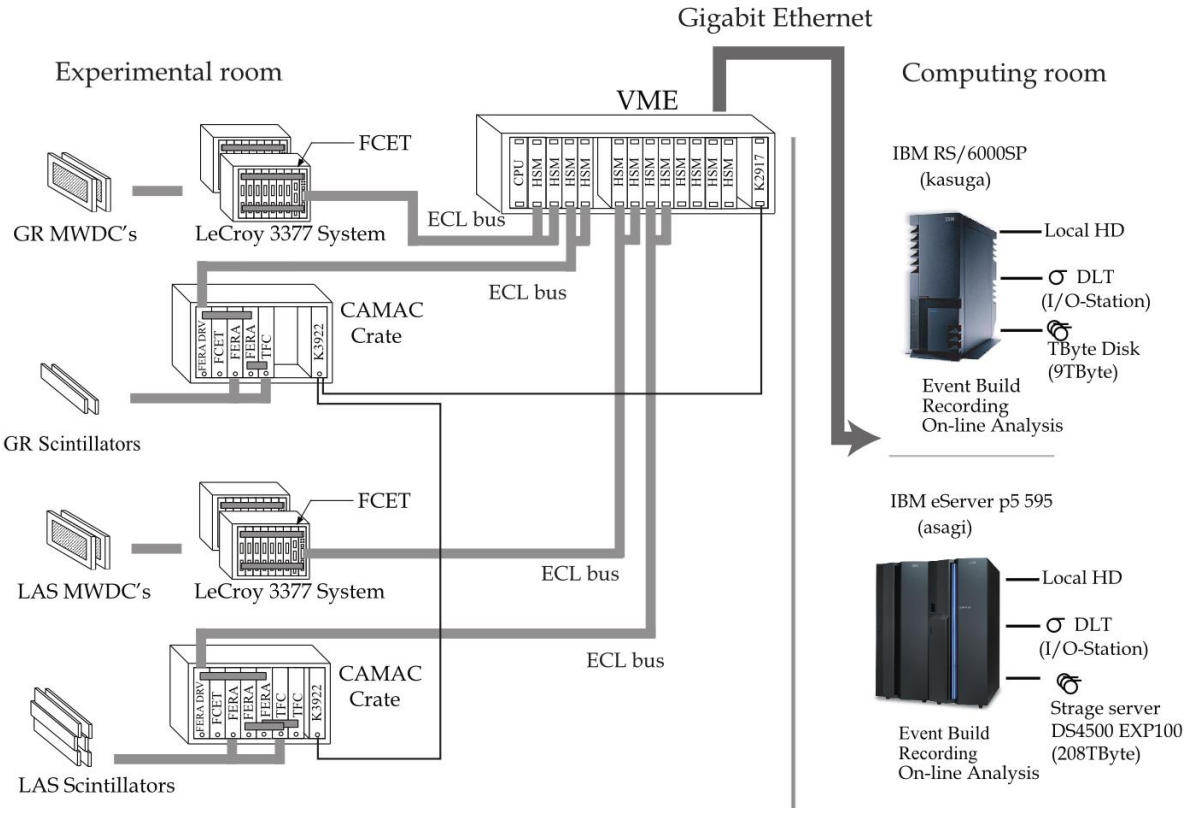

Figure 2.12: Schematic view of the data acquisition system.

total.

Achromatic beam tuning

First, a beam tuning in the achromatic transportation mode was performed by using the GR. The proton elastic scattering on the ^{197}Au foil target with an areal density of 1.68 mg/cm^2 at 8°was measured to study the momentum dispersion of the beam. A gold target is ideal to examine beam quality because of the availability of thin foils and the small kinematical effect to change the proton energy depending on the scattering angle. The beam transportation till the RING cyclotron was tuned to achieve an energy resolution of 35−40 keV (FWHM) typically. Figure 2.13 shows the best energy resolution of 31 keV (FWHM) with online analysis.

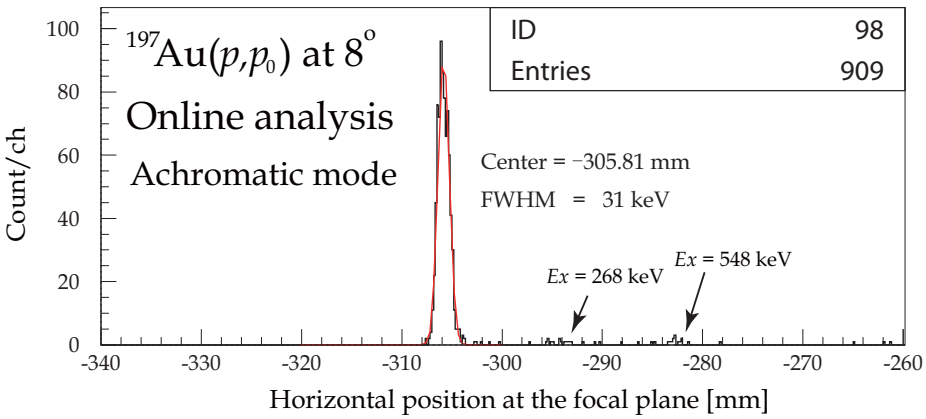

Figure 2.13: The best energy resolution of 31 keV (FWHM) obtained by the online analysis in the achromatic beam transportation. The energy resolution corresponds to the momentum dispersion of the beam. The reaction was ^{197}Au(p, p_0) at 8°. The areal density of the target was 1.68 mg/cm^2.

Halo-free tuning

Second, a tuning to reduce a halo component of the beam was performed. The GR was set at 0° and a beam duct to the 0° FC was connected. The high voltages to the cathode of the MWDC's were turned off for safety. A blank target *i.e.*, a target holder without a target foil, was placed in the scattering chamber. A primary beam was led to the 0° FC by finely tuning the magnetic fields of the D1, D2, and DSR of the GR monitoring the beam position on the three beam viewers drawn in Fig. 2.4. After the beam transmission to the 0° FC, a halo-component of the beam was studied by a count rate of the trigger scintillator of the GR. The count rate was mainly due to background originated from scattering of a halo of the beam on the target holder. Starting from the trigger rate at the GR counter of more than 1 kHz/nA, the rate was reduced below 100 Hz/nA by adjusting parameters

of the beam line, mainly beam collimators and quadrupole magnets, between the AVF and the RING.

Dispersion matching

Finally, the beam line operation was switched to the dispersive mode [23] for dispersion matching with the GR spectrometer [21, 22]. A faint beam with an intensity of $\sim 10^3$ particles/s was transported to the central at the GR focal plane so that the beam width was directly profiled by the focal plane detector. A blank target was used. The lateral and angular dispersion matching conditions were realized by adjusting quadrupole fields in the WS beam line to minimize the size of both the lateral and the angular spreads of the beam at the focal plane [22]. An energy resolution of 12 keV (FWHM) was typically achieved by the dispersion matching for a faint beam of an energy spread of 35 keV. Figure 2.14 shows a typical result with a foil target after the dispersion matching. Excitation energies and spin-parities were taken from the data base of Ref. [37].

After establishing the matching condition, all the magnetic fields of the WS beam line, except for the dipole fields, were fixed during the experiment.

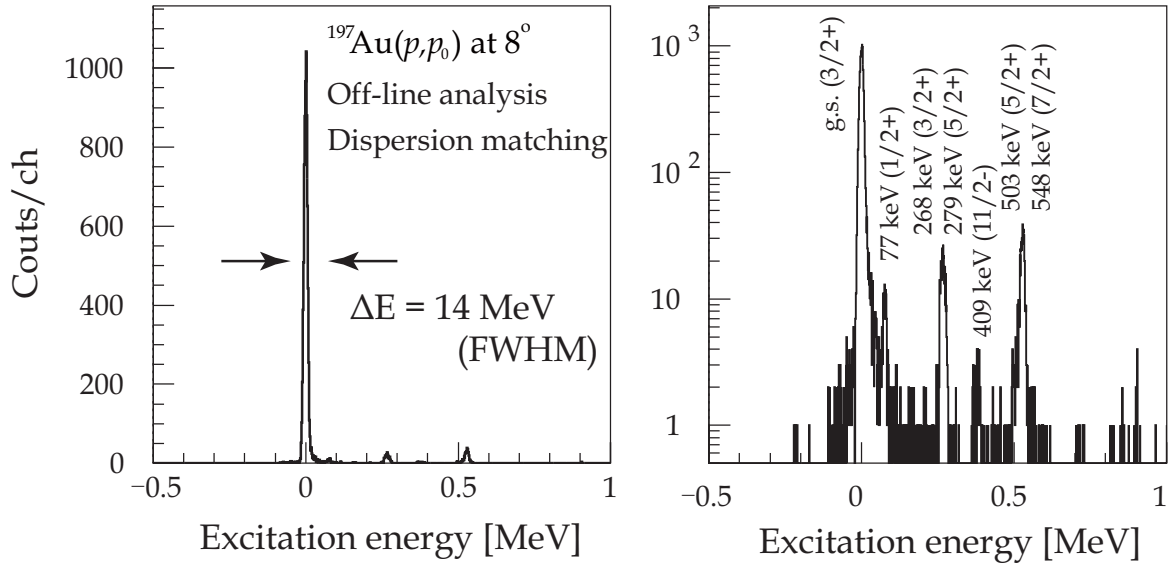

Figure 2.14: A typical result of energy resolution of 14 keV (FWHM) was achieved in the $^{197}\mathrm{Au}(p, p_0)$ reaction using 295 MeV proton beams at 8° by employing dispersion matching. The same energy spectra are scaled in linear and logarithms in the right and left panel, respectively. Excitation energies and spin-parities were taken from the data base of Ref. [37]

2.4 "Under focus" mode

Purpose of under focus mode

The GR spectrometer was operated in the under focus mode, decreasing the magnetic field of the first quadrupole Q1 magnet by 5% relative to the standard setting, for the two purposes *i.e.*, a software-cut of the data in terms of scattering angles at the target position and an improvement of the scattering angle measurement. Since a slit to determine the solid angle of GR spectrometer was not used in the measurement at 0°, a software-cut is expected to be applied for the data analysis. In the measurement at 0°, both the scattering angular resolution in the horizontal and the vertical planes at the target position equally affects the total scattering angle resolution. In the standard magnetic filed setting, the particle trajectories in both the plane are focused at the focal plane. Although the vertical scattering angle is determined from the vertical incidence angle at the focal plane in the standard setting, the vertical scattering angle at the target position is evaluated to be worse than 1° owing to the small vertical angular magnification of 1/5.98. Since the horizontal scattering angle resolution at the target position is evaluated to be better than $0.1-0.2°$ from the horizontal scattering angle at the focal plane, the improvement of the measurement for the vertical scattering at the target position is desired for a better level accuracy of the scattering angle. Thus, the vertical position was measured at an off-focus plane for the vertical scattering angle at the target position under the setting of the under focus mode [38].

With the under focus mode, the angle resolution in the vertical direction was improved to be $0.5-0.6°$from 1°. See Sec. 4.3 for the reconstruction from the vertical position to the vertical scattering angle.

Sieve-slit measurement

An ion optics of the under focus mode should be known to reconstruct the scattering angles at the target position from the particle information measured by the focal plane detector. For this purpose, the sieve-slit measurement was performed as described in the followings. The sieve-slit had several through holes on a brass plate as shown in Fig. 2.15. The diameter of the holes was 2 mm except for the one at the center. The central hole was 3 mm in diameter. The slit was placed at the entrance of the GR, 638 mm downstream of the target position. Particles scattered on the target passed through the holes of the slit, and were measured by the focal plane detector. Thus, the vertical position and angle of the particle measured by the focal plane detector can be connected to scattering angle at the target position based on the distance between the target and the holes. The ^{58}Ni(p, p_0) reaction at 15° was employed as the sieve-slit measurement. The areal density of the target was 100 mg/cm^2. The D1 and D2 magnetic fields of the GR

spectrometer was increased by 1.0%, 1.8%, 2.6%, 3.4%, and 4.2% relative to the standard setting for the optics study in terms of the horizontal position dependence. Those position corresponded to the excitation energies of 6, 10, 14, 18, and 22 MeV, respectively, in the (p, p') measurement at 0°. The beam spot position at the target was artificially shifted to ± 1 mm in the vertical direction for the study of the beam position dependence. In total, 15 sets of the sieve-slit data were taken. The reconstruction of the scattering angle is described in Sec. 4.3.

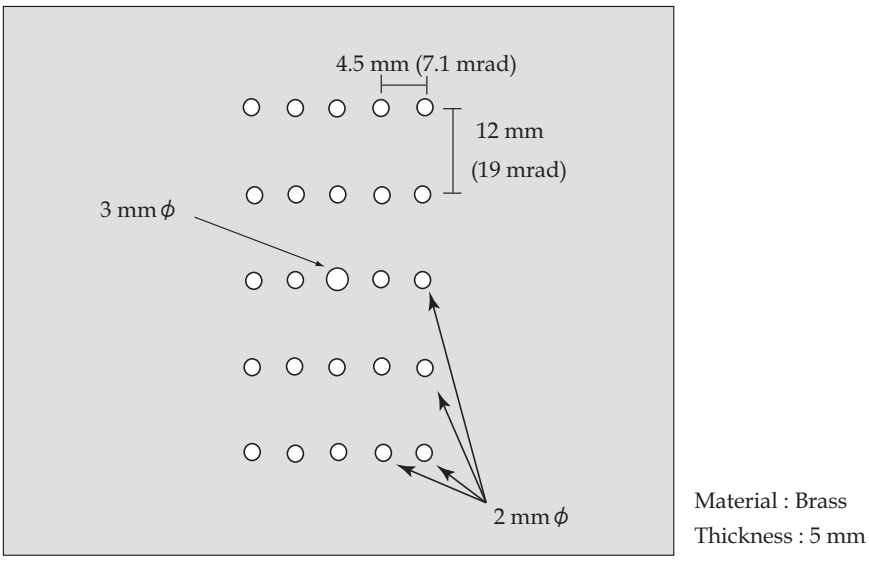

Figure 2.15: The design of the sieve-slit used for the study of an ion optics in the under focus mode.

Chapter 3

Targets

Eight nuclei of ^{12}C, ^{16}O, ^{20}Ne, ^{24}Mg, ^{28}Si, ^{32}S, ^{36}Ar, and ^{40}Ca were employed for the proton inelastic scattering measurement at 0° with high energy-resolution. Some nuclei of them have to be arranged to be employed as a target for the experiment.

3.1 Requirement for target

A target with a size of $\sim 2 \times 2$ cm^2 is required for use in measurements using a dispersed beam at 0° at the Grand Raiden spectrometer. As shown in Fig. 3.1, a target width of 2 cm is required in one direction to account for the dispersed beam, and a target height of 2 cm is required in the other direction with a target frame having a window height of 14 mm. The beam spot of a dispersed beam at the position of the target in the WS beam line of the RCNP is broad in the horizontal (dispersive) direction and narrow in the vertical direction. The horizontal size of the beam is evaluated to be approximately 7 mm if the 300 MeV proton beam with the typical momentum dispersion of 40 keV (FWHM) is employed. In order for the matching condition to be satisfied, a target must be larger than the beam spot. Therefore, the minimum target width should be 10 mm. In addition, for measurements at 0°, sufficient space is required for the beam to pass through without any scattering in the target frame. Even if a halo component of the beam would cause an unacceptably large number of events in the frame, a huge number of background events hides the true events. The typical target frame used at the RCNP has a window size of 44 mm in the horizontal (dispersive) direction and 14 mm in the vertical direction, as shown in Fig. 3.1. Because the target frame is required to hold a target, the length of the target must preferably be $\sim$20 mm.

Furthermore, since it is desirable to have a minimum number of impurities in a target, a self-supporting target made of the isotopically pure element is most suited for scattering experiments. If a target contains backing material or is formed from a chemical compound, contaminant peaks must be identified in a scattering energy spectrum. In medium energy-

resolution measurements, physical background events attributed to contaminant materials can be subtracted by measuring the corresponding excitation energy spectra of the backing material. In contrast, for high energy-resolution measurement, such subtraction is not practical because of the following reason. Even if the thickness of the backing material used for the background measurement is adjusted to be equal to that of the main target, conditions such as angular spread and energy loss in the target would never be identical. No other background target would have the same density distribution of nuclei as that of the backing of the original target. Therefore, the energy resolution and scattering angle resolution would not be reproduced precisely, causing difficulty in a background subtraction. This difficulty increases with an increase in the energy resolution.

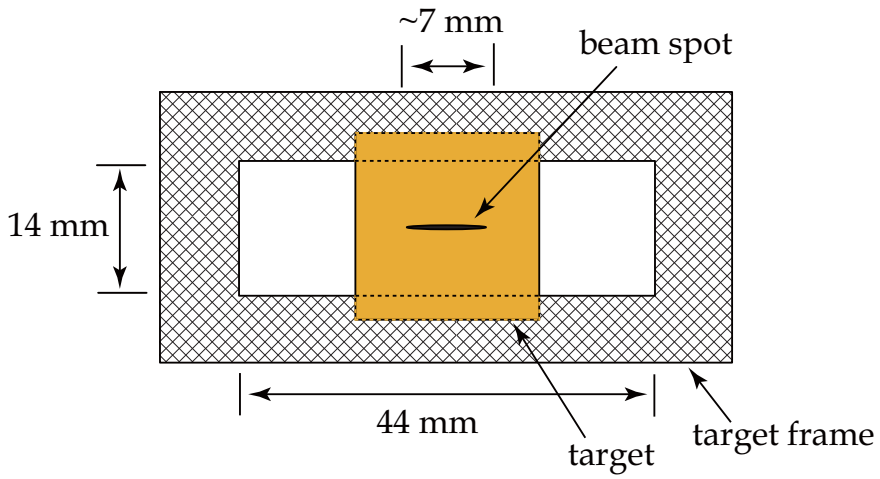

Figure 3.1: Schematic view of target and target frame used at the RCNP together with the spot of a dispersed beam. The target size must be $\sim 2 \times 2$ cm^2 for it to be employed with the frame. In addition, an aluminium foil is used to mount an ice target (Sec. 3.2.2) and a sulfur target.

3.2 Targets preparation

Table 3.1 summarizes the targets used in the experiment. The error of an areal density is assumed to be 1% if it is unknown. Three kinds of new developments for targets to be used in the (p, p') experiment at 0° with high energy-resolution were performed for the self-supporting target of ^{16}O and ^{32}S, and for the gas target of ^{20}Ne and ^{36}Ar. In the following, the target preparation and the usage in each target are briefly described.

3.2.1 Carbon, magnesium, silicon, and calcium

A metallic foil of ^{12}C, ^{24}Mg, ^{28}Si, and ^{40}Ca were simply prepared and used with the target frame as a self-supporting target. The thicker ones of ^{12}C, ^{24}Mg, and ^{28}Si were mainly used

Table 3.1: The targets used in the experiment. The error of an areal density for ^{20}Ne and ^{36}Ar originates from the uncertainties of the cell length.

Nucleus	State	Areal density (mg/cm^2)	Enrichment (%)	Comment
^{12}C	foil	30.0(3)	98.93	
	foil	1.02(1)	98.93	
^{16}O	ice sheet	10.0(7)	99.76	on the cooled ladder [39]
SiO_2	glass	6.2(1)		
^{20}Ne	gas	1.06(3)	100	with aramid
^{24}Mg	foil	2.50(3)	100	
	foil	50.0(5)	100	
^{28}Si	foil	2.29(2)	92.23	
	foil	58.5(6)	92.23	
^{32}S	sheet	23.5(5)	95.02	on the cooled ladder [39]
	sheet	59.9(6)	95.02	on the cooled ladder [39]
	powder	3.38(3)	100	packed with gold
^{36}Ar	gas	1.04(3)	100	with aramid
^{40}Ca	foil	2.98(3)	100	
	foil	3.55(2)	96.94	

in the elastic scattering measurement for high statistics with sacrificing energy resolution. The ^{24}Mg and ^{40}Ca targets were installed to the target ladder in an atmosphere of argon and carefully employed in the scattering chamber because they were easily oxidized in air.

3.2.2 Oxygen

An ice sheet of a self-supporting type was used as an ^{16}O target by using the cooling target system [39]. The hydrogen atoms in the ice target did not provided any physical background because the difference of the kinematics between hydrogen and oxygen prevented for hydrogen from contaminating into an energy spectrum of ^{16}O at small scattering angles within 5°. The preparation of an ^{16}O target will be described in Sec. 3.2.3. The cooling target system was described in detail in Ref. [39], and its structure was shown in Fig. 3.2. Liquid nitrogen (LN_2) was periodically introduced into the system, and then the target ladder was kept at the temperature of LN_2 to cool the ice target on it. A photograph of an ice target on the cooled ladder is shown in the left panel of Fig. 3.3. The areal density of the ice target was determined to be 10.0 ± 0.7 mg/^{2}from from the cross section value obtained by the SiO_2 target. The error was taken from the mean square error of the cross section. In the right panel of Fig. 3.3, the count rate per the beam charge collection, corresponding to an areal density of the target, in each run is plotted to show the stability of the target. The irradiation was for 10 h. The mean value of the count rate was normalized to unity.

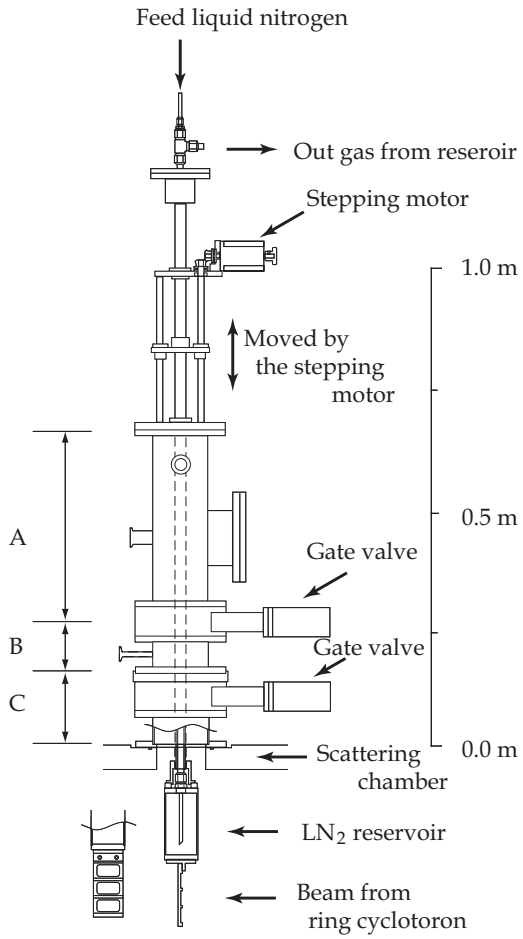

Figure 3.2: The cooing target system developed for the ^{16}O(p,p') experiment at 0° [39].

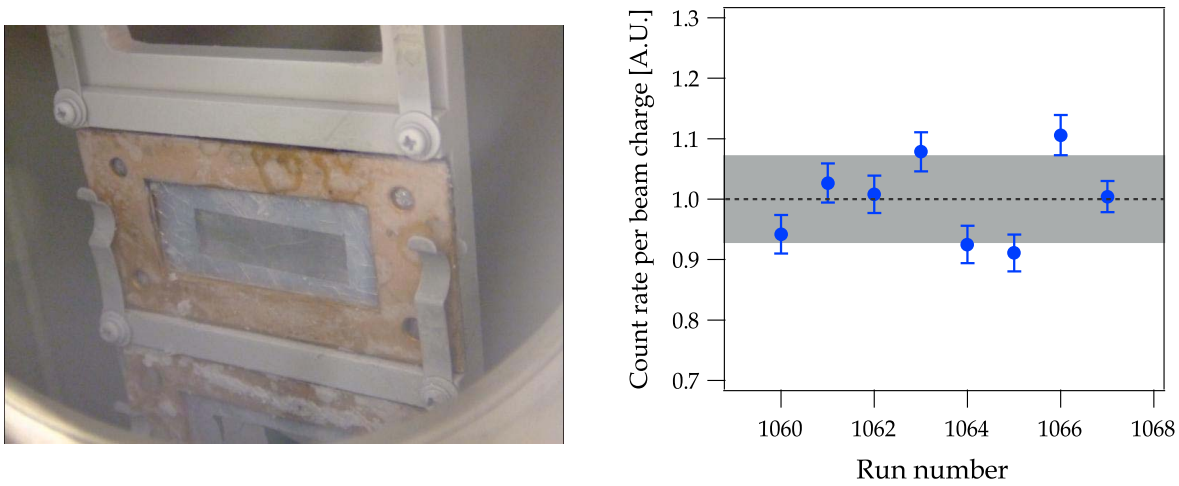

Figure 3.3: (Left): Photograph of the ^{16}O target on the cooled ladder. (Right): The stability of the areal density of the ice target during the measurement. The mean square error of the count rates was $\pm 7\%$ from the mean value, drawn as the shaded area. The mean value was normalized to unity. The time was for 10 h.

3.2.3 Rapid preparation of ice target

The preparation of an ice sheet for an ^{16}O target has been reported in Ref. [39]; a few drops of pure water is poured into a space between polyester films, and then they are cooled in a freezer box of a refrigerator to be frozen. An ice sheet made by this method, however, is often cracked when it is placed on the cooled ladder of the cooling target system since the crystal structure of ice at a temperature in a refrigerator (-18°C) is different from that at a temperature of LN_2 (-196°C).

A new method to freeze an ice sheet in a second by LN_2 was developed to reduce a hazard of cracking on the sheet. The process of a rapid preparation of an ice sheet is shown in Fig. 3.4. A few drops of water were poured into a space of polyester film with a size of $\sim 2 \times 2$ cm^2. The thickness of the polyester film of 0.1 mm was selected to determine an areal density of an ^{16}O target to be 10 mg/cm^2. The water was poured on an aluminium foil with a window of 25×8 mm^2. The thickness of the aluminium was 12 μm. See Ref. [39] for the role of the aluminium. The water and the aluminium foil were sandwiched by two polyester films to pack the water inside. Then, they were further sandwiched by two copper plates. The two copper plates including the water were placed on a copper block that was cooled at a temperature of LN_2. The two copper plates were cooled and then the water inside was frozen in a second through them from the both sides uniformly. LN_2 was stored in a bawl and the copper block was dipped into it (the left panel of Fig. 3.5). After the frozen, the two polyester sheets were carefully opened. A frozen ice sheet often stuck on the aluminium foil in a successful case. The ice sheet on the aluminium foil was pasted on a copper frame that was cooled (the right panel of

Fig. 3.5). The window of the copper frame was the same to that of a standard target frame (Fig. 3.1), 44 × 14 mm^2. Ethyl alcohol was used as an adhesive to fix the aluminium foil on the copper frame because the melting point of ethyl alcohol was −114°C, being lower than that of LN_2.

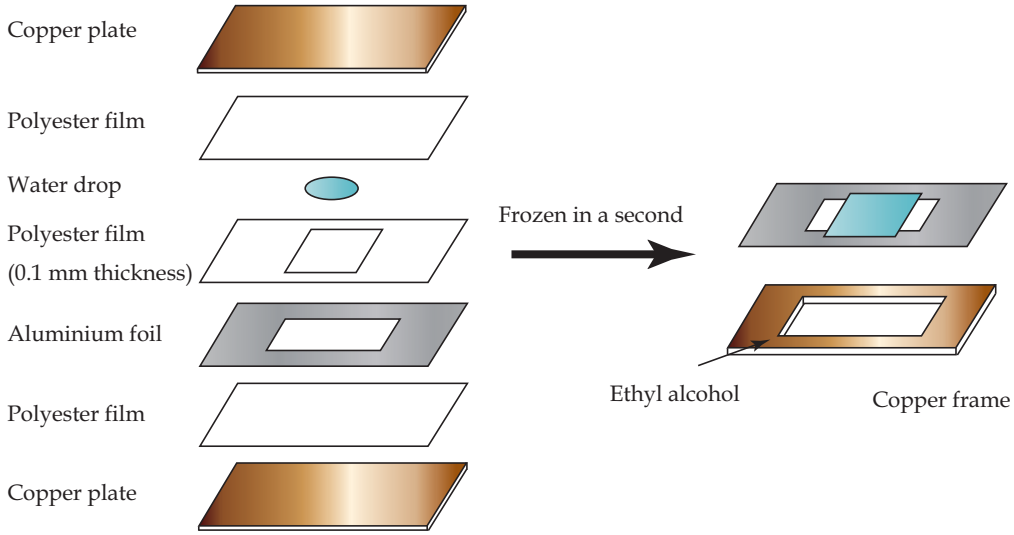

Figure 3.4: Process for preparing a thin ice target with freezing in a second. Two copper plates were used to freeze the whole area from both sides uniformly. Ethyl alcohol was pasted on the copper frame to fix the aluminium foil.

Figure 3.5: Photograph in preparing an ice target by the rapid preparation technique. (Left): A copper block in a bawl is cooled by LN_2. (Right): An ice sheet on the aluminium foil and the copper frame.

3.2.4 Sulfur

A self-supporting and elemental sulfur target was successfully used for the first time. Elemental sulfur sublimates in vacuum due to the heat by the energy loss in the target with an irradiation of charged particles. In order to reduce the sublimation process, the

sulfur target was placed on the ladder that was cooled by LN_2 using the cooling target system [39] (or see Fig. 3.2). Areal densities of the target used for the inelastic and the elastic scattering measurements were 23.5 ± 0.5 and 58.5 ± 0.6 mg/cm^2, respectively. The photograph of the targets are shown in Fig. 3.6. The areal densities were determined from the cross section value obtained by using the sulfur target that was packed with thin gold layers to prevent the sublimation. The thinner sulfur target was stable for 10 h with an energy deposition in it by a proton beam of 0.2 mW, while the sublimation process was significant with that of 0.6 mW (Fig. 3.7). See Ref. [40] for details.

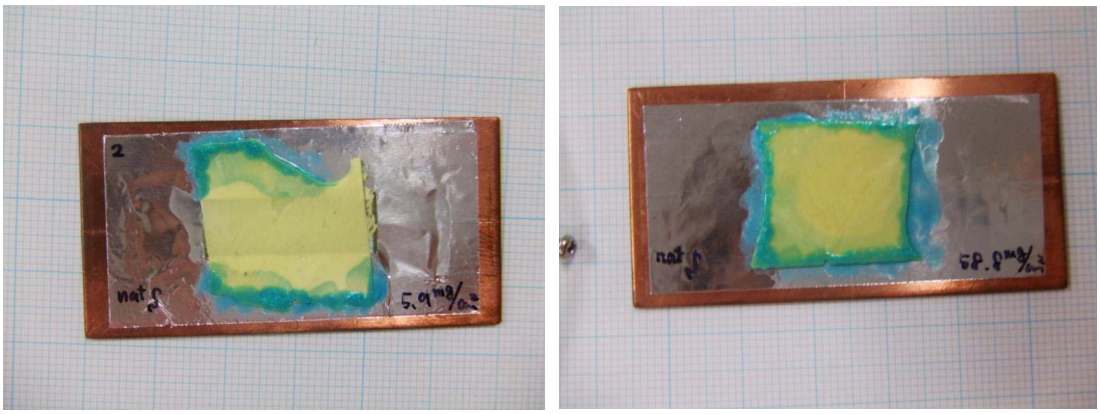

Figure 3.6: Photograph of the sulfur targets on a copper frame. Enamel used to fix the sheet to the aluminium foil is seen in right blue. The areal density is 23.5(5) and 58.5(6) mg/cm^2 from the left, respectively. The number in the photo was found to be incorrect.

3.2.5 Preparation of sulfur targets

Sulfur powders of natural sulfur (^{32}S: 95.02%, ^{33}S: 0.75%, and ^{34}S: 4.21%) and isotropically enriched ^{32}S (>99.86%) are prepared and made molten. No special treatment was required when using the enriched isotope in the procedure described below. Two polytetrafluoroethylene[1] (PTFE) sheets without scratches were used to sandwich and press the molten sulfur. The thickness of the PTFE sheets was 10 mm. This was sufficient for flattening the sulfur sheets. Thinner PTFE sheets tend to bend during heating and cooling. Details are as follows.

First, sulfur powder was placed in a mortar and a pair of PTFE sheets are placed on a hot plate heated to temperature of up to 200−230°C (melting point of sulfur ∼110°C). The sulfur powder melted in the mortar when placed on a hot plate. Sulfur melted to a temperature that is slightly higher than the melting point still appeared yellow (λ-sulfur, shown in the left panel of Fig. 3.8). At 160°C, the colour of the sulfur goes to dark red, indicating a change in the molecular structure and the formation of μ-sulfur

[1]Teflon® (E. I. du Pont de Nemours and Company) is a product of polytetrafluoroethylene.

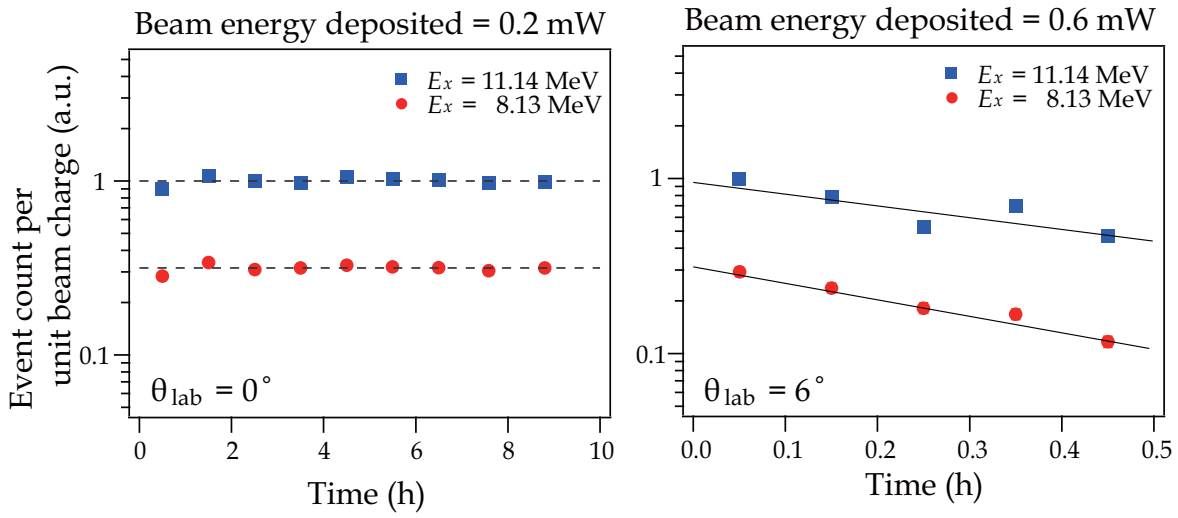

Figure 3.7: Stability of target thickness indicated by the event count per unit beam charge at E_x = 11.14 and 8.13 MeV with a beam energy deposition in the sulfur target of 0.2 mW (left) and 0.6 mW (right). Statistical errors are smaller than the sizes of the symbols. To guide the eye, the mean values of the event rate at $\theta_{lab} = 0°$ are indicated by dashed lines. Solid lines fitted to the data at $\theta_{lab} = 6°$ show the effect of sublimation of the sulfur target.

(shown in the right panel of Fig. 3.8). Since μ-sulfur is sticky and highly viscous, molten sulfur with an intermediate orange colour was poured onto the heated PTFE sheet before the completion of the transformation. A sheet made of molten sulfur that is orange in colour is sturdier than a sheet made of λ-sulfur. It should be noted that sulfur dioxide gas, which is poisonous and flammable, was produced when sulfur was heated, thus requiring a well ventilated room for the process. Feeler gauges (thickness gauges) with an appropriate thickness was used to control the areal density of the sulfur target. Gauges with a thickness between 30−300 μm were set on the PTFE to prepare a sulfur target with areal densities of 6−60 mg/cm^2, respectively. The thinnest successfully prepared target had an areal density of 5.9 mg/cm^2. Molten sulfur was then poured onto an area surrounded by the gauges on the PTFE sheet placed on the hot plate, as shown in Fig. 3.9(a).

The poured molten sulfur was rapidly sandwiched by another PTFE sheet; a brass block used as a weight was placed on top of this sheet to apply a pressure of 12 $\times$ 10^3 Pa. The volume of the block was 500 cm^3. To ensure that the sulfur sheet is sturdy, the molten sulfur must be cooled rapidly. The hot plate was switched off and water was poured rapidly onto it until room temperature was reached. Before use, the brass block should be at room temperature. After cooling by water, the PTFE sheets were carefully separated. The solidified sulfur sheet often sticks to one PTFE sheet without cracking. In such a case, the sheet should be peeled off by bending the PTFE sheet or by using a thin knife. A feeler gauge with a thickness of 10 μm was also useful for peeling. After

drying the sulfur sheet in air, its mass and area were measured to determine the areal density. Drying the sheet in air was important for removing water absorbed during the cooling process.

Finally, the sulfur sheet was mounted on a target frame. The target frame was made of copper because of its high thermal conductivity. As shown in Fig. 3.1, the copper frame has a large window with a size of 44×14 mm^2 in order to prevent the scattering of the halo component of the dispersed beam. Sulfur has a low conductivity. To ensure effective cooling of the sulfur sheet, a thin aluminium foil with a smaller window size of 25×8 mm^2 was firstly pasted onto the copper frame as shown in Fig. 3.9(b) to increase the thermal contact. The thickness of the aluminium foil was 3.2 mg/cm^2. Enamel was then used to fix the sulfur sheet to the aluminium foil. Because the sulfur sheet is cooled in vacuum just through the contact points between the sheet and the foil, it was essential to paste as large an area as possible of the sulfur sheet onto the aluminium foil.

The foil played another crucial role: since its softness would cause a reduction in the stress in the foil caused by the difference between thermal expansion of the sulfur sheet and the copper frame, the hazard of formation of cracks in the sulfur sheet would be prevented. In contrast to the copper frame, the aluminium is relatively soft and helps to prevent cracking of the sulfur foil due to differences between the thermal expansion of the sulfur foil and the copper frame. Figure 3.6 shows the sulfur targets used in the experiment. The left one was used for the inelastic measurement at small scattering angles including 0°. Therefore, the aluminium foil had the window with the size of 25×8 mm^2. The right one in the figure was used for the elastic measurement. Thus, the aluminium foil had a small window of 12 mm in diameter because the measurement was not performed at 0° and an achromatic beam, not broad at the target position, was employed.

The preparation process of the sulfur target is summarized below. It should be noted that in order to prepare a sturdy sheet of sulfur, it is important to perform steps (3) to (5) as rapidly as possible.

1. Heat the sulfur powder in a mortar and a pair of PTFE sheets on a hot plate at 200−230°C.

2. Set feeler gauges on one of the PTFE sheets to control the thickness of the sulfur target.

3. Pour molten sulfur onto the PTFE sheet with the feeler gauges when the sulfur powder melts and its colour has changed from yellow to orange.

4. Sandwich the molten sulfur using the other PTFE sheet, and press it uniformly.

5. Turn off the hot plate and pour water onto it to rapidly cool the molten sulfur.

6. Peel the sulfur sheet off the PTFE sheets.

7. After drying the sulfur sheet in air, measure the mass and area of the sheet to determine its thickness.

8. Paste an aluminium foil onto a copper frame.

9. Use enamel to fix the sulfur sheet to the aluminium foil.

Figure 3.8: Photographs of λ-sulfur (left) and μ-sulfur (right).

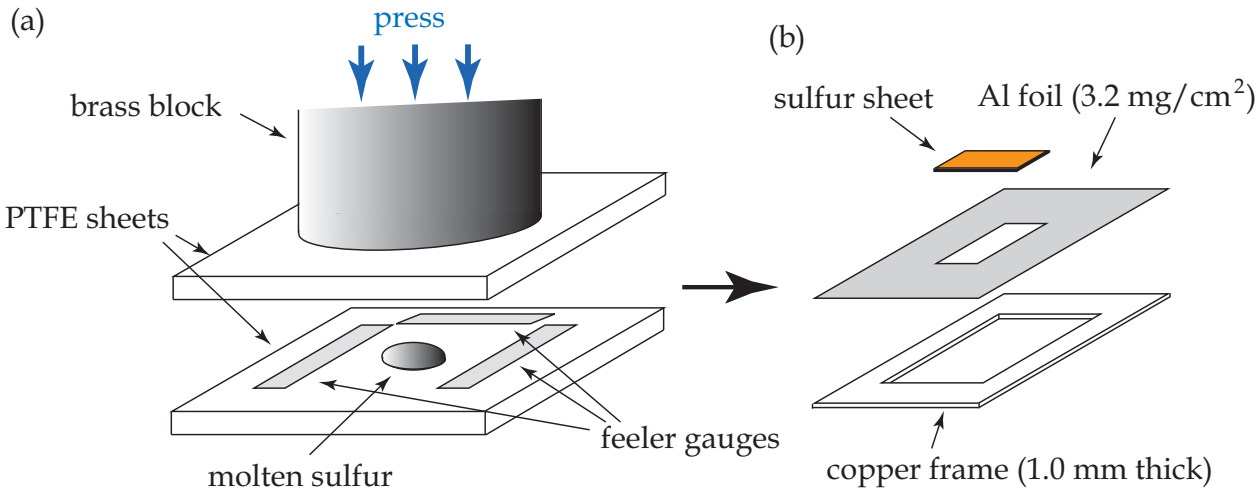

Figure 3.9: Process for preparing elemental sulfur target. (a) Melted sulfur is sandwiched by PTFE sheets and pressed by a brass block. The thickness of the sulfur sheet is determined by the use of the feeler gauges. (b) Sulfur sheet peeled off the PTFE and subsequent mounting using enamel on the aluminium foil attached to copper frame.

3.2.6 Neon and argon

^{20}Ne and ^{36}Ar were used a gas target with the gas target system that was newly developed (Figs. 3.10 and 3.11). The target system consists of the three parts *i.e.*, the target cell, the gas handling, and the cooling parts. The structure of the pipe was illustrated in Fig. 3.12; it is the quadruplet structure for the cooling by using LN_2. The target gas was packed into a cell and was isolated from vacuum by windows of an aramid film (Toray CO., Ltd., Mictron). The aramid film had a compositional formula of $C_{14}O_2N_2Cl_2H_8$, and its thickness was 6 μm. It is to be noted that the compositional formula of the aramid made by Toray CO., Ltd. is different from that by Asahi-kase CO. Ltd that was used as the BLP target (Sec. 2.1.2 and Appendix F). The cell length along the beam direction was adjusted to be 8 mm including an expansion of the aramid windows owing to an inner pressure by using the cover plates made of Al as drawn in Fig. 3.13. A cell length was required to be short for high energy resolution measurement at finite angles. A realistic cell length including an expansion of the windows was determined from the cross section of ^{12}C in CO_2 gas in the cell. The energy resolution achieved with employing the gas target cell is shown in Fig. 3.14. The energy resolution better than 20 keV (FWHM) was achieved at the small scattering angles within 4°. The energy resolution deteriorated at the larger scattering angles because of the finite cell length. An areal density of the ^{20}Ne and ^{36}Ar target was obtained as 1.06 ± 0.03 and 1.04 ± 0.03 mg/cm^2, respectively, following the ideal gas low by using the realistic cell length and by using the data of temperature and pressure electronically monitored in the target cell. The error was attributed mainly from the uncertainty of the cell length. The gas target system had a cooling system by using LN_2 to increase an areal density three times larger. An areal density of 2.08 ± 0.08 mg/cm^2 was obtained for ^{20}Ne with the cooling as shown in Fig. 3.15.

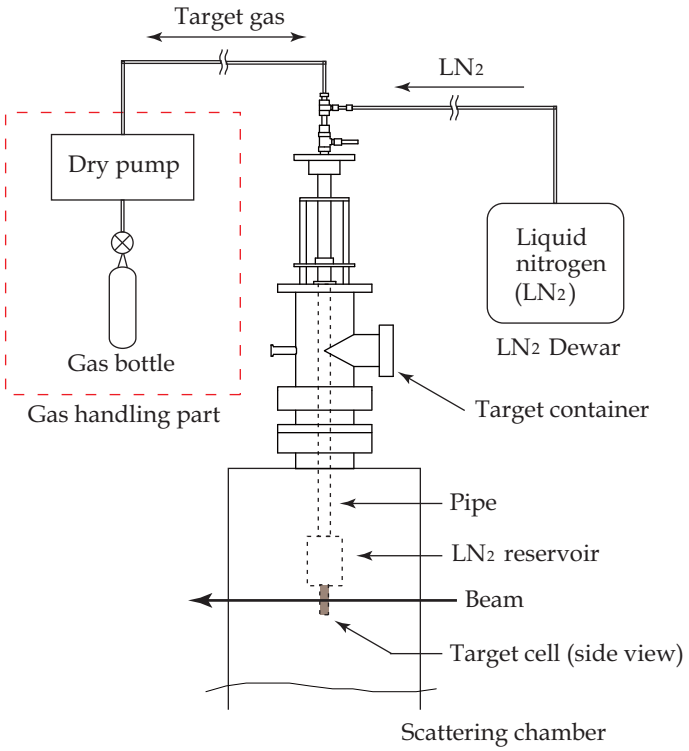

Figure 3.10: A schematic view of the gas target system on the scattering chamber.

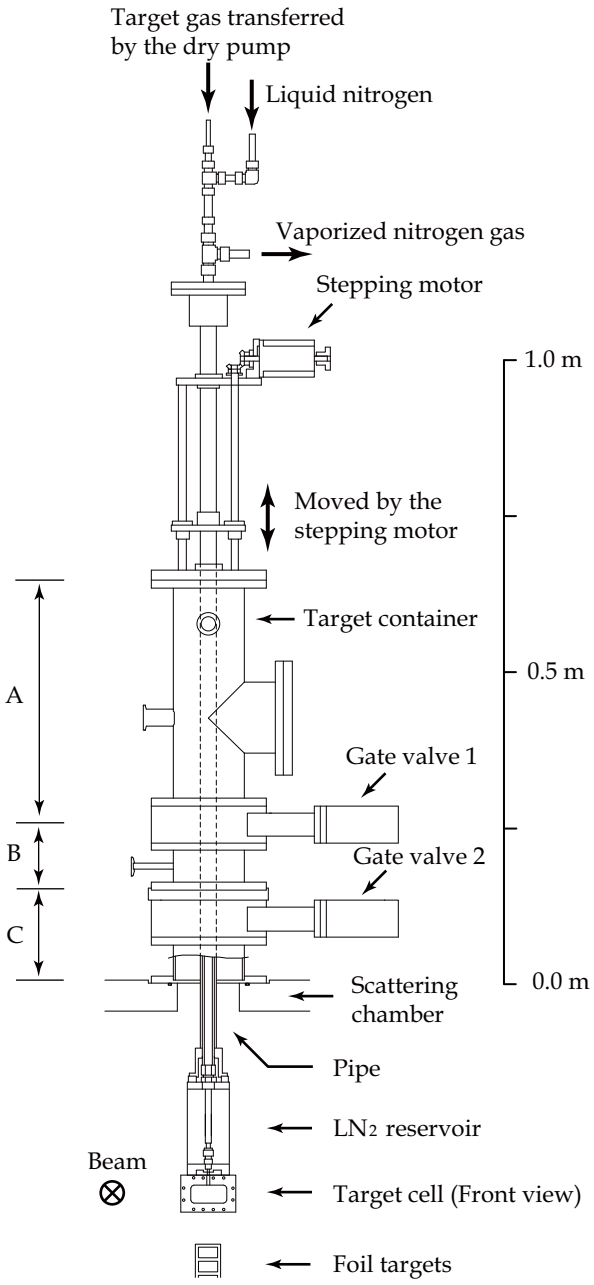

Figure 3.11: A schematic view of the target container and the pipe that passes target gas, LN_2 for cooling, and its vaporized gas.

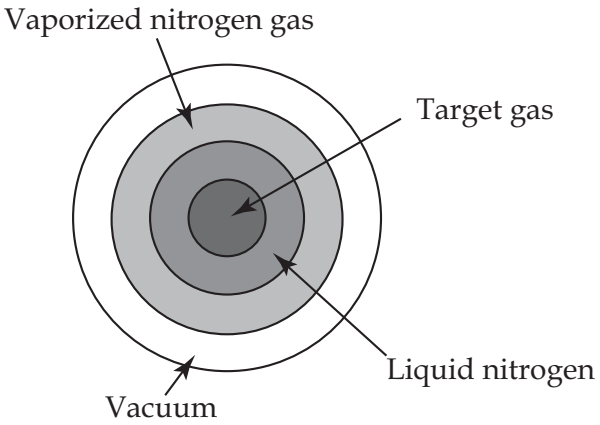

Figure 3.12: A schematic view of cross section of the pipe in the target container. Target gas, liquid nitrogen, and vaporized nitrogen gas are passed through the spaces of each pipe from the central, respectively. The outside pipe is connected to the scattering chamber and is pumped in vacuum to isolate the heat.

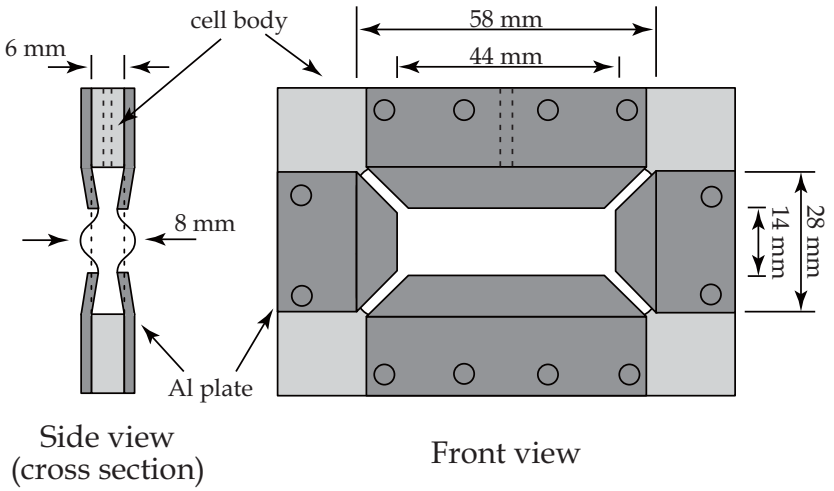

Figure 3.13: A schematic figure of the target cell. The cell body made of copper has a window with the size of $58^W \times 28^H$ mm^2. The thickness of the cell body is 6 mm. Aramid films with the thickness of 6 μm are used as cell windows to contain target gas. The cover plates made of aluminium with the thickness of 2 mm are used to adjust the cell length to 8 mm including an expansion of the films. Polytetrafluoroethy (Teflon®) sheets with the thickness of 0.1 mm are inserted into the space between the aramid film and the cover plate in order to reduce a hazard of the leackage from the flim. Target gas is transferred into the cell from the top through the central pipe that is shown in Fig. 3.12.

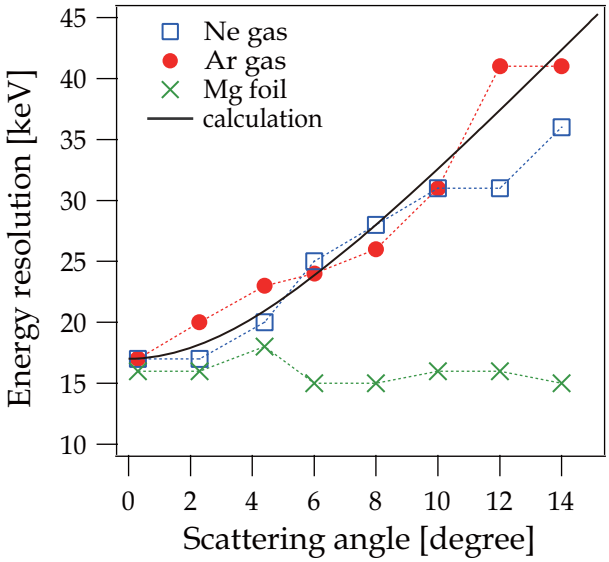

Figure 3.14: Energy resolutions (FWHM) of typical peaks at each scattering angle for the gas of neon and argon with employing the target cell and for a standard foil target of magnesium. The curve corresponds to the calculation using the realistic cell length of 8.5 mm.

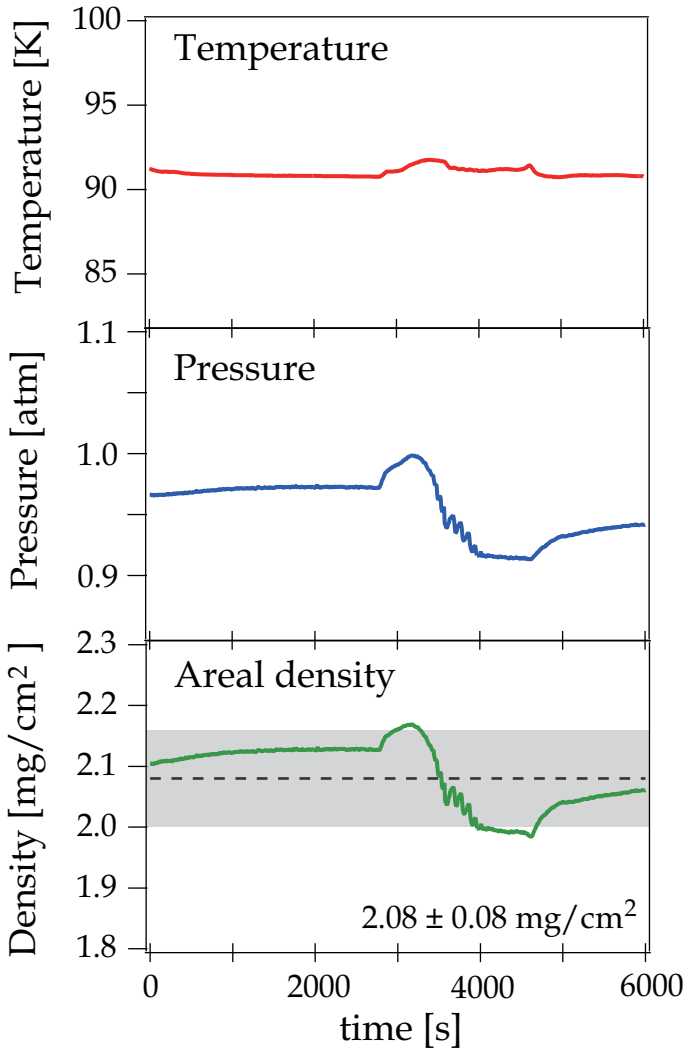

Figure 3.15: Temperature and pressure monitored by the sensors during measurement in cooling, and areal density of ^{20}Ne deduced with the cell length of 8.2 ± 0.3 mm. The mean value of the areal density is 2.08 ± 0.08 mg/cm^2, where the error comes from the uncertainty of the cell length. The dotted line and the shaded area indicate the mean value and the error of the areal density, respectively. See the text for the bump of pressure.

Chapter 4

Analysis on inelastic scattering data

The data analysis were performed by using a program code, FRED (Tamii analyzer) [43], that was developed for processing of the data taken by the GR and the LAS. Data visualization in the online and the offline analyses were realized using the HBOOK and the PAW program packages from the CERN library.

4.1 Particle selection

The particle selection for proton events was performed by using time-of-fight (TOF) information and the energy loss in the PS1 of the GR. In the proton inelastic experiment at small scattering angles, the most of the particles detected by the focal plane counter were protons. Particles of γ-rays and neutrons were excluded in the tracking process of the MDWC's (see Sec. 4.2) since they do not have charge. Thus, background particles measured by the detector were mainly deuterons, and they were excluded as the followings.

The time information was measured as the difference between the trigger timing and the RF signal from the AVF cyclotron. For an effective exclusion of deuterons, the time information (RF) was corrected to be independence on x_{dt} and θ_{dt} as

$$RFC = RF - 0.120 \times x_{dt} + 20.0 \times \theta_{dt}, \tag{4.1}$$

where RFC was the corrected time information in channel, and x_{dt} and θ_{dt} were the horizontal position in mm and the scattering angle in the horizontal direction measured at the focal plane detector in degree, respectively. The coordinate system is given in Sec. 4.2. A typical result of the correction on the time information is shown in Fig. 4.1. The time difference between the two bunches in the figure corresponded to a beam pulse period of 61.6 ns (the RF frequency of 16.244 MHz) from the AVF cyclotron.

An energy loss of a charged particle in the PS1 depends on its charge and velocity as described by the Bethe-Bloch formula [44]. An intensity of a light emission in the PS1 was proportional to an energy loss. The intensity, however, was attenuated along the

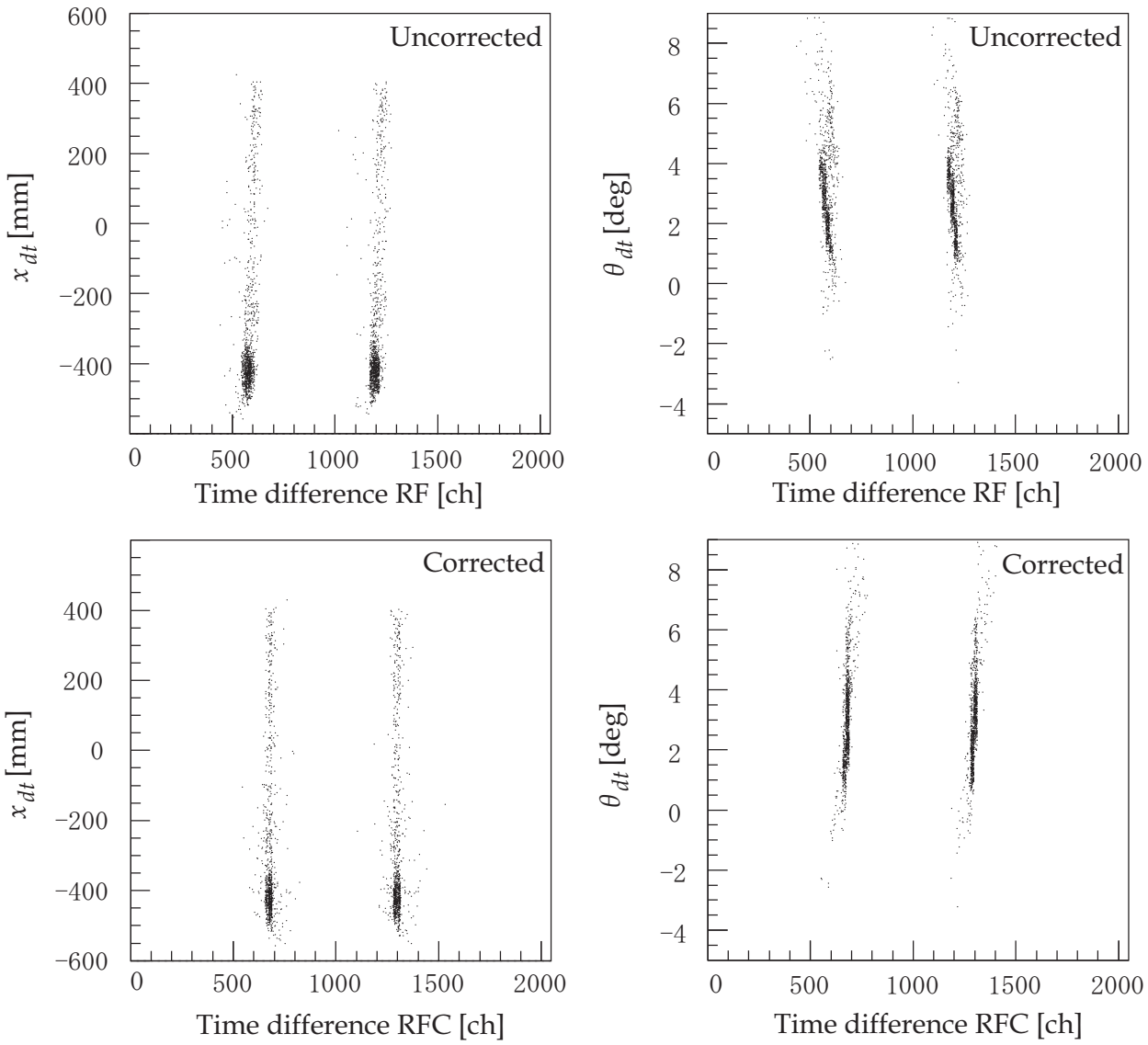

Figure 4.1: The correction for the time information to be independent on x_{dt} and θ_{dt}. The top figures are without the correction, and the bottom ones are with the correction. The time difference between the two bunches corresponds to a beam pulse period of 61.6 ns.

passage in the PS1 to the PMT. An intensity emitted at a position x that was detected by a PMT was given by

$$I(x) = I_0 \ \exp\Big(-\frac{x}{l}\Big), \tag{4.2}$$

where I_0 was the emitted light intensity, and l was the attenuation length of the PS1. The mean intensity of the light outputs I_{mean} from the PMT's of the both sides was expressed as

$$I_{mean} = \sqrt{I(x)I(L-x)} = I_0 \ \exp\Big(-\frac{L}{2l}\Big) \propto \Delta E, \tag{4.3}$$

where L was the length of the scintillator of the PS1.

Figure 4.2 shows a typical scatter plot of the time difference with the correction RFC versus the energy loss in the PS1. The areas enclosed by a square in red, indicating deuterons, were rejected. The energy loss of proton showed a continuous tail to the top in the figure (2000 channel). Thus, by the rejection to deuterons, all protons were saved and the background particles were almost excluded.

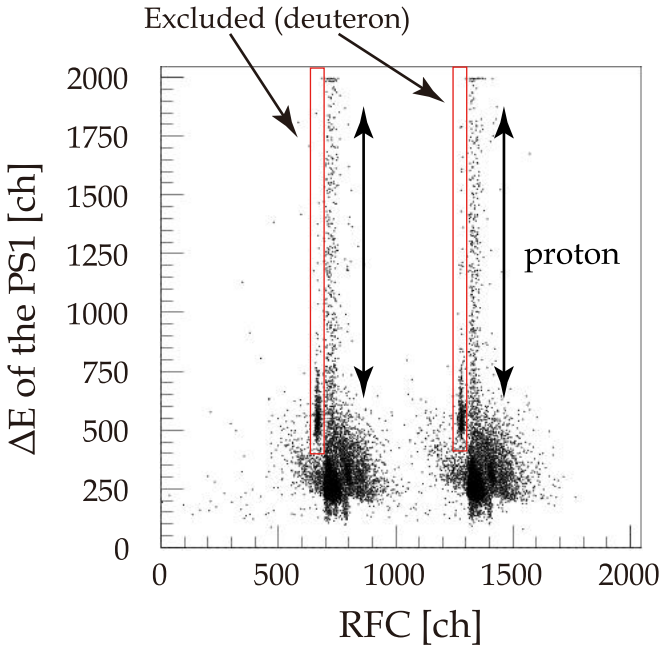

Figure 4.2: A typical scatter plot of the particle selection for protons. Deuterons enclosed by a square in red were rejected and all protons were saved.

4.2 Track reconstruction

Ray tracking

The trajectories of charged particles into the focal plane were determined with the MWDC's. The structure of the wire plane in the MDWC is illustrated in Fig. 4.3. When a charged

particle passed through the MWDC, electron-ion pairs were created along the trajectory by ionizing argon gas inside the MWDC. Since the cross section for the ionization is much small for particles without charge, such γ-rays and neutrons, they can not be detected by the MWDC's. The electrons produced by the ionization moved to an anode wire by the electric field due to the high voltages on the cathode planes. They were multiplied at the place close to the anode wire and then generated a negative signal. Usually particles passed through the MDWC's in the 45° direction and the electrons usually hit more than three sense wires. A group of wires that induced a signal was called a cluster. The vertical drift length of d_{i-1}, d_i, ... (Fig. 4.3) was determined from the drift time and gave a particle position at the anode wire plane. The drift velocity is almost constant but it considerably deviates near the wires due to the irregular electric fields. The drift length histogram should have a flat distribution in a range of 0−10 mm. The conversion tables from the drift time to the drift length have been created from the data of continuum excitation so that the drift length histogram has a flat distribution (Fig. 4.4).

The intercept position of a trajectory at the wire plane was calculated by a least square fitting from the drift length of hit wires. By combining the deduced position at the four wire planes, a trajectory was uniquely determined. The following rules were applied for the determination of the trajectory.

- A cluster had two hit wires at least and ten hit wires at most. A single hit wire was not considered as a cluster and was ignored.
- The distribution of drift lengths in a cluster had only one local minimum.
- A number of clusters in each plane was one. (A multi cluster event was rejected.)

The position resolution of the MWDC's was about 0.29 mm (FWHM), corresponding to an energy resolution of 6.7 keV in the present experiment. The angular resolution was $\tan^{-1}(0.29/250) = 0.066°$, where 250 mm is the distance between the MWDC1 and the MWDC2 of the GR (Fig. 2.6). That corresponds to a horizontal scattering angle resolution of 0.028° at the target.

Coordinate definition

The coordinates system at the focal plane detector of the GR is shown in Fig. 4.5. The z-axis was taken to be perpendicular to the MWDC's from the upstream. The x-axis was taken to indicate the low momentum side in the horizontal plane at the X1-plane. The center point of the X1-plane in the horizontal position was taken as the origin of the x-axis, and the intersection of the x-axis with the central orbit of the GR was x = -200 mm. The y-axis was taken to indicate upward in the vertical plane, and the intersection

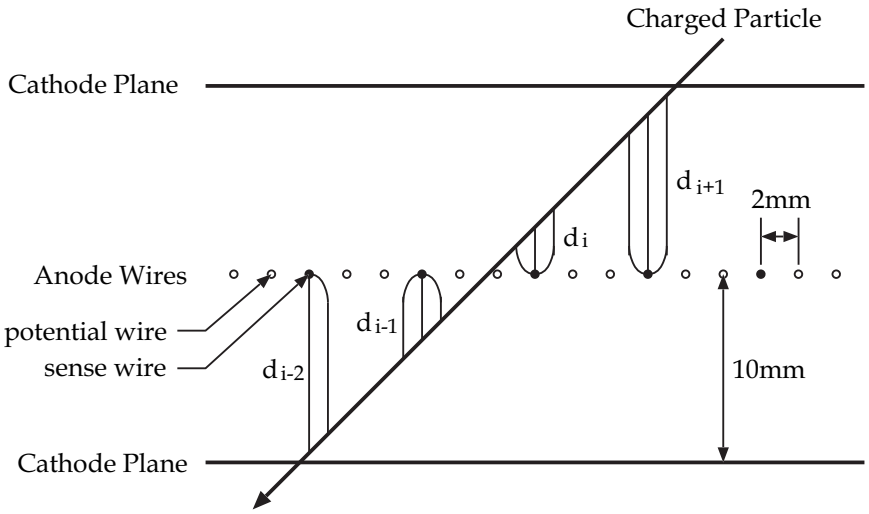

Figure 4.3: The structure of an X-plane of the MWDC.

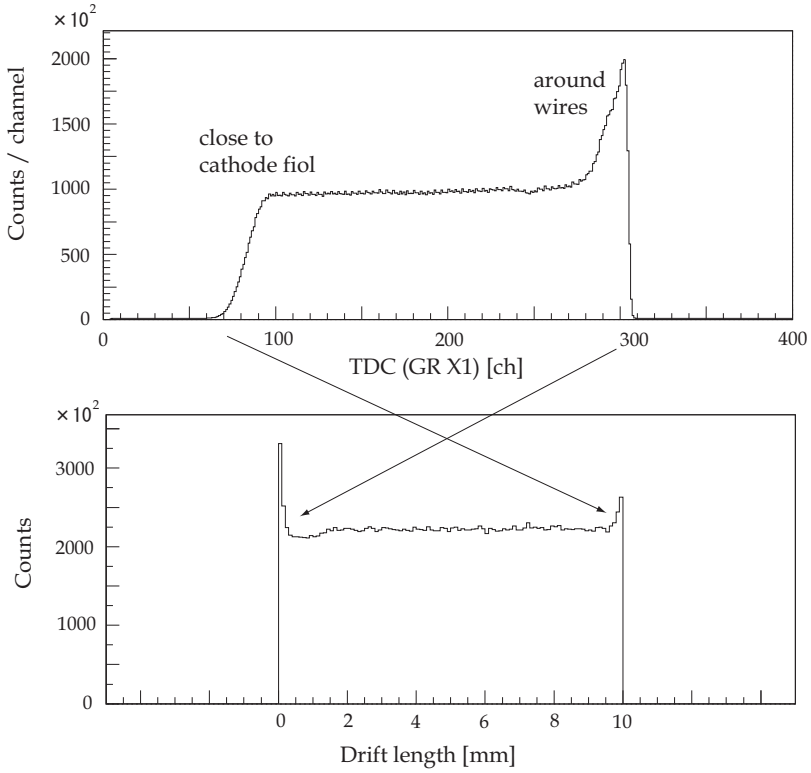

Figure 4.4: A typical result of the conversion of the timing spectrum of the sense wires to the drift length in the MWDC.

of the y-axis with the central orbit of the GR was taken to be the origin of the x-axis. Figure 4.5 (B) shows the definition of the horizontal incident angle θ and that of the vertical incident angle ϕ of a particle ray.

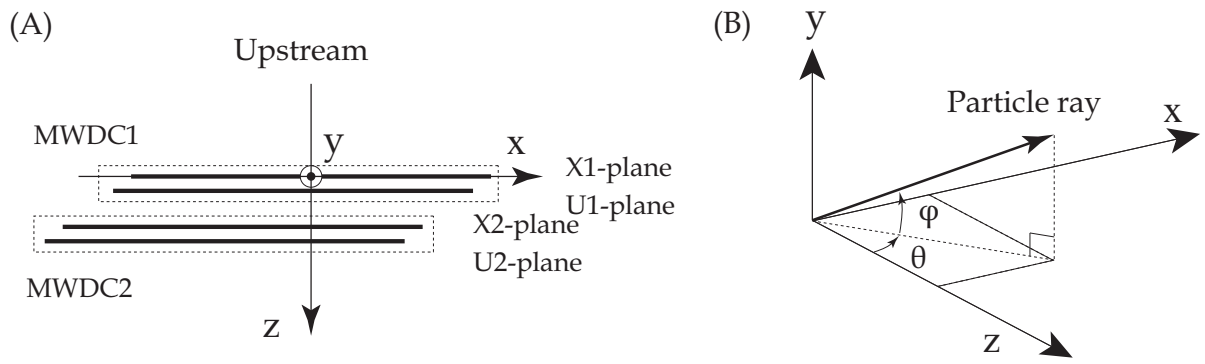

Figure 4.5: Coordinate system for the particle trajectory at the focal plane of the GR. The definition of the x, y, and z axes (A), and the definition of the horizontal incident angle θ and the vertical incident angle ϕ of a particle ray (B).

Detection efficiency of MWDC's

The detection efficiency for the X1 wire plane was roughly estimated as

$$\eta_{X1} = \frac{N_{U1\cap X2\cap U2}}{N_{X1\cap U1\cap X2\cap U2}}, \tag{4.4}$$

where $N_{X1\cap U1\cap X2\cap U2}$ denoted the number of events successfully determined for all of the four wire planes, and $N_{U1\cap X2\cap U2}$ denoted the number of events successfully determined for the other wire planes of the X1 plane. The efficiency of other planes was calculated in the same manner. Typical efficiencies of each wire plane and the total efficiency ($\eta = \eta_{X1} \times \eta_{U1} \times \eta_{X2} \times \eta_{U2}$) were 98% and 90%, respectively. The η was used in Eq. 4.14 to deduce cross sections. A position dependence of the efficiency was not taken into consideration.

4.3 Calibration of scattering angle

Horizontal and vertical scattering angles in the solid angle of the GR were calibrated by using the sieve-slit data (Sec. 2.4). The horizontal scattering angle (A_{tgt}) at the target position was determined mainly from the horizontal incident angle (θ_{dt}) of the particle at the focal plane detector. The vertical scattering angle (B_{tgt}) at the target position was determined mainly from the vertical position (y_{dt}) of the particle at the focal plane detector, instead of the vertical incident angle (ϕ_{dt}). Since the B_{tgt} value is sensitive

to the beam position in the vertical direction, it was monitored by the LAS during the measurement.

From a two-dimensional image of θ_{dt} versus y_{dt} as shown in the top panel of Fig. 4.7, the (θ_{dt},y_{dt}) coordinate sets of the hole positions in the image were obtained by projection the two-dimensional plot to each axis and fitting to them. The (θ_{dt},y_{dt}) coordinate sets for the all holes in the slit were obtained from the data in employing the beam at the standard position (0 mm), and those of only the central hole were obtained from the data in employing the beam artificially shifted to $\pm$1 mm from the standard position.

The vertical position of the central hole of the sieve-slit was not usually measured at $y_{dt} = 0$ mm because the positions of the beam and the central hole of the sieve-slit were not coincided. The disagreement is expected to be corrected to obtain the reconstructing coefficients for the angle calibration. As shown in Fig. 4.6, there was the relation between the beam position at the target and the y_{dt} position of the central hole image at the focal plane against for x_{dt}-dependence. The relative beam positions at the target position in the vertical direction were measured by the LAS (y_{LAS}). The x_{dt}-dependence was taken by changing the magnetic field of the GR since elastic scattering events were selected for the sieve-slit data. When the beam position at the target position is 0 mm ($\pm$1 mm), the position of the central hole of the sieve-slit image should be measured at $y_{dt} = 0$ ($\pm$5.98 mm, respectively) because of the vertical magnification of the GR as summarized in Table 2.1. In the figure, the dotted lines denote the y_{dt} position for the central hole of the sieve-slit image to be measured. Thus, the y_{dt} values of the sieve-slit data were corrected by the equation using x_{dt} and y_{LAS} as

$$y_0 = y_{dt} - \sum_{i=0}^{1}\sum_{j=0}^{1} \alpha_{ij} {x_{dt}}^i {y_{LAS}}^j, \tag{4.5}$$

where y_0 was the corrected vertical position, and the parameters α_{ij} were determined in each experiment by a multi-dimensional least square fitting. Typical α_{ij} parameters are summarized in Table 4.2. The equation corrects the relation between the beam position at the target and the position of the sieve-slit. With this correction, we can search and use a standard coefficients to reconstruct the scattering angle, which is described in the followings.

From the sieve slit data with the correction of Eq. 4.5, A_{tgt} and B_{tgt} were calibrated as a function of x_{dt}, θ_{dt}, y_0 and y_{LAS} by the equations

$$A_{tgt} = \sum_{i=0}^{2}\sum_{j=0}^{2}\sum_{k=0}^{2} a_{ijk} {x_{dt}}^i {\theta_{dt}}^j {y_0}^k \tag{4.6}$$

$$B_{tgt} = \sum_{i=0}^{2}\sum_{j=0}^{2}\sum_{k=0}^{2} b_{ijk} {x_{dt}}^i {\theta_{dt}}^j {y_0}^k + \sum_{l=0}^{2}\sum_{m=0}^{1} c_{lm} {x_{dt}}^l {y_{LAS}}^m, \tag{4.7}$$

where the parameters a_{ijk} and b_{ijk} were determined by a multi-dimensional least squares

fitting. The fitting was performed for the hole positions in the (θ_{dt},y_{dt}) coordinate to be the (A_{tgt}, B_{tgt}) position based on the actual hole positions of the sieve-slit. The parameters a_{ijk} and b_{ijk} are listed in Table 4.1. The numbers in the table are generally applicable to every experiment of the (p, p') reaction using 295 MeV protons employing the under focus mode of -5%. The parameters c_{lm} were determined by a fitting on the sieve-slit data for the beam at ± 1 mm after the parameters a_{ijk} and b_{ijk} were obtained. Typical number of the parameters c_{lm} and α_{ij} in Eq. 4.5 are listed in Table 4.2. They should be determined in each experiment. In summary, the terms including y_{LAS} should be determined in each experiment because they are highly sensitive to the beam spot position at the target and the B_{tgt} value.

The bottom panel in Fig. 4.7 shows the two dimensional plots of the sieve-slit data after the angle calibration. A typical result of the three different excitation energy regions at 10, 14, 18 MeV ($x_{dt} = -300$, -150, 0 mm, respectively) are shown. The horizontal angular resolution was 0.15° (FWHM), and the vertical angular resolution was 0.5−0.6° (FWHM).

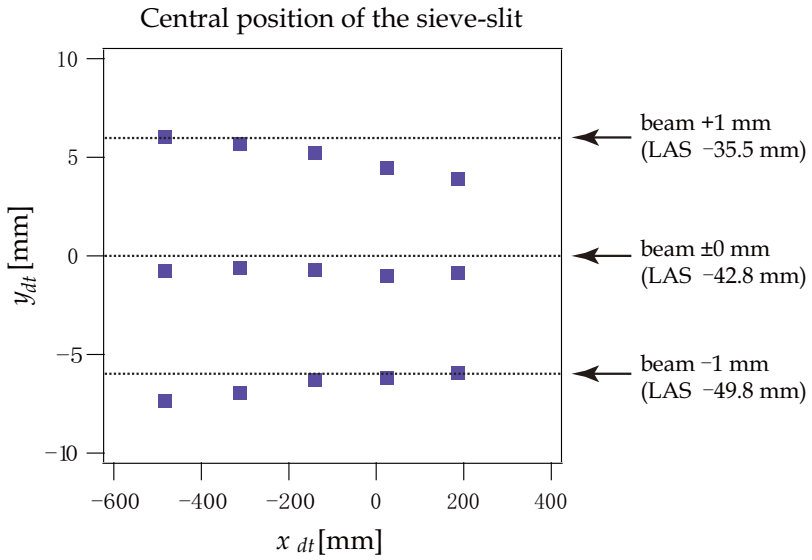

Figure 4.6: The horizontal position dependence between the beam height at the target position and at the focal plane detector. The correlation between the beam position at the target and the y_{dt} position of the central hole of the sieve-slit image at the focal plane against for x_{dt}-dependence. The dotted lines denote an ideal position for the y_{dt} to be measured.

4.4 Background subtraction

Although we succeeded to reduce the background due to scattering in the target frame by using the halo-free condition beam and the wide target frame, background events owing

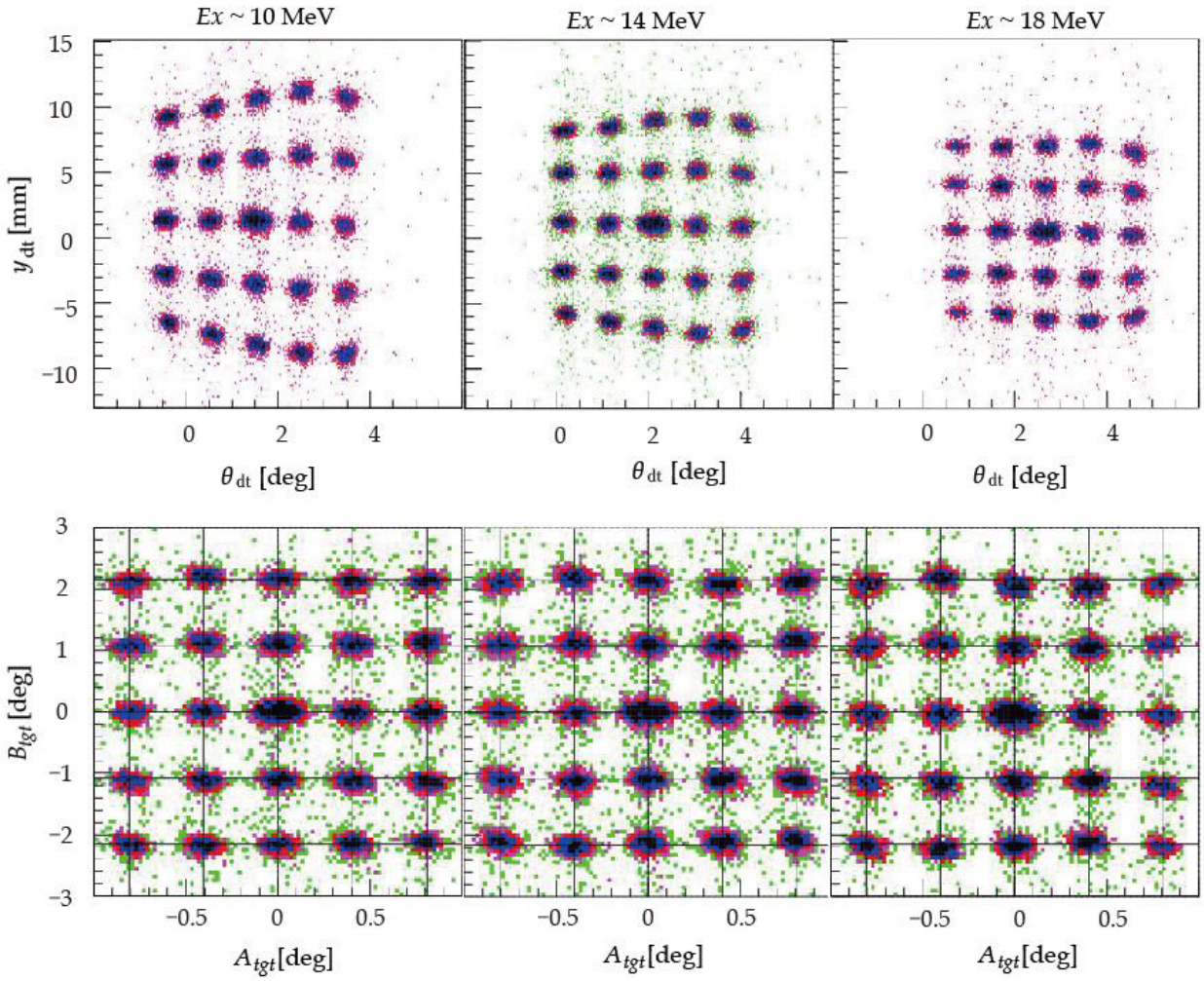

Figure 4.7: The reconstruction of the scattering angle. The two dimensional plots of θ_{dt} and y_{dt} in the top panel have been calibrated to those of A_{tgt} and B_{tgt} in the bottom panel by Eq. (4.6) and (4.7). The intersection of the lines in the bottom panel corresponds to the position of the holes of the sieve-slit, and the hole images are calibrated to be seen there. The results are shown for three different excitation energy regions.

Table 4.1: Table of the standard coefficients a_{ijk} and b_{ijk} determined in Eqs. (4.6) and (4.7) in order to reconstruct A_{tgt} and B_{tgt}, respectively, in radian. The coefficients are written in mm and radian. These parameters can be used in every experiment for the (p, p') reaction using 295 MeV beams employing the under focus mode of -5% with the correction of Eq. (4.5).

ijk	a_{ijk}	ijk	b_{ijk}
000	1.869e-02	000	−1.161e-03
010	−4.146e-01	001	6.146e-03
020	−4.540e-02	002	−3.326e-06
001	−1.791e-05	010	1.027e-02
011	8.781e-04	011	−2.816e-02
021	−6.985e-03	012	4.630e-04
002	1.616e-05	020	3.014e-01
012	−3.451e-04	021	2.877e-01
022	2.620e-03	022	−5.883e-03
100	2.573e-05	100	−7.318e-06
110	−2.718e-05	101	5.552e-06
120	1.337e-04	102	−2.669e-08
101	−6.798e-08	110	1.485e-04
111	1.975e-06	111	−1.055e-06
121	−9.804e-06	112	2.158e-06
102	4.276e-08	120	−9.175e-04
112	−3.063e-07	121	3.110e-04
122	−8.660e-07	122	−2.603e-05
200	2.904e-09	200	−1.564e-08
210	−2.763e-08	201	1.239e-09
220	1.210e-07	202	−2.719e-11
201	−1.099e-10	210	5.319e-07
211	3.793e-09	211	1.214e-08
221	−3.359e-08	212	2.446e-09
202	3.064e-11	220	−4.043e-06
212	5.854e-10	221	4.841e-07
222	−9.120e-09	222	−3.666e-08

Table 4.2: Typical coefficients α_{ij} and c_{lm} in Eqs. 4.5 and 4.6, respectively. The coefficients are expressed in mm. These parameters should be determined in each experiment.

ij	α_{ij}	lm	c_{lm}
00	−1.287e-00	00	−1.815e-00
01	−4.848e-02	01	−4.228e-03
10	−1.794e-02	10	−1.896e-04
11	−3.995e-04	11	−4.448e-06
		20	−1.055e-07
		21	−2.626e-09

to multiple scattering in the target still remained in the 0° data. In fact, the trigger rate with and without a target foil were >1000 Hz/nA and <100 Hz/nA, respectively. In this section, the determination and the subtraction of the background events originating from the multiple scattering in the target are described.

Correction for subtraction

The background events due to multiple scattering in the target are expected to have a flat distribution in the y direction at the focal plane of the GR spectrometer because they re-scatter in the spectrometer. In the standard magnetic field setting for the GR spectrometer, the true events are focused in the y position at the focal plane, while the background events are scattered to be flat in the y histogram. Thus, it is easy to distinguish the true events from background event in the y spectrum because a peak in the y spectrum denotes the true events. Such focusing for the true events, however, is not realized at the focal plane when the under focus mode is employed. Therefore, the y_{dt} values were corrected to be focused in the y spectrum for the effective separation of the true events from the background events. The correction, the true events to be along y_c=0 in the two dimensional plot of y_{dt} versus ϕ_{dt} or to stand in the one dimensional histogram of y_c, was performed by the equation

$$y_c = \left(y_{dt} + \sum_{i=0}^{3}\sum_{j=0}^{1} d_{ij} {x_{dt}}^i {\phi_{dt}}^j\right) + \sum_{k=0}^{2}\sum_{l=0}^{1} e_{kl} {x_{dt}}^k {y_{LAS}}^l, \tag{4.8}$$

where y_c was the corrected y coordinate, and ϕ_{dt} was the vertical incident angle of the particle at the focal plane detector. The parameters d_{ij} were determined by using multi-dimensional fitting to one shot data, as shown in Fig. 4.8. The coefficients d_{ij} are listed in Table 4.3, and they can be used in every experiment for the (p, p') reaction using 295 MeV beams employing the under focus mode of -5% to stand the true events in the one dimensional histogram of y_c. The parameters d_{ij}, however, do not always concentrate the true event at $y_c = 0$ mm depending on the beam height. The parameters e_{ij}, thus, were obtained by a fitting on the result of the parameters d_{ij} using y_{LAS}. The coefficients e_{ij} are listed in Table 4.3. They should be determined in each experiment because the correction is sensitive to the beam height.

Subtraction method

The subtraction method for the background due to multiple scattering at the target makes use of the vertical focusing property of the GR. Figure 4.9 shows the conventional method for the background subtraction; the region of the true events in the y spectrum is selected, and the gates with the same size are applied to select the background. The background events are averaged to subtract them from an excitation energy spectrum. This method,

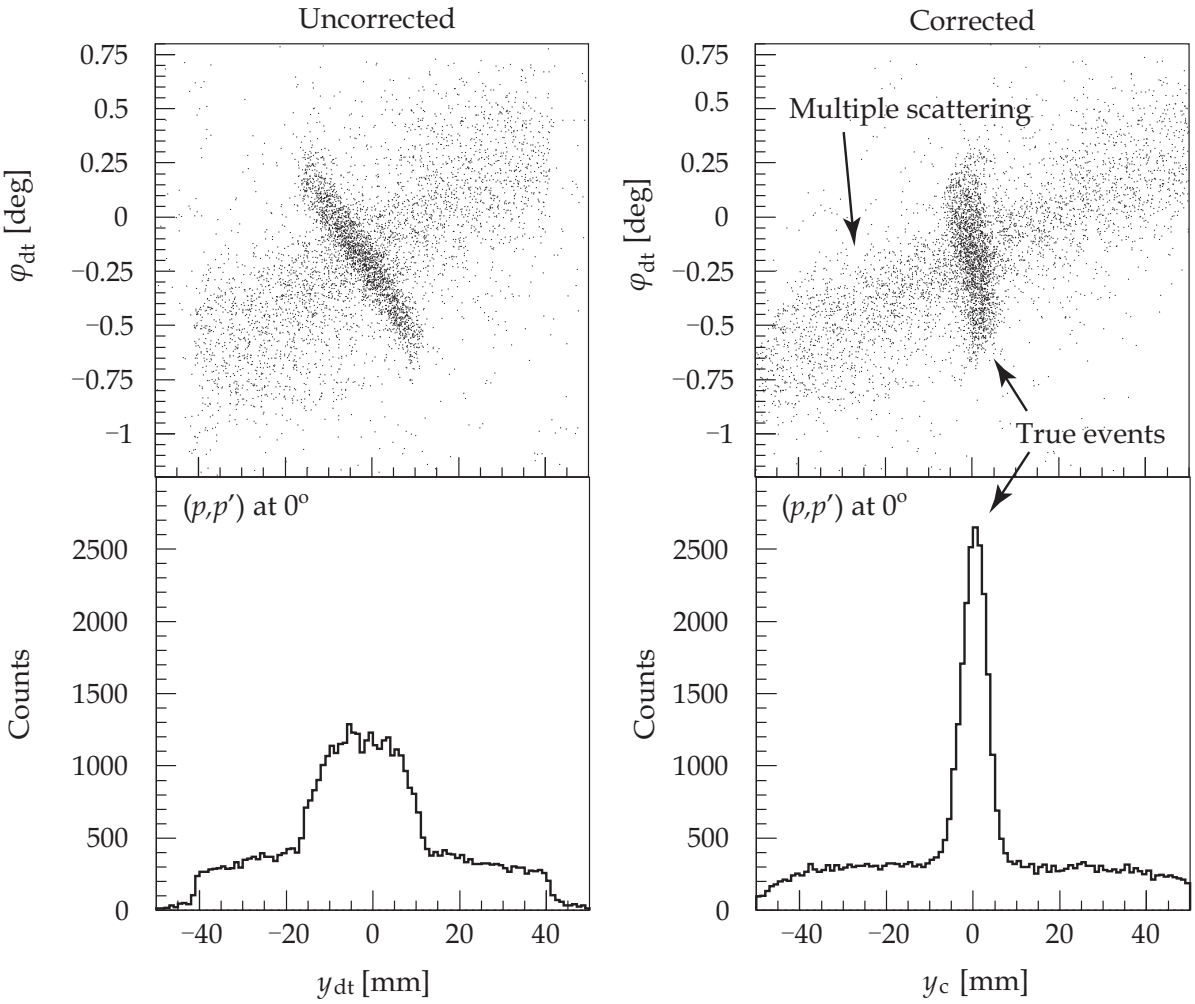

Figure 4.8: The correction on the y coordinate for the background subtraction. The left panels show the two dimensional plot of y_{dt} and ϕ_{dt} and the y_{dt} histogram of the 0° data without the correction. The right panels show the similar data but with the correction for y_c. The parameters for the correction have been determined so that the true events in the two dimensional plot to be on the y_c=0 line.

Table 4.3: Table of the coefficients of d_{ij} and e_{kl} in Eq. 4.8. x_{dt}, y_{LAS}, and y_c are used and expressed in mm. ϕ_{dt} is in radian unit. The coefficients d_{ij} can be used in every experiment for the (p, p') reaction using 295 MeV beams employing the under focus mode of -5%, while the coefficients e_{ij} should be determined in each experiment.

ij	d_{ij}	kl	e_{kl}
00	−2.309E-00	00	−2.950E+01
01	9.525E+02	10	1.523E-02
10	−6.549E-04	20	−1.570E-05
11	−1.493E-00	01	−8.034E-01
20	−5.226E-07	11	4.94E-04
21	1.528E-03	21	−6.122E-07
30	1.007E-06		
31	−1.962E-06		

however, can be applied only to the case of handling the data with full acceptance because the vertical position cannot be simultaneously determined to estimate the background region and to reconstruct B_{tgt} used for software cut. Therefore, an extended method was developed for the background subtraction in handling the data with software cut in terms of the scattering angle. Figure 4.10 shows the extended method for the background subtraction; all events are artificially moved along to the background in the two-dimensional plot of y_c versus ϕ_{dt}, and then the central region in each y_c histogram is selected in an excitation energy spectrum (Fig. 4.11). A width to be selected for an energy spectrum has an x-dependence as shown in the bottom panels of Fig. 4.10. A size of the width to be selected and a distance to be shifted were determined in manual for each experiment. The two background parts were averaged for the subtraction.

4.5 Correction for high energy resotlution

Low lying discrete states in two-dimensional plot of x_{dt} versus θ_{dt} are curved as shown in the top panel of Fig. 4.12. The curve deteriorates an energy resolution because a position resolution of the discrete peak in the x histogram, indicating momentum spread, becomes worse. The curve in the plot originates from two factors *i.e.*, the kinematical effect of the particle and the aberration of the GR spectrometer. The former can be corrected by a calculation. A parameters set for the correction to the latter factor was obtained in each experiment for high energy resolution. Once the aberration of the GR spectrometer is experimentally known by using multi-dimensional fittings, the correction parameters for high energy resolution can be applied to all nucleus because the kinematical correction is computed.

Firstly, for the correction to cancel the ion optical property of the GR spectrometer,

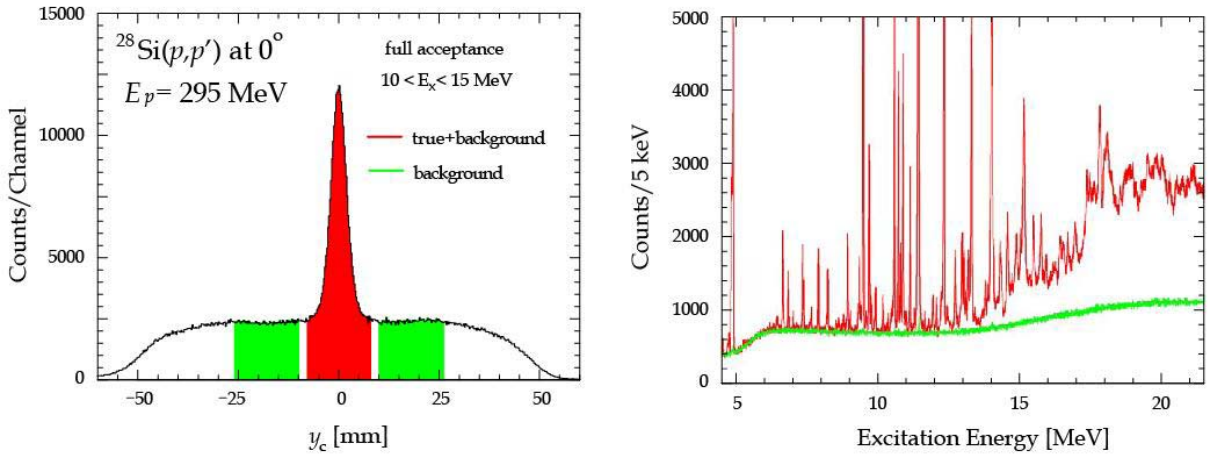

Figure 4.9: The conventional method of background subtraction. True events including the background and background events are shown in red and green, respectively, in a y spectrum (left) and an excitation energy spectrum (right). Since this method to determine the background events is valid for the case of handling data of full acceptance, this techinique is not used in the present analysis. The correction to improve the energy resolution (Sec. 4.5) has been applied on the spectrum.

---

the kinematical effect was removed from the data by the equation

$$x_k = x_{dt} - \frac{(k_1 {\Theta_{tgt}}^2 - k_2 \Theta_{tgt}) \times 10^{-3}}{0.0230}, \tag{4.9}$$

where x_k was the position in mm with the kinematical correction on x_{dt}, 0.0230 MeV/mm was the energy calibration value used in the present study which was roughly estimated from the relationship between the excitation energy and the horizontal position at the focal plane. The coefficients k_1 and k_2 were obtained from a relativistic kinematical calculation, *e.g.*, k_1=3.30 MeV/deg^2 and k_2=0.162 MeV/deg for the case of ^{28}Si. The total scattering angle at the target position, Θ_{tgt}, was difined as $\sqrt{(\theta_s + A_{tgt})^2 + {B_{tgt}}^2}$ in degree, where the parameter θ_s is the angle which the spectrometer is placed at. As shown in the middle panel of Fig. 4.12, the kinematical correction increased a curvature but made the image of the curve sharpen. The curvature in the two dimensional plot of x_k versus θ_{dt} denotes the aberration of the GR spectrometer to be corrected.

Next, the (x_k,θ_{dt}) coordinates of typical discrete states to denote the curvature were obtained by the projection to each axis. This study to know the curvature of the discrete states is called "profiling". After the profiling, the correction to straighten them in the two-dimensional plot was realized by the equation

$$x_{ck} = \sum_{i=0}^{3} \sum_{j=0}^{4} f_{ij} {x_k}^i {\theta_{dt}}^j, \tag{4.10}$$

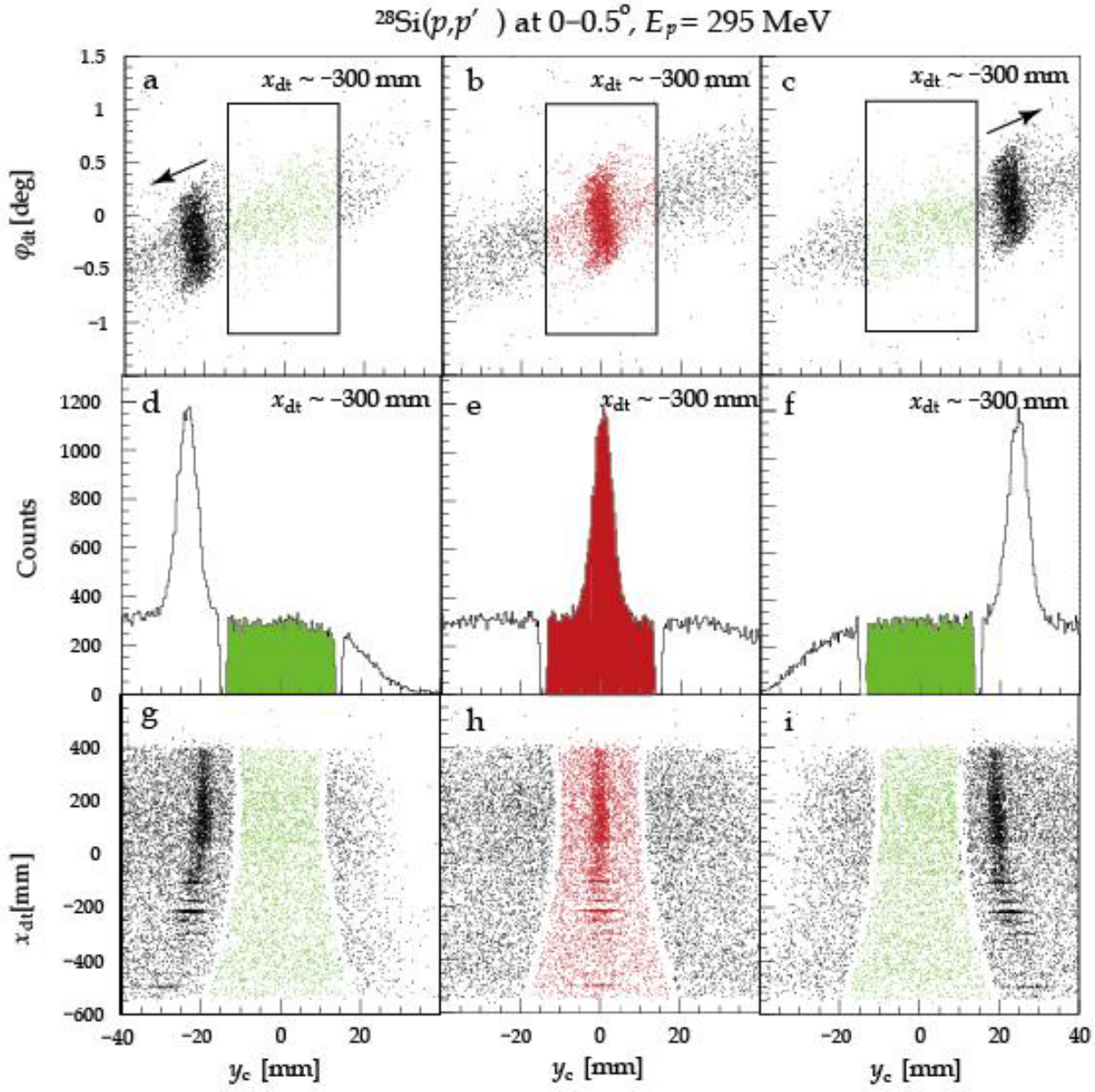

Figure 4.10: The extended method for background subtraction. The top panels show the two-dimensional plot of y_c versus ϕ_{dt}. The plot (b) is artificially shifted along the background to the both sides (a,c). The areas surrounded by the square in the top panels are shown in red and green and selected for an excitation energy spectrum in Fig. 4.11. The middle panels show one-dimensional histograms of y_c (d,e,f). The x-dependence of the width of the square to be selected is shown in the bottom panels (g,h,i). A typical peak at $x_{dt} \sim -300$ mm is selected in the top and the middle panels.

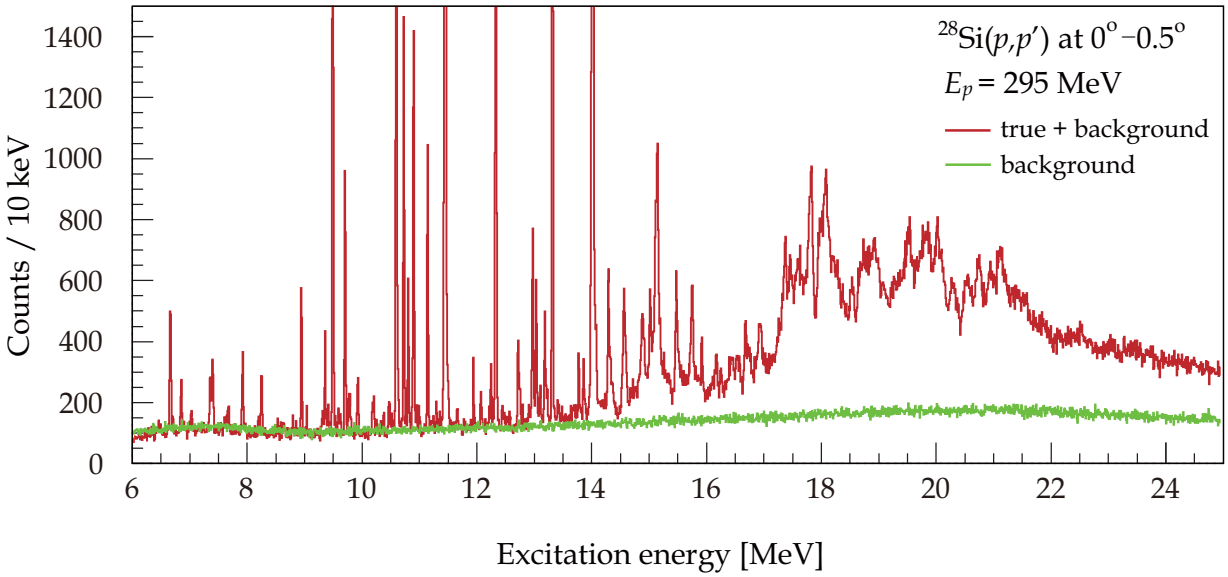

Figure 4.11: An excitation energy spectrum created by the extended background subtraction method with a scattering angle cut of 0−0.5°. The correction to improve the energy resolution (Sec. 4.5) has been applied on the spectrum.

---

where x_{ck} was the corrected position in mm, and the parameters f_{ij} were determined by using a multi-dimensional least squares fitting on the profiling data to make them straight. Since f_{ij} are the correction parameters to cancel the aberration of the GR spectrometer, the correction

$$x_c = \sum_{i=0}^{3} \sum_{j=0}^{4} f_{ij} {x_{dt}}^i {\theta_{dt}}^j \tag{4.11}$$

will be used to form an excitation energy spectrum because the kinematical effect is analytically included (Sec. 4.6). The correction to straighten the curve in the two-dimensional plot was performed for it to be fixed at the point where $A_{tgt} = B_{tgt} = 0$ was satisfied. The profiling data were taken for the several nuclei and combined because the region which discrete states well isolated from other states are limited. This is bad for a smooth fitting in terms of x-dependence. Unfortunately, discrete states can be observed in the region $x_{dt} < 0$ mm of the GR spectrometer in the (p, p') experiment using 295 MeV protons. Therefore, the aberration at the lower momentum region ($x_{dt} > 0$ mm) was profiled by increasing all the magnetic fields of the GR spectrometer for discrete states to be measured there. The profiling data taken in this setting were used for the fitting with a small weight since the data do not reflect the same aberration but are enough for a rough correction. A typical result of x_c with the kinematical correction is shown in the bottom panel of Fig. 4.12 as the two-dimensional plot of x_{ck} versus θ_{dt}.

The correction to improve the high energy resolution was performed only for the x and θ correlation. The correction between the x and the y or the x and the ϕ was not

performed because the kinematical correction and the parameters f_{ij} were essential to straighten a discrete state in these two-dimensional plots.

4.6 Calibration of excitation energy

The excitation energy of the target nucleus was calculated by using the equation

$$B\rho = \frac{p(x_c)}{q_c}, \tag{4.12}$$

where B was the magnetic field of the GR, ρ was the mean orbit radius, p and q_c were the momentum and the charge of the scattered particle. The momentum p was a function of x_c as obtained by Eq. 4.11. By solving the two-body scattering problem in relativistic, the excitation energy of the target nucleus (E_x) was calculated from the $p(x_c)$.

The above calculation, however, sensitively depends on the condition of the beam transportation owing to the high energy resolution. therefore, the E_x was further corrected by the following conversion

$$E_x{}' = \alpha E_x + \beta, \tag{4.13}$$

where $E_x{}'$ was the corrected excitation energy, the parameters α and β were determined in each experiment and run, respectively. The α was determined by the two levels at $E_x =$ 7.654 and 15.110 MeV of ^{12}C in each experiment, and β was determined by a typical peak in each run using Ref. [37]. A typical result of the excitation energy calibration on ^{28}Si by $\alpha = 1.0096$ is compared with that without the α correction ($\alpha = 1.0000$) in Fig. 4.13. The β was determined by the state at $E_x = 11.446$ MeV. The energy difference was calculated by using Ref. [37]. The calibration with $\alpha = 1.0096$ realized the uncertainty better than $\pm$10 keV within the region at 8$-$14 MeV in excitation energy, where most 1^+ states are present. The energy difference of the state at $E_x = 4.980$ MeV, however, was $-$80 keV for the $\alpha = 1.0096$, where no 1^+ states are present. In this thesis, Eq. 4.13 with the α correction will be employed because the determination of excitation energy is not our purpose and the uncertainty of excitation energy with the correction is better than that without the correction at the region for most 1^+ transition to be observed.

4.7 Excitation energy spectrum

Differential cross section

Double differential cross sections were deduced by the equation

$$\frac{d^2\sigma}{d\Omega dE} = \alpha N \frac{1}{\Omega}\frac{1}{L}\frac{1}{\eta}\frac{1}{\tau}\frac{e}{Q\epsilon c_{rel}}\frac{A}{N_A t a}J, \tag{4.14}$$

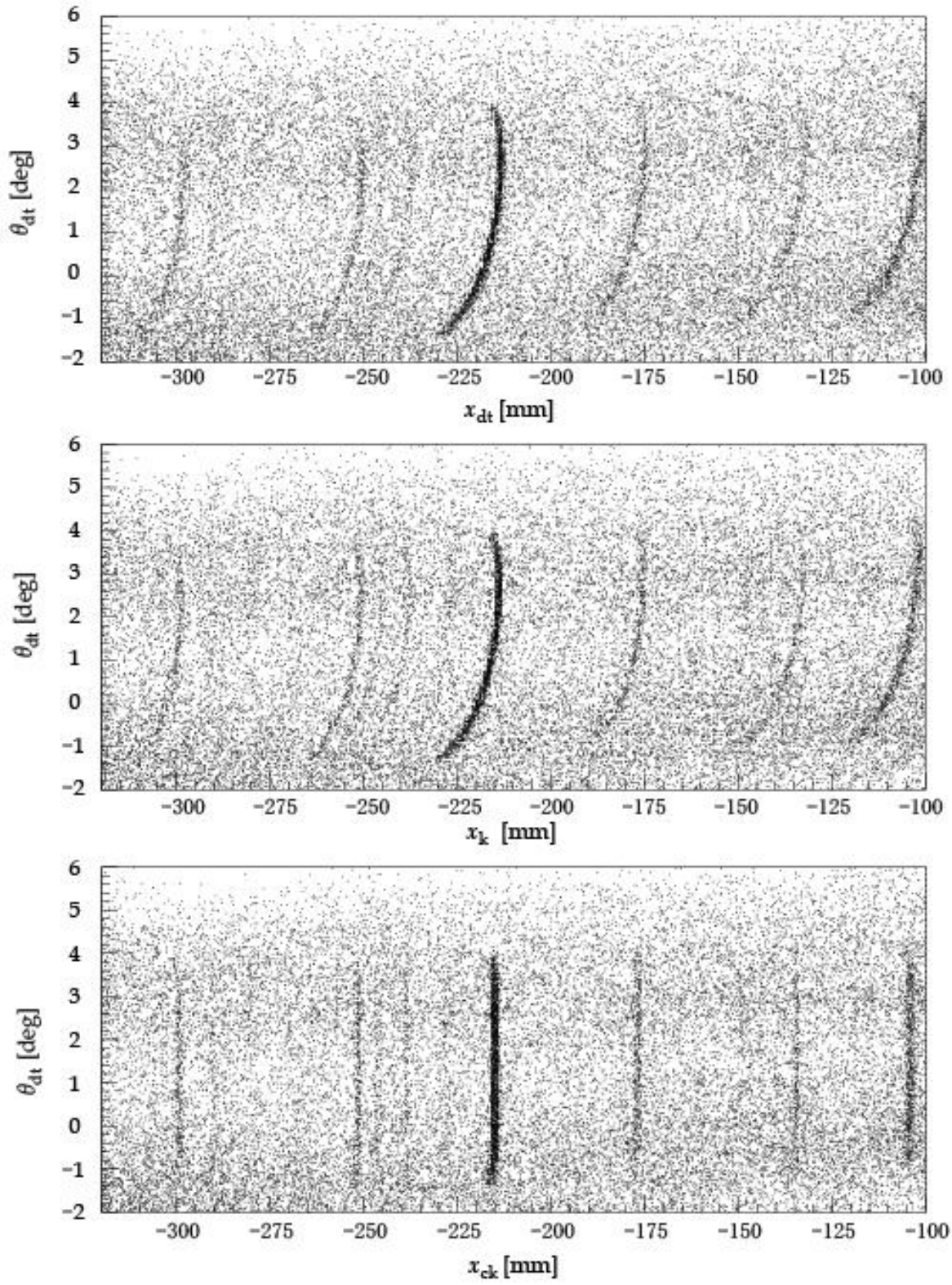

Figure 4.12: The correction to improve the energy resolution. The discrete states in the top panel (x_{dt} versus θ_{dt}) are curved owing to the kinematical effect and the aberration of the GR spectrometer. Firstly, the kinematical effect is removed by a calculation (the middle panel). The correction to cancel the aberration (x_c) is obtained by Eq. 4.10. The result with the kinematical correction (x_{ck}) is shown in the bottom panel. The data taken in the reaction of ^{28}Si(p, p') at 0° are shown.

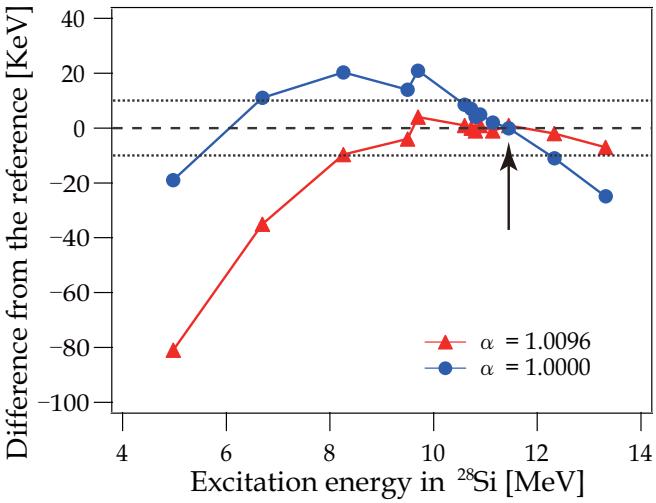

Figure 4.13: A typical result of the excitation energy calibration on ^{28}Si. Energy differences from the reference [37] with and without the α corrections are compared. The α correction ($\alpha = 1.0096$) will be used in this thesis. The arrow indicates the state used for the determination of the β. The uncertainty of excitation energy is $\pm$10 keV within 8$-$14 MeV.

where the notation of the variables are summarized in Table 4.4. For the absolute cross section, the corrections for the absolute efficiency on the SCFC (ϵ) and for the absolute trigger efficiency on the scintillation counters with the aluminium plate (τ) were employed (see Ref. [29] and Sec. 2.1.4). For the SCFC, the relative correction $c_{rel} = 1$ was employed. The statistical and systematic uncertainties were given by the equations

$$\Delta \frac{d^2\sigma}{d\Omega dE}\Big|_{stat} = \frac{1}{\sqrt{N}} \frac{d^2\sigma}{d\Omega dE} \tag{4.15}$$

$$\Delta \frac{d^2\sigma}{d\Omega dE}\Big|_{sys} = \sqrt{\left(\frac{\Delta\tau}{\tau}\right)^2 + \left(\frac{\Delta\epsilon}{\epsilon}\right)^2 + \left(\frac{\Delta c_{rel}}{c_{rel}}\right)^2 + \left(\frac{\Delta t}{t}\right)^2} \frac{d^2\sigma}{d\Omega dE}, \tag{4.16}$$

respectively, where the systematic uncertainties are summarized in Table 4.5. The systematical uncertainty was mainly due to the uncertainly of the target.

The excitation energy spectra of the (p, p') reaction at $E_p = 295$ MeV and at 0, 6, 12° on ^{12}C, ^{16}O, ^{20}Ne, ^{24}Mg, ^{28}Si, ^{32}S, ^{36}Ar, and ^{40}Ca are summarized in Appendix B. Peaks originated from the aramid film, $C_{14}O_2N_2Cl_2H_8$ made by To-re CO. Ltd.[1], were contaminated in the spectra of ^{20}Ne and ^{36}Ar. The (p, p') spectra on the aramid film, derived with the kinematical condition of ^{12}C, are shown in Fig. B.9. The $p - p$ elastic scattering from the hydrogen in the ice target and the aramid film are seen as a broad bump at $E_x = 12-15$ MeV in the energy spectra of ^{16}O, ^{20}Ne, ^{36}Ar, and the aramid at 12°. The background subtraction was imperfect and some of them remained at $E_x =$

[1]It is to be noted that the aramid film used as the BLP target was made by Asahi-kase CO. Ltd., $C_{14}O_2N_2H_3$.

6−7 MeV in the spectra of ^{20}Ne, ^{24}Mg, ^{36}Ar, and ^{40}Ca. A typical energy resolution was 20 keV (FWHM).

Table 4.4: Notation of the variables used in the expression of the differential cross section in Eqs. 4.14, 5.8 and 5.9. See Table 3.1 for t and a.

$d^2\sigma/d\Omega dE$	double differential cross section		[mb/sr·MeV]
α	unit conversion constant	10^{30}	[mb/cm^2·mg/g]
N	yields between E and $E + \Delta E$		[counts/MeV]
Ω	solid angle (lab.)		[sr]
L	live time ratio of DAQ		[-]
η	VDC efficiency		[-]
τ	trigger efficiency		[-]
e	elementary charge	1.60×10^{-19}	[C]
Q	integrated beam charge		[C]
ϵ	absolute correction on the SCFC	0.986	[-]
c_{rel}	relative correction for FC		[-]
A	target atomic weight		[g/mol]
N_A	Avogadro number	6.02×10^{24}	[mol^{-1}]
t	target thickness		[mg/cm^2]
a	target enrichment		[%]
J	Jacobian		

Table 4.5: Typical systematic uncertainties for cross section.

	Uncertainty (%)	
trigger efficiency ($\Delta\tau/\tau$)	0.1	From Table 2.3
the SCFC ($\Delta\epsilon/\epsilon$)	0.8	Ref. [29]
each FC ($\Delta c_{rel}/c_{rel}$)	0.3	From Table 2.5
target ($\Delta t/t$)	1−7	From Table 3.1
total	1−7	

Peak fitting

The differential cross sections to the discrete state were obtained by fitting to the excitation energy spectra. A Gaussian function with a tail were used for the fitting procedure. The Gaussian function was folded by a peak-shape taken from a typical discrete state which was isolated well from other state. The peak fitting was performed by using the function $f(x) = g(x)t(x)$, where

$$g(x) = A\exp\left\{-\frac{(x-E_x)^2}{2\sigma^2}\right\} \quad (4.17)$$

$$t(x) = 1 + a\exp\Big\{b\,(x-E_x)\Big\}. \quad (4.18)$$

The parameters A and E_x are the peak height and the central energy position, respectively, taken from Ref. [37]. The symbols a, b, and σ are peak-shape parameters. The peak-shape parameters were determined in each spectrum, and used for the fitting to the spectrum. The uncertainty of ΔA was taken as the fitting error.

The result of the obtained cross sections to the discrete state is summarized as the angular distribution in Appendix C. A typical result of the peak fitting for the data of $^{28}\mathrm{Si}(p, p')$ at $0-0.5^\circ$ at $E_x = 9-10$ MeV is shown in Fig. 4.14.

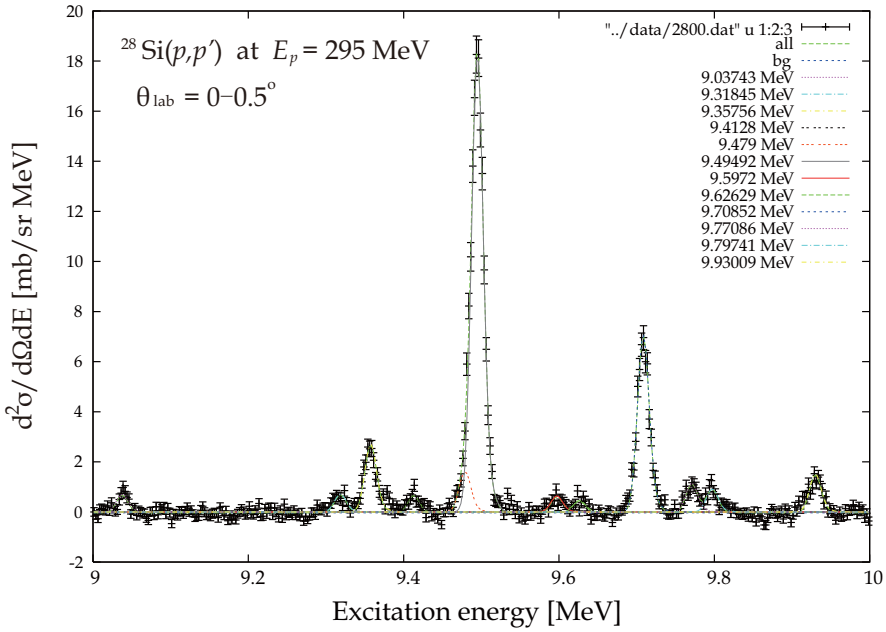

Figure 4.14: Typical result of peak fitting for the data of $^{28}\mathrm{Si}(p, p')$ at $0-0.5^\circ$ at $E_x = 9-10$ MeV.

Chapter 5

Analysis on elastic scattering data and result

The distorted wave Born approximation calculations, which are used for the extraction of spin-flip strengths as described in Chapter 6 , are extremely sensitive to the distortion effect in the inelastic scattering process [10]. The distortion effect can be calculated from the optical model potential parameters which are derived from the elastic scattering data. We took elastic scattering data at incident proton energy $E_p = 295$ MeV on ^{12}C, ^{20}Ne, ^{24}Mg, ^{28}Si, ^{32}S, and ^{36}Ar in the present experiment and ^{16}O and ^{40}Ca from Ref. [47]. In the following sections, the optical model potential parameters are obtained from these nuclei.

5.1 Deduction of differential cross sections and analyzing powers

Beam polarization

The beam polarization (p) was derived from the BLP's data by the equation

$$p = \frac{1}{A_y^{BLP}} \frac{L - R}{L + R}, \tag{5.1}$$

where A_y^{BLP} was the analyzing power of the BLP target (see App. F), L and R were yields detected by the L−L' pair and the R−R' pair of the BLP, respectively. The beam polarization was cycled between spin-up (↑) and spin-down (↓) to cancel the asymmetry of the experimental appartus. Being the yields of L and R as $L_\uparrow$, $R_\uparrow$ during the spin-up, and $L_\downarrow$ and $R_\downarrow$ during the spin-down, the beam polarization for each spin direction can be obtained by the equation

$$p_\uparrow = \frac{1}{A_y^{BLP}} \frac{L_\uparrow - R_\uparrow}{L_\uparrow + R_\uparrow} = \frac{1}{A_y^{BLP}} \frac{1 - R_\uparrow/L_\uparrow}{1 + R_\uparrow/L_\uparrow} \tag{5.2}$$

$$p_\downarrow = \frac{1}{A_y^{BLP}} \frac{L_\downarrow - R_\downarrow}{L_\downarrow + R_\downarrow} = \frac{1}{A_y^{BLP}} \frac{1 - R_\downarrow/L_\downarrow}{1 + R_\downarrow/L_\downarrow}. \tag{5.3}$$

Assuming $p_\uparrow = -p_\downarrow$, the equations can be rewritten as

$$p = \frac{1}{A_y^{BLP}} \frac{1-x}{1+x}, \tag{5.4}$$

where

$$x \equiv \sqrt{\frac{R_\uparrow L_\downarrow}{L_\uparrow R_\downarrow}} \tag{5.5}$$

using the relation

$$\frac{R_\uparrow}{L_\uparrow} = \Big(\frac{R_\downarrow}{L_\downarrow}\Big)^{-1} = \frac{L_\downarrow}{R_\downarrow}. \tag{5.6}$$

The uncertainty for the polarization can be written as

$$\Delta p = \frac{1}{A_y^{BLP}} \frac{x}{(x+1)^2} \sqrt{\left(\frac{1}{L_\uparrow} + \frac{1}{L_\downarrow} + \frac{1}{R_\uparrow} + \frac{1}{R_\downarrow}\right)}. \tag{5.7}$$

The beam polarization was stable within during $\pm 3\%$ the measurement. A typical beam polarization was 71%, 54%, and 52% depending on the condition of the HIPIS.

Differential cross sections and analyzing powers

The measured yields in each spin ($N_\uparrow$ and $N_\downarrow$) can be derived as

$$N_\uparrow = \Big(\frac{d\sigma}{d\Omega}\Big)_{lab} (1 + pA_y) \tau \Omega T \eta_\uparrow L_\uparrow Q'_\uparrow \tag{5.8}$$

$$N_\downarrow = \Big(\frac{d\sigma}{d\Omega}\Big)_{lab} (1 + pA_y) \tau \Omega T \eta_\downarrow L_\downarrow Q'_\downarrow, \tag{5.9}$$

where $(d\sigma/d\Omega)_{lab}$ and A_y were the differential cross section and the analyzing power of the ground state, respectively, p was the beam polarization as derived in Eq. 5.4, T was defined as $T = N_A ta/A$, and Q' was defined as $Q' = Q\epsilon/e$ (see Table 4.4 for the notation). Thus, the differential cross section in the center of mass flame and the analyzing power can be derived as

$$\frac{d\sigma}{d\Omega} = \frac{1}{2}\Big(\alpha N_\uparrow + \beta N_\downarrow\Big) \frac{J}{\tau \Omega T} \tag{5.10}$$

$$A_y = \frac{1}{p} \frac{\alpha N_\uparrow - \beta N_\downarrow}{\alpha N_\uparrow + \beta N_\downarrow}, \tag{5.11}$$

where

$$\alpha = \frac{1}{\eta_\uparrow L_\uparrow Q'_\uparrow} \tag{5.12}$$

$$\beta = \frac{1}{\eta_\downarrow L_\downarrow Q'_\downarrow}. \tag{5.13}$$

The uncertainties of the cross section and the analyzing power can be written as

$$\Delta\frac{d\sigma}{d\Omega} = \frac{d\sigma}{d\Omega}\sqrt{\frac{1}{N_\uparrow+N_\downarrow}+\left(\frac{\Delta\tau}{\tau}\right)^2+\left(\frac{\Delta T}{T}\right)^2+\left(\frac{\Delta\epsilon}{\epsilon}\right)^2} \tag{5.14}$$

$$\begin{aligned}\Delta A_y &= A_y\frac{2\alpha\beta N_\uparrow N_\downarrow}{(\alpha N_\uparrow)^2-(\beta N_\downarrow)^2} \\ &\quad\times\sqrt{\left(\frac{1}{N_\uparrow}+\frac{1}{N_\downarrow}\right)+\left(\frac{\Delta\tau}{\tau}\right)^2+\left(\frac{\Delta T}{T}\right)^2+\left(\frac{\Delta\epsilon}{\epsilon}\right)^2+\left(\frac{\Delta p}{p}\right)^2},\end{aligned} \tag{5.15}$$

where $(\Delta T/T)$ was taken from $(\Delta t/t)$, and the uncertainty of the polarization was included as systematic error of ΔA_y. The numerical data of the measured cross sections and analyzing powers of ^{12}C, ^{20}Ne, ^{24}Mg, ^{28}Si, ^{32}S, and ^{36}Ar are summarized in the tables in Appendix D.

5.2 Optical model potential

The differential cross sections and the analyzing powers of the ground state obtained in Sec. 5.1 were used to derive the optical model parameters by using ECIS88 program code [45]. The derived parameters of the optical potential was input to the distorted wave Born approximation calculation (see Sec. 6.2). The optical potential was assumed to be Woods-Saxon form as

$$\begin{aligned}V(r) &= V_{Coul}(r)-V_rF_r(r)-iV_iF_i(r) \\ &\quad+4V_{sur}a_{sur}G_{sur}(r)+4iV_{sui}a_{sui}G_{sui}(r) \\ &\quad+\left(\frac{\hbar}{m_\pi c}\right)^2\Big\{V_{sor}G_{sor}(r)+iV_{soi}G_{soi}(r)\Big\}\boldsymbol{L}\cdot\boldsymbol{\sigma},\end{aligned} \tag{5.16}$$

where

$$\begin{aligned}V_{Coul}(r) &= \frac{Ze^2}{2R_c}\left(3-\frac{r^2}{{R_c}^2}\right) \qquad (r<R_c) \\ &= \frac{Ze^2}{r} \qquad (r>R_c)\end{aligned} \tag{5.17}$$

$$F_k(r) = \left\{1+\exp\left(\frac{r-r_kA^{1/3}}{a_k}\right)\right\}^{-1} \tag{5.18}$$

$$\begin{aligned}G_k(r) &= \frac{1}{r}\frac{d}{dr}F_k(r) \\ &= -\frac{1}{ra_k}\exp\left(\frac{r-r_kA^{1/3}}{a_k}\right)\left\{1+\exp\left(\frac{r-r_kA^{1/3}}{a_k}\right)\right\}^{-2}\end{aligned} \tag{5.19}$$

and $k = r, i, sur, sui, sor, soi$ for $F_k(r)$ and $G_k(r)$. Depth parameter, reduced radius parameter, and diffuseness parameter were expressed as V_k, r_k, and a_k, respectively, in each term, where $k = r, i, sur, sui, sor, soi$. The factor $(\hbar/m_\pi c)$ is the pion mass, and its

square was taken to be 2. The vectors $\boldsymbol{L}$ and $\boldsymbol{\sigma}$ were the orbital angular momentum and the Pauli spin operator, respectively. The factor V_{Coul} represented the Coulomb potential with spherical uniform charges with the radius R_c. The second line in Eq. 5.16 represents the surface term for the central potential. The potential parameters (V_k, r_k, and a_k, where $k = r, i, sur, sor, soi$) were determined by fitting to the experimental data for the minimum chi-square value per number of data N using the equation

$$\chi^2 = \sum_{i=1}^{N} \left(\frac{O_{exp}(\theta_i) - O_{calc}(\theta_i)}{\Delta O_{exp}(\theta_i)} \right)^2, \tag{5.20}$$

where O_{exp} was the experimental differential cross section and the analyzing power as obtained in Eqs. 5.10 and 5.11, and O_{calc} was the ones obtained in the calculation. ΔO_{exp} was the uncertainty for O_{exp} as obtained in Eqs. 5.14 and 5.15. The initial parameters for the fitting was taken from one of the global Dirac optical model potentials (EDAD Fit1−3 [46]), that were converted to the Schrödinger equivalent form. The initial parameters were obtained by a manual search. The imaginary part of the surface term for the central potential (V_{sui}, r_{sui}, a_{sui}) was not included in the fitting because the term was not required to reproduce the potential predicted by EDAD's. In the fitting procedure for the optical potential, the Coulomb radius R_c was fixed at 1.25 fm. The data of ^{16}O and ^{40}Ca that were not measured in the experiment were taken from Ref. [47]. Typical results of the optical potential and the fitting to the data are shown in Figs. 5.1 and 5.2 and the best-fit parameters are listed in Table 5.1. The functions $U_r(r)$, $U_i(r)$, $U_{sor}(r)$, and $U_{soi}(r)$ were used in the figures to denote the real part of the central potential, the imaginary part of the central potential, the real part of the spin-orbit potential, and the imaginary part of the spin-orbit potential, respectively, as defined

$$\begin{aligned}
U_r(r) &= -V_r F_r(r) + 4 V_{sur} a_{sur} G_{sur}(r) && (5.21)\\
U_i(r) &= -V_i F_i(r) && (5.22)\\
U_{sor}(r) &= 2 V_r G_{sor}(r) && (5.23)\\
U_{soi}(r) &= 2 V_r G_{soi}(r), && (5.24)
\end{aligned}$$

where the factor 2 for $U_{sor}(r)$, and $U_{soi}(r)$ comes from square of the pion mass. The surface term of the imaginary part for the central potential was not used as described above. In the figures, the global optical potentials parameterized in the proton energy range of 20−1040 MeV for ^{12}C−^{208}Pb [46] and ^{4}He−^{208}Pb [48] are compared with the fitting results as EDAD and new2009, respectively. The obtained optical model potential parameters, listed in Table 5.1, were used to represent the distortion effect in the distorted wave Born approximation calculations (Sec. 6.2).

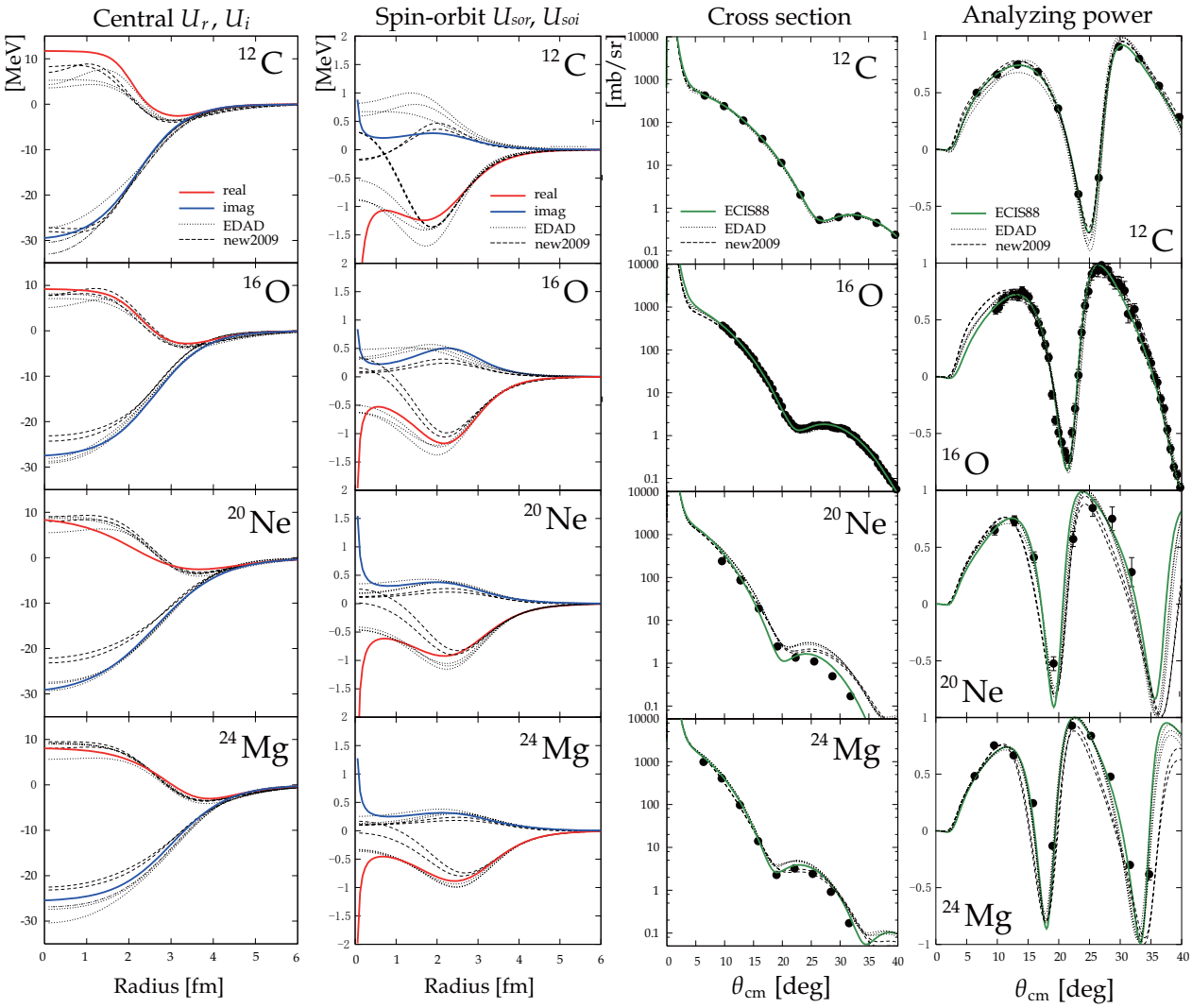

Figure 5.1: The optical model potentials for ^{12}C, ^{16}O, ^{20}Ne, and ^{24}Mg obtained by the code ECIS88 [45] and the fitting results for the cross section and the analyzing power. The derived parameters are listed in Table 5.1. The global optical potentials parameterized in the proton energy range of 20−1040 MeV for ^{12}C−^{208}Pb [46] and ^{4}He−^{208}Pb [48] are shown as EDAD (dotted curves) and new2009 (dashed curves), respectively. The initial parameters for the fitting were taken from one of EDAD by a manual search. The experimental data for ^{16}O were taken from Ref. [47], and others are from the present thesis.

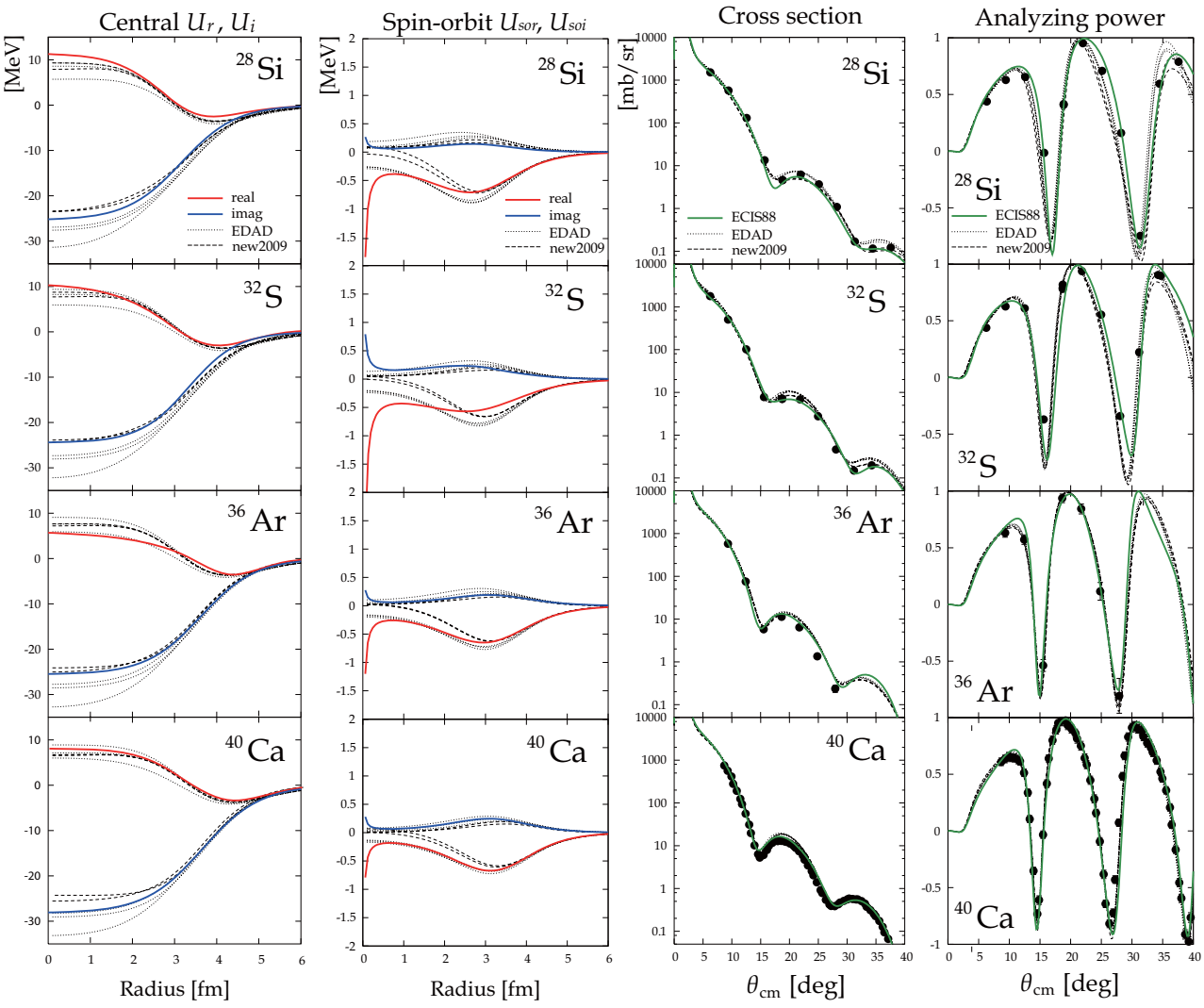

Figure 5.2: Same as Fig. 5.1, but for ^{28}Si, ^{32}S, ^{36}Ar, and ^{40}Ca. The experimental data for ^{40}Ca were taken from Ref. [47].

Table 5.1: Table of the optical potential parameters used in the form of Eq. 5.16 obtained by the fitting using ECIS88 [45] code. The parameter V_k is expressed in MeV, and the parameters r_k and a_k are expressed in fm, where $k = r, i, sur, sui, sor, soi$. In the fitting procedure, the Coulomb radius r_c has been fixed at 1.25 fm. The imaginary part of the surface term for the central potential (V_{sui}, r_{sui}, a_{sui}) is not included in the present fitting. The potentials and the fitting results are shown in Figs. 5.1 and 5.2. The parameters are used in the distoted wave Born approximation calculation (Sec. 6.2).

	V_r	r_r	a_r	V_i	r_i	a_i	V_{sur}	r_{sur}	a_{sur}
^{12}C	-11.7271	0.8936	0.2303	30.0244	0.9642	0.5577	2.7002	1.3567	0.4629
^{16}O	-9.2196	0.8844	0.3124	27.8003	1.0427	0.5952	3.1033	1.2854	0.5506
^{20}Ne	-9.0559	1.2356	0.5682	30.0252	0.9767	0.7715	7.6628	1.0521	0.7694
^{24}Mg	-8.1733	1.1501	0.4131	25.7177	1.0488	0.6667	5.7071	1.1450	0.6483
^{28}Si	-11.4276	1.1644	0.5242	25.3639	1.0403	0.6459	8.0902	1.0763	0.6237
^{32}S	-10.5791	1.2274	1.0902	24.4626	1.0499	0.5791	8.5048	1.1749	0.7241
^{36}Ar	-6.0904	0.9061	1.1335	25.5578	1.0967	0.6460	4.9719	1.3000	0.5213
^{40}Ca	-7.7000	0.8650	0.5000	28.2000	1.0700	0.6800	4.2000	1.2500	0.6200
	V_{sui}	r_{sui}	a_{sui}	V_{sor}	r_{sor}	a_{sor}	V_{soi}	r_{soi}	a_{soi}
^{12}C	0.0000	-	-	2.8993	0.9321	0.6052	-0.7199	0.9979	0.5886
^{16}O	0.0000	-	-	2.8573	0.9646	0.5280	-1.2961	0.9941	0.5404
^{20}Ne	0.0000	-	-	2.8102	0.9438	0.6401	-1.1475	0.9063	0.6809
^{24}Mg	0.0000	-	-	2.8919	0.9579	0.6261	-1.0860	0.9144	0.7114
^{28}Si	0.0000	-	-	2.7536	0.9827	0.6903	-0.5101	0.9735	0.6323
^{32}S	0.0000	-	-	2.5435	0.9546	0.8018	-0.8784	0.8910	0.7090
^{36}Ar	0.0000	-	-	2.7672	0.9900	0.6838	-0.8140	1.0200	0.6644
^{40}Ca	0.0000	-	-	2.8000	0.9900	0.6400	-1.0000	0.9800	0.6300

Chapter 6

Extraction of $B(M1)_\sigma$ and $B(M1)_{\sigma\tau}$

The first step of the present work was the extraction of spin-$M1$ transition strengths to the low-lying discrete states. For this purpose and the detection of the $M1$ transition, a shell model and a DWBA calculation codes were employed to obtain the 1^+ state wave function and the angular distribution of the inelastic scattering.

6.1 Shell-model calculation

For the calculation of one-body transition densities (OBTDs) of nucleon-nucleus scattering and theoretical spin-$M1$ transition strengths, the shell-model calculations were performed by using the code Nushell@MSU [49]. The calculations gave realistic wavefunctions of the nuclear states in question with the effective interaction in a truncated shell model space. The effective interactions of CKPOT and CKII were used for the calculation of the p-shell nuclei within $0\hbar\omega$. The CKPOT and CKII interactions are identical to the (8-16)POT and the (8-16)2BME, respectively, in Ref. [51]. For the calculation of the sd-shell nuclei, the effective interactions of USD [13, 52], USDA and USDB [53] were employed within the shell model space of $0\hbar\omega$ excitation. The USD interaction has been derived from the fit of 63 two-body matrix elements and three single-particle-energies to reproduce the experimental values of 380 energy levels in the sd-shell nuclei within the root-mean-square (rms) deviation of 150 keV in 1980s. Recently, the new interactions of USDA and USDB have become available, based on the updated set of energies of 608 levels in 77 nuclei. The USDA and USDB have been obtained with resulting rms deviations of 170 keV and 130 keV, respectively.

The OBTDs obtained from the shell-model calculation were used for the input data to the code DWBA07 [54] to calculate differential cross sections.

6.2 Distorted wave Born approximation

In this thesis, distorted wave Born approximation (DWBA) calculations were used to evaluate differential cross section of the inelastic scattering. The calculations were performed by using the computer code DWBA07 [54].

6.2.1 Differential cross section and distorted approximation

In the direct reaction process where the one-step reaction is dominant, the microscopic description of nucleon-nucleus scattering is made available by the Born approximation [55]. The differential cross section of inelastic scattering in this approximation takes the form

$$\frac{d\sigma}{d\Omega} = \frac{M^2}{(2\pi\hbar)^2}\frac{k_f}{k_f}|T_{fi}|^2, \tag{6.1}$$

where M is the reduced mass of the system, k_i and k_f are the wavenumbers of the incoming and the outgoing particles, respectively, and T_{fi} is the transition matrix element from the initial state i to a definite final state f. The transition matrix element can be written as

$$T_{fi} = \int \chi_f^{-*}(\boldsymbol{k}_f, \boldsymbol{r})\langle\phi_f|V|\phi_i\rangle\chi_i^{+}(\boldsymbol{k}_i, \boldsymbol{r})d\boldsymbol{r}, \tag{6.2}$$

where $\chi^{\pm}$ are the distorted wavefunctions for the projectile and the ejectile, and V is the potential of the nuclear reaction, and ϕ_i and ϕ_f are the wavefunctions of the ground and the excited states of the target nucleus, respectively. The distortion effect of the wavefunctions is represented by the optical model potential parameters that are modified to reproduce the elastic scattering data.

6.2.2 Parameters used in DWBA07 code

Optical model potential parameters

The optical model potential parameters were taken from Table 5.1, which were determined by the fitting to the data of elastic scattering taken by the present experiment and from Ref. [47]. The differential cross section of inelastic scattering is sensitive, compared with the case of elastic scattering, to the distortion effect described by the optical model potential parameters [10]. Thus, the optical potential parameters derived by the same manner for all the nuclei in question were adopted, in order to reduce systematic uncertainties. The optical model potential parameters were taken from Table 5.1. See Chapter 5 for the deriving procedure of the parameters.

One-body transition densities

One-body transition densities (OBTDs) of the transitions to the $J^\pi = 0^+$, 1^+, and 2^+ states were obtained from the shell-model calculations. The effective interactions of USD,

USDA, USDB were used for ^{20}Ne, ^{24}Mg, ^{28}Si, ^{32}S, and ^{36}Ar and those of CKPOT and CKII were used for the p-shell nuclei (^{11}B and ^{12}C). The OBTD's obtained for ^{20}Ne and ^{36}Ar were used to produce the angular distribution of the inelastic scattering cross section in ^{16}O and ^{40}Ca, respectively, since the shell-model calculation for the double-closed nucleus can not be performed within $0\hbar\omega$ excitation in the sd-shell. The OBTDs obtained from the shell model calculation were input to the DWBA07 with a factor of $1/\sqrt{2}$. For a transition to the $J^\pi = 1^-$ state, a simple $1p1h$ configuration caused by $1\hbar\omega$ particle jump $e.g.$, a $(2p_{3/2}, 1d_{5/2}^{-1})$ configuration for ^{28}Si, was considered as the OBTDs of the non-normal-parity transition. The other J^π transitions ($\Delta L \geq 2$) were not considered for the present study since they are hindered in the region of small momentum transfer.

Oscillator parameter

The single-particle radial wavefunctions, used for the calculation of the transition matrix element, were assumed to take a form of the harmonic-oscillator potential type. The global harmonic-oscillator parameter b with a mass dependence given in Ref. [56] was used in the present study, although in some cases b parameter can be obtained from literature. The formulae of the global b parameters for the protons (b_π) and for the neutrons (b_ν) in Ref. [56] are

$$b_\pi^{\,2} = 0.983(4)A^{1/3} + 0.373(23) \quad \mathrm{fm}^2 \tag{6.3}$$

$$b_\nu^{\,2} = 0.859(5)A^{1/3} + 0.699(24) \quad \mathrm{fm}^2, \tag{6.4}$$

where A is mass number. The formula for b_π has been determined from experimental root mean square charge radii of nuclei with a correction for the internal charge distributions of the proton and neutron. The formula for b_ν has been estimated by the use of empirical relations between the neutron skin thickness and the relative neutron excess. The b parameters for protons and neutrons used in the DWBA calculation are listed in Table 6.1.

Effective nucleon-nucleon interaction

The effective nucleon-nucleon (NN) interaction was taken from the t-matrix of the free NN interaction parameterized at 325 MeV by Franey and Love (FL325) [5].

We have examined three different sets of NN interactions, FL325, FL270, and Paris, to determine the most suitable interaction for the extraction of the strengths. The interaction FL270 is the free NN t-matrix parameterized at 270 MeV. The Paris interaction [57] has been generated from the G-matrix type interactions that include medium effects in the description of NN scattering [58].

Figure 6.1 shows the results of the ^{28}Si(p, p') inelastic scattering cross sections obtained in the present experiment and the DWBA calculations using the effective interactions

Table 6.1: The oscillation parameters for protons (b_π) and neutrons (b_ν) calculated from the formulae for the global harmonic-oscillator parameters of Eqs. (6.3) and (6.4), respectively. They have been determined in Ref. [56].

nuclei	b_π (fm)	b_ν (fm)
^{12}C	1.620(25)	1.633(24)
^{16}O	1.688(25)	1.692(24)
^{20}Ne	1.744(25)	1.741(24)
^{24}Mg	1.791(26)	1.782(24)
^{28}Si	1.832(26)	1.819(24)
^{32}S	1.869(26)	1.851(24)
^{36}Ar	1.902(27)	1.880(24)
^{40}Ca	1.932(27)	1.907(24)

mentioned above. The left and right panels show the angular distributions of the IS and IV 1^+ transitions, respectively, for the strongest excitation in ^{28}Si at 0° to the states at E_x = 9.495 and 11.447 MeV, respectively. The DWBA calculation results were normalized to the experimental results at 0.74° in the laboratory frame. The reproducibility for the eight experimental points at forward scattering angles, $0-7^\circ$ in center of mass frame, was evaluated by calculating the reduced chi-squares as

$$\chi^2 = \sum_{i=1}^{8} \left(\frac{O_{exp}(\theta_i) - O_{DWBA}(\theta_i)}{\Delta O_{exp}(\theta_i)} \right)^2, \tag{6.5}$$

where O_{exp} and ΔO_{exp} are the experimental differential cross section and its uncertainty, and O_{DWBA} is the cross section obtained by the DWBA calculation with the normalization. Because the shape of the angular distribution of the 1^+ transitions does not depend on wavefunctions at forward scattering angles (see Sec. 6.3), the data points at only small scattering angles were considered. The result of the chi-square values are summarized in Table 6.2. The FL325 interaction was found to achieve the best reproducibility from the total chi-square value. The FL270 interaction seemed to show slightly worse reproducibility. The Paris interaction underestimated the IS cross sections at finite scattering angles in the range of $5-15^\circ$, although good agreement was achieved for the IV cross section. We determined to use the FL325 interaction in the present analysis. The observation mentioned above is consistent with the study of NN interaction [19] from the energy dependence of the IS and IV 1^+ transition cross section ratio.

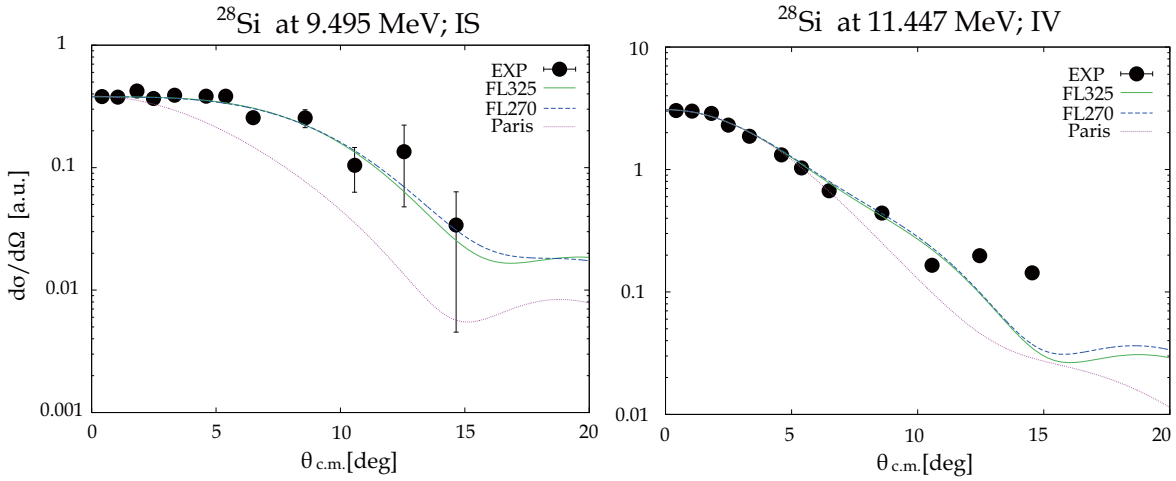

Figure 6.1: The angular distributions by the DWBA calculations using three kinds of NN interactions, compared with those of the experimental results (closed circles) for the strongest IS and IV transitions to the 1^+ states in the ^{28}Si(p, p') reaction.

Table 6.2: The calculated chi-square values following Eq. (6.5) for the IS and the IV 1^+ transitions in ^{28}Si and the sum of the chi-square values. The FL325 interaction shows the best reproducibility in the angular distribution.

	isoscalar	isovector	total
FL325	12.5	41.4	53.8
FL270	12.8	53.4	66.3
Pairs	143	20.1	164

6.3 J^π and isospin assignment

6.3.1 Shape of typical angular distribution of 1^+ transition

Typical shape of 1^+ transition

The cross section of a $\Delta L = 0$ nuclear excitation shows a typical angular distribution of forward peaking character, being a maximum at 0°. In figure 6.2, the angular distributions of the 1^+ transitions in ^{28}Si based on the wavefunctions for the USD, USDA, and USDB interactions are drawn with the normalizations to unity at 0°. The IS and the IV 1^+ transitions are shown in red and blue, respectively. The bold curves in black were artificially produced by averaging the respective distribution curves of the IS and IV transitions with weights of the strengths, *i.e.*, $B(M1)_\sigma$ for IS and $B(M1)_{\sigma\tau}$ for IV. The artificial curves were treated as the shape standards for the IS and IV 1^+ transitions and were used for the J^π as well as T assignments.

There are two points to be noted in Fig. 6.2. One is that there is a marked difference in shape of the angular distribution of the 1^+ transitions between the IS and the IV transitions. The distribution of the IS transition changes with angle more slowly than the IV one. The exchange effect in the nuclear reaction seems to cause such difference in the angular distribution between the IS and the IV excitations, as seen in Fig. 6.3 obtained for different assumptions on the reaction mechanism by changing the logical controls in the code DWBA07. The artificial curves in Fig 6.2 are also drawn in Fig. 6.3 for comparison. The other point is that the angular distributions in the range of scattering angles at $0-7°$ in center of mass frame are nearly independent of the wavefunction for each transition. These angular distributions based on different wave functions are almost identical within this region, while they differ considerably at the scattering angles of $>7°$. Therefore, the IS/IV assignment may be made by fitting the artificial curves to the experimental angular distribution at the small scattering angles.

Typical angular distributions of different J^π excitations

Not only the 1^+ transitions but also 0^+ and other $\Delta L \geq 1$ transitions (for example 1^- and 2^+ ones) are observed at 0°. Figure 6.4 shows the typical angular distributions of different J^π excitations for ^{28}Si. They were normalized to unity at 0°. The shape of angular distribution of the 1^- and 2^+ transitions are clearly different from those of the IS and IV 1^+ transitions, while those of 0^+ transitions are not simply distinguishable from are the 1^+ transitions. Various wavefunctions of the 0^+ transitions obtained by the shell-model calculation are drawn in the figure in order to study the wavefunction dependence of the 0^+ transitions on the angular distribution. The angular distributions of the 0^+ transitions are similar to that of the IV 1^+ transition and one of them is similar to the

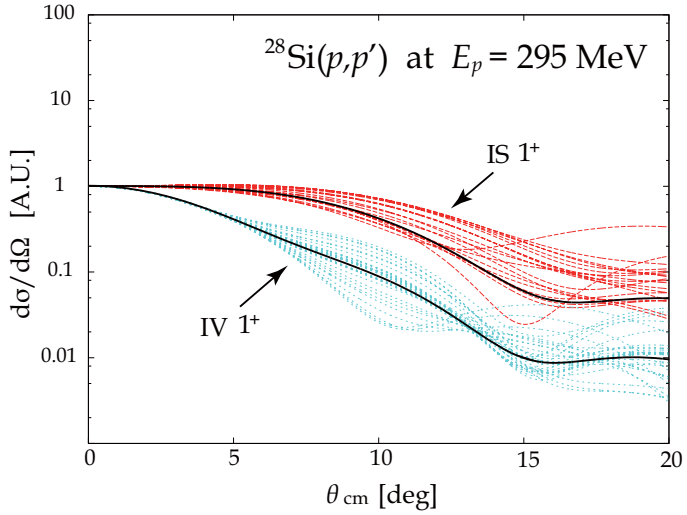

Figure 6.2: Angular distributions of the IS (red) and IV (blue) transitions in ^{28}Si calculated by DWBA07. The distributions have been normalized to unity at 0°. Several 1^+ angular distributions based on the USD, USDA, and USDB interactions were drawn to show the ambiguity of the wavefunctions. The bold curves in black have been artificially produced by averaging the distributions of each isospin with a weight of strength obtained from shell model calculation.

IS 1^+ transition at the angular range of 0° to 7°. However, the difference of the angular distributions between the 1^+ and 0^+ transitions becomes large at ∼15°; the cross section of the 1^+ transition almost monotonously decreases with scattering angle, while that of the 0^+ transitions increases in the range of >10°. Thus, we may take the following criteria in assigning the IS and IV 1^+ transitions;

- The angular distribution shows the maximum at 0°.
- The cross section decreases with scattering angle in the range of <10°.
- A local maximum at a finite angle is to be much (10 times or more) smaller than at 0°.

6.3.2 Assignment procedure

The J^π and T assignments were performed by comparing the experimental angular distributions of the proton inelastic scattering with the artificial curves of the IS and the IV 1^+ transitions and the typical distributions of the 0^+, 1^-, and 2^+ transitions obtained by the DWBA calculation. The experimental data taken by the GR placed at 0° was divided into three spectra at 0.40°, 1.00°, and 1.74° in laboratory frame (0.42°, 1.05°, and 1.82°, respectively, in center of mass frame in the case of ^{28}Si). The artificial curves of the 1^+ transitions and the typical curves of the other J^π transitions by the DWBA

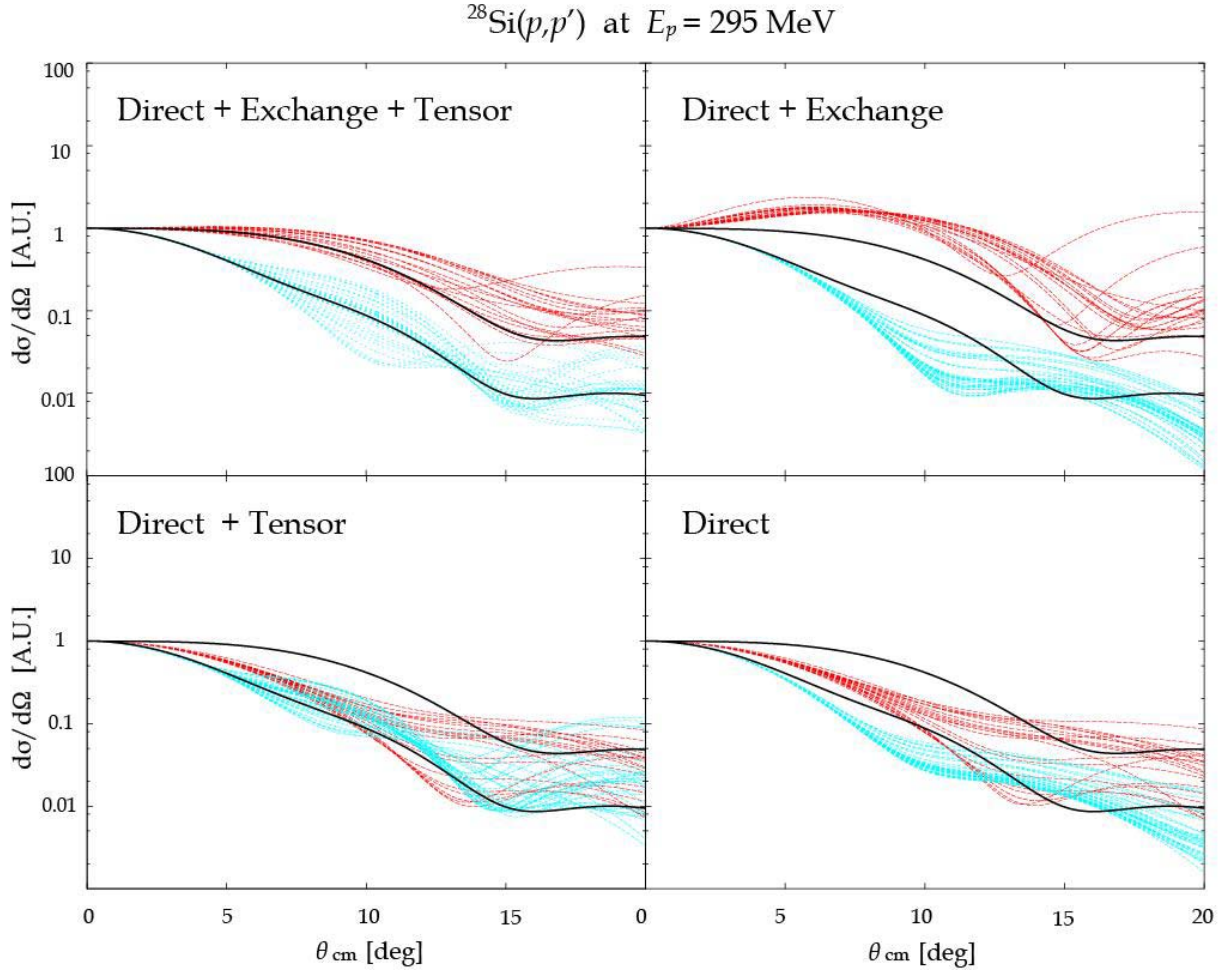

Figure 6.3: Angular distributions of the IS and the IV 1^+ transitions in ^{28}Si calculated by the DWBA07 with different assumptions on reaction mechanisms. The angular distributions of the IS and IV transitions are shown in red and blue, respectively. The artificial curves presented in Fig. 6.2 are also in black drawn for the comparison. The amplitudes are normalized to unity at 0°. The figure for the full calculations denoted as (Direct + Exchange + Tensor) is the same with Fig. 6.2.

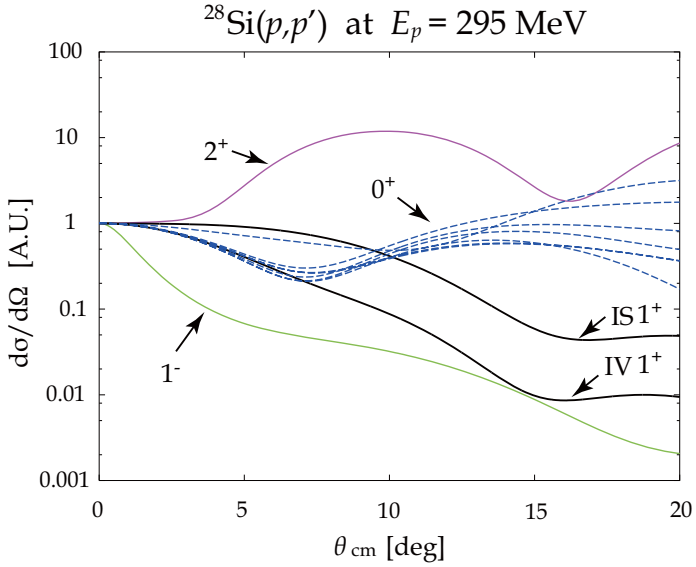

Figure 6.4: Calculated angular distributions of the 0^+, 1^-, 1^+, and 2^+ transitions. The cross sections are normalized to unity at 0°. Various wavefunctions of the 0^+ transition obtained from the shell-model calculation are drawn in blue for the comparison with the shape of the 1^+ transitions.

---

calculation were normalized to the average of the experimental cross sections at 0.40° and 1.0°. Then, the assignments of 0^+, IS-1^+, IV-1^+, 1^-, or $\Delta L \geq 1$ transitions to the discrete states were made by a "search-by-eye" (pattern recognition) considering especially the criteria mentioned in the previous sub-section for the IS and the IV 1^+ transitions. The reason why assignments based on chi-squares value as presented by Eq. (6.5) was not used, since the calculated angular distribution at finite scattering angles (>7°) significantly depends on the wavefunction used, making it hard to rely on the chi-squares in the practical assignment.

Typical results of the assignment by the "search-by-eye" for the IS and the IV 1^+ transitions in ^{28}Si are shown in Fig. 6.5. The experimental angular distributions clearly disagree with the 0^+, 1^-, and 2^+ transitions, and well agree with the artificial curves of the IS and IV 1^+ transitions within the range of scattering angles 0−10°. Figure 6.6 shows typical examples of the cases where definite assignments to the IS and the IV 1^+ transitions were not made in ^{28}Si. The experimental angular distributions are seen to be close to the shape standards of the IS and the IV 1^+ transitions at the region of small scattering angles. They, however, deviate from the standards at >10°. Such transitions were treated as those of indefinite assignment. The ambiguous assignment of the IS 1^+ transition was considered to be caused by the mixing of the 0^+ transition in the experimental yields. (see Sec. 6.3.4)

All the results of the assignment and the experimental angular distributions of inelastic

scattering cross section for the discrete state are summarized in Appendix C. The DWBA calculations are not presented for some discrete states when yields of the state were not extracted from the energy spectra at 0.40° and 1.0°.

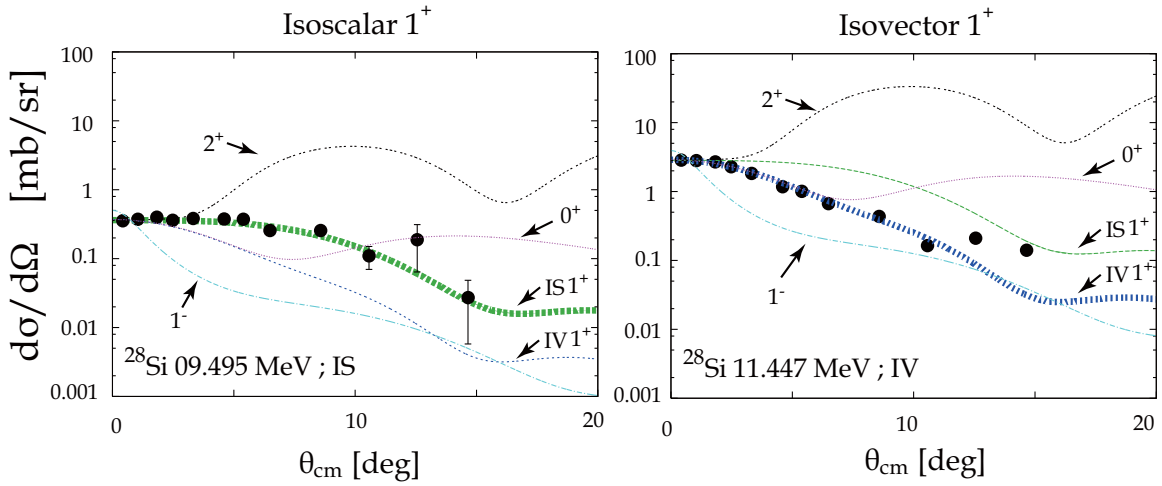

Figure 6.5: Typical assignments to the IS and IV 1^+ transitions in ^{28}Si. The typical angular distributions of the 0^+, 1^-, and 2^+ transitions and the artificial curves of the IS and IV 1^+ transitions are compared with the experimental data.

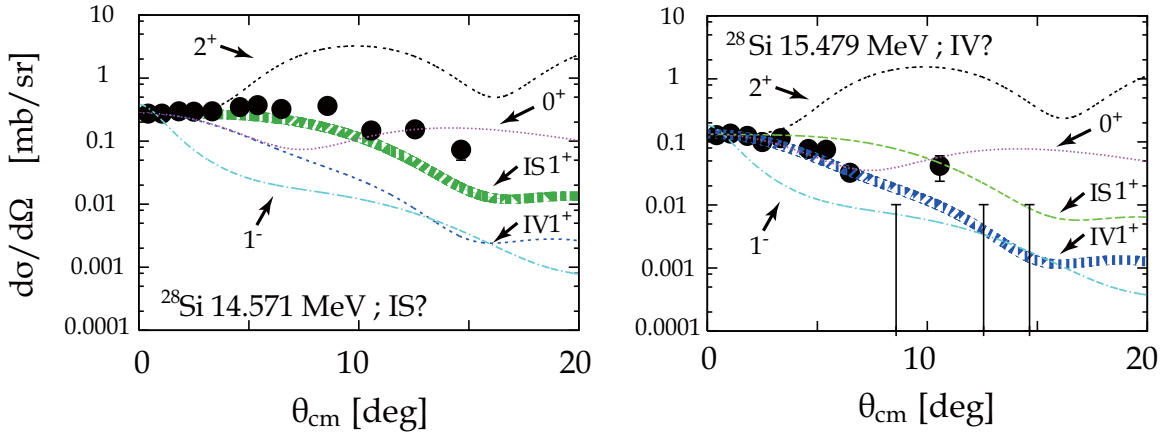

Figure 6.6: Typical examples of the uncertainly assignments to the IS and IV 1^+ transitions in ^{28}Si.

6.3.3 Cross check from polarization transfer observables on ^{28}Si

Since the J^π and T assignments of the excited states form a basis for deriving the $M1$ strengths, the examination of the validity of the present method of assignment was of utmost importance. Fortunately, there has been available a set of detailed experimental data on the polarization transfers (PT) of the proton inelastic scattering in the case of

^{28}Si [59]. The PT observables also give the information on ΔS and ΔT of the scattering, independent from the angular distributions of the cross sections [7]

Following the convention in Ref. [8], the total spin transfer (Σ) at scattering angle 0° is expressed as

$$\Sigma = \frac{3 - (2D_{SS} + D_{LL})}{4}, \tag{6.6}$$

where D_{SS} and D_{LL} denote the PT observables (see Ref. [8]). The quantity Σ takes 1 and 0 for spin-flip and non-spin-flip transitions, respectively. If the quantity T_{PT} is defined as

$$T_{PT} = S_{LL} - S_{SS} = \frac{1}{2}(D_{SS} - D_{LL}), \tag{6.7}$$

T_{PT} takes negative and positive values for the IS and the IV transitions, respectively. Therefore, the product of these two quantities at 0° takes

$$\Sigma \cdot T_{PT} \begin{cases} > 0 & (\text{IS } 1^+ \text{ transition}) \\ < 0 & (\text{IV } 1^+ \text{ transition}) \\ = 0 & (0^+ \text{ or other natural parity } \Delta L \geq 1 \text{ transition}). \end{cases} \tag{6.8}$$

It is to be noted that above assignments are only valid at 0°. The magnitude of the product of $\Sigma \cdot T_{PT}$ does not have any sense in the present discussion.

Figure 6.7 shows the result of the products of $\Sigma \cdot T_{PT}$ for ^{28}Si using the PT observables, taken from Ref. [59] and tabulated in Table 6.3. The present assignments from the angular distributions are written in the figure for comparison. The three transitions may be seen to be assigned as the 0^+ or other natural parity $\Delta L \geq 1$ (other than 1^+) ones from the products of $\Sigma \cdot T_{PT}$ are consistent with zero within errors. These assignments from the PT observables agree with the assignments from the angular distributions in the present work, as shown in Fig. 6.8. Thus, the present J^π and T assignments, based on the angular distributions of the cross sections, were found to be reliable enough for both the IS and the IV 1^+ transitions. It is also of interest that the 0^+ assignment from the angular distribution seems to be reliable as well.

6.3.4 Possible cause for indefinite 1^+ assignment

The transition to the $E_x = 14.571$ MeV state in ^{28}Si was indefinitely assigned to be the IS 1^+ transition; the experimental angular distribution was observed close to the IS 1^+ transition in the angular range of 0−10°, but somewhat deviate to become close to the 0^+ transition in the range of 10−15° (left panel of Fig. 6.6). Since, unfortunately, the PT observables in Ref. [59] were not available for this transition, the ^{28}Si(p, p') data at 160 MeV measured at 0° and at the Indiana University Cyclotron Facility (IUCF) [60]

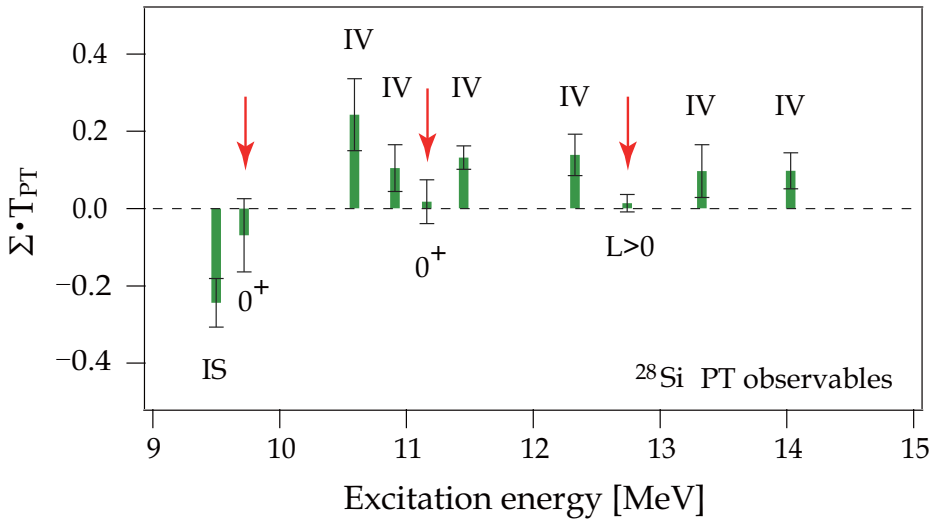

Figure 6.7: The J^π and T assignments by the polarization transfer observables. The product of the total spin transfer and the T_{PT} calculated from the PT observables measured for ^{28}Si [59], as listed in Table 6.3. The present J^π and T assignments are shown for comparison.

Table 6.3: Polarization transfer observables measured in the ^{28}Si$(\vec{p},\vec{p}')$ experiment at 0° using a 392 MeV proton beam at the RCNP [59].

E_x [MeV]	D_{SS}	D_{NN}
9.50	0.707 ± 0.133	-0.085 ± 0.124
9.72	0.600 ± 0.298	0.294 ± 0.276
10.59	-0.638 ± 0.138	-0.143 ± 0.125
10.91	0.040 ± 0.165	0.444 ± 0.151
11.16	0.562 ± 0.310	0.700 ± 0.292
11.45	-0.453 ± 0.047	-0.175 ± 0.042
12.33	-0.255 ± 0.102	0.112 ± 0.093
12.74	0.686 ± 0.215	0.906 ± 0.203
13.33	-0.280 ± 0.188	-0.050 ± 0.108
14.03	-0.437 ± 0.072	-0.237 ± 0.063

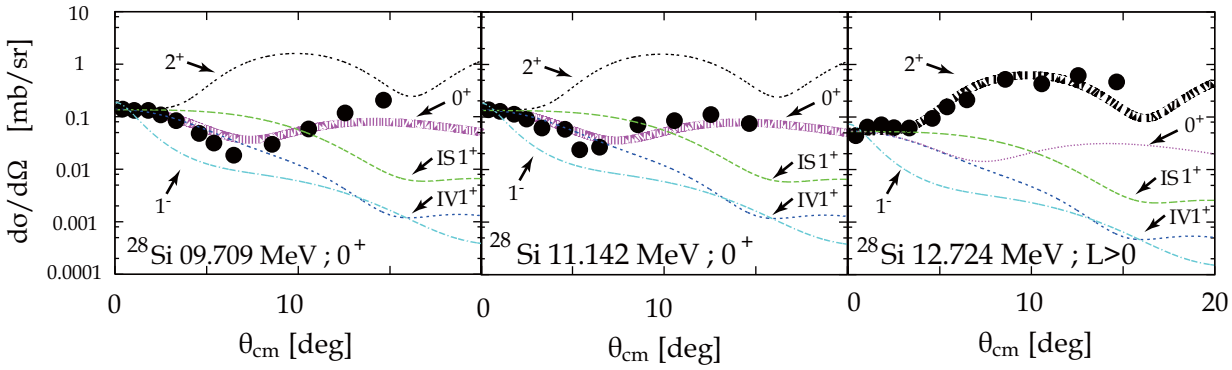

Figure 6.8: Angular distribution assigned as the 0^+ or $\Delta L \geq 1$ transition in ^{28}Si. The experimental distributions corresponding to the state indicated by the arrow in Fig. 6.7 are compared with the DWBA calculations.

---

were used for the examination of the assignment, based on the different energy dependence of the cross section for different J^π and T.

The energy spectrum around the $E_x = 14.571$ MeV transition from the ^{28}Si(p, p') at 160 MeV taken at the IUCF is shown in the middle panel of Fig. 6.9 after the background subtraction. The yields of the lines were calculated relative to the most intensive IS 1^+ transition to the 9.495 MeV state, and the results were compared between the measurements with different beam energies (*e.g.* 160 and 295 MeV) by introducing the ratio

$$R_{295/160} = \frac{\sigma(E_x)_{295}/\sigma(9.495)_{295}}{\sigma(E_x)_{160}/\sigma(9.495)_{160}}, \tag{6.9}$$

where $\sigma(E_x)_{E_p}$ denotes the yield of the transition to the state at E_x MeV for the proton beam energy of E_p ($E_p = 160$ and 295 MeV). The ratio $R_{295/160}$ is to be dependent on the J^π and T character of the transition and is expected to take unity for the IS 1^+ transition to the state at E_x.

In the energy range shown in Fig. 6.9, there are four 0^+ states definitely assigned at 9.709, 10.807, 11.142, and 12.971 MeV. The R values for these 0^+ states are plotted in the bottom panel against E_x together with that for the 14.571 MeV transition in question. The values for the 0^+ states are seen to be constant around the average of 0.43(2), while the value for the 14.571 MeV state is 0.74(10) lying midway between unity and 0.43. Since the yield seen at 0° is supposed to be mainly due to the $\Delta L = 0$ transition, the situation with the 14.571 MeV transition suggests that there may be a mixture of unresolved 0^+ component in the transition. The 0^+ mixing was estimated to be 54(7)% from the R value.

The present work found eight similar indefinitely assigned IS 1^+ transition; to the states at 12.398 MeV in ^{20}Ne, at 13.767, 13.933, and 14.009 MeV in ^{24}Mg, at 13.188, and

13.231, and 14.571 MeV in ^{28}Si, and 14.482 MeV in ^{36}Ar. The 0^+ mixing ratio of 54(7)% was assumed for these indefinitely assigned IS 1^+ transition in deriving the $B(M1)_\sigma$ values from the cross section at 0°.

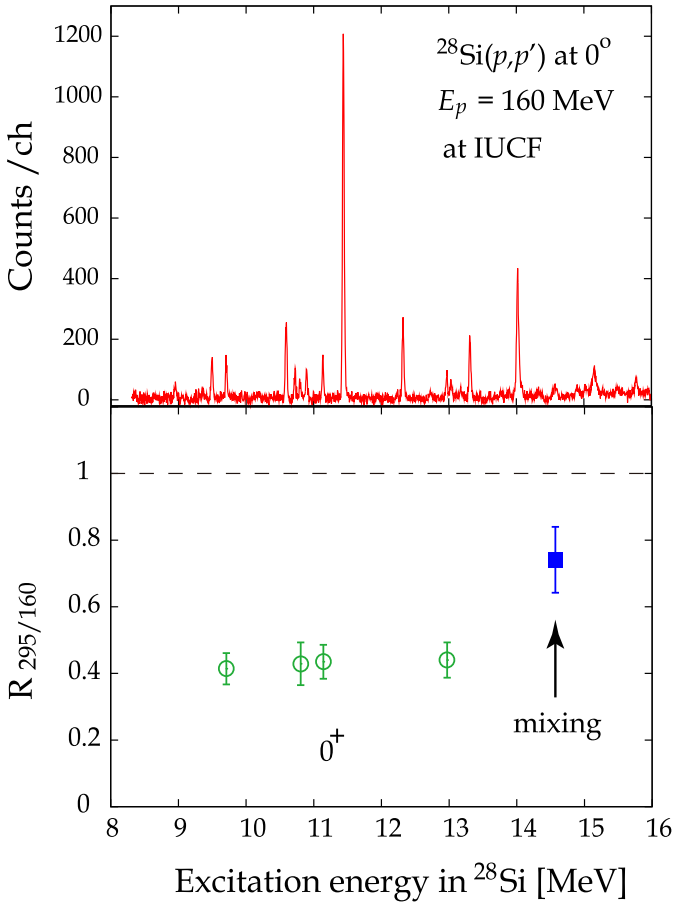

Figure 6.9: The energy dependence of the yields in ^{28}Si(p, p') spectra for the J^π and T assignment. The excitation energy spectra at E_p = 295 and 160 MeV, performed at the RCNP the IUCF [60], respectively, are shown in the top and middle panels. The yield ratio $R_{295/160}$'s for the 0^+ (opened circles) transitions and the indefinitely assigned IS 1^+ (closed square) transition to the 14.571 MeV state in ^{28}Si are shown in the bottom panel. The ratio $R_{295/160}$ is expected to take unity and 0.43(2) for the IS 1^+ and 0^+ transitions, respectively.

6.4 Unit cross section

As mentioned in Ref. [61], at incident beam energies above 100 MeV/u, a $\Delta L = 0$ transition becomes relatively enhanced as the one step direct reaction becomes dominant. Thus, the cross section of $\Delta L = 0$ transition of charge exchange reaction at the small momentum transfer becomes proportional to Gamow-Teller (GT) strength, B(GT). The unit cross section is defined as a proportionality constant between the cross section and the reduced

transition strength. This proportionality was used in the present thesis to obtain the IS and the IV spin-$M1$ transition strengths of $B(M1)_\sigma$ and $B(M1)_{\sigma\tau}$, respectively, from the cross sections at 0°. It should be noted that the isospin symmetry was assumed in the followings. More complicated problems *e.g.*, isospin mixing and the effect of meson exchange current (MEC) which violates the proportionality between the B(GT) and the $B(M1)_{\sigma\tau}$ due to relativistic effect, were not considered in the present thesis because their effect are expected to be small as discussed in Secs. 7.2.1 and 7.3.3.

The definitions of the unit cross section used in this thesis are given in Sec. 6.4.1. The deduction of unit cross section values from experiments is presented in Sec. 6.4.3. Using these experimental unit cross section values, the mass dependent formulae of the IV and the IS unit cross sections are determined in Secs. 6.4.4 and 6.4.5, respectively.

6.4.1 Definition of unit cross section

The unit cross sections $\hat{\sigma}_{IS}$ and $\hat{\sigma}_{IS}$ for the IS and the IV spin-$M1$ transitions, respectively, were defined as

$$\left.\frac{d\sigma}{d\Omega}\right|_{IS}(0^\circ) = \hat{\sigma}_{IS} F_{IS}(q,\omega) B(M1)_\sigma \tag{6.10}$$

$$\left.\frac{d\sigma}{d\Omega}\right|_{IV}(0^\circ) = \hat{\sigma}_{IV} F_{IV}(q,\omega) B(M1)_{\sigma\tau}, \tag{6.11}$$

where $d\sigma/d\Omega|_T(0^\circ)$ $(T = IS,\ IV)$ is the differential cross section at 0°, and $B(M1)_\sigma$ and $B(M1)_{\sigma\tau}$ are the IS and the IV spin-$M1$ transition strengths, respectively. The cross section value at 0° was obtained from the experimental cross section value measured at 0.40° in laboratory frame by the extrapolation using the artificial curve by the DWBA calculation (see Sec. 6.3.2 for the artificial curve). The factor $F_T(q,\omega)$ $(T = IS,\ IV)$ is the kinematical factor, which gives the dependence on momentum transfer (q) and energy transfer (ω), defined as

$$F_T(q,\omega) = \frac{\sigma(q,\omega)}{\sigma(0,0)} \quad (T = IS, IV), \tag{6.12}$$

where $\sigma(q,\omega)$ is the differential cross section at 0° of the 1^+ transition obtained by the DWBA calculation. The dependence of $F(q,\omega)$ on the energy transfer for ^{28}Si is shown in Fig. 6.10.

There are little dependence due to the wavefunctions in the $F(q,\omega)_{IV}$ function. Although simple $1p1h$ configurations of $(1d_{3/2},\ 2s^{-1}_{1/2})$ and $(2s_{1/2},\ 1d^{-1}_{3/2})$ transitions have different distribution curve of $F(q,\omega)_{IV}$ from the realistic ones, their cross section values at 0° are 10^2 smaller than those of realistic ones because they are not ΔL=0 transition. Thus, the realistic distribution of the $F(q,\omega)_{IV}$ function has to be considered. The

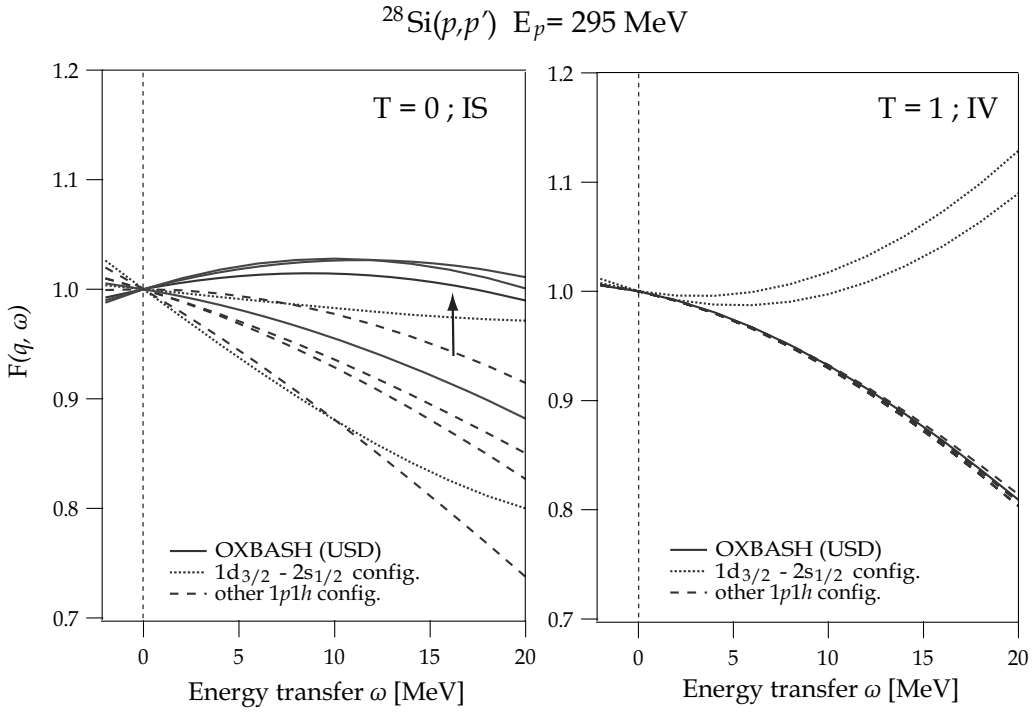

Figure 6.10: The calculated energy transfer (ω) dependence of the kinematical factor $F(q,\omega)$ in the case of ^{28}Si. The distribution of the strongest state among the IS 1^+ transitions is indicated by the arrow in the left panel.

$F_{IV}(q,\omega)$ function was assumed to be express with the mass number (A) and excitation energy (E_x) dependence as

$$F_{IV}(q,\omega) = F_{IV}(A,E_x) = \sum_{i=0}^{1}\sum_{j=0}^{2} \alpha_{ij} A^i {E_x}^j, \tag{6.13}$$

where α_{ij}, which is summarized in Table 6.4, is the parameter obtained by fitting to $F_{IV}(q,\omega)$ functions calculated for each nucleus. The obtained $F_{IV}(A,E_x)$ function is valid for $A = 11{-}58$ and $E_x = 0{-}20$ MeV. The uncertainty in $F_{IV}(A,E_x)$ was smaller than 1%.

Problem lies on the $F_{IS}(q,\omega)$ function. The energy transfer distribution is not unity as seen in the left panel of Fig. 6.10. This indicates that the $F_{IS}(q,\omega)$ function depends on the wavefunction. Because the energy transfer distributions of the realistic wavefunction predicted by the USD interaction are flat within $\pm 5\%$ in this energy transfer region as indicated by the arrow, the $F_{IS}(q,\omega)$ function was assumed to be

$$F_{IS}(q,\omega) = F_{IS}(A,E_x) = 1.00 \pm 0.05. \tag{6.14}$$

Table 6.4: Coefficients determined by the fitting for the $F_{IV}(A, E_x)$ function of Eq. (6.13) to the calculations using the wave function based on the USD interaction. The symbol A denotes the mass number, and E_x is the excitation energy in MeV.

ij	α_{ij}
12	−2.68e-06
02	−2.02e-04
11	−2.07e-05
01	−3.10e-03
10	+1.54e-05
00	+1.00e-00

6.4.2 Theoretical study of unit cross section

The relationship between the cross section and the spin-$M1$ transition strength was theoretically examined by using the DWBA calculation in order to study the validity of the proportionality. The decomposition of the nucleon-nucleus interaction into the central, the spin-orbit, and the tensor interactions at $E_p = 295$ MeV in the case of ^{28}Si is shown in the top panel of Fig. 6.11. Since the central component was found to be dominant in the IV transition, the transition strength is expected to be given from the observed cross section at 0° by using the unit cross section. The total cross section at 0° in the IS 1^+ transition, however, is mainly due to not the central interaction but the tensor interaction. We will study the proportionality between the cross section by tensor interaction and the spin-flip cross section later.

In order to know the contribution of the "σ" and the "$\sigma\tau$" operators in the cross section to the IS and the IV 1^+ transitions, respectively, the central interaction was decomposed into the spin-isospin components V_0, V_σ, V_τ, and $V_{\sigma\tau}$ by usign the equations

$$\begin{pmatrix} V_0 \\ V_\sigma \\ V_\tau \\ V_{\sigma\tau} \end{pmatrix} = \frac{1}{4} \begin{pmatrix} -1 & -1 & 1 & 1 \\ 3 & -1 & -3 & 1 \\ -1 & 3 & -3 & 1 \\ 3 & 3 & 9 & 1 \end{pmatrix} \begin{pmatrix} t^{SE} \\ t^{TE} \\ t^{SO} \\ t^{TO} \end{pmatrix}, \tag{6.15}$$

where t^{SE}, t^{TE}, t^{SO}, and t^{TO} denote the singlet-even, the triplet-even, the singlet-odd, and the triplet-odd components of the free nucleon-nucleon t-matrix [6], respectively. The results of the decomposition of the central interactions in the case of ^{28}Si are shown in the bottom panel of Fig. 6.11. It is obvious that the V_σ and the $V_{\sigma\tau}$ components are dominant in the IS and the IV transitions at 0°, while the total central interaction in the IS transition is hindered owing to the destructive interference of the pieces of the central components.

Next, the proportionality between the cross section by tensor interaction and the spin-flip cross section in the IS 1^+ transition was considered. The two dimensional plot of the

$B(M1)_\sigma$ versus the cross section ratio of the tensor interaction to the central interaction, mainly due to the V_σ interaction, is drawn in Fig. 6.12. The USD interaction was used for the $B(M1)_\sigma$ and to calculate the tensor and central cross sections. The result indicates that the cross section ratio is constant within $\pm 10\%$ accuracy for the strong state which is detectable ($> 0.01\ \mu_N^2$). Thus, the equation for the IS unit cross section, Eq. (6.10), was supposed to be valid within the uncertainty of 10%. This accuracy was taken as an additional error in the IS unit cross section, being $\Delta c_{IS} = 0.1$ in Eq. (6.23).

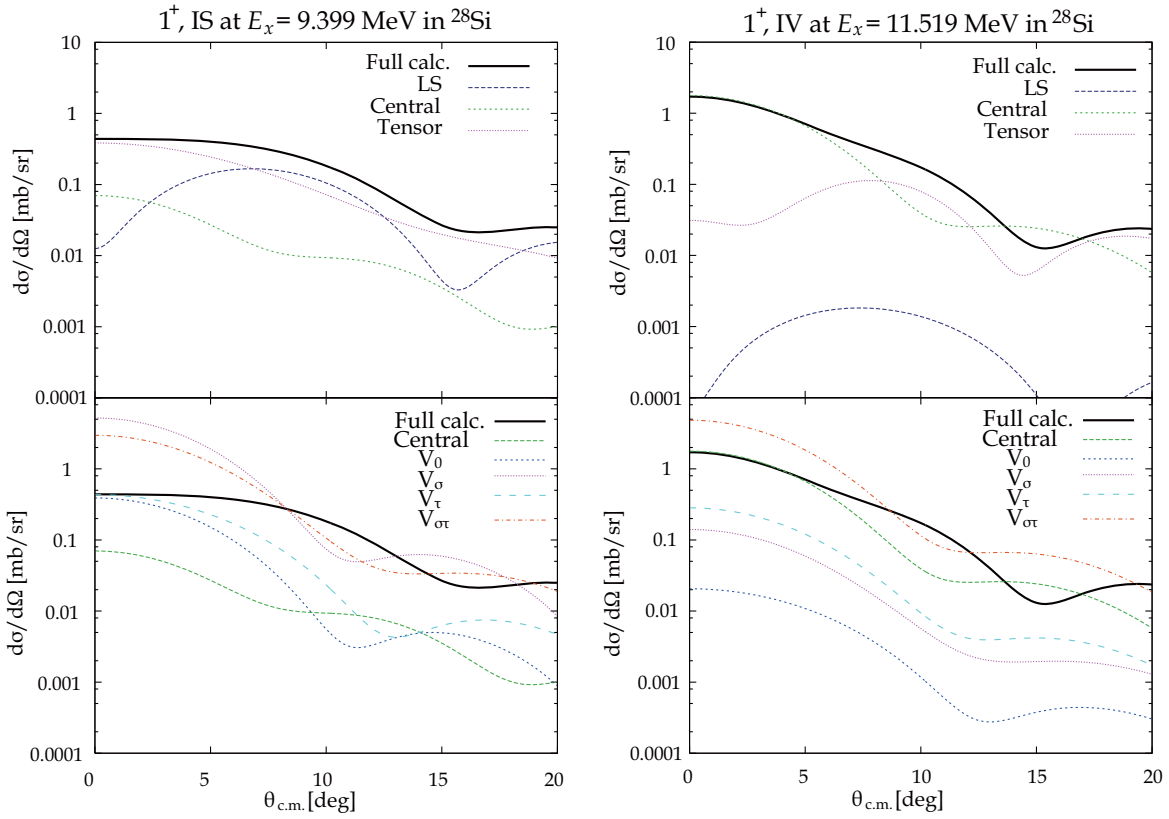

Figure 6.11: The decompositions of the nucleon-nucleus interaction at $E_p = 295$ MeV in the case of ^{28}Si. The results of the IS and the IV 1^+ transition to the $E_x = 9.399$ and 11.519 MeV, respectively, predicted as the strongest states by the USD interaction, are shown in the left and the right panels, respectively. In the top panel, the decomposition into the central, the spin-orbit (LS), and the tensor interactions are shown. The central interaction is decomposed into the spin-isospin components (V_0, V_σ, V_τ, and $V_{\sigma\tau}$) in the bottom panel. The full calculation is denoted as the bold curve in black.

6.4.3 Unit cross section from experiment

The IV unit cross section $\hat{\sigma}_{IV}$ can be experimentally obtained by using the (p, p') cross section and the $B(M1)_{\sigma\tau}$ value determined from the corresponding β-decay strength assuming the isospin symmetry. However, it is rare that the unit cross section can be directly

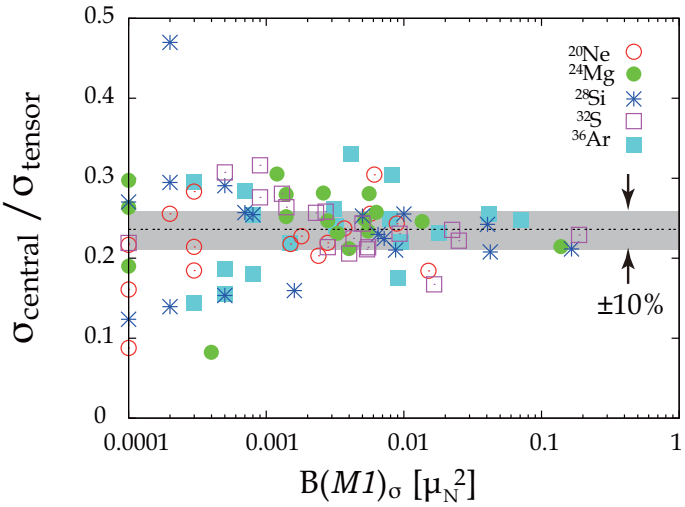

Figure 6.12: Two dimensional plot of the $B(M1)_\sigma$ and the cross section due to the V_σ interaction in the IS 1^+ transition, based on the shell model and the DWBA calculations using the USD interaction. The cross section ratio of the tensor interaction to the central interaction mainly due to V_σ is constant within $\pm 10\%$ accuracy for the strong state which is detectable ($> 0.01\ \mu_N^2$).

obtained from experiments because the β-decay is to be the transition where inverse excitation is measureable by the (p, n) and other reactions at 0° [62,63]. In the present thesis, the IV unit cross sections for ^{12}C, ^{26}Mg, ^{58}Ni, and ^{11}B were determined experimentally as summarized in Table 6.5. Then, they were used for deriving the A-dependence of $\hat{\sigma}_{IV}(A)$ (Sec. 6.4.4). For the case of ^{11}B, the situation was special since both the unit cross sections of $\hat{\sigma}_{IS}$ and $\hat{\sigma}_{IV}$ were determined. Those of ^{24}Mg and ^{32}S were not obtained because their corresponding β-decays from the first 1^+ excited state to the ground state are the forbidden transition. That is why those transitions were not considered in Ref. [62].

In the following subsections, the deduction of each experimental unit cross section is described.

Table 6.5: The unit cross sections obtained from experiments assuming isospin symmetry in unit of mb/sr/μ_N^2. Effects of isospin mixing and meson exchange current are not taken into account.

	$\hat{\sigma}_{IS}$	$\hat{\sigma}_{IV}$
^{11}B	2.1 ± 0.4	1.4 ± 0.1
^{12}C	-	1.60 ± 0.10^a
^{26}Mg	-	1.45 ± 0.09
^{58}Ni	-	0.713 ± 0.082

[a] Average of ft-values of ^{12}B and ^{12}N.

Relationship between $B(M1)_{\sigma\tau}$ and $B(\mathrm{GT})_\beta$

The reduced transition strength of a β-decay, $B(\mathrm{GT})_\beta$, can be obtained from the experimental ft-value as

$$B(\mathrm{GT})_\beta = \frac{C}{(g_A/g_V)^2 ft}, \tag{6.16}$$

where $C = 2\times(3071.4\pm0.8)$ s [64] (see Ref. [64] for the detail) and $g_A/g_V = 1.2695\pm0.0029$ [65] is the ratio of axial-vector to vector coupling constants of the neutron β-decay. Thus, the relationship between the β-decay strength $B(\mathrm{GT})_\beta$ and the corresponding "excitation" GT strength $B(\mathrm{GT})\uparrow$ can be expressed as

$$B(\mathrm{GT})\uparrow = \frac{2J_f+1}{2J_i+1}\, B(\mathrm{GT})_\beta, \tag{6.17}$$

where the suffixes were taken for the "excitation" transition. Thus, we can obtain an experimental $B(M1)_{\sigma\tau}$ value by using Eqs. (6.16), (6.17), and (A.25).

Case of ^{12}C

Figure 6.13 shows the isospin symmetry structure in $A = 12$ isobars. The ft-values experimentally determined from the β-decays from ^{12}B and ^{12}N have been reported to be $(1.167 \pm 0.004)\times10^4$ s and $(1.318 \pm 0.008)\times10^4$ s [67], respectively. Although a small asymmetry can be seen in the ft-values between the mirror nucleus, which is supposed to originate from the G-parity irregular [68], we do not deal with this subject here. Applying the average of the two ft-values, $\hat{\sigma}_{IV}(^{12}\mathrm{C}) = 1.60 \pm 0.10$ mb/sr/${\mu_N}^2$ was obtained from the experimental cross section of 3.429 ± 0.076 mb/sr at 0.40° in laboratory frame. The error of $\hat{\sigma}_{IV}(^{12}\mathrm{C})$ was taken to cover the two data.

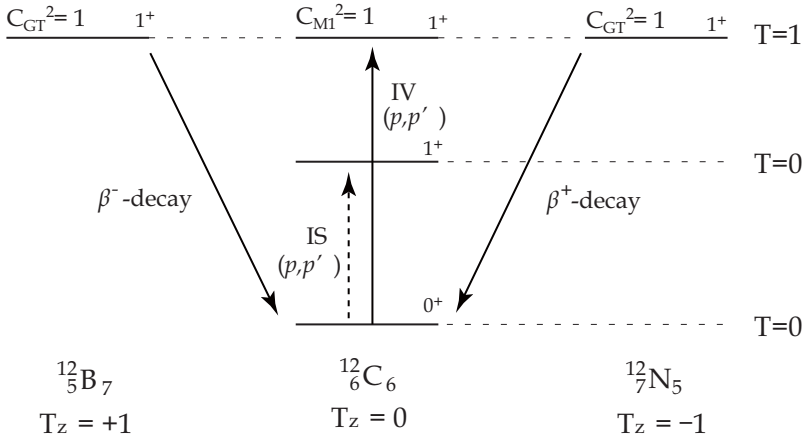

Figure 6.13: Schematic diagram of isospin symmetry structure in $A = 12$ isobars.

Case of ^{26}Mg

Figure 6.14 shows the isospin symmetry structure in $A = 26$ isobars. The $B(\mathrm{GT})\uparrow$ values to the low lying discrete states in ^{26}Al ($J^\pi = 1^+$) by the (^{3}He,t) reaction from ^{26}Mg were obtained from the corresponding β-decay transitions from ^{26}Si in Ref. [69, 70]. Applying the proportionality between the yields and the $B(\mathrm{GT})\uparrow$ value, $B(\mathrm{GT})\uparrow$ values with $T = 2$ in ^{26}Na and ^{26}Mg were identified by using the (^{3}He,t) and (t,^{3}He) reactions [71]. The strongest state with $T = 2$ observed at $E_x = 13.302$ MeV in the ^{26}Mg(p, p') spectrum was found to be double to the state at 13.324 MeV. The cross sections by the (p, p') reaction at 0.40° in laboratory frame were obtained to be 0.607 ± 0.011 and 0.372 ± 0.008 mb/sr at 13.302 and 13.324 MeV, respectively. Hence, $\hat{\sigma}_{IV}(^{26}\mathrm{Mg}) = 1.45 \pm 0.09$ mb/sr/$\mu_N{}^2$ was obtained using the corresponding strength $B(\mathrm{GT})\uparrow = 0.41 \pm 0.02$ [71]. We note that an excitation of $T = 1 \rightarrow 1$ can not be used for the present calculation because the transition is mixed with the IS and IV components.

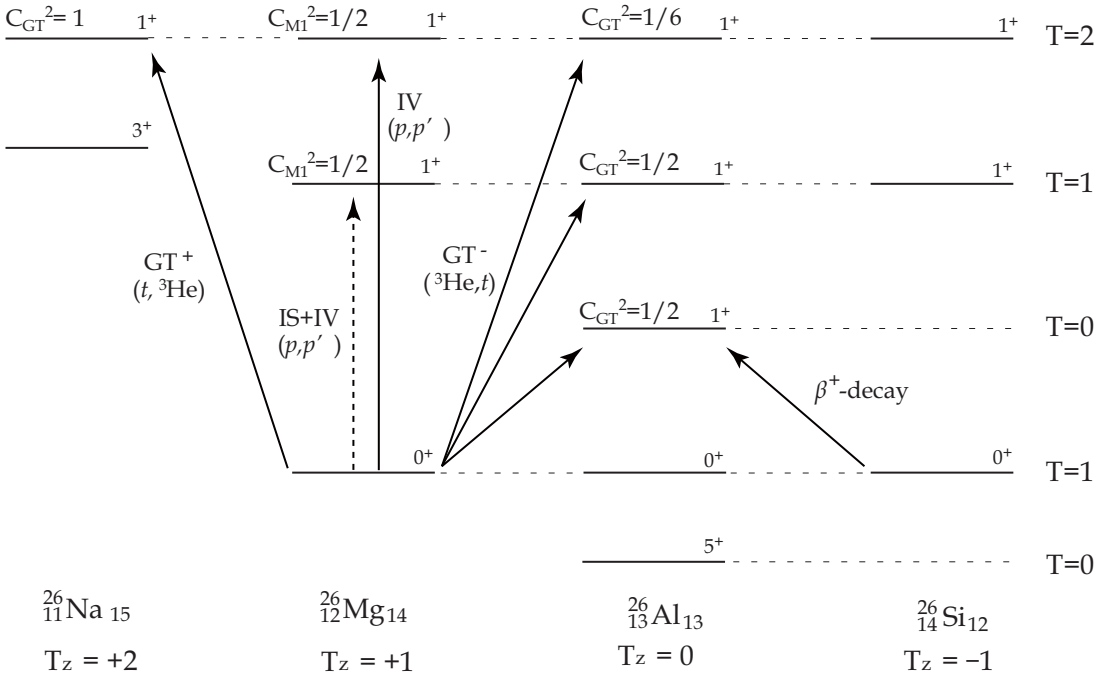

Figure 6.14: Schematic diagram of isospin symmetry structure in $A = 26$ isobars.

Case of ^{58}Ni

Figure 6.15 shows the isospin symmetry structure in $A = 58$ isobars. The ft value of the β-decay to the ground state of ^{58}Ni from ^{58}Cu has been reported to be 4.870 ± 0.003 s [72]. As done for ^{26}Mg, the $B(M1)_{\sigma\tau}$ strength in the transition of $T = 1 \rightarrow 2$ was determined from the corresponding $B(\mathrm{GT})\uparrow$ by using the proportionality between the yields in the (^{3}He,t) reaction [73, 74] and the $B(\mathrm{GT})_\beta$. Here, we note that there is a disproportionate

relationship for the yields by the (^{3}He,t) probe between the excitations to the ground state and other states in ^{58}Cu from ^{58}Ni [75]. Therefore, the correction factor was applied for the B(GT) values, which has been deduced from the ratio of the yields by the (^{3}He,t) reaction to those by the (p, n) reaction [75] as

$$R((^3\mathrm{He}, t)/(p, n)) = \frac{2.74 \pm 0.05}{1.71}. \tag{6.18}$$

The strongest state with $T = 2$ reported in Ref. [74] was observed at $E_x = 10.655$ MeV in the (p, p') spectrum with the cross section of 0.981 ± 0.012 mb/sr. Thus, $\hat{\sigma}_{IV}(^{58}\mathrm{Ni}) = 0.713 \pm 0.082$ mb/sr/${\mu_N}^2$ was obtained.

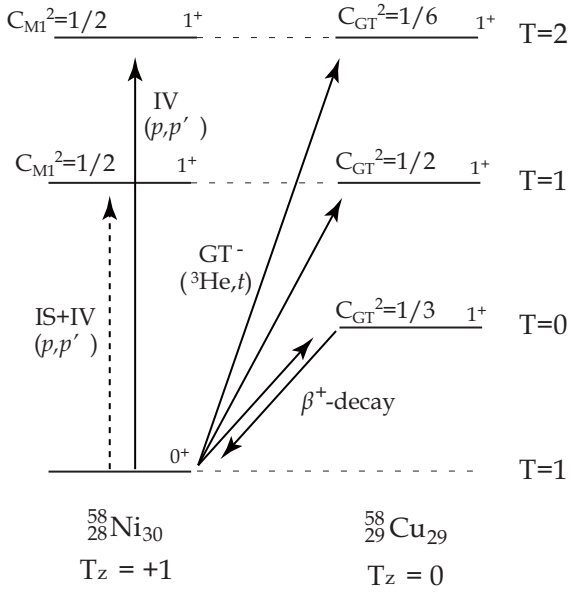

Figure 6.15: Schematic diagram of isospin symmetry structure in $A = 58$ isobars. We note that there is a disproportionate relationship for the yields by the (^{3}He,t) probe between the excitations to the ground state and other states in ^{58}Cu from ^{58}Ni [75]

Case of ^{11}B

— Derivation of $B(M1)_\sigma$ and $B(M1)_{\sigma\tau}$ in ^{11}B

The case of ^{11}B is different from the above. An excited transition in ^{11}B is always mixed with the IS and IV components because the ground state of ^{11}B is not $T = 0$ but $T = 1/2$. Figure 6.16 shows the level scheme for the ground and the first excited states in ^{11}B and ^{11}C. In Refs. [76, 77], the decomposition of the $B(M1)_{IS}$, $B(M1)_{IV}$, $B(M1)_\sigma$, and $B(M1)_{\sigma\tau}$ in the transition between the ground and the first states of ^{11}B has been performed by using experimental results as the following.

Applying the β-decay measurement [78] and Fermi transition strength, the $B(\mathrm{GT})\uparrow$ values from ^{11}B to ^{11}C have been determined by the (p, n) [79] and the (^{3}He,t) [77]

measurements. Thus, the $B(M1)_{\sigma\tau}$ has been derived. The $B(M1)_{IS}$ and the $B(M1)_{IS}$ values for the transition to the first excited state from the ground state in ^{11}B have been decomposed [76] from the γ-decay widths of the mirror states, which have been obtained from the experimental half life of 3.8(3) and 7.1(5) fs for ^{11}B and ^{11}C [37,80], respectively. The $B(M1)_{IS}$ value has been decomposed into the IS orbital and the IS spin parts, $B(M1)_l$ and $B(M1)_\sigma$, by applying the following restriction

$$\left\langle f \left| \sum_k^A \left(\mathbf{l}_k + \frac{1}{2}\sigma_k \right) \right| g.s. \right\rangle = 0, \tag{6.19}$$

where A is a mass number, $|g.s.\rangle$ and $|f\rangle$ represent the ground state and an excited state, respectively, and $\sum(\mathbf{l}_k + \frac{1}{2}\sigma_k)$ corresponds to the total angular momentum spin operator. Since the total angular momentum spin operator gives a good quantum number for the eigenvector of the wavefunctions, the equation (6.19) stands up as long as $|f\rangle$ is an excited state from $|g.s.\rangle$. Therefore, from Ref. [77], the $B(M1)_\sigma$ and the $B(M1)_{\sigma\tau}$ values were taken as 0.029(5) and 0.57(4) ${\mu_N}^2$, respectively.[1]

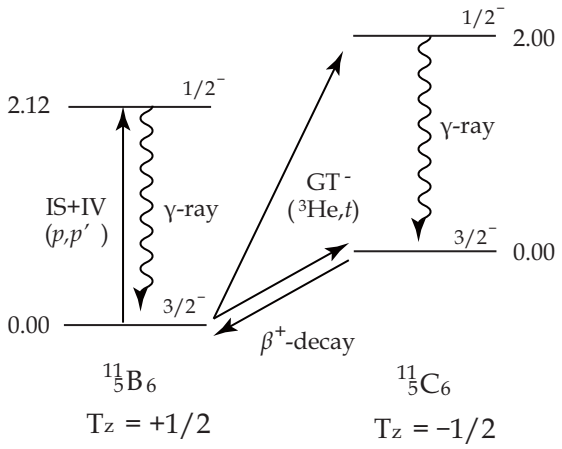

Figure 6.16: Level scheme for the ground and the first excited states in ^{11}B and ^{11}C. Energies are given in MeV.

— Derivation of cross section in ^{11}B

Since, unfortunately, the cross section of the corresponding transition measured by $^{11}\mathrm{B}(p,p')$ reaction at $E_p = 295$ MeV was unknown, we made use of the data of $^{11}\mathrm{B}(p,p')$ reaction at

[1] We note that the unit used in the reference [77] is different from that in this thesis owing to the definition. The units can be connected as

$$B(M1)_\sigma = \left(g_s^{IS}\right)^2 {\mu_N}^2 B(\sigma)_{Ref} \tag{6.20}$$

$$B(M1)_{\sigma\tau} = \left(g_s^{IV}\right)^2 {\mu_N}^2 B(\sigma\tau_z)_{Ref} \tag{6.21}$$

where $B(M1)_\sigma$ and $B(M1)_{\sigma\tau}$ are IS and IV strengths with the unit used in this thesis, and $B(\sigma)_{Ref}$, and $B(\sigma\tau_z)_{Ref}$ are those in the reference.

$E_p = 392$ MeV in literature [77] for the derivations of $\hat{\sigma}_{IS}(^{11}\mathrm{B})$ and $\hat{\sigma}_{IV}(^{11}\mathrm{B})$. The angular distribution of the $^{11}\mathrm{B}(p,p')$ reaction at $E_p = 392$ MeV to the state at E_x=2.12 MeV is shown in Fig. 6.17. Firstly, the contribution of the IS 1^+, the IV 1^+, and the 2^+ transitions to the cross section at 0° was estimated by using the DWBA calculation since the transition to the state at $E_x = 2.12$ MeV includes the $M1$ and $E2$ (2^+) transitions. The optical model potential parameters were taken from Ref. [48]. The effective nucleon-nucleon interaction derived at 425 MeV [5] was used. The oscillator parameters were taken from Eqs. (6.3) and (6.4) as 1.600 and 1.615 fm for protons and neutrons, respectively. In the DWBA calculation, the (p,p') cross sections were given by an incoherent sum of the 1^+ and 2^+ transition. The cross section for each J^π transition was described by a coherent sum of the IS and the IV contributions. The OBTD based on the CKPOT interaction was normalized to reproduce the experimental transition strengths, applying the factor of 0.827, 0.716, 1.00 for the IS 1^+, the IV 1^+, and the 2^+ transitions, respectively. The experimental $B(E2)$ has been reported to be 2.6(4) $e^2\mathrm{fm}^4$ [80]. Since the normalized OBTD did not reproduce the experimental angular distribution, an additional normalization factors of 1.1 and 1.3 were applied to the OBTD's of the 1^+ and the 2^+ transitions, respectively, by the "search-by-eye" method. As shown in Fig. 6.17, the DWBA calculation with the additional normalization denotes that the cross sections at 0° of the total, the IS 1^+, the IV 1^+, and the 2^+ transitions are 0.829, 0.064, 0.827, and 0.052 mb/sr, respectively. Assuming this angle between the IS and the IV 1^+ transitions, the contribution to the cross section at 0° for the IS and the IV was estimated to be 7.7% and 99.7% in the total cross section, respectively. Because the total cross section at 0° in the $^{11}\mathrm{B}(p,p')$ reaction at E_p=392 MeV was 0.82 mb/sr [77], the IS and the IV 1^+ cross section at 0° at 392 MeV was derived as 0.063 and 0.82 mb/sr.

Secondly, the obtained cross sections at E_p=392 MeV were converted to the (p,p') cross sections E_p=295 MeV by making use of the cross section ratio of the $^{12}\mathrm{C}(p,p')$ reaction to the states E_x=12.71 and 15.11 MeV since ^{12}C was expected to be a good reference for the energy dependence of the cross section of the IS and the IV 1^+ transitions. The cross sections of the $^{12}\mathrm{C}(p,p')$ reaction at E_p=295 and 392 MeV were taken from the present work and Ref. [8]. The cross section ratios at 0° ($q \neq 0$, $\omega \neq 0$) of 295 MeV to 392 MeV were obtained to be 0.97(8) and 0.94(5) for the IS and the IV 1^+ transitions, respectively. Thus, the unit cross sections at E_p=295 MeV were derived as $\hat{\sigma}_{IS}(^{11}\mathrm{B})$=2.1 ± 0.4 and $\hat{\sigma}_{IV}(^{11}\mathrm{B})$=1.4 ± 0.1 mb/sr/${\mu_N}^2$.

— Comments for unit cross sections of ^{11}B

In deriving the unit cross sections of ^{11}B, we took the following experimental results in literature,

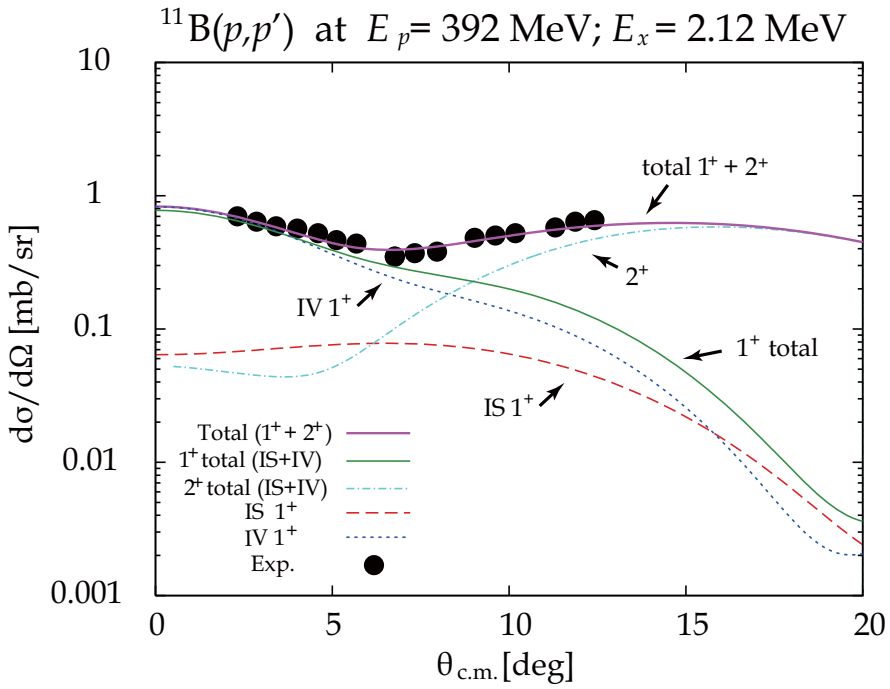

Figure 6.17: The angular distribution of the cross sections of the ^{11}B(p, p') reaction at E_p=392 MeV to the state at E_x=2.12 MeV. The experimental results are taken from Ref. [77]. The DWBA calculations are drawn with the normalization and the additional normalization factors to reproduce the experimental results. The IS 1^+, the IV 1^+ and the 2^+ transitions are denoted as red dashed, blue dotted, right blue dashed-dotted curved, respectively. The total (1^++2^+) and the total 1^+ (IS+IV) transitions are drawn in pink and green solid curves, respectively.

- $B(M1)_{\sigma\tau} = 0.57(4){\mu_N}^2$ (β-decay measurement [78]).
- $B(M1)_{\sigma} = 0.029(5)\ {\mu_N}^2$ (γ-decay measurement [37, 80]).
- The cross section of ^{11}B(p,p') to the 2.12 MeV state was 0.82 mb/sr (^{11}B(p,p') at E_p=392 MeV [77]).
- The cross section ratio of ^{12}C(p,p') to the states at E_x=12.71 and 15.11 MeV of E_p=295 to 392 MeV were 0.97(8) and 0.94(5) for the IS and the IV transitions, respectively (this work and Ref. [8]).

Furthermore, we applied these assumptions

1. The cross section angle between the IS and the IV 1^+ transitions followed the DWBA calculation.
2. Relative transition strength between the IS and the IV 1^+ transitions followed the experimental results.
3. Relative transition strength between the 1^+ and the 2^+ transitions was modified to reproduce the experimental angular distribution.
4. The energy dependence of the cross sections to the IS and the IV 1^+ transitions in ^{11}B followed that in ^{12}C.

As for the second assumption, if the relative strength of $B(M1)_\sigma / B(M1)_{\sigma\tau}$ changes $\pm$10%, the IS unit cross section also changes $\pm$10%. The IV unit cross section, however, hardly changes within 1%. As for the third assumption, if the additional normalizations are not applied, the IS and the IV unit cross sections do not change within 2%.

6.4.4 Unit cross section for IV

The IV unit cross sections listed in Table 6.5 are shown in Fig. 6.18. Following Refs. [61, 63], a smooth function against for mass number A can be defined for $\hat{\sigma}_{IS}(A)$ and $\hat{\sigma}_{IV}(A)$ as

$$\hat{\sigma}_T(A) = N_T \exp(-x_T A^{1/3}) \tag{6.22}$$

$$\Delta\hat{\sigma}_T(A) = \hat{\sigma}_T(A)\sqrt{\left(\frac{\Delta N_T}{N_T}\right)^2 + \left(\Delta x_T A^{1/3}\right)^2 + \left(\Delta c_T\right)^2}, \tag{6.23}$$

where T = IS and IV, respectively, N_T represents the unit cross section at $A = 0$, x_T denotes an A-dependence, and Δc_T denotes an additional error to be determined independently from the fitting. The value of Δc_{IV} was zero. The parameters N_T and x_T were searched by the fitting to the experimental data, and they are summarized in Table 6.6.

In the figure, the GT unit cross section, which has been determined in the mass region of $A = 58-120$ at $E_p = 297$ MeV by the (p, n) reaction [63], was extrapolated to the region at $A = 5-60$ and shown in the figure in dashed green with the conversion factors of 2×2.644 arising from the CG coefficient for cross section and the g_s-factor as obtained in Eq. (A.24). The IV and the GT unit cross sections were consistent within error bar.

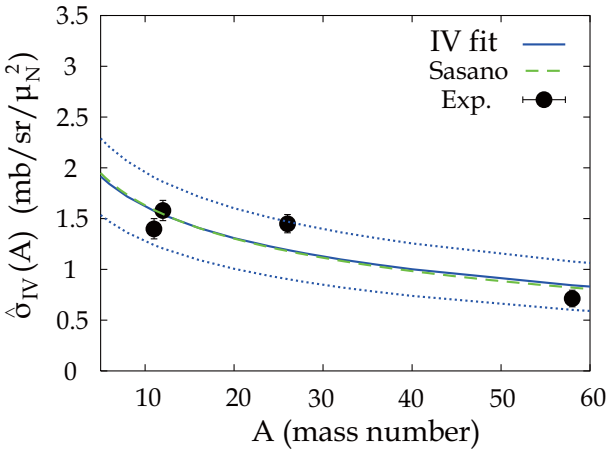

Figure 6.18: The mass dependence for $\hat{\sigma}_{IV}(A)$ at $E_p = 295$ MeV. The result (solid) and the error band (dotted) have been obtained in th fitting procedure of Eq. (6.22) to the experimental data. The mass dependence of the GT unit cross section for the (p, n) reaction at $E_p = 297$ MeV [63] is also drawn as Sasano (dashed) applying the conversion factors (2×2.644) to allow the direct comparison. The error bar for the dashed curve is not shown.

Table 6.6: Parameters for the A-dependence of $\hat{\sigma}_{IS}$ and $\hat{\sigma}_{IV}$ at $E_p = 295$ MeV, expressed in Eq. (6.22). The symbol Δc_T denotes an additional error for the unit cross section.

	N_T(mb/sr/μ_N^2)	x_T	Δc_T
$T = IS$	4.89 ± 0.93	0.38 ± 0.06	0.1
$T = IV$	3.67 ± 0.62	0.38 ± 0.06	0

6.4.5 Unit cross section for IS

The IS unit cross section listed in Table 6.5 is drawn in Fig. 6.19. The value of Δc_{IS} was taken to be 0.1 (see Sec. 6.4.2). The same manner to the IV case, unfortunately, can not be applied for the IS case because there was only one experimental value; the parameter search for the equation (6.22) requires two data points at the least. Thus, we assumed the same A-dependence parameter to the IS unit cross section, $x_{IS} = x_{IV} = 38(6)$. This assumption was found to be supported by the prediction using the DWBA and the shell model calculations as shown in 6.20. The error bar for the data points originated from the

standard deviation owing to a number of transitions predicted by the USD interaction. The calculation shows that the mass dependences for the IS and IV unit cross sections are identical within 2%. The magnitude of the ratio of IS to IV does not relate to the present discussion.

The obtained parameter of N_{IS} is written in 6.6. The uncertainty of $\hat{\sigma}_{IS}$ was as much as 26%, which originated from the experimental value of $\hat{\sigma}_{IS}(^{11}\mathrm{B})$ and the uncertainty of the spin-flip component in the IS spin-$M1$ cross section (see Sec. 6.4.2).

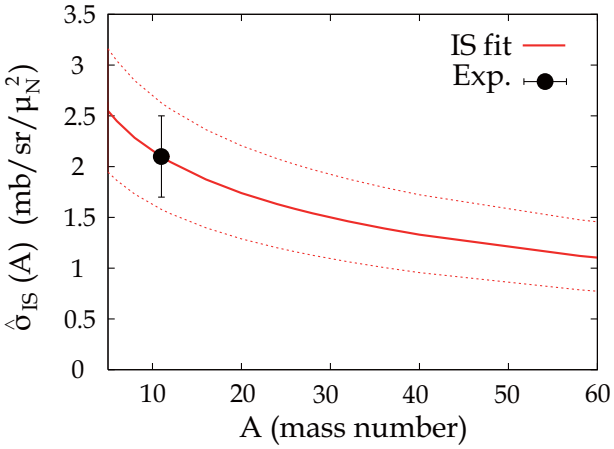

Figure 6.19: The mass dependence for $\hat{\sigma}_{IS}(A)$ at $E_p = 295$ MeV. The result (solid) and error band (dotted) are determined from the $\hat{\sigma}_{IS}(^{11}\mathrm{B})$ assuming the same x_T parameter to that of IV.

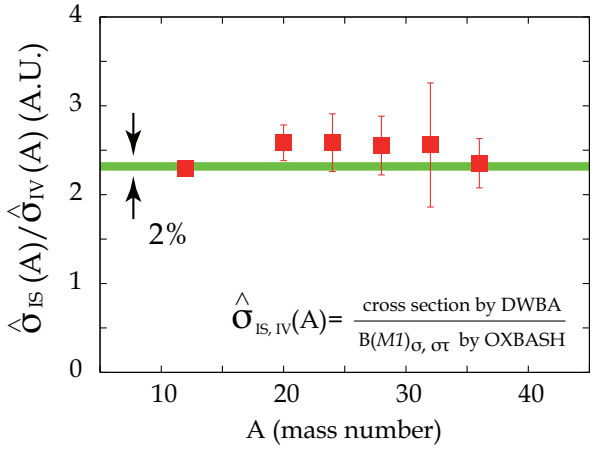

Figure 6.20: Mass dependence of the unit cross section ratio of the IS to the IV transitions, calculated by the DWBA and the OXBASH codes. The error bar for the data points originates from the standard deviation owing to a number of transitions predicted by the USD interaction.

6.5 Extrapolation to 0°

As mentioned in Sec. 6.3.2, the cross section was measured at 0.40°, 1.00°, and 1.74° in laboratory frame. Since the cross section at 0°was to be used to derive the 1^+ transition strengths as described in Eqs. (6.10) and (6.11), the observed cross section was extrapolated into the point at 0.00° by using the artificial curves that were obtained in Sec. 6.3. The normalization factor (N_{DWBA}) for the artificial curve was obtained as

$$N_{DWBA} = \frac{\sigma_1 e_2 + \sigma_2 e_1}{e_1 + e_2} \tag{6.24}$$

where the cross sections measured at 0.40°, 1.00° in labratory frame are expressed as $\sigma_1 \pm \sigma_1 e_1$ and $\sigma_2 \pm \sigma_2 e_2$, respectively. The aritificial curve was normalized to reproduce the factor N_{DWBA} at point of 0.70° in laboratory frame. Applying the normalization, the magnitude of the artificial curve at 0.00° was taken as $d\sigma/d\Omega|_{IS}(0°)$ and $d\sigma/d\Omega|_{IV}(0°)$ in Eqs. (6.10) and (6.11).

6.6 Results of $B(M1)_\sigma$ and $B(M1)_{\sigma\tau}$

The excitation energies, differential cross sections at 0.40° in laboratory flame for the 0^+ and 1^+ transitions measured at $E_p = 295$ MeV are tabulated in Appendix E. The uncertainties in the excitation energies were ±10 keV in the excitation energy region of 7−15 MeV. The error of the cross section arises from the quadratic sum of the statistical, the systematical, and the fitting errors. They were 1−10%, 1−30%, and 1−7%, respectively, depending on the target and the state. The errors of $B(M1)_\sigma$ and $B(M1)_{\sigma\tau}$ were taken as the quadratic sum of the uncertainties of the cross section and the unit cross section. They were 1−30%, and 24−32%, respectively.

The comparison with the shell-model calculations is given in Sec. 6.6.1, and that with the previous experimental data is given in Sec. 6.6.2.

6.6.1 Comparison with theoretical prediction

The strength distributions of $B(M1)_\sigma$ and $B(M1)_{\sigma\tau}$ in the *sd*-shell region are compared with the shell-model calculations based on the USDA and USDB interactions with free g_s-factors as shown in Figs. 6.21 and 6.22 for $B(M1)_\sigma$ and $B(M1)_{\sigma\tau}$, respectively. The experimental symbol with a circle represents a state that was indefinitely assigned as the IS and the IV 1^+ transitions. The horizontal lines in red in Fig. 6.21 represent the experimental detection limit, which was determined from the lower limit of the detectable cross section as summarized in Table 6.7. The $B(M1)_\sigma$ value obtained in the shell model calculation but below the detection limit were excluded from the figures. The excitation energy as well as the strength were well reproduced for the strongest IS states in each

target except for ^{20}Ne. The IS transition in ^{36}Ar to the state at $Ex = 8.985$ MeV was experimentally observed for the first time, which is reasonably predicted at 8.461 and 8.551 MeV by the calculations besed on the USDA and USDB interactions, respectively. Unfortunately, no IS state was confirmed in ^{20}Ne.

The magnitudes of the strongest IV states were well reproduced by the calculation for the individual targets, while those for the other states were overestimated. Serious problem lies on ^{32}S. Even for the strongest and the second strongest states in ^{32}S, the calculation overestimated the experimental $B(M1)_{\sigma\tau}$ values twice.

Table 6.7: The lower limit of detectable cross section in the present study at 0°.

	$d\sigma/d\Omega$(mb/sr)
^{12}C	0.01
^{16}O	0.02
^{20}Ne	0.02
^{24}Mg	0.01
^{28}Si	0.01
^{32}S	0.01
^{36}Ar	0.05
^{40}Ca	0.02

6.6.2 Comparison with previous experimental data

The $B(M1)_\sigma$ and $B(M1)_{\sigma\tau}$ values from the previous (p, p') experiments [12, 83, 84] are presented in the tables in Appendix E for comparison with the present results in the cases of ^{16}O, ^{20}Ne, ^{24}Mg, ^{28}Si, and ^{32}S. The $B(M1)$ values from the (e, e') experiments [81,82,85,86] are also shown in the tables for reference in the cases of ^{12}C, ^{36}Ar, and ^{40}Ca since the previous $B(M1)_\sigma$ and $B(M1)_{\sigma\tau}$values are not available from literature. In the following, some comments on the $B(M1)_\sigma$ and $B(M1)_{\sigma\tau}$ are presented;

- The strongest IS state in ^{28}Si at 9.495 MeV was successfully decomposed from the 2^+ transition at 9.479 MeV in the present study. The angular distributions, successfully decomposed into the two states, are shown in Fig. 6.23. The yields at 0° in the IS 1^+ transition was definitely derived for the first time.

- The IS state in ^{28}Si at 9.495 MeV was 2.5 times larger than that of the previous one, whereas although other strong IS states, in ^{24}Mg (9.828 MeV) and in ^{32}S (9.965 MeV), were consistent. The IS unit cross section for ^{28}Si used in the previous study might have been incorrect since we derived it by using the experimental values from literature, while the previous study used it derived by the theoretical calculation.

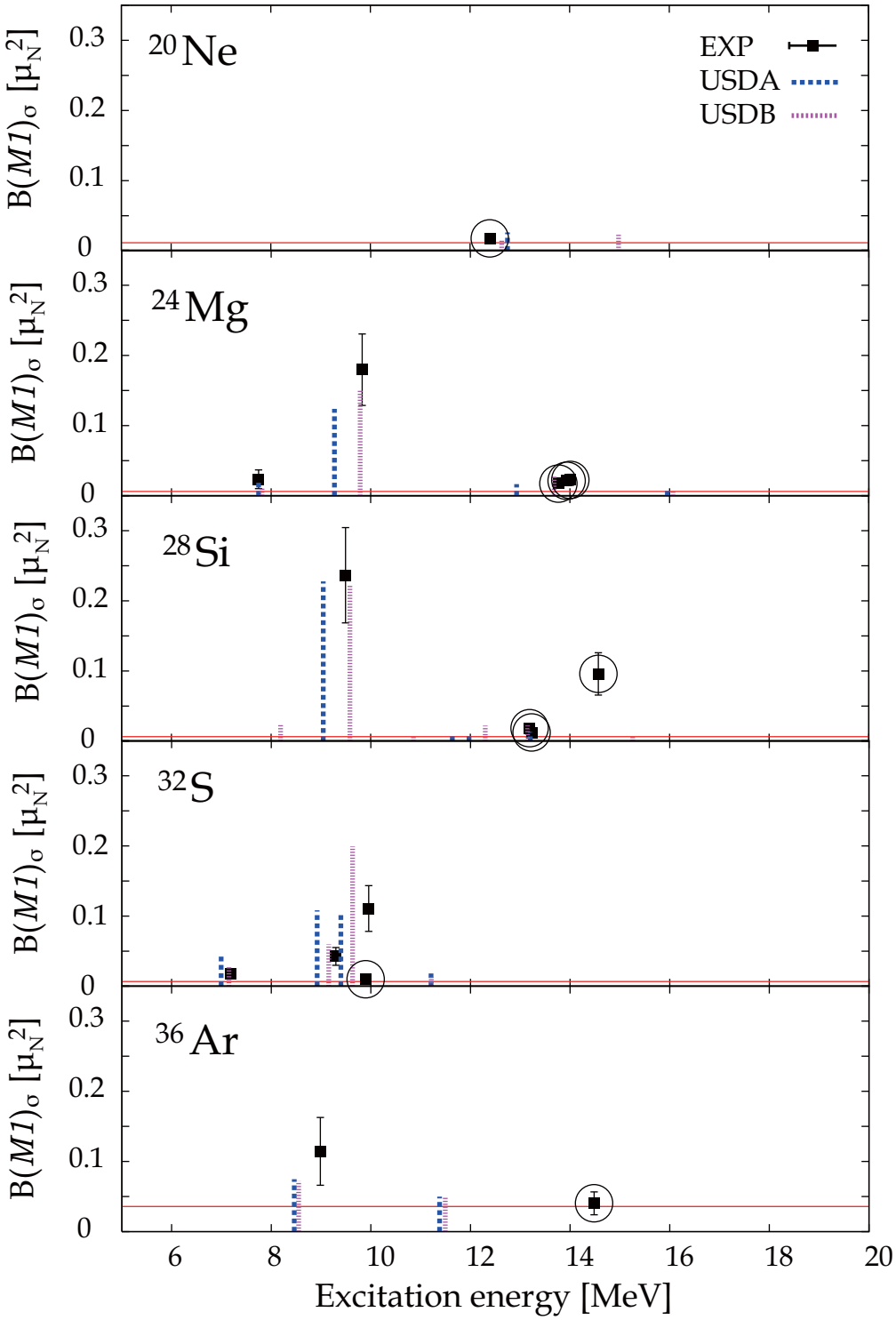

Figure 6.21: The experimental $B(M1)_\sigma$ distributions in the *sd*-shell. The shell-model calculations using the USDA and USDB interactions with the free g_s-factors are shown for comparison by the blue and red dotted lines, respectively. The circles represent a state that were uncertainly assigned as the IS state. The red lines represent the experimental detection limits for an individual nuclei.

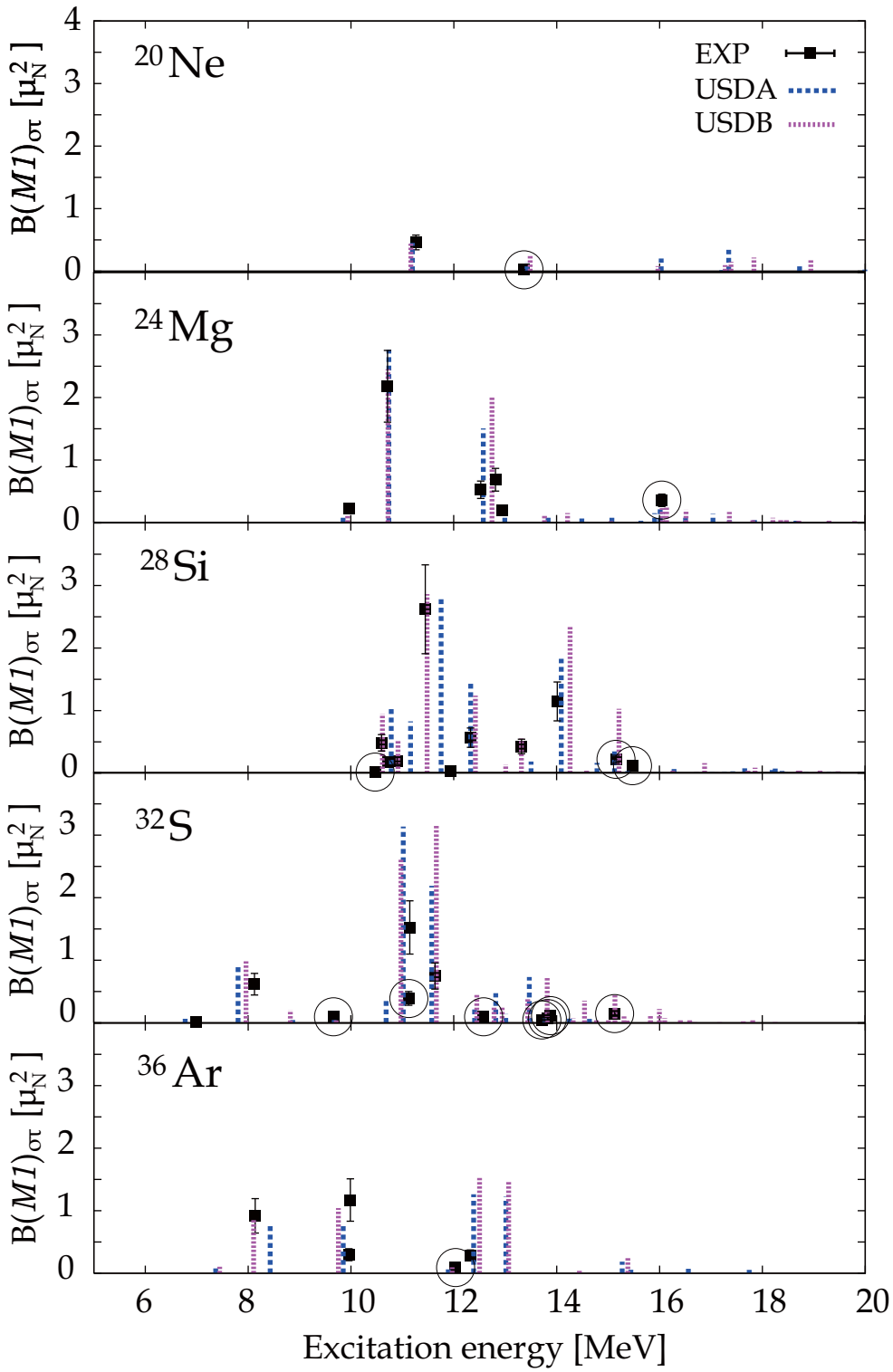

Figure 6.22: Same as Fig. 6.21, but for $B(M1)_{\sigma\tau}$. The experimental detection limit is too low to show in the figure.

- No IS state was observed in ^{20}Ne.
- The IS state in ^{36}Ar was observed at 8.985 MeV for the first time in reasonable agreement with predictions by the shell model calculations based on the USDA and USDB interactions.
- For IV states, the excitation energies and the $B(M1)_{\sigma\tau}$values of relatively strong states were almost consistent with the previous results, except for those of ^{32}S.
- The cross section for the ^{32}S states in the previous study [12] might have been incorrect, possibly due to the calibration of the target thickness. The ratio of the (p,p) [12] to the (p,n) [15] cross sections in ^{32}S has been inconsistent with those for ^{20}Ne, ^{24}Mg, and ^{28}Si [16]. If the (p,p') cross section of ^{32}S is modified to reproduce the ratio, the previous $B(M1)_{\sigma\tau}$ values for ^{32}S become consistent with the present results.
- Some transition, which have been assigned to be of the IV 1^+ nature in the previous study, were omitted in the present study because they were assigned to be of 0^+ or other natural parity transition of $\Delta L \geq 1$.
- The strongest IV state in ^{32}S was found to consist of two peaks at 11.123 and 11.144 MeV.
- Similarly, the strongest IV state in ^{36}Ar was found to consist of two peaks at 9.960 and 9.987 MeV.

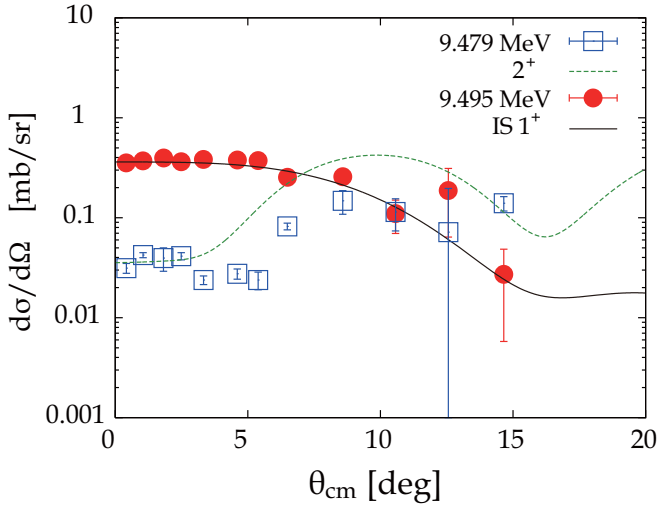

Figure 6.23: The angular distributions to the two excited states at E_x = 9.479 and 9.495 MeV in ^{28}Si. The IS 1^+ transition to the state at 9.495 MeV and the 2^+ transition to the state at 9.479 MeV have been successfully decomposed for the first time.

Chapter 7

Discussion

7.1 Quenching phenomena

7.1.1 Quenching factors for $B(M1)_\sigma$ and $B(M1)_{\sigma\tau}$

The cumulative sum of the experimental $B(M1)_\sigma$ and $B(M1)_{\sigma\tau}$ values up to $E_x = 16$ MeV are shown against mass number A in Fig. 7.1. The gray bands in the figures denote the uncertainties arising from the ambiguities in the 1^+ and T assignments of the states. The error bars for the experimental results originate from the statistical and the systematic error and the uncertainty due to the unit cross section. Because the cross sections and the transition strengths for the IS transitions are much smaller than those for the IV transitions, the magnitude of the vertical axis for the $\Sigma B(M1)_\sigma$ is expanded in the figure. Thus, the width of the error band and the size of the error bars for $\Sigma B(M1)_\sigma$ are seen to be relatively larger than those for $\Sigma B(M1)_{\sigma\tau}$.

For comparison, the results of the shell-model calculation based on the USDA and the USDB interactions with the free g_s-factor were summed within the region of the excitation energies observed in the experiment, as also shown in the same figures. The error bars for the calculation represent the difference between the sum over all the predicted states and the sum of only the strengths that are larger than the experimental detection limit. Since there are no transition strengths predicted for ^{16}O and ^{40}Ca within $0\hbar\omega$ calculation, the calculated sums were assumed to be zero. On the whole, there is no difference between the results obtained by the USDA and the USDB interactions.

The experimental $\Sigma B(M1)_{\sigma\tau}$ values are smaller than the theoretical ones. This is called the quenching phenomenon of the spin-isospin $M1$ transition. The quenching phenomena observed in the IV transition is considered to be analogous to that in the GT transition. The quenching of the IS transition, however, is not seen in the $\Sigma B(M1)_\sigma$ although the uncertainties of the experimental values are somewhat large. For quantitative discussion on the difference of the quenching between $\Sigma B(M1)_\sigma$ and $\Sigma B(M1)_{\sigma\tau}$, the

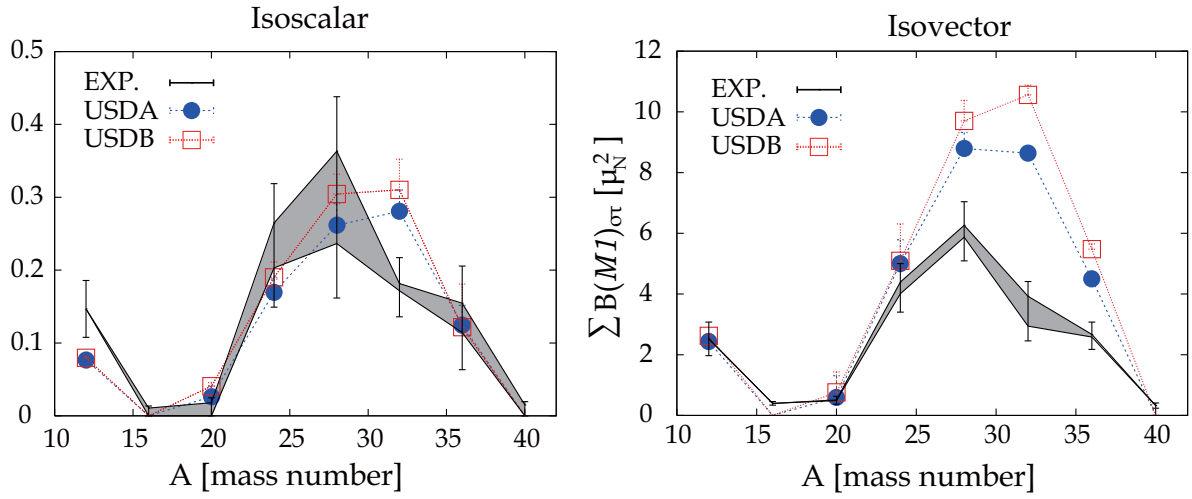

Figure 7.1: The mass dependence of the cumulative sum of the experimental $B(M1)_\sigma$ and $B(M1)_{\sigma\tau}$ values. The upper and the lower bands of the experimental values, arising from the ambiguities in the J^π assignments of the states, are connected by the solid lines, and the regions between them are shown in gray. The shell-model calculations using the USDA and the USDB interactions (the CKPOT and the CKII interactions for ^{12}C, respectively) are shown in blue circles and red squares, respectively, with the free g_s-factors.

quenching factors for the IS and IV transitions are introduced as

$$Q_{IS} = \frac{\sum B(M1)_\sigma^{Exp}}{\sum B(M1)_\sigma^{SM}} \tag{7.1}$$

$$Q_{IV} = \frac{\sum B(M1)_{\sigma\tau}^{Exp}}{\sum B(M1)_{\sigma\tau}^{SM}}, \tag{7.2}$$

respectively, where the summation was taken in the range of $E_x = 0-16$ MeV. The suffixes "Exp" and "SM" denote the spin-$M1$ strengths obtained from the experiment and the shell-model calculation, respectively. In the followings, the quenching factors calculated with using free g_s-factor in the shell-model calculation are denoted as $Q_{IS}^{\rm free}$ and $Q_{IV}^{\rm free}$, in order to distinguish from the quenching factors of $Q_{IS}^{\rm emp}$ and $Q_{IV}^{\rm emp}$ derived with the empirical g_s-factor [50]. The empirical g_s-factors have been obtained as the effective $M1$ operator by the least-squares fit to experimental values of the magnetic moments and the decay strengths of the $M1$ transition for the nucleus A=17−39 assuming a mass dependence of $A^{0.35}$ [50]. The empirical g_s-factors used in the present study are listed in Table 7.1.

The results of the quenching factors of the $Q_{IS}^{\rm free}$ and $Q_{IV}^{\rm free}$ ($Q_{IS}^{\rm emp}$ and $Q_{IV}^{\rm emp}$) in the *sd*-shell region are shown in the top (bottom) panel of Fig. 7.2, in blue and red, respectively. The quenching factors for the nucleus in the *p*-shell and the double closed shell nuclei are excluded to be shown since the effective g_s-factors for them were unavailable from Ref. [50]. The gray colored and red shaded bands represent the uncertainties due to

the J^π assignment.

Although the IV quenching factors slightly depended on nucleus, the quenching phenomena were systematically observed for the first time and their quenching factors were roughly estimated to be $Q_{IV}^{\rm free} \sim 0.6$. The result of $Q_{IV}^{\rm free}$ was found to be analogous to the GT shell-model quenching factors, the ratio of the total sum of the experiment to that of the shell model calculation with the free g_s-factors, of 65±10% obtained from the experimental GT strengths observed in (p,n) reactions on ^{20}Ne, ^{24}Mg, ^{28}Si [16] and ^{32}S [15]. In applying the empirical g_s-factors, the quenching factors became $Q_{IV}^{\rm emp} \sim 0.9$. The effective g_s-factors deduced from the quenching of the matrix elements based on the theoretical considerations [17,87] have been found to reasonably agree with the empirical g_s-factors [18,50]. Because the theoretical modification on the free g_s-factors mainly arises from the second-order configuration mixings (core polarization effect), the quenching results observed in the IV spin-$M1$ transition is expected to be explained by the coupling of $2p2h$ configuration mixings to the $1p1h$ state, as analogous to the GT quenching phenomena. Therefore, it may be concluded that the quenching phenomena in the IV spin-$M1$ transition were generally observed in the nuclei across the *sd*-shell region mainly due to the $2p2h$ excitations.

Next, the IS quenching factors are discussed. The $Q_{IS}^{\rm free}$ values were scattered around unity, and the situation of the quenching in the IS transition completely differed from that in the IV transition. Although the error bars for the $Q_{IS}^{\rm free}$ are somewhat large, the result suggests that the IS spin-$M1$ transition have no quenching. It is noticed that the error band of the $Q_{IS}^{\rm free}$ in ^{20}Ne almost ranges from zero to unity because no IS transitions were confirmed in ^{20}Ne. Thus, the results of Q_{IS} in ^{20}Ne may not have any sense. In applying the empirical g_s-factors, the $Q_{IS}^{\rm emp}$ values were overestimated from unity. Thus, it was found that the quenching degree in the IS spin-$M1$ transition was little and the empirical factor failed to reproduce the experimental result. It is interesting that the result of the IS transition was found to disagree with the expectation based on the quenching observed in the GT and IV spin-$M1$ transitions.

The $2p2h$ excitations which are believed to be a main source of the spin-$M1$ quenching phenomena have been supposed to be independent on the isospin. Thus, a similar amount of the quenching owing to the $2p2h$ excitations has been expected to be observed in the IS spin-$M1$ transitions. The quenching phenomena in the IS spin-$M1$ transitions, however, have been unobserved as seen in the quenching factors $Q_{IS}^{\rm free} \sim 1$. It is to be noted that the result of the $Q_{IS}^{\rm free} \sim 1$ does not support the presence of the Δ-*hole* admixture to the $1p1h$ state in the IV $M1$ transitions, since the Δ-*hole* excitations have been found to play a minor role in the GT quenching phenomena from both the experimental and the theoretical sides [3].

Thus, it was found that the quenching phenomena observed in the spin-$M1$ transitions

have the difference between the IS and the IV transitions. This fact may suggest that the coupling of $2p2h$ configuration mixings which is supposed to be a main source of the spin-$M1$ quenching has the different transition mechanism. Such a significant difference of the quenching factor has not been predicted so far by the shell model calculation.

Table 7.1: The empirical g_s-factors in the *sd*-shell region determined as the effective $M1$ operator from experiments in Ref. [50]. The g_s-factors for the free nucleons are also written.

nuclei	${g_s}^{IS}$	${g_s}^{IV}$
^{20}Ne	0.769	-4.083
^{24}Mg	0.761	-4.042
^{28}Si	0.754	-4.005
^{32}S	0.749	-3.971
^{36}Ar	0.743	-3.941
free	0.880	-4.706

7.1.2 Strength ratio of $\Sigma B(M1)_\sigma$ to $\Sigma B(M1)_{\sigma\tau}$

The quenching degree in the IS and the IV spin-$M1$ transitions are considered from other side. A new parameter ($R_{IS/IV}$) to give the direct comparison between the total sums of the reduced matrix element representing for the IS and the IV spin-$M1$ transitions was introduced as

$$R_{IS/IV} = \frac{\sum |M(\sigma)|^2}{\sum |M(\sigma\tau)|^2} \tag{7.3}$$

$$= \frac{\sum B(M1)_\sigma/(g_s^{IS})^2}{\sum B(M1)_{\sigma\tau}/(g_s^{IV})^2}, \tag{7.4}$$

where the sum is taken for all excited states observed up to $E_x = 16$ MeV, and the transformation from Eq. (7.3) to Eq. (7.4) is followed to the definitions for $B(M1)_\sigma$ and $B(M1)_{\sigma\tau}$ as described in Eqs. (A.16) and (A.17). Thus, the $R_{IS/IV}$ value corresponds to the strength ratio of the IS spin-$M1$ transitions to the IV ones in a nucleus with a modification of the squared g_s-factors. The $R_{IS/IV}$ values obtained from the experiment and the shell-model calculation are expressed as ${R_{IS/IV}}^{Exp}$ and ${R_{IS/IV}}^{SM}$, respectively, in the followings.

The results of the ${R_{IS/IV}}^{Exp}$ are shown in black line against mass number in Fig. 7.3. The gray band originates from the ambiguities in the J^π assignments and the error bars denote the statistical and systematic error and the uncertainties arising from unit cross sections (the experimental error). The numerical values of the ${R_{IS/IV}}^{Exp}$ are listed in Table 7.2; the R_2 and the R_3 denote the lowest and the highest points of the error bands, and the R_1 and the R_4 denote those of the error bars, respectively, as shown in Fig. 7.3. The ${R_{IS/IV}}^{Exp}$

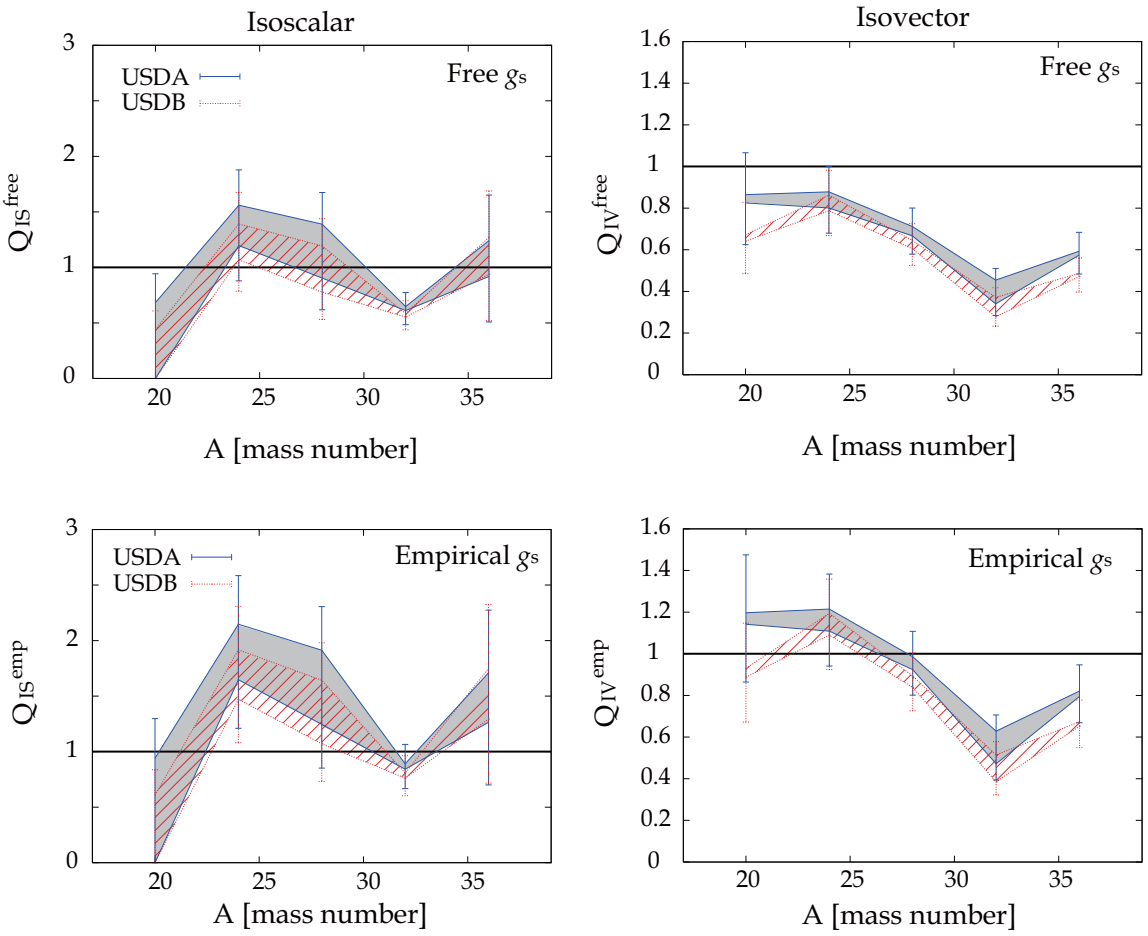

Figure 7.2: The quenching factors observed in ^{20}Ne, ^{24}Mg, ^{28}Si, ^{32}S, and ^{36}Ar, as defined in Eqs. (7.1) and (7.2). The gray colored and red shaded bands represent the uncertainties due to the J^π assignment in calculating with the USDA and the USDB interactions, respectively. The error bars originate from the statistical error, the systematic error and the uncertainty due to unit cross section. The results with using free g_s-factors are shown in the top panel, while those with using empirical g_s-factors listed in Table 7.1 are shown in the bottom panel. The results of the p-shell and the double closed shell nuclei are not shown since their empirical g_s-factors are not available.

Table 7.2: Data table of $R_{IS/IV}^{Exp}$. The R_2 and the R_3 denote the lowest and the highest points of the error bands, and the R_1 and the R_4 denote those of the error bars, respectively, as shown in Fig. 7.3. The results of ^{16}O, ^{20}Ne, and ^{40}Ca are unavailable because no IS spin-$M1$ transitions have been confirmed in those nuclei.

nuclei	R_1	R_2	R_3	R_4
^{12}C	1.57	1.66	1.66	1.77
^{24}Mg	1.34	1.45	1.72	1.85
^{28}Si	1.03	1.15	1.66	1.83
^{32}S	1.32	1.39	1.58	1.66
^{36}Ar	1.18	1.27	1.66	1.77

values for ^{16}O, ^{20}Ne, and ^{40}Ca were unavailable since no IS spin-$M1$ transitions were confirmed in those nuclei. Although the quenching factors were scattered depending on nucleus as seen in Fig. 7.2, the ${R_{IS/IV}}^{Exp}$ values were surprisingly constant for the nucleus in the *sd*-shell region including ^{12}C. They were roughly averaged to be

$$ {R_{IS/IV}}^{Exp} = 1.5 \ \pm \ 0.2 \ \pm \ 0.1, \tag{7.5} $$

where the errors originate from the ambiguities in the J^{π} assignments and from the experimental error, respectively. This result suggests that the total sum of the squared matrix element for the IS spin-$M1$ transitions be approximately 1.5 times as much as that for the IV ones, although the IS transition strength is smaller than the IV one because of the g_s-factors in the magnitude. If the spin-$M1$ transition strengths follow such a proportionality of the ${R_{IS/IV}}^{Exp}$ value, the IS spin-$M1$ transition of $B(M1)_{\sigma} = 0.026\ \mu_N^2$ (0.046 mb/sr) would be found in ^{20}Ne in total according to the total sum of the $B(M1)_{\sigma\tau}$ observed in ^{20}Ne.

For comparison, the results of the ${R_{IS/IV}}^{SM}$ using the USDA and the USDB interactions are also shown in blue circle and red square, respectively, in Fig. 7.3. The difference between the ${R_{IS/IV}}^{SM}$ values calculated with using the free and the effective g_s-factors was less than 1%. The average of the ${R_{IS/IV}}^{SM}$ values were roughly 0.9. The ${R_{IS/IV}}^{SM}$ values were surprisingly constant including the case of ^{12}C. It may be worth noting that there is the following relation between the $R_{IS/IV}$'s and the quenching factors as

$$ \begin{aligned} {R_{IS/IV}}^{Exp} / {R_{IS/IV}}^{SM} &= \frac{\sum {B(M1)_{\sigma}}^{Exp}/(g_s^{IS})^2}{\sum {B(M1)_{\sigma\tau}}^{Exp}/(g_s^{IV})^2} \Big/ \frac{\sum {B(M1)_{\sigma}}^{SM}/(g_s^{IS})^2}{\sum {B(M1)_{\sigma\tau}}^{SM}/(g_s^{IV})^2} \\ &= \frac{\sum {B(M1)_{\sigma}}^{Exp}}{\sum {B(M1)_{\sigma}}^{SM}} \Big/ \frac{\sum {B(M1)_{\sigma\tau}}^{Exp}}{\sum {B(M1)_{\sigma\tau}}^{SM}} \\ &= Q_{IS}/Q_{IV}, \end{aligned} \tag{7.6} $$

where suffixes "Exp" and "SM" denote the strength values obtained from the experiment and the shell-model calculation, respectively. It is shown that the ratio of the $R_{IS/IV}$'s corresponds to that of the quenching factors. Thus, the difference of the quenching factors between the isospin indicates that of the $R_{IS/IV}$'s between the experimental and the shell-model calculation values. Because the present result clearly indicates

$$ \frac{{R_{IS/IV}}^{Exp}}{{R_{IS/IV}}^{SM}} > 1, \tag{7.7} $$

it was obvious that the quenching factors have the difference between the isospins. The ${R_{IS/IV}}^{Exp}$ value suggests that the total sum of the matrix element of the IS spin-$M1$ transitions be more than those of the IV ones, while the shell-model calculation predicts that they are almost equal.

The difference in the $R_{IS/IV}$ values between the experiment and the prediction may be explained by sizes of the model space since the wavefunctions predicted in the shell-model calculation were truncated in the *sd*-shell space. The shell-model calculations extended to the $(0+1)\hbar\omega$ model space, however, failed to reproduce the ${R_{IS/IV}}^{Exp}$ value since their ${R_{IS/IV}}^{SM}$ values were again around unity. Two effective interactions used here were PSDMK [49] and SDPFM [88] for the calculation in ^{12}C and ^{20}Ne within the model space of the *psd*-shell and *sdpf*-shell, respectively. The calculations for other nucleus were not able to be performed because of the limitation of a computer in terms of memory. The strength distributions and the excitation energy dependence of the ${R_{IS/IV}}^{SM}$ values calculated in ^{20}Ne are shown in Fig. 7.4. Although the strengths with the SDPFM interaction are predicted to be smaller than those with the USD interaction, the strength ratio of the IS to the IV transitions was found to be unchanged for the case of ^{20}Ne. Therefore, the ${R_{IS/IV}}^{SM}$ values in other nuclei were believed not to be improved by the extension of the model space for the shell model calculation. Thus, it was found that the difference of the quenching facotors between the IS and the IV spin-$M1$ transitions has been incorrectly involved in the effective interactions or for the shell model calculation.

On the basis of the results of Q_{IS}, Q_{IV}, and $R_{IS/IV}$ observed in the nucleus at the *sd*-shell region and in ^{12}C, the results are summarized as the followings,

- The quenching phenomena were observed in the IV spin-$M1$ transitions but unobserved in the IS transitions. The isospin dependence of the quenching phenomena in the spin-$M1$ transitions were observed for the first time.
- The ${R_{IS/IV}}^{Exp}$ values were surprisingly constant. This implies that the effect of the isospin dependence of the quenching phenomena is universal in the $N = Z$ nucleus and independent on the nuclear structure.
- It was found that an extension of the model space was not essential to describe the isospin dependence of the quenching phenomena. The present result encourages an improvement to theory.

7.1.3 Strengh distribution into high excitation energy region

The origin of the different quenching factor between the IS and the IV spin-$M1$ transitions is considered in this section.

As described in Sec. 1.2.2, the GT quenching factor observed in the low excitation energy range reflects an amount of the missing strength distributed into the high excitation energy region. The GT strength distribution at the high excitation energy region has been experimentally observed in the (p, n) and the (n, p) reactions [3]. The observed GT strengths, accumulated in the low excitation energy region (0−16 MeV) [15, 16], have

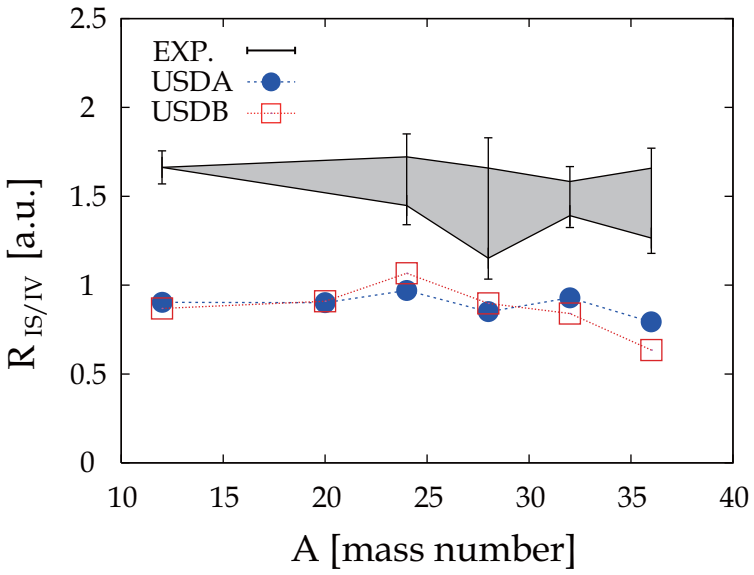

Figure 7.3: The total strength ratio of the IS transitions to the IV ones of $R_{IS/IV}$, as defined in Eq. (7.3). The experimental results are shown in black line, and the gray band originates from the ambiguities in the J^π assignments and the error bars denote the experimental error. The experimental result of ^{20}Ne is not shown because no IS-spin-$M1$ transitions have been to be confirmed. The results of the shell-model calculations using the USDA and the USDB interactions are shown in blue circle and red square, respectively. The difference between the results for the shell model calculations using the free and the effective g_s-factors is better than 1%.

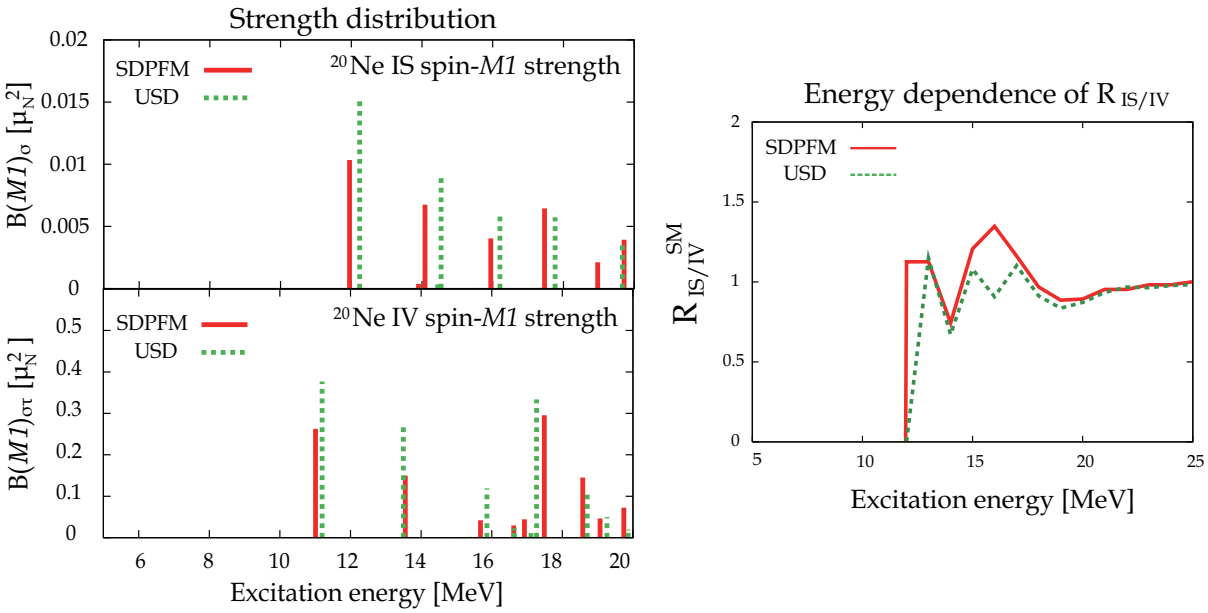

Figure 7.4: The shell-model calculations for ^{20}Ne within the model space of $0\hbar\omega$ and $(0+1)\hbar\omega$. The calculations performed with the SDPFM [88] and the USD [13] interactions using the free g_s-factors are shown in red solid and green dashed lines, respectively. (Left): The spin-$M1$ strength distributions of IS and IV strengths are shown from the top, respectively. (Right): The excitation energy dependence of $R_{IS/IV}^{SM}$ summed up from 0 MeV are show.

corresponded to be ∼60% of the shell model calculation, as schematically drawn in the top panel of Fig 7.5. Because the similar quenching factor of $Q_{IV} \sim 60\%$ was observed for the IV spin-$M1$ transitions within the low excitation energy region, the transition strength may be expected to be shifted up into the high excitation energy region due to the $2p2h$ configuration mixing, as seen in the GT strength distribution and drawn in the middle panel of the figure. The IS quenching factor $Q_{IS} \sim 100\%$, however, suggests that the most of the IS spin-$M1$ transition strength locate in the low excitation energy region and little strength be shifted up into the high excitation energy region, as shown in the bottom panel of the figure. Thus, the present result implies that the contribution of the $2p2h$ excitation differs in the transition operators "σ" and "$\sigma\tau$".

Such difference of the transition operators may be understood by introducing the one meson exchange model for the nucleon-nucleon interaction [89]. The IS and the IV 1^+ nuclear transitions are believed to occur by exchanging the pseudoscalar meson η and π, respectively, between the nucleons. Since the mass and the coupling constant of η is heavier and smaller than those of π as listed in Table 7.3, it may be natural that there is little contribution of the $2p2h$ mixings into the high excitation energy region owing to η-meson in the IS transition. On the other hand, the $2p2h$ configuration mixings in the IV and GT transitions due to π-meson is significant because the mass of π-meson is lighter and the coupling to the nucleons is strong.

Table 7.3: Mass and coupling constant of pseudoscalar mesons of π and η [89].

meson	mass [MeV]	$g_\alpha^2/4\pi$
π	138	13
η	549	0−0.4

7.1.4 Possible interpretation of spin-$M1$ quenching

Another possible physical interpretation based on one assumption to understand the difference observed in the IS and the IV spin-$M1$ quenching factors is introduced in this subsection.

Cumulative sum and ground state wavefunction

Taking $|g.s.\rangle$ and $|f\rangle$ as the ground state and the f-th 1^+ excited state, respectively, the cumulative sums of the IS and IV spin-$M1$ transition strengths can be transformed as

$$\begin{aligned}\sum_f B(M1)_{spin}{}^f &\propto \sum_f \left|\left\langle f \left|\hat{O}(M1)_{spin}\right| g.s.\right\rangle\right|^2 \\ &= \sum_f \left\langle g.s. \left|\hat{O}(M1)_{spin}\right| f\right\rangle \left\langle f \left|\hat{O}(M1)_{spin}\right| g.s.\right\rangle\end{aligned}$$

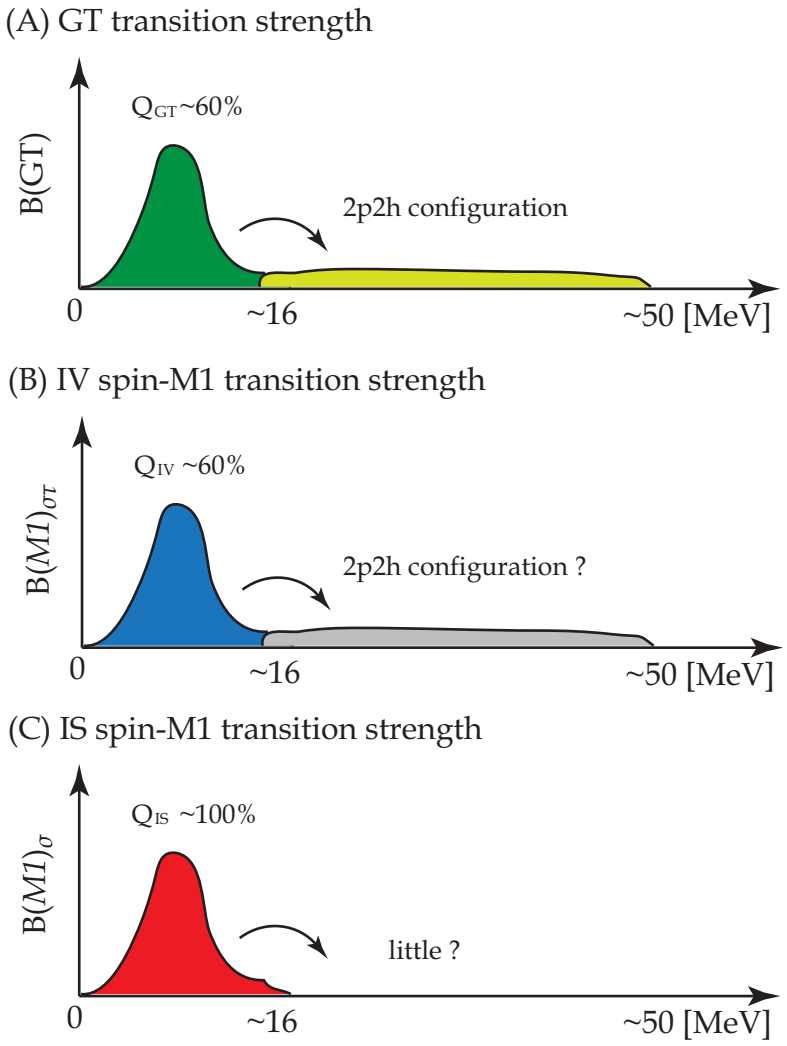

Figure 7.5: The schematic figure of the strength distributions in the cases of the GT, the IV and IS spin-$M1$ transition strengths, from the top, respectively. The GT quenching factor of $\sim$60% within the low excitation energy region (0$-$16 MeV) observed in the (p, n) reaction [15, 16] has been derived by using the shell model calculation. The GT strength distribution at the high excitation energy region has been observed in the (p, n) and the (n, p) reactions [3]. On the basis of the quenching factors observed in the low excitation energy region, the IV spin-$M1$ transition strengths may be expected to distribute in the higher excitation energy region owing to the $2p2h$ configuration mixing, while all the IS spin-$M1$ transition strengths may be located in the region 0$-$16 MeV.

$$
\begin{aligned}
&= \sum_{F \ni f} \left\langle g.s. \left| \hat{O}(M1)_{spin} \right| F \right\rangle \left\langle F \left| \hat{O}(M1)_{spin} \right| g.s. \right\rangle \\
&= \left\langle g.s. \left| \hat{O}(M1)_{spin}{}^2 \right| g.s. \right\rangle \qquad (7.8)
\end{aligned}
$$

where the sufix "*spin*" denotes σ and $\sigma\tau$ for the IS- and IV-spin-$M1$ transition strength, respectively, and $\hat{O}(M1)_{spin}$ represent the IS- or the IV-spin term in the $M1$ operator. The wavefunction $|F\rangle$ denotes all excited states in the nucleus including the 1^+ states. Thus, the $\Sigma B(M1)_\sigma$ and $\Sigma B(M1)_{\sigma\tau}$ values are evaluated by the ground state and the squared transition operator if the summation is taken for all 1^+ transitions.

Total spin operator

Using the total spin operators of

$$
\mathbf{S}_p = \sum_{k=1}^{Z} \mathbf{s}_k, \quad \mathbf{S}_n = \sum_{k=Z+1}^{A} \mathbf{s}_k, \qquad (7.9)
$$

for proton and neutron, respectively, the cumulative sum of the $B(M1)_\sigma$ can be expressed as

$$
\begin{aligned}
\sum B(M1)_\sigma &= \frac{1}{2J_i+1} \frac{3}{4\pi} \sum_f \left| \left\langle 1_f^+ \right| \frac{g_s^{IS}}{2} \left(\mathbf{S}_p + \mathbf{S}_n \right) \left| 0^+ \right\rangle \right|^2 \mu_N^2 \\
&= \frac{1}{2J_i+1} \frac{3}{4\pi} \left| \left\langle 0^+ \right| \frac{g_s^{IS}}{2} \left(\mathbf{S}_p + \mathbf{S}_n \right) \left| 0^+ \right\rangle \right|^2 \mu_N^2 \\
&= \frac{1}{2J_i+1} \frac{3}{4\pi} \left(\frac{g_s^{IS}}{2} \right)^2 \left\langle 0^+ \right| \left(\mathbf{S}_p + \mathbf{S}_n \right)^2 \left| 0^+ \right\rangle \mu_N^2, \qquad (7.10)
\end{aligned}
$$

where the suffix f is taken for all excited states of 1^+. Similarly, the $\Sigma B(M1)_{\sigma\tau}$ can be written as

$$
\sum B(M1)_{\sigma\tau} = \frac{1}{2J_i+1} \frac{3}{4\pi} \left(\frac{g_s^{IV}}{2} \right)^2 \left\langle 0^+ \right| \left(\mathbf{S}_p - \mathbf{S}_n \right)^2 \left| 0^+ \right\rangle \mu_N^2. \qquad (7.11)
$$

Thus, the $R_{IS/IV}$ can be rewritten in a simple form from Eqs. (7.4), (7.10) and (7.11) as

$$
\begin{aligned}
R_{IS/IV} &= \frac{\left\langle 0^+ \left| \left(\mathbf{S}_p + \mathbf{S}_n \right)^2 \right| 0^+ \right\rangle}{\left\langle 0^+ \left| \left(\mathbf{S}_p - \mathbf{S}_n \right)^2 \right| 0^+ \right\rangle}. \qquad (7.12) \\
&= \frac{\left\langle 0^+ \left| \left(\mathbf{S}_p^2 + \mathbf{S}_n^2 + 2\mathbf{S}_p \cdot \mathbf{S}_n \right) \right| 0^+ \right\rangle}{\left\langle 0^+ \left| \left(\mathbf{S}_p^2 + \mathbf{S}_n^2 - 2\mathbf{S}_p \cdot \mathbf{S}_n \right) \right| 0^+ \right\rangle}. \qquad (7.13)
\end{aligned}
$$

Thus, Eq. (7.13) can be transformed as

$$
\frac{R_{IS/IV} - 1}{R_{IS/IV} + 1} = \frac{2 \left\langle 0^+ \left| \left(\mathbf{S}_p \cdot \mathbf{S}_n \right) \right| 0^+ \right\rangle}{\left\langle 0^+ \left| \left(\mathbf{S}_p{}^2 + \mathbf{S}_n{}^2 \right) \right| 0^+ \right\rangle}, \qquad (7.14)
$$

where the term $\left\langle 0^+ \left| \left(\mathbf{S}_p \cdot \mathbf{S}_n \right) \right| 0^+ \right\rangle$ denotes the "two-nucleons spin correlation" between proton and neutron in the ground state, and the term $\left\langle 0^+ \left| \left(\mathbf{S}_p{}^2 + \mathbf{S}_n{}^2 \right) \right| 0^+ \right\rangle$ denoted that between the identical particles in the ground state.

Although the experimental result of $R_{IS/IV}^{Exp} \sim 2$ was obtained by the summation up to E_x=16 MeV, the summation is assumed to be performed for all the strengths in the followings. Thus, the $R_{IS/IV}^{Exp}$ value can be applied to Eq. (7.14). If $R_{IS/IV}$=2 is input to Eq. (7.14), the term $\left\langle 0^+ \left| \left(\mathbf{S}_p \cdot \mathbf{S}_n \right) \right| 0^+ \right\rangle$ should be positive because the term $\left\langle 0^+ \left| \left(\mathbf{S}_p{}^2 + \mathbf{S}_n{}^2 \right) \right| 0^+ \right\rangle$ is positive. The positive sign of the $\left(\mathbf{S}_p \cdot \mathbf{S}_n \right)$ value implies that a pair of proton and neutron in the ground state tends to make a constructive interference in terms of spin. It might be understood that the "two-nucleons spin correlation" is formed by a tensor force effect. Applying $R_{IS/IV}$=1, being the case of the shell model calculation, the term $\left\langle 0^+ \left| \left(\mathbf{S}_p \cdot \mathbf{S}_n \right) \right| 0^+ \right\rangle$ is found to be zero. There is no "two-nucleons spin correlation" in the shell-model calculation. It might imply that a tensor force effect is not described in the shell-model calculation. Thus, the $R_{IS/IV}$ value might imply the core polarization effect in the nucleus.

The assumption used here can be justified by the observation of the excitation energy dependence of the $R_{IS/IV}$ value as shown in Fig. 7.6 for the present result. If the trend of the $R_{IS/IV}^{Exp} > 1$ is seen up to $\sim$30 MeV, the above prediction on the core polarization effect in the nucleus is supposed to be true.

7.2 Isospin mixing

7.2.1 Effect of isospin mixing in $B(M1)_\sigma$ by hadronic interaction

The isospin breaking occurs owing to the Coulomb interaction, which mixes wavefunctions of IS and IV transitions. For this reason, the $B(M1)_\sigma$ value observed in experiments may contain some contributions from the IV spin $M1$ transition strength $B(M1)_{\sigma\tau}$, while the contribution of $B(M1)_\sigma$ to $B(M1)_{\sigma\tau}$ is expected to be negligible because $B(M1)_{\sigma\tau}$ is much larger than $B(M1)_\sigma$. Thus, the observed $B(M1)_\sigma$ value does not represent the pure IS transition strength but gives the transition strengths of the mixed wavefunction of the pure IS and IV transitions. Since we did not consider the effect of isospin mixing in evaluating the $B(M1)_\sigma$ value in the present analysis, the estimation of the mixing effect within the most simple two-state model was performed following the manner described in Ref. [81].

Defining the IS and IV 1^+-state wavefunctions as $|IS\rangle$ and $|IV\rangle$, respectively, they are assumed to be written in the sum of isospin-pure wavefunctions as

$$|IS\rangle = \alpha\,|IS^{pure}\rangle + \beta\,|IV^{pure}\rangle\,, \tag{7.15}$$

$$|IV\rangle = \beta\,|IS^{pure}\rangle - \alpha\,|IV^{pure}\rangle\,, \tag{7.16}$$

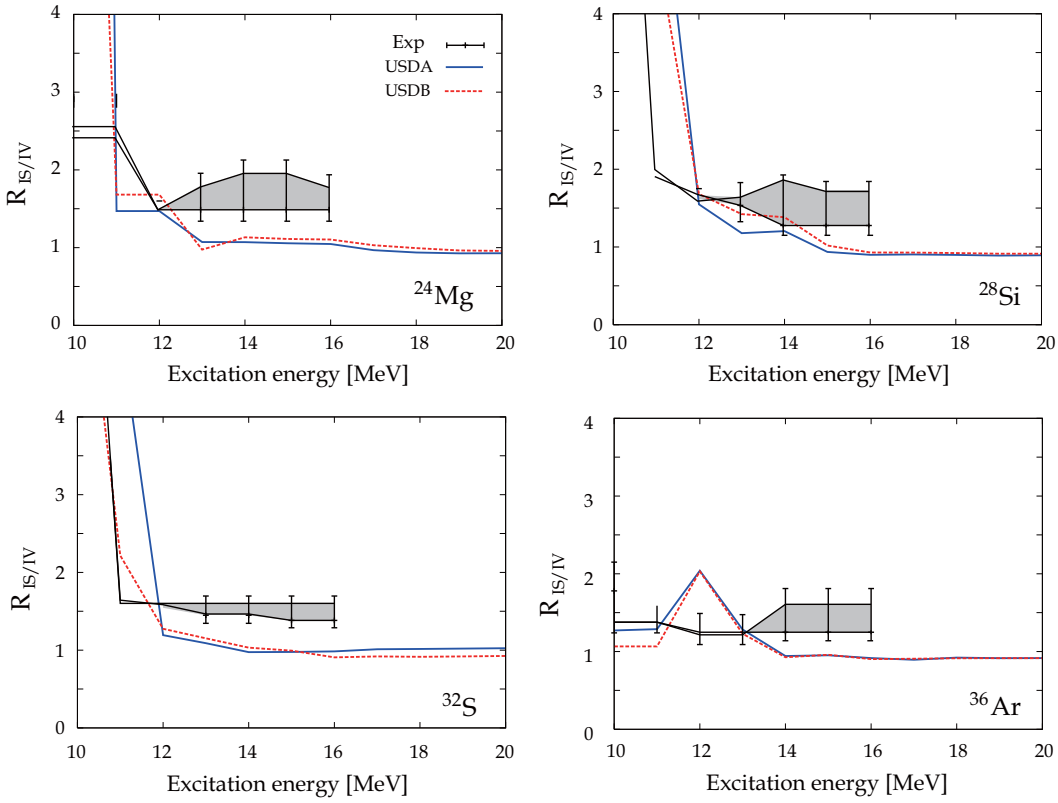

Figure 7.6: The excitation energy dependence of the $R_{IS/IV}$ values. The $R_{IS/IV}^{Exp}$ values are shown in black up to E_x=16 MeV. The gray band originates from the ambiguities in the J^π assignments and the error bars denote the experimental error. The shell model calculations with the USDA and the USDB interactions are shown in blue solid and red dashed lines, respectively.

where $\alpha^2 + \beta^2 = 1$, and $\alpha \gg \beta$. The strength ratio of the two IS and IV transitions can be expressed as

$$\frac{B(M1)_\sigma}{B(M1)_{\sigma\tau}} = \frac{|\alpha M_\sigma{}^{pure} + \beta M_{\sigma\tau}{}^{pure}|^2}{|\beta M_\sigma{}^{pure} - \alpha M_{\sigma\tau}{}^{pure}|^2}, \tag{7.17}$$

where $M_\sigma{}^{pure}$ and $M_{\sigma\tau}{}^{pure}$ stand for the IS and the IV matrix elements without isospin mixing, respectively. With $\alpha \simeq 1$ and the predominance of IV over IS $M1$ transition strength, one can neglect the term $\beta M_\sigma{}^{pure}$ and assume

$$B(M1)_{\sigma\tau} \simeq |M_{\sigma\tau}{}^{pure}|^2 . \tag{7.18}$$

Inserting the retio

$$\frac{M_\sigma{}^{pure}}{M_{\sigma\tau}{}^{pure}} = \sqrt{\frac{B(M1)_\sigma{}^{pure}}{B(M1)_{\sigma\tau}}} \tag{7.19}$$

into Eq. (7.17) leads to a relation quadratic in $M_\sigma{}^{pure}$,

$$(1-\beta^2)(M_\sigma{}^{pure})^2 + 2\alpha\beta\sqrt{B(M1)_{\sigma\tau}}(M_\sigma{}^{pure}) + \beta^2 B(M1)_{\sigma\tau} - B(M1)_\sigma = 0. \tag{7.20}$$

The coefficients $\alpha\beta$ and β^2 can be obtained from the Coulomb mixing matrix element $\langle H_c \rangle$ and energy difference between the two states ΔE as

$$\langle H_c \rangle = \alpha\beta|\Delta E|, \tag{7.21}$$

where the sign for $\alpha\beta$ follows that for $\langle H_c \rangle$. The coefficient of β^2 was assumed to be $(\alpha\beta)^2 \simeq \beta^2$ from $\alpha \simeq 1$. The Coulomb mixing matrix element $\langle H_c \rangle$ was taken from the empirical equation, which has been determined from a comparison of α-capture cross sections into the giant dipole resonance of self-conjugate and non-conjugate nuclei in Refs. [93, 94]. The $\langle H_c \rangle$ can be expressed by the equation

$$|\langle H_c \rangle| = H_c^0 \exp\left\{-C\sqrt{A(E_x - \Delta)}\right\}, \tag{7.22}$$

where the parameters of H_c^0 and C are 6.26 MeV and 0.36 MeV$^{-1/2}$, and the parameters have been searched by a fit to the experiment [94]. A is the mass number, E_x is the excitation energy, and Δ is the pairing energy, where $\Delta = 12/A^{1/2}$ MeV [95] was assumed. Applying the empirical $\langle H_c \rangle$ value to Eq. (7.21), $M_\sigma{}^{pure}$ can be obtained from Eq. (7.20). Since, unfortunately, the empirical $\langle H_c \rangle$ value has the uncertainty in terms of sign, we tried both cases.

The derived $B(M1)_\sigma{}^{pure}$ are compared with the observed $B(M1)_\sigma$ in Table 7.4. Because we got two solutions from Eq. (7.20), they were assumed to be the edge point of the range of $B(M1)_\sigma{}^{pure}$. For the most cases, except for the cases of ^{12}C and ^{24}Mg, the

range of $B(M1)_{\sigma}^{pure}$ is smaller than the error of $B(M1)_{\sigma}$. The fact indicates that the uncertainties arising from the isospin mixing can be ignored because the experimental uncertainties are significant.

For the case of ^{24}Mg, the uncertainty owing to isospin mixing is dominant. This is supposed to arise from the fact that the energy difference of the two states between the IS and the IV spin-$M1$ transitions are small ($\Delta E = 140$ keV) and thus the effect of the mixing seems to be dominant. However, it was found that all the data are on the line within the error bars. Therefore, the effect of the isospin mixing in the $B(M1)_{\sigma}$ values can be ignored within the experimental error bars. It can be seen that most $B(M1)_{\sigma}^{pure}$ values are consistent with the $B(M1)_{\sigma}$ value within the error bar, while there are two special cases to be considered the contribution of isospin mixing, for ^{12}C and ^{24}Mg with 0.216(60) μ_N^2. For the most cases, there is no need to consider the effect of isospin mixing to the IS states. For the special two cases, the assumptions of $(\alpha\beta)^2 \simeq \beta^2$ may not stand up because the IV transition strength of the mixing pair is ten times larger for ^{12}C and the two states are very close ($\Delta E = 140$ keV) for ^{24}Mg. The empirical equation of the Coulomb mixing matrix element may be invalid for these cases. However, further discussion on the isospin mixing is beyond the present work.

The followings are the assumptions that were applied to the present two-state model analysis

- Only one isovector state, which is the closest, was considered to mix to the isoscalar state.
- The empirical equation [93, 94] was employed to estimate the Coulomb matrix element, which gives the degree of isospin mixing between the two states.
- The approximations of $(\alpha\beta)^2 \simeq \beta^2$ and $B(M1)_{\sigma\tau} \simeq |M_{\sigma\tau}^{pure}|^2$ were employed.
- The sign of $\langle H_c \rangle$ was determined to follow the empirical $R_{IS/IV}^{Exp}$ value (Sec. 7.1.2).

7.2.2 Estimation of isospin mixing degree in IS $M1$ state

It is to be noted that a $B(M1)_{\sigma}$ value is proportional to the $B(M1)_{IS}$ value observed in the same IS $M1$ transition. Applying the restriction between the IS orbital and the IS spin operators as written in Eq. (6.19), the proportionality can be obtained as

$$\begin{aligned} B(M1)_{IS} &= \frac{1}{2J_i+1}\frac{3}{4\pi}\left|\left\langle f\left| g_l^{IS}\sum_k^A \mathbf{l}_k + \frac{g_s^{IS}}{2}\sum_k^A \sigma_k \right| i\right\rangle\right|^2 {\mu_N}^2 \\ &= \frac{1}{2J_i+1}\frac{3}{4\pi}\left|\left\langle f\left| g_l^{IS}\sum_k^A \mathbf{l}_k \right| i\right\rangle + \left\langle f\left| \frac{g_s^{IS}}{2}\sum_k^A \sigma_k \right| i\right\rangle\right|^2 {\mu_N}^2 \end{aligned}$$

Table 7.4: Experimental $B(M1)_\sigma$ and $B(M1)_{IS}^{pure}$ values, derived by the two-state model analysis. All the IS 1^+ states that were definitely assigned are compared with the calculation.

nuclei	E_x (MeV)	$B(M1)_\sigma$ (μ_N^2)	$B(M1)_\sigma^{pure}$ (μ_N^2)
^{12}C	12.708	0.147 ± 0.039	0.084−0.228
^{24}Mg	9.828	0.180 ± 0.051	0.064−0.453
^{28}Si	9.495	0.237 ± 0.068	0.214−0.262
^{32}S	7.187	0.018 ± 0.006	0.007−0.035
	9.297	0.043 ± 0.013	0.036−0.051
	9.956	0.111 ± 0.033	0.097−0.126
^{36}Ar	8.985	0.114 ± 0.048	0.099−0.130

$$
\begin{aligned}
&= \frac{1}{2J_i+1}\frac{3}{4\pi}\left| g_l^{IS}\left\langle f\left|\sum_k^A \mathbf{l}_k\right|i\right\rangle + \frac{g_s^{IS}}{2}\left\langle f\left|\sum_k^A \sigma_k\right|i\right\rangle\right|^2 {\mu_N}^2 \\
&= \frac{1}{2J_i+1}\frac{3}{4\pi}\left| g_l^{IS}\left(-\frac{1}{2}\left\langle f\left|\sum_k^A \sigma_k\right|i\right\rangle\right) + \frac{g_s^{IS}}{2}\left\langle f\left|\sum_k^A \sigma_k\right|i\right\rangle\right|^2 {\mu_N}^2 \\
&= \frac{1}{2J_i+1}\frac{3}{4\pi}\left|\frac{g_s^{IS}-g_l^{IS}}{2}\left\langle f\left|\sum_k^A \sigma_k\right|i\right\rangle\right|^2 {\mu_N}^2 \\
&= \left(\frac{g_s^{IS}-g_l^{IS}}{g_s^{IS}}\right)^2 \frac{1}{2J_i+1}\frac{3}{4\pi}\left|\frac{g_s^{IS}}{2}\left\langle f\left|\sum_k^A \sigma_k\right|i\right\rangle\right|^2 {\mu_N}^2 \\
&\simeq (5.36)^{-1}\, B(M1)_\sigma, \qquad (7.23)
\end{aligned}
$$

where the free g-factors are employed to obtain the proportional factor of 5.36. This proportionality is supposed to result in that there is always destructive interference between the spin and orbital operators, which has been reported in Ref. [90].

In Table 7.5, the $B(M1)_\sigma$ values experimentally observed by the (p,p') reaction are compared with the corresponding $B(M1)_{IS}$ value observed in (e,e') reaction on ^{12}C, ^{24}Mg, and ^{32}S, and (γ,γ') reaction on ^{24}Mg. Although the IS strength ratio of $B(M1)_\sigma$ to $B(M1)_{IS}$ should be 5.36 with the free g-factors, the experimental ratios were scattered from 0 to 5.36. This scattering for the IS strength ratio are of interest. Since the proportional factor with the empirical g-factors [50] becomes 9.54 for the case of ^{24}Mg using g_s^{IS}= 0.766 and g_l^{IS}= 0.518, the scattering of the IS strength ratio can not be explained by the empirical g-factors.

Such scattering of the IS strength ratio is supposed to originate from the isospin mixing. It is to be noted that the sensitivity to the IV transition is 29 times larger than that to the IS transition for the electro-magnetic interactions, while they are almost equal for the hadronic interactions. For this reason, the influence for the $B(M1)_{IS}$ value observed by electro-magnetic interactions is drastically changed even if the mixing degree of the isospin is little. If the isospin mixing occurs in the IS transition, the $B(M1)_{IS}$ value

Table 7.5: Experimental $B(M1)_\sigma$ and $B(M1)_{IS}$ values.

nuclei	E_x (MeV)	$B(M1)_\sigma$ $(\mu_N^2)^a$	$B(M1)_{IS}$ (μ_N^2)	$B(M1)_\sigma/B(M1)_{IS}$
^{12}C	12.708	0.147 ± 0.039	0.040 ± 0.003^b	3.7 ± 1.0
^{24}Mg	9.828	0.180 ± 0.051	0.28 ± 0.07^c	0.64 ± 0.24
			0.30 ± 0.11^d	0.60 ± 0.28
^{28}Si	9.495	0.237 ± 0.068	$(\geq 0.04)^e$	-
^{32}S	7.187	0.018 ± 0.006	0.011 ± 0.005^f	1.6 ± 0.9
^{36}Ar	8.985	0.114 ± 0.048	$(\geq 0.02)^e$	-

[a]From the present work.

[b]From (e, e') measurement [81, 82].

[c]From (e, e') measurement [91].

[d]From (γ, γ') measurement [92].

[e]Expected value following the assumption of $B(M1)_\sigma/B(M1)_{IS} \leq 5.36$.

[f]From (e, e') measurement [42].

becomes larger owing to the mixing of the wavefunction of the IV transition and, thus, the IS strength ratio decreases from 5.36 as experimentally observed.

In the followings, the mixing degrees of isospin in ^{12}C and ^{24}Mg observed by electromagnetic interactions are estimated through the proportionality of Eq. (7.23) assuming no isospin mixing in the $B(M1)_\sigma$ values by hadronic interactions. The mixing in ^{32}S, unfortunately, was unavailable since the errors in the transition strengths of $B(M1)_\sigma$ and $B(M1)_{IS}$ were too much to obtain a certain result. Following the manner described in Sec. 7.2.1, the ratio of the $M1$ transition strengths of Eq. (7.17) can be rewritten as

$$\frac{B(M1)_{IS}}{B(M1)_{IV}} = \frac{|\alpha M_{IS}^{pure} + \beta M_{IV}^{pure}|^2}{|\beta M_{IS}^{pure} - \alpha M_{IV}^{pure}|^2}, \tag{7.24}$$

where M_{IS}^{pure} and M_{IV}^{pure} stand for the IS and the IV transition matrix elements without isospin mixing, respectively. The M_{IS}^{pure} was assumed to be proportional to the observed $B(M1)_\sigma$ value as

$$|M_{IS}^{pure}|^2 = B(M1)_{IS}^{pure} \simeq \frac{B(M1)_\sigma}{5.36}. \tag{7.25}$$

Thus, a quadratic equation on β can be obtained from the analogy to Eq. (7.20) as,

$$(1-\beta^2)B(M1)_{IS}^{pure} + 2\alpha\beta\sqrt{B(M1)_{IV}B(M1)_{IS}^{pure}} + \beta^2 B(M1)_{IV} - B(M1)_{IS} = 0. \tag{7.26}$$

Applying the approximation $\alpha\beta \simeq \beta$, the mixing degree of β^2 was experimentally obtained from Eq. (7.26). The results of $\alpha\beta$ values experimentally obtained are compared with those empirically evaluated from Eq. (7.21), as shown in Table 7.6. For ^{12}C, the mixing degree was evaluated less than 1%. It was found that the IS strength ratio changes from 5.36 even though only 1% mixing of the IV transition contributes to the IS one. The mixing

degree in ^{24}Mg was evaluated to be 10−15%, and the $\alpha\beta$ values were found to be close to the empirical one. The isospin mixing even at the 10% order drastically changes the $B(M1)_{IS}$ value. Although the isospin effect by hadronic interactions is hard to be observed in $B(M1)_{\sigma}$ value, that can be seen in the shape of the angular distribution of differential cross section as shown in Fig. 7.7. The excitation to the state at $E_x = 9.828$ MeV in ^{24}Mg was assigned as the IS-$M1$ transition in the present thesis. The observed slope of the distribution, however, was slightly steeper than the calculated one of the IS-$M1$ transition as seen in Fig. 7.7. The angular distributions of 1^+ transition obtained from the DWBA calculation are drawn in the figure for comparison; pure IS and IV 1^+ transitions in red dashed and blue dotted curves, respectively, and 10 and 20% degree mixing of the IV component to the IS transitions in thin and bold green solid curves, respectively. The experimental distribution is well reproduced by the DWBA curve with 20% degree mixing, and this mixing degree agrees with the evaluation based on the IS strength ratio of $B(M1)_{\sigma}/B(M1)_{IS}$, as summarized in Table 7.6. Thus, it was found that the scattering of the IS strength ratio $B(M1)_{\sigma}/B(M1)_{IS}$ from 5.36 originates mainly from the isospin mixing and that the ratio allows us to experimentally evaluate the mixing degree of the isospin in the $B(M1)_{IS}$ value observed in electro-magnetic measurement.

The IS $M1$ transitions in ^{28}Si and ^{36}Ar have not been observed so far. The $B(M1)_{IS}$ value to be observed in electro-magnetic interactions is expected to be estimated following the IS strength ratio of $B(M1)_{\sigma}/B(M1)_{IS} \leq 5.36$, where the sign of inequality originates from the effect of the isospin mixing. On the basis of the $B(M1)_{\sigma}$ values in ^{28}Si and ^{36}Ar by the (p, p') reaction, their $B(M1)_{IS}$ values are evaluated to be ≥ 0.05 and ≥ 0.03 μ_N^2, respectively, as written in Table 7.5.

Table 7.6: Mixing degree observed in $B(M1)_{IS}$. The $\alpha\beta^{Exp}$ has been experimentally obtained from Eq. (7.26) assuming no isospin mixing in the hadronic interaction, while the $\alpha\beta^{emp}$ has been empirically evaluated from Eq. (7.21).

nuclei	$B(M1)_{\sigma}/B(M1)_{IS}$	mixing degree	$\alpha\beta^{Exp}$	$\alpha\beta^{emp}$
^{12}C	3.7 ± 1.0^a	<1%	0.02 ± 0.02	0.06
^{24}Mg	0.64 ± 0.24^b	7−14%	0.30 ± 0.05	0.37
	0.60 ± 0.28^c	8−24%	0.36 ± 0.06	0.37

[a]From (e, e') measurement [81, 82].

[b]From (e, e') measurement [91].

[c]From (γ, γ') measurement [92].

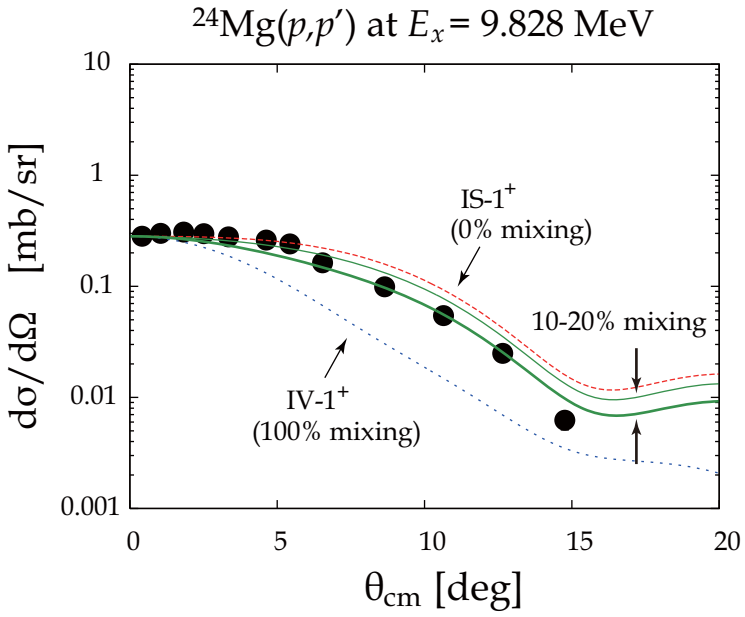

Figure 7.7: The effect of the isospin mixing on angular distribution of the IS $M1$ transition to the state at E_x = 9.828 MeV in ^{24}Mg. The angular distribution of differential cross section observed in the experiment is compared with those of the 1^+ transition obtained from the DWBA calculation by changing the mixing degree in terms of isospin. The pure isospin 1^+ transitions of the IS and the IV are denoted in red dashed and blue dotted curves, respectively. The transitions with the isospin mixing of 10 and 20% are shown in thin and bold green solid curves, respectively.

7.3 Related topic

7.3.1 Modification of effective interaction on $s_{1/2}$ orbit

There is an interesting feature in the mass distribution of the cumulative sums in the *sd*-shell region as shown in Fig. 7.1. The experimental result have a peak at ^{28}Si, while the shell-model calculations with using the USDA and USDB interactions predicts a peak at ^{28}Si and ^{32}S. Their amounts of the prediction were comparable. We tried to change the matrix elements of $2s_{1/2}$ orbit in the USD interaction to reproduce the experimental strength distribution of the cumulative sums. The original matrix elements were changed to $\pm 20\%$ from the original values, and the results are shown in Fig. 7.8. Although the peak position of the sum distribution was moved at ^{28}Si by reducing the matrix element to 80%, no strength was predicted for ^{36}Ar. The modification to 120% from the original values overestimated the calculated strengths at ^{32}S and ^{36}Ar and underestimated those at ^{20}Ne, ^{24}Mg, and ^{28}Si. Thus, this modification ended in failure to reproduce the experimental result.

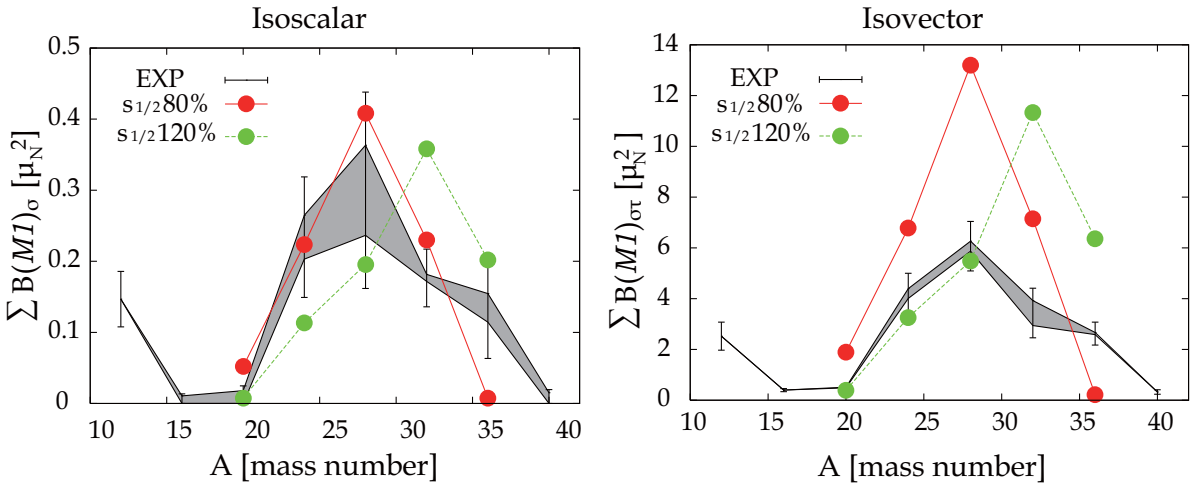

Figure 7.8: The mass dependence of the cumulative sums of the experimental result and the shell model calculations using the USD interaction. The matrix elements relating to $s_{1/2}$ orbit in the effective interaction is changed to 80% and 120% from the original value. The gray bands originate from the uncertainties in the J^π assignments.

7.3.2 Centroid energy

The centroid energy E_c is defined as

$$E_c = \sum_i \frac{B(M1)_T^i \times {E_x}^i}{B(M1)_T^i}, \tag{7.27}$$

where $T = \sigma$ and $\sigma\tau$, and ${E_x}^i$ and $B(M1)_T^i$ denote the i-th excitation energy and the spin-$M1$ transition strength, respectively. The distributions of the centroid energy of the IS and IV excitations in the *sd*-shell region are compared with the shell-model calculations with the USD interaction as shown in Fig. 7.9.

All the matrix elements of the interaction were modified to be 0, and the calculation result with it is denoted as 0%. The result with the original interaction is presented as 100%. The residual interaction is expected to be studied from the difference between the results of 0% and 100%. It is interesting that the calculations for the IV transition predict the different trend to the experimental results. It was found that the reproducibility to the experiment by the calculation for the IS transition was better than that for the IV.

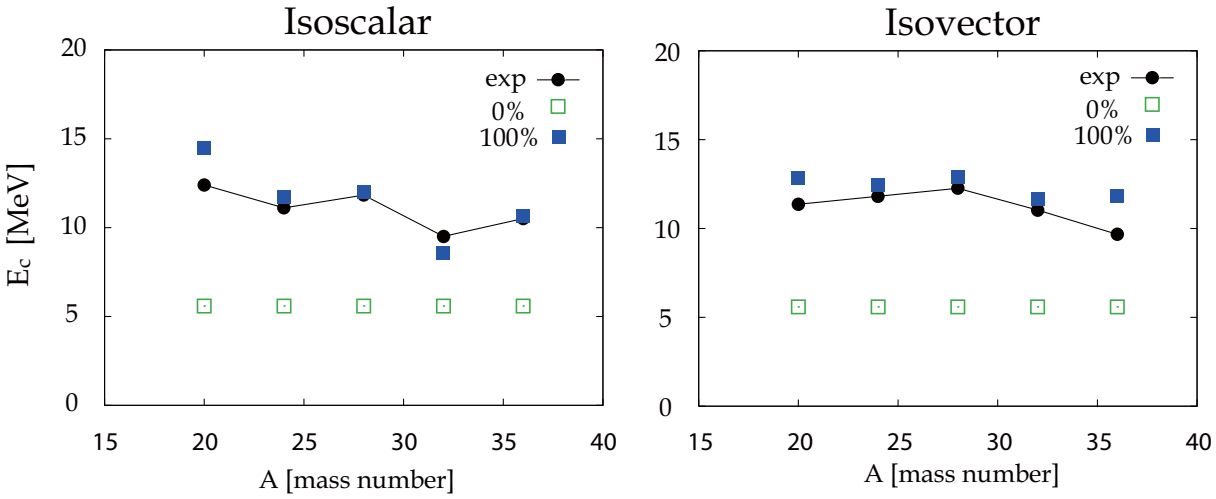

Figure 7.9: The centroid energies for the $N = Z$ and even-even nuclei in the *sd*-shell. The experimental results are compared with the shell-model calculations using the original USD interaction (100%) and the interaction to be modified to 0 (0%).

7.3.3 Effect of meson exchange current

It is known that the MEC contributions which come mainly from one-pion exchange are different for the $M1$ (vector) and GT (axial-vector) operators [18]. The MEC effect has been discussed in a number of experiments of the (e, e') and (^{3}He,t) reactions [96–100]. As defined in Eq. (A.23), the MEC effect changes the proportionality between the $B(M1)_{\sigma\tau}$ and B(GT) values. Therefore, the unit cross section for the $B(M1)_{\sigma\tau}$ is changed by introducing the MEC contribution, while that for the $B(M1)_\sigma$ is not changed because the IS transition strength is not affected by it to the first order. The R_{MEC} value has been reported as 1.3−1.8 in the *sd*-shell, *i.e.*, 1.85(29) in ^{24}Mg [96] and 1.42(10) in ^{28}Si [97]. The R_{MEC} value in ^{32}S, however, was estimated to be 0.79(8) from Ref. [42], and it scattered from the empirical value. That was one of reason why we did not consider

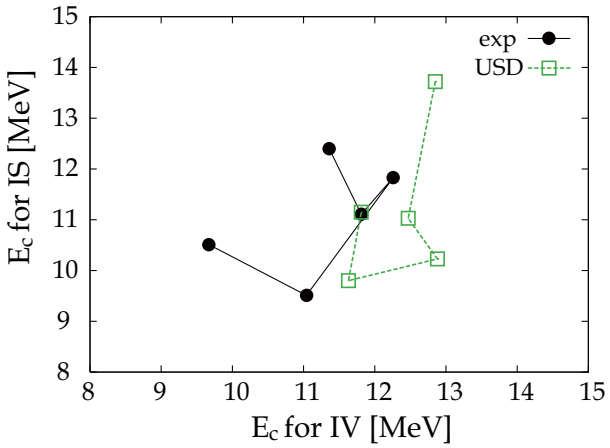

Figure 7.10: Two-dimensional plot of centroid energies in the *sd*-shell. The shell-model calculations by the USD interaction is shown for the comparison.

---

the MEC effect into the calculation for the unit cross section in the present study. If the MEC contribution is taken to the present analysis as $R_{MEC} = 1.3$, the IV unit cross section decrease, and the obtained $B(M1)_{\sigma\tau}$ increases. Thus, the quenching amount of the IV transition shown in Fig. 7.2 is reduced and the IV quenching factor becomes close to unity. It is to be noted that the IS transition strengths and the IS quenching factors are not changed by the R_{MEC} value.

7.4 Future perspective

The IS and the IV spin-$M1$ strength distribution into the high excitation energy region owing to the $2p2h$ configuration mixing coupling to the $1p1h$ excitation were predicted on the basis of the quenching factors. The errors for the quenching factors, however, were significant, which were arising from the ambiguities of the J^π assignments of the states and the derivations of the unit cross section, especially for the IS case. The ambiguities of the former can be reduced by an combined analysis with the (d, d') experiment at 0° to discriminate the ΔT=0 and 1 transitions. The latter factor can be reduced by a refined measurement of $\hat{\sigma}_{IS}(^{11}\mathrm{B})$ or the measurement in other nucleus to reduce the systematic uncertainty. The nucleus ^{27}Al is a candidate to derive another IS unit cross section because the γ-rays in the mirror nuclei are measureable for the decomposition of the IS and the IV components of B($M1$) [66].

In the present study, we estimated the strength distribution in the high excitation energy region by using the quenching factors, derived from the observed strengths within the low excitation energy region and the shell model calculations. Thus, we did not confirm and observe the strength distribution at the higher excitation energy region ex-

perimentally. It is essential to perform the direct observation of the strength distribution at the high excitation energy region for the study of mechanism of the $2p2h$ configuration mixings, mediated by the transition operators of "σ" and "$\sigma\tau$". The feasible experiment for the direct observation of the strength distribution is supposed to be a polarization transfer measurement at 0°. The model independent analysis by using the polarization transfer observables is a powerful tool for the identification of the IS and IV 1^+ transitions, especially at the continuum region. Although a multi-pole decomposition analysis (MDA) is also a powerful method to decompose the contributions from each L transition in the continuum region, it is supposed to be hard for it to be applied to identify the IS and IV 1^+ transitions because their angular distributions are similar.

Finally, it is to be noted that the different transition mechanism between the transition operators of "σ" and "$\sigma\tau$" was experimentally suggested for the first time. Although the shell model calculation reached the great success to predict the strength distribution within the low excitation energy region, it did not reasonably reproduce the IS/IV strength distribution into the high excitation energy region. This represents the limitation of the shell model calculation. Since it is believed to be natural that the transition mechanism differs between the IS and the IV 1^+ transitions within the one meson exchange potential model, an explicit treatment of psuedscalar meson, π and η, in theory would be expected to improve the prediction of the strength distribution in the high excitation energy region. Thus, the present study leads us to the way of the further interesting studies on nuclear physics.

Chapter 8

Summary

The IS and the IV spin-$M1$ transition strengths were systematically measured in order to study the difference of the 1^+ transition operators of "σ" and "$\sigma\tau$". The cross sections in the (p, p') reaction at $0-14^\circ$ were measured using 295 MeV proton beam on the $N = Z$ and even-even nuclei. The experiment was performed at the RCNP by using the Grand Raiden spectrometer applying the dispersion matching technique for high energy resolution. The target nuclei of ^{12}C, ^{16}O, ^{20}Ne, ^{24}Mg, ^{28}Si, ^{32}S, ^{36}Ar, and ^{40}Ca were measured for the systematic study. These nuclei allowed us to separately observe the pure IS and the IV transition because their ground states are $T = 0$. The gas target system was newly developed to employ neon and argon gas, and the elemental sulfur was successfully used as a target with charged particle irradiation for the first time.

The shape of the angular distribution of the differential cross section for low-lying discrete states were compared with the prediction based on the DWBA calculation using the shell model wavefunctions in order to make the J^π and T assignment to the transitions. The cross sections at 0° of the transition to the IS and IV 1^+ state were converted to the spin-$M1$ transition strengths of the $B(M1)_\sigma$ and $B(M1)_{\sigma\tau}$, respectively, using the unit cross sections. The unit cross sections used in the present study were determined from the results of the β-decay and γ-decay experiments in literature.

The cumulative sums of $B(M1)_\sigma$ and $B(M1)_{\sigma\tau}$ observed up to $E_x = 16$ MeV were compared with the shell model calculations based on the USDA and the USDB interactions. The quenching factors of the IV spin-$M1$ transitions in the *sd*-shell region were roughly averaged to be $\sim$0.6 with the free g_s-factors and became to unity by applying the empirical g_s-factors. This quenching degree was consistent with the GT quenching factors, derived with not the sum rule but the shell model calculation, observed in the (p, n) experiments. The quenching phenomena, however, were unobserved in the IS spin-$M1$ transitions. The IS quenching factors with the free g_s-factors were 1.0 but those with the empirical ones overestimated the experimental results. An amount of the spin-$M1$ transition strength distributed into the high excitation energy region owing to the $2p2h$

configuration mixing was estimated from the quenching factors. Because the GT quenching factors based on the shell model calculation were consistent with the IV ones, similar amount of the strength distributed into the continuum region was expected to be observed in the IV 1^+ transition. The IS quenching factor, however, suggested that the most of the IS strength locate in the low excitation energy region and little strength be shifted up into the high excitation energy region. Thus, the different quenching factors and the different strength distribution in the high excitation energy region owing to the $2p2h$ configuration mixing between the IS and the IV transitions were experimentally observed for the first time. Such difference between the IS and the IV transitions may be understood by the model that the transition is mediated by different psuedoscalar meson of η and π, respectively. The difference of the strength distributions is supposed to originate from the difference of the mass and the coupling constant between η and π. Since the IV 1^+ transition is supposed to be mediated by π, an explicit treatment of π is desired to be developed in theory.

The new parameter ($R_{IS/IV}$) to denote the total strengths ratio of the IS to the IV spin-$M1$ transitions was introduced. The $R_{IS/IV}$ values observed in the experiment and obtained from the shell-model calculations were surprisingly constant for the $N = Z$ and even-even nuclei in the *sd*-shell region. The experimental $R_{IS/IV}$ values were found to be 1.5 times as high as the predicted values in the shell-model calculations *i.e.*, $R_{IS/IV}^{Exp} \sim 1.5$ and $R_{IS/IV}^{SM} \sim 1$. The shell-model calculations failed to reproduce the experimental values even employing the empirical g_s-factors or an extension to the $(0+1)\hbar\omega$ model space. Thus, it was found that the shell model calculation can not reproduce the $R_{IS/IV}$ value.

Another possible interpretation may reach the "two-nucleons spin correlation" between proton and neutron. If one assumes that all the strengths are accumulated in the observed $R_{IS/IV}^{Exp}$ value, the experimental $R_{IS/IV}$ value implies that a pair of proton and neutron in the ground state tends to make a constructive interference in terms of spin. It is expected that the assumption used here is justified whether the $R_{IS/IV}^{Exp} > 1$ is kept up to higher excitation energy.

Finally, this work was the first systematic measurement of the IS and the IV 1^+ transition strength distributions at low excitation energy region. The quenching factors, derived with the shell model calculation, suggested that the strength distribution into the high excitation energy region owing the $2p2h$ configuration mixing differ between the IS and the IV 1^+ transitions. Since such difference between the IS and the IV 1^+ transitions has not been considered in theory, the development of the calculation for an explicit treatment of pion is highly encouraged.

Appendix A

Formalism of spin-$M1$ transition strength

A.1 Magnetic moment

The operator $\hat{O}(M1)$ for a magnetic-dipole ($M1$) transition and a magnetic-dipole moment (magnetic moment) is written by

$$\hat{O}(M1) = \left[\sum_{k=1}^{Z}(g_l^{\pi}\mathbf{l}_k + g_s^{\pi}\mathbf{s}_k) + \sum_{k=Z+1}^{A}(g_l^{\nu}\mathbf{l}_k + g_s^{\nu}\mathbf{s}_k)\right]\mu_N \quad (A.1)$$

$$= \left[\sum_{k=1}^{A}\left\{\left(g_l^{IS}\mathbf{l}_k + g_s^{IS}\frac{\sigma_k}{2}\right) + \left(g_l^{IV}\mathbf{l}_k + g_s^{IV}\frac{\sigma_k}{2}\right)\tau_z(k)\right\}\right]\mu_N, \quad (A.2)$$

where μ_N is the nuclear magneton, and the eigenvalues for the isospin operator τ_k are defined as $+1$ for neutron and -1 for protons. The gyromagnetic factors (g-factors) of g_l^{IS}, g_s^{IS}, g_l^{IV}, and g_s^{IV} are taken as $g_l^{IS} = \frac{1}{2}(g_l^{\pi} + g_l^{\nu}) = 0.5$, $g_s^{IS} = \frac{1}{2}(g_s^{\pi} + g_s^{\nu}) = 0.880$, $g_l^{IV} = -\frac{1}{2}(g_l^{\pi} - g_l^{\nu}) = -0.5$, and $g_s^{IV} = -\frac{1}{2}(g_s^{\pi} - g_s^{\nu}) = -4.706$ using the g-factors for protons and neutrons in the free space, $g_l^{\pi} = 1$, $g_l^{\nu} = 0$, $g_s^{\pi} = 5.586$, and $g_s^{\nu} = -3.826$. The suffixes of IS and IV denote isoscalar and isovector, respectively. Following the convention of Edmonds [4], the magnetic moment can be expressed as

$$\mu = \sqrt{\frac{J}{(J+1)(2J+1)}}\left\langle i \left|\left|\hat{O}(M1)\right|\right| i\right\rangle \quad (A.3)$$

$$= \sqrt{\frac{J}{(J+1)(2J+1)}}\left(g_l^{IS}M(l) + \frac{g_s^{IS}}{2}M(\sigma) + g_l^{IV}M(l\tau_z) + \frac{g_s^{IV}}{2}M(\sigma\tau_z)\right)\mu_N, \quad (A.4)$$

where the initial state is denoted by $|i\rangle$, and J is used to represent the total angular momentum spin. The reduced matrix element in spin but not in isospin is defined as

$$M(\hat{O}) = \left\langle f \left|\left|\hat{O}\right|\right| i\right\rangle, \quad (A.5)$$

where the initial and the final states in the transition denote $|i\rangle$ and $|f\rangle$, respectively, following the convention of Edmonds [4]. We note that the final state is identical to the

initial state for the magnetic moment. The magnetic moment can be divided into the IS and the IV components as

$$\mu_{IS} = \sqrt{\frac{J}{(J+1)(2J+1)}}\left(g_l^{IS}M(l)+\frac{g_s^{IS}}{2}M(\sigma)\right)\mu_N \quad (A.6)$$

$$\mu_{IV} = \sqrt{\frac{J}{(J+1)(2J+1)}}\left(g_l^{IV}M(l\tau_z)+\frac{g_s^{IV}}{2}M(\sigma\tau_z)\right)\mu_N, \quad (A.7)$$

respectively. If isospin symmetry is assumed, the IS and IV magnetic moments can be obtained from the corresponding magnetic moments of $\mu(T_z=\pm T)$ in mirror nuclei as

$$\mu_{IS} = \frac{\mu(T_z=+T)+\mu(T_z=-T)}{2} \quad (A.8)$$

$$\mu_{IV} = \frac{\mu(T_z=+T)-\mu(T_z=-T)}{2}, \quad (A.9)$$

respectively. The g-factors for the IS and IV magnetic moment can be defined as

$$g_{IS} = \frac{\mu(T_z=+T)+\mu(T_z=-T)}{2J} \quad (A.10)$$

$$g_{IV} = \frac{\mu(T_z=+T)-\mu(T_z=-T)}{2J}, \quad (A.11)$$

respectively.

A.2 Spin-$M1$ transition strength

Applying Eqs. (1.2) and (A.5), the $M1$ transition strengths can be written as

$$B(M1) = \frac{1}{2J_i+1}\frac{3}{4\pi}\left|\left\langle f||\hat{O}(M1)||i\right\rangle\right|^2 \quad (A.12)$$

$$= \frac{1}{2J_i+1}\frac{3}{4\pi}\left|g_l^{IS}M(l)+\frac{g_s^{IS}}{2}M(\sigma)+g_l^{IV}M(l\tau_z)+\frac{g_s^{IV}}{2}M(\sigma\tau_z)\right|^2{\mu_N}^2 \quad (A.13)$$

The IS and IV components in $B(M1)$ can be defined as

$$B(M1)_{IS} = \frac{1}{2J_i+1}\frac{3}{4\pi}\left|g_l^{IS}M(l)+\frac{g_s^{IS}}{2}M(\sigma)\right|^2{\mu_N}^2 \quad (A.14)$$

$$B(M1)_{IV} = \frac{1}{2J_i+1}\frac{3}{4\pi}\left|g_l^{IV}M(l\tau_z)+\frac{g_s^{IV}}{2}M(\sigma\tau_z)\right|^2{\mu_N}^2, \quad (A.15)$$

respectively. In the spin-$M1$ transition by hadronic scattering, like the (p,p') reaction, the orbital components are suppressed. Thus, the IS and IV spin-$M1$ transition strengths can be defined as

$$B(M1)_{\sigma} = \frac{1}{2J_i+1}\frac{3}{4\pi}\left|\frac{g_s^{IS}}{2}M(\sigma)\right|^2{\mu_N}^2 \quad (A.16)$$

$$B(M1)_{\sigma\tau} = \frac{1}{2J_i+1}\frac{3}{4\pi}\left|\frac{g_s^{IV}}{2}M(\sigma\tau_z)\right|^2{\mu_N}^2, \quad (A.17)$$

respectively.

A.3 GT transition strength

Since the GT transition operator [101] is written by

$$\hat{O}(\mathrm{GT}^{\pm}) = \sum_{k=1}^{A} \frac{1}{\sqrt{2}} \sigma_k \tau_{\pm}(k), \tag{A.18}$$

following the convention of Edmonds [4], the reduced GT transition strength $B(\mathrm{GT}^{\pm})$ can be expressed by the equation

$$B(\mathrm{GT}^{\pm}) = \frac{1}{2J_i+1} \left| \frac{1}{\sqrt{2}} M(\sigma\tau_{\pm}) \right|^2, \tag{A.19}$$

where $M_{GT}(\sigma\tau_{\pm})$ is a GT matrix element. Applying the Wigner-Eckart theorem in the isospin space for the direct comparison of the GT and IV $M1$ matrix elemtns, we get

$$B(\mathrm{GT}^{\pm}) = \frac{1}{2J_i+1} \left| \frac{1}{\sqrt{2}} \frac{C_{GT}}{\sqrt{2T_f+1}} M'(\sigma\tau_{\pm}) \right|^2, \tag{A.20}$$

$$B(M1)_{\sigma\tau} = \frac{3}{4\pi} \frac{1}{2J_i+1} \left| \frac{g_s^{IV}}{2} \frac{C_{M1}}{\sqrt{2T_f+1}} M'(\sigma\tau_z) \right|^2 {\mu_N}^2, \tag{A.21}$$

where C_{GT} and C_{M1} are the isospin Clebsch-Gordan (CG) coefficients $\langle T_i T_{zi} 1 \pm 1 | T_f T_{zf} \rangle$ and $\langle T_i T_{zi} 10 | T_f T_{zf} \rangle$ for the GT and the IV $M1$ transitions, respectively. The suffixes i and f denote the initial and the final states of the transition, and those of zi and zf are the initial and the final state of the z-component of the isospin (T). The reduced matrix element in spin and isospin is defined as

$$M'(\hat{O}) = \left\langle f \left| \left| \left| \hat{O} \right| \right| \right| i \right\rangle. \tag{A.22}$$

The meson exchange current (MEC) contributions (Sec. 7.3.3) can be defined by the ratio of squared matrix elements of the IV $M1$ and the corresponding GT transitions [66] as

$$R_{MEC} = \frac{[M(\sigma\tau_z)]^2}{[M(\sigma\tau_{\pm})]^2}. \tag{A.23}$$

In the present study, R_{MEC} was assumed to be 1 for simplicity, suggesting the assumption of the isospin symmetry. Thus, applying the equation

$$[M_{M1}(\sigma\tau)]^2 = [M_{GT}(\sigma\tau)]^2, \tag{A.24}$$

the relationship between $B(\mathrm{GT}^{\pm})$ and $B(M1)_{\sigma\tau}$ can be expressed as

$$\frac{B(\mathrm{GT}^{\pm})}{B(M1)_{\sigma\tau}/{\mu_N}^2} = \frac{8\pi}{3} \frac{1}{(g_s^{IV})^2} \frac{\langle T_i, T_{iz}, 1, \pm 1 | T_f, T_{fz} \rangle^2}{\langle T_i, T_{iz}, 1, 0 | T_f, T_{fz} \rangle^2} \tag{A.25}$$

under the assumption of the isospin symmetry.

Appendix B

Excitation energy spectra

Observed excitation energy spectra of inelastic scattering at $E_p = 295$ MeV are summarized in the following. The procedure of the data reduction is described in Sec. 4

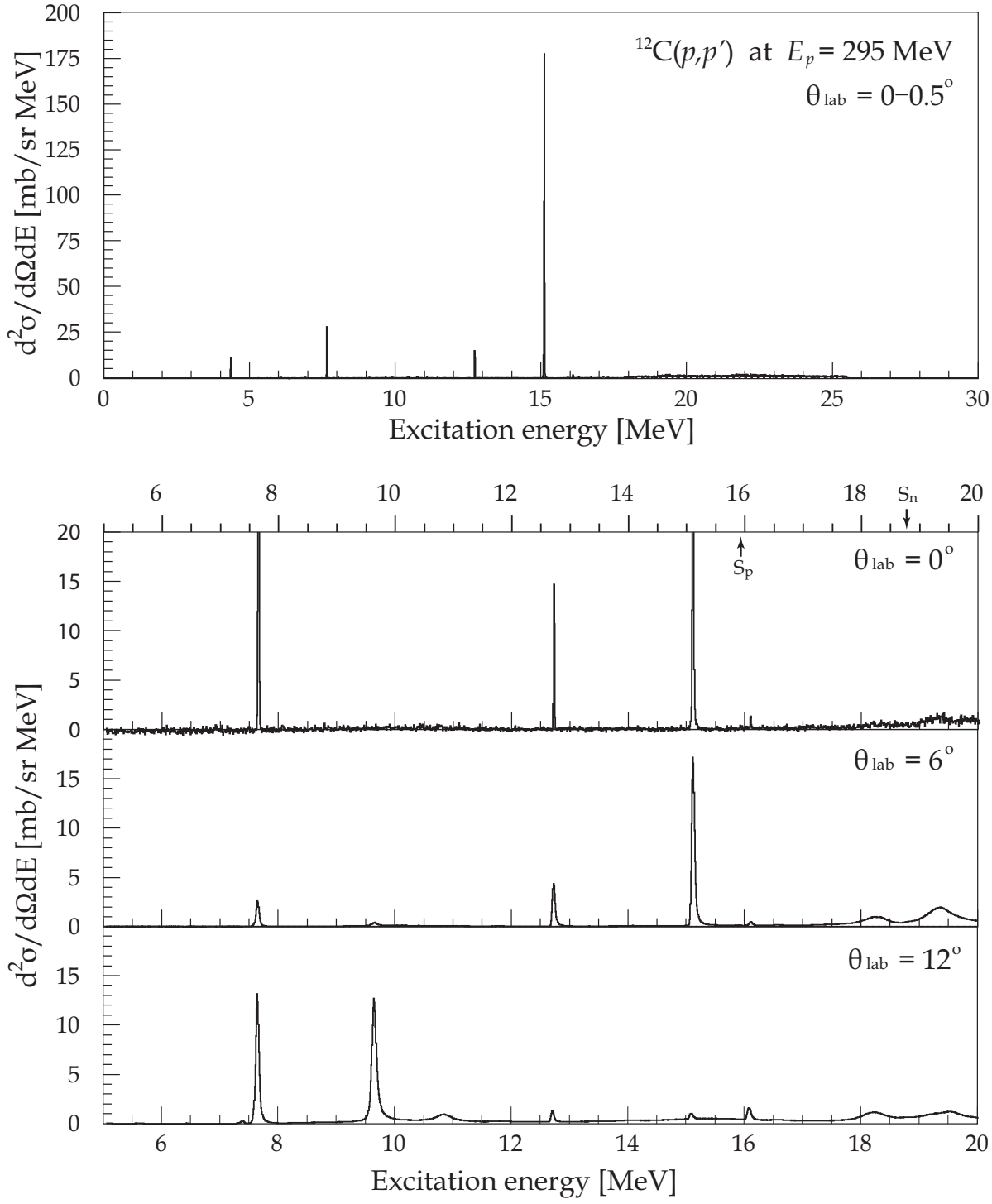

Figure B.1: Excitation energy spectra for the ^{12}C(p, p') reaction at $E_p = 295$ MeV and at 0, 6, 12°.

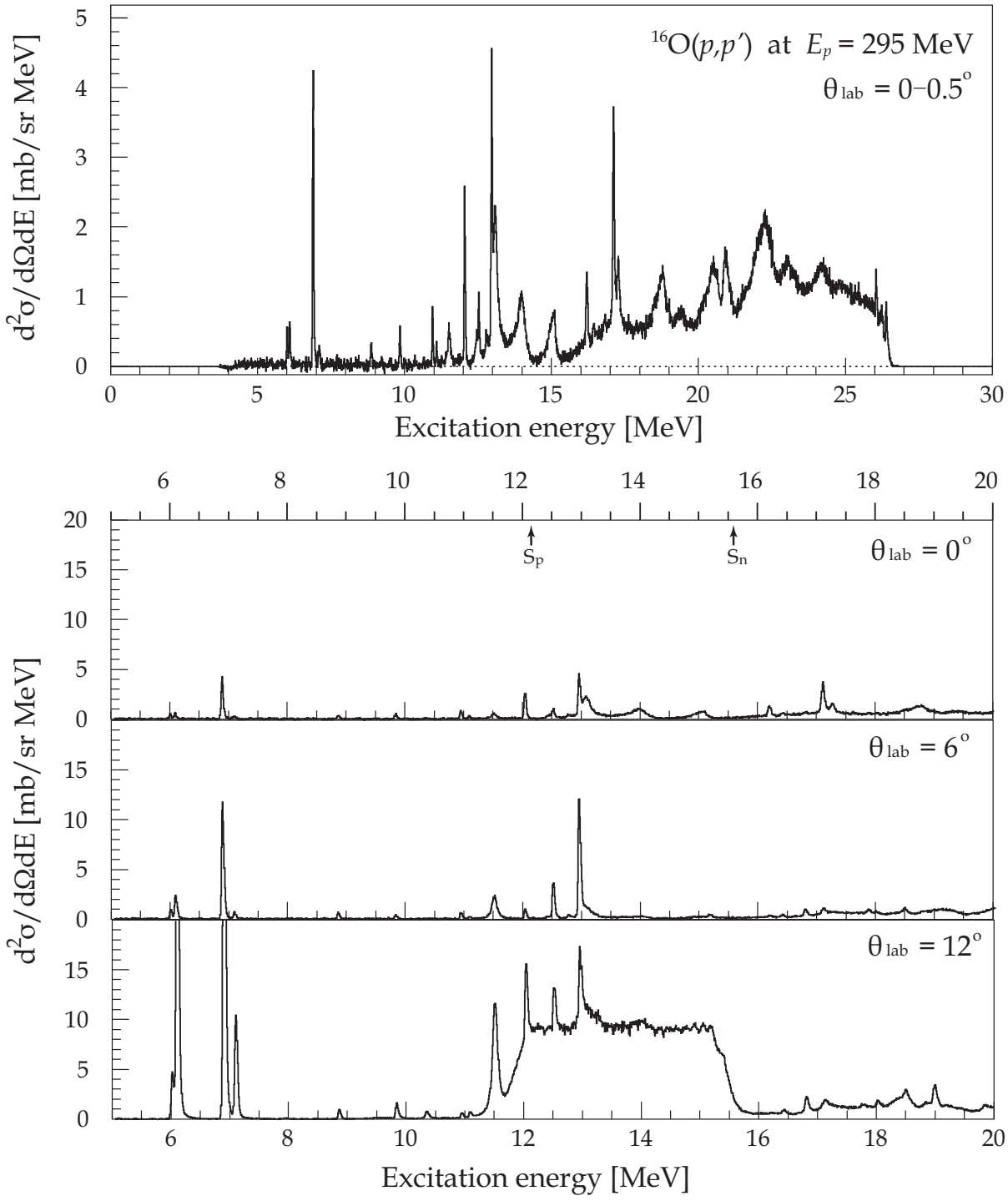

Figure B.2: Excitation energy spectra for the ^{16}O(p, p') reaction at $E_p = 295$ MeV and at 0, 6, 12°. The $p - p$ elastic scattering are seen as a broad bump at $E_x = 12{-}15$ MeV at 12°.

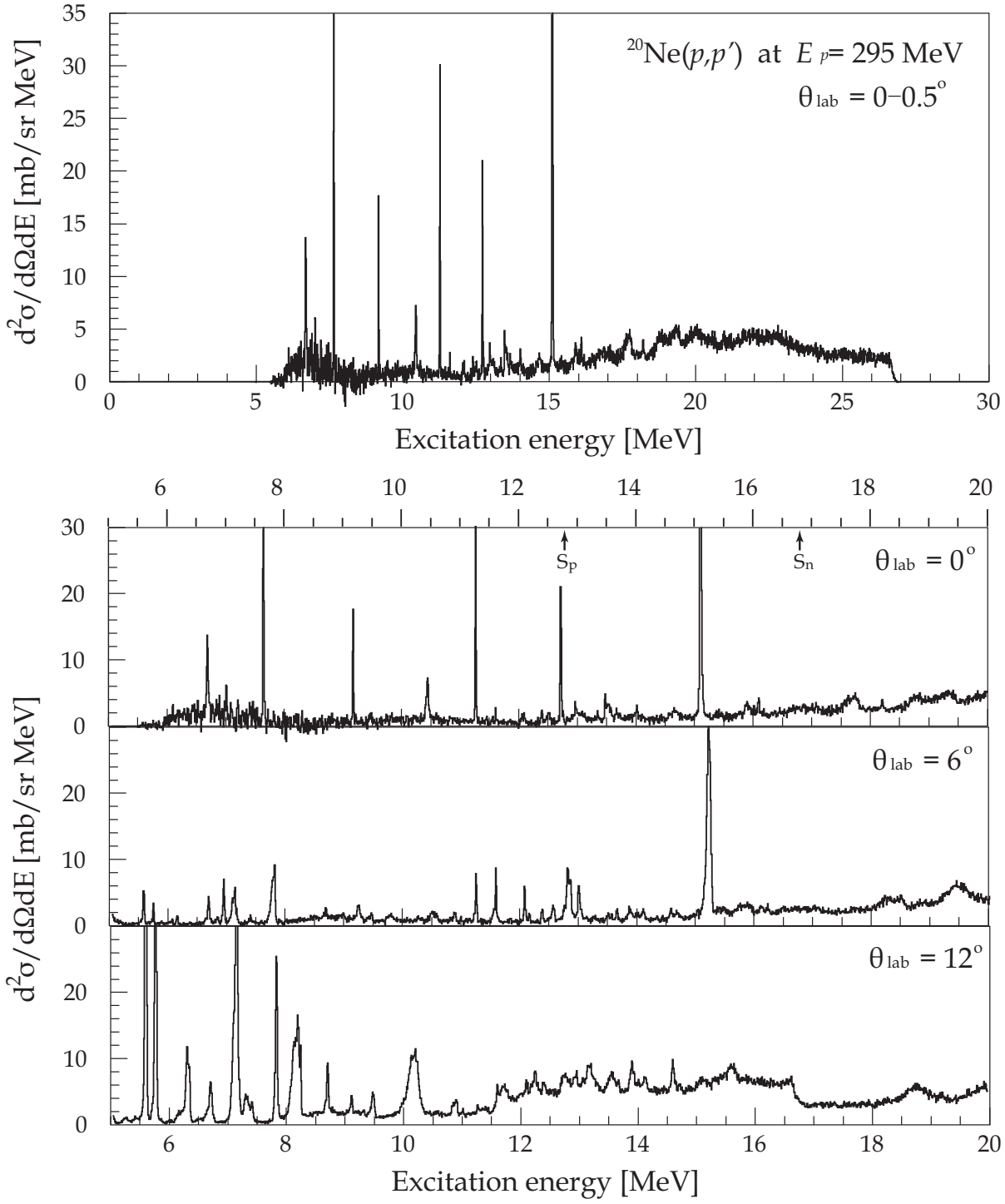

Figure B.3: Excitation energy spectra for the ^{20}Ne(p, p') reaction at $E_p = 295$ MeV and at 0, 6, 12°. Peaks due to the aramid window are contaminated. The $p-p$ elastic scattering are seen as a broad bump at $E_x = 12-15$ MeV at 12°. Background events failed to be subtracted remain at $E_x = 6-7$ MeV in the 0° spectra.

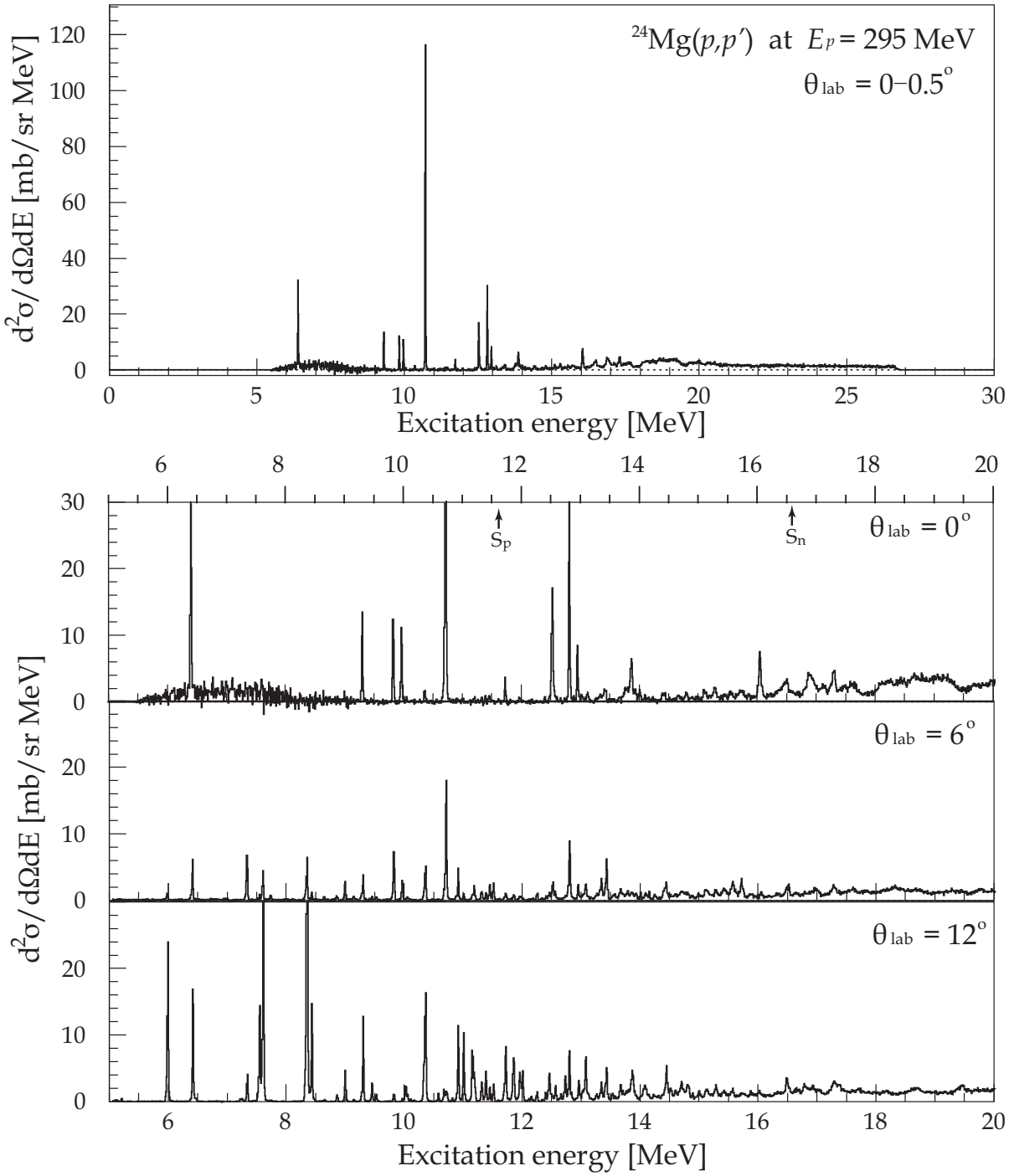

Figure B.4: Excitation energy spectra for the ^{24}Mg(p,p') reaction at $E_p = 295$ MeV and at 0, 6, 12°. Background events failed to be subtracted remain at $E_x = 6-7$ MeV in the 0° spectra.

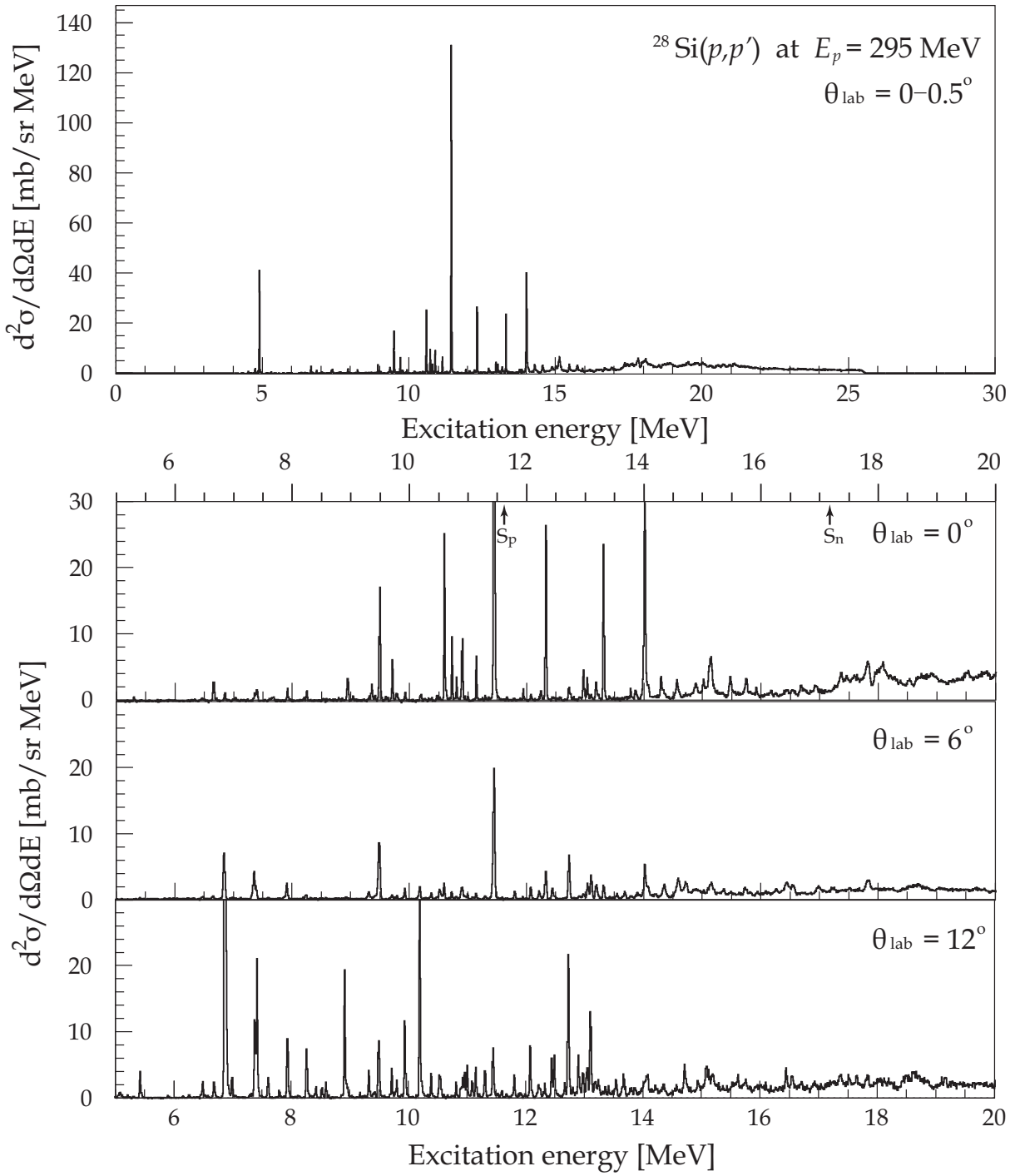

Figure B.5: Excitation energy spectra for the ^{28}Si(p, p') reaction at $E_p = 295$ MeV and at 0, 6, 12°.

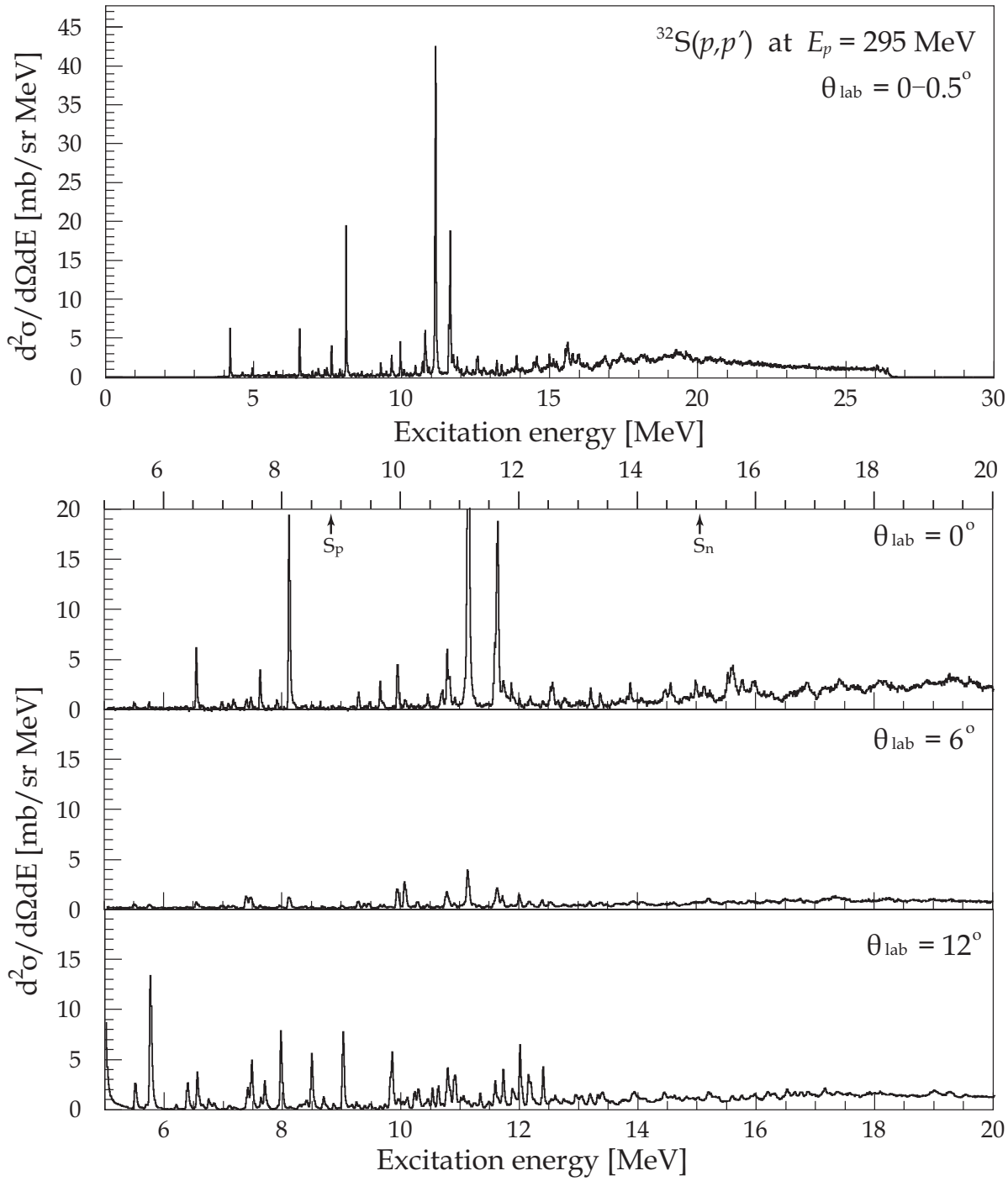

Figure B.6: Excitation energy spectra for the ^{32}S(p, p') reaction at $E_p = 295$ MeV and at 0, 6, 12°.

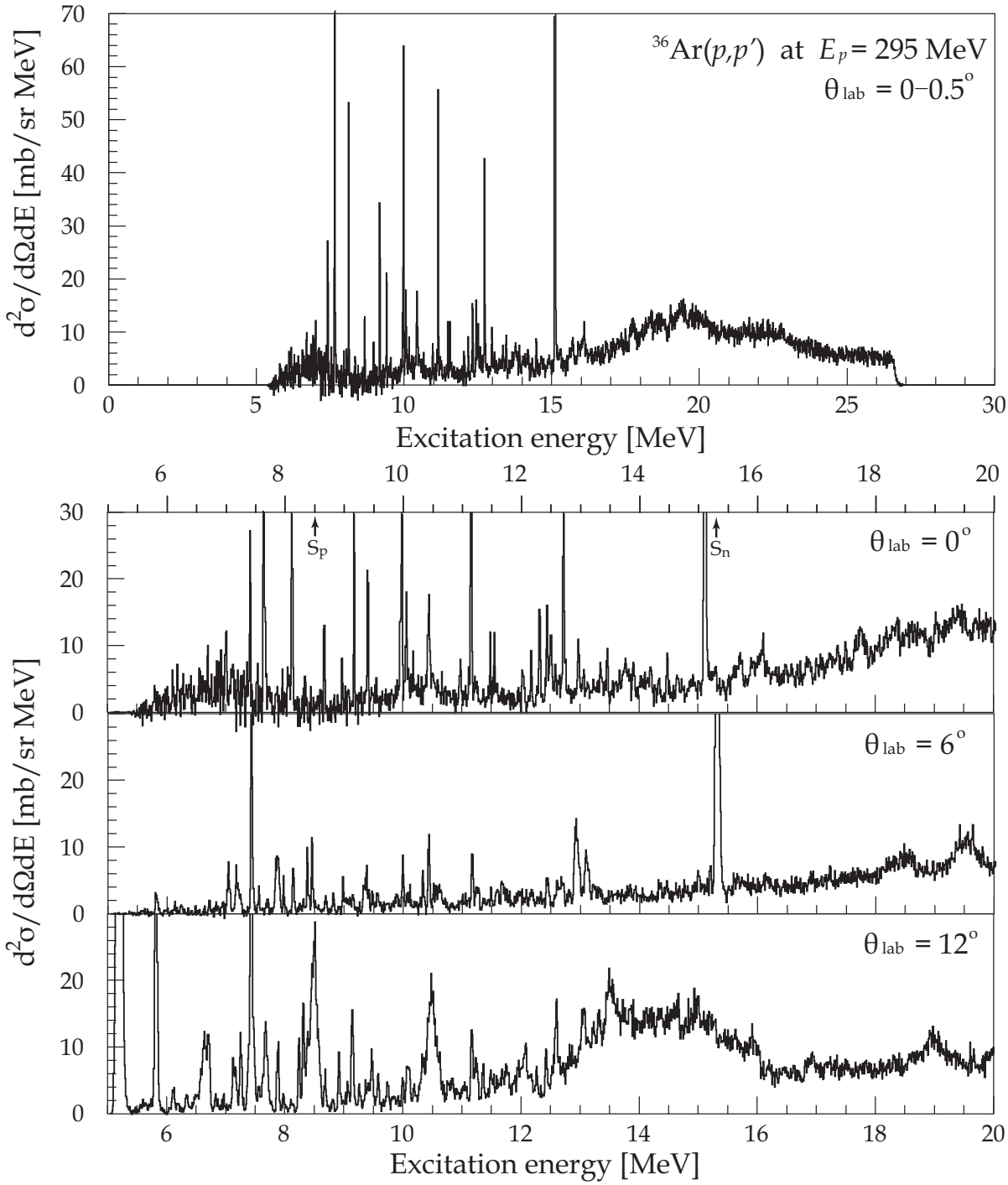

Figure B.7: Excitation energy spectra for the ^{36}Ar(p, p') reaction at $E_p = 295$ MeV and at 0, 6, 12°. Peaks due to the aramid window are contaminated. The $p-p$ elastic scattering are seen as a broad bump at $E_x = 12-15$ MeV at 12°. Background events failed to be subtracted remain at $E_x = 6-7$ MeV in the 0° spectra.

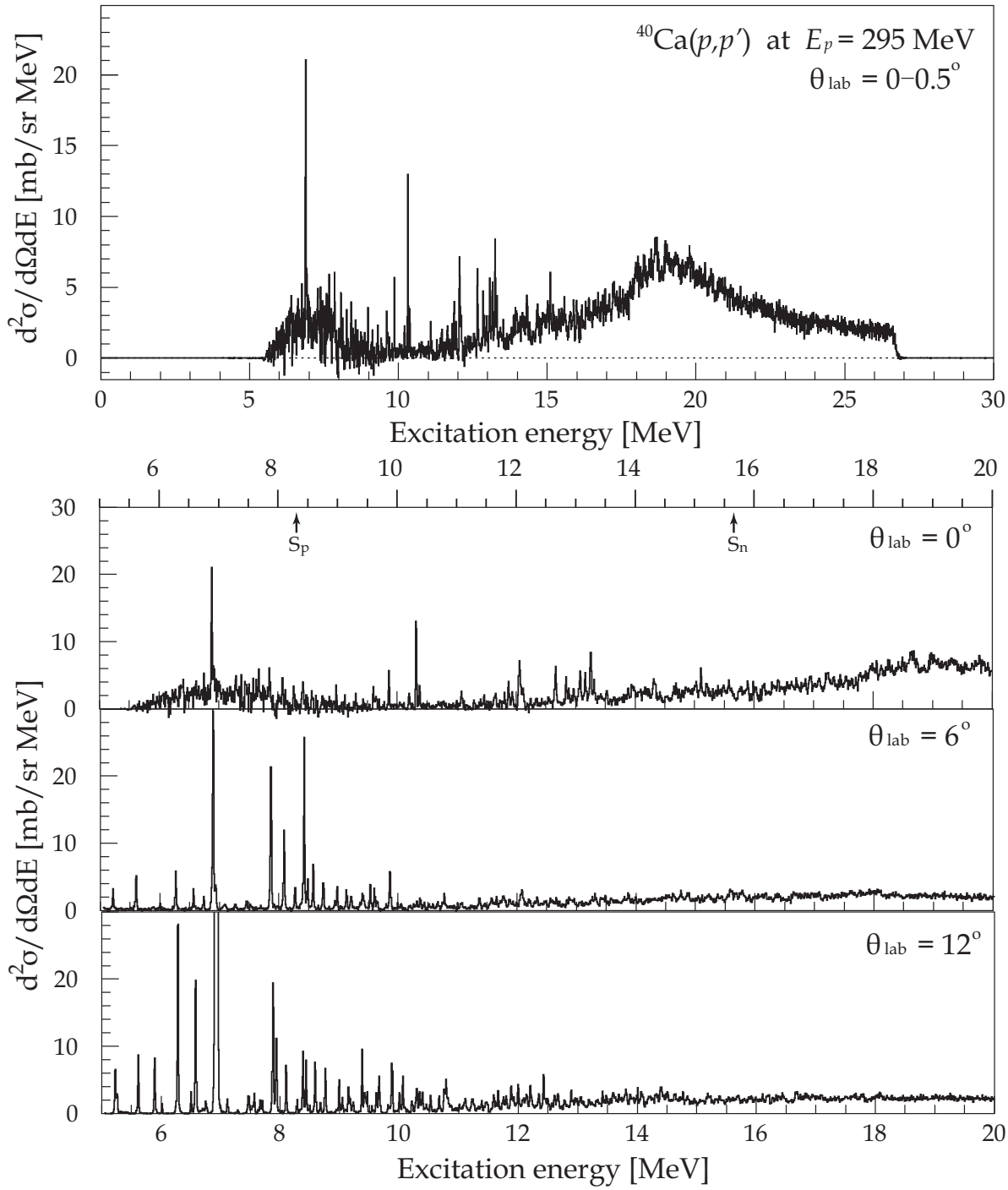

Figure B.8: Excitation energy spectra for the ^{40}Ca(p, p') reaction at $E_p = 295$ MeV and at 0, 6, 12°. Background events failed to be subtracted remain at $E_x = 6-7$ MeV in the 0° spectra.

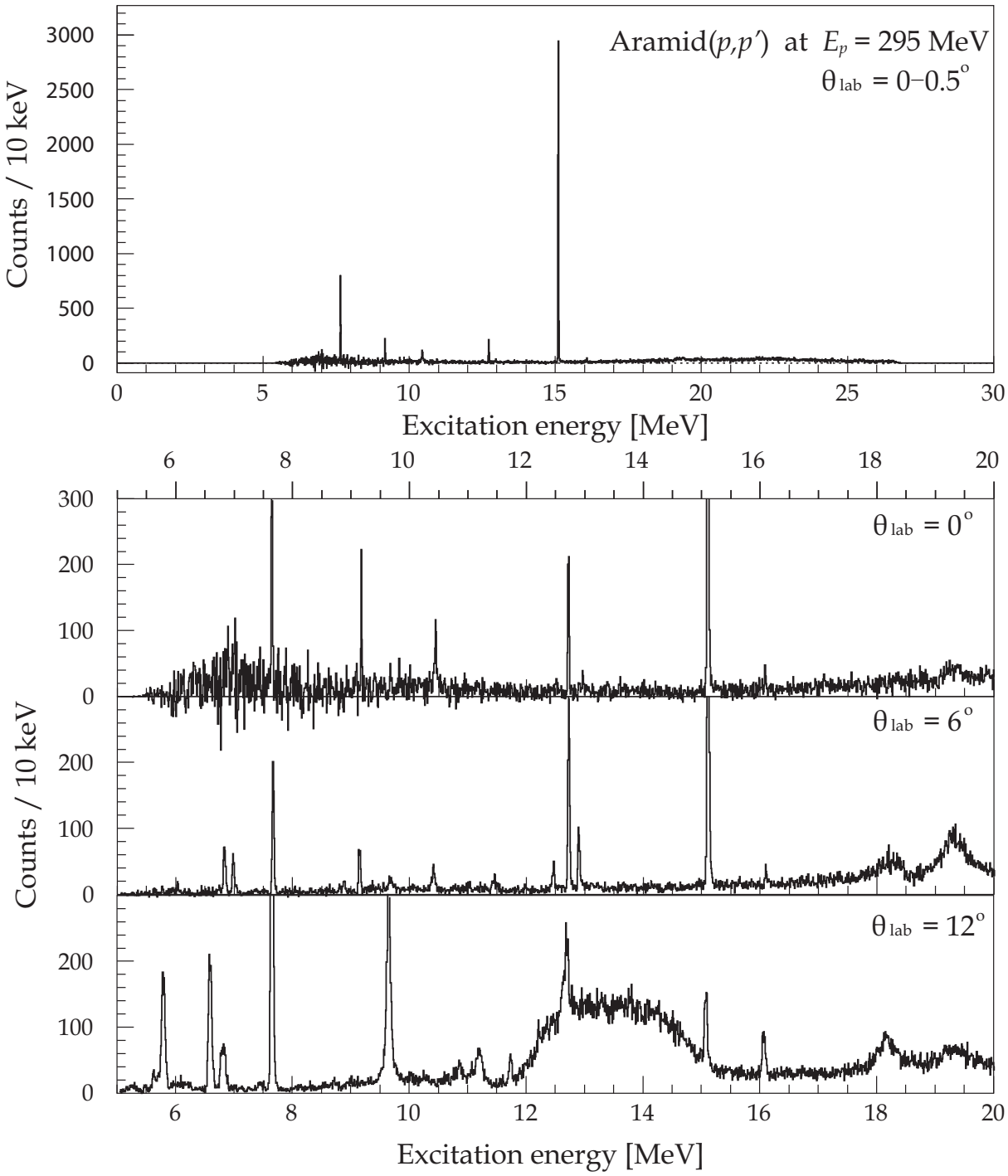

Figure B.9: Excitation energy spectra for the (p, p') reaction on the aramid film, $C_{14}O_2N_2Cl_2H_8$, at $E_p = 295$ MeV and at 0, 6, 12°. The kinematical condition for ^{12}C is employed to deduce the excitation energy. The $p-p$ elastic scattering are seen as a broad bump at $E_x = 12-15$ MeV at 12°. Background events failed to be subtracted remain at $E_x = 6-7$ MeV in the 0° spectra.

Appendix C

Angular distribution of inelastic scattering cross section

The results of angular distribution of inelastic scattering cross section for a discrete state are displayed in this chapter. A discrete state that was observed in the 0° spectrum was compared with the DWBA calculations, and then its J^π assignment, 0^+, IS, IV, 1^-, or $\Delta L \geq 1$, was given. The DWBA calculations of the angular distributions of 0^+, IS, IV, 1^-, and 2^+ transitions are drawn in Fig. 6.4. The DWBA calculations are not presented for some discrete states when yields of the state were not extracted from the energy spectra at 0.40° and 1.0°. See Sec. 6.3.2 for the procedure of the assignment.

In the following figures, the horizontal axis denotes scattering angle in the range of 0° to 20° in center of mass frame, while the vertical axis expresses the cross section from 10^{-4} to 10^{1} mb/sr in the logarithmic scale. The error bar denotes the squared sum of the statistical, the fitting, and the systematic uncertainties.

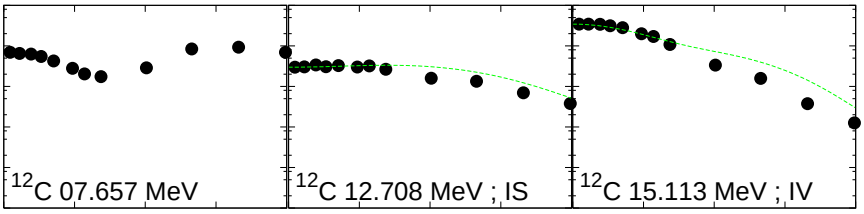

Figure C.1: Angular distributions of inelastic scattering cross section for ^{12}C. The horizontal axis is the scattering angles in the range of $0-20°$ in center of mass frame, while the vertical axis is the cross section in the range of $10^{-4} - 10^{1}$ mb/sr in log-scale.

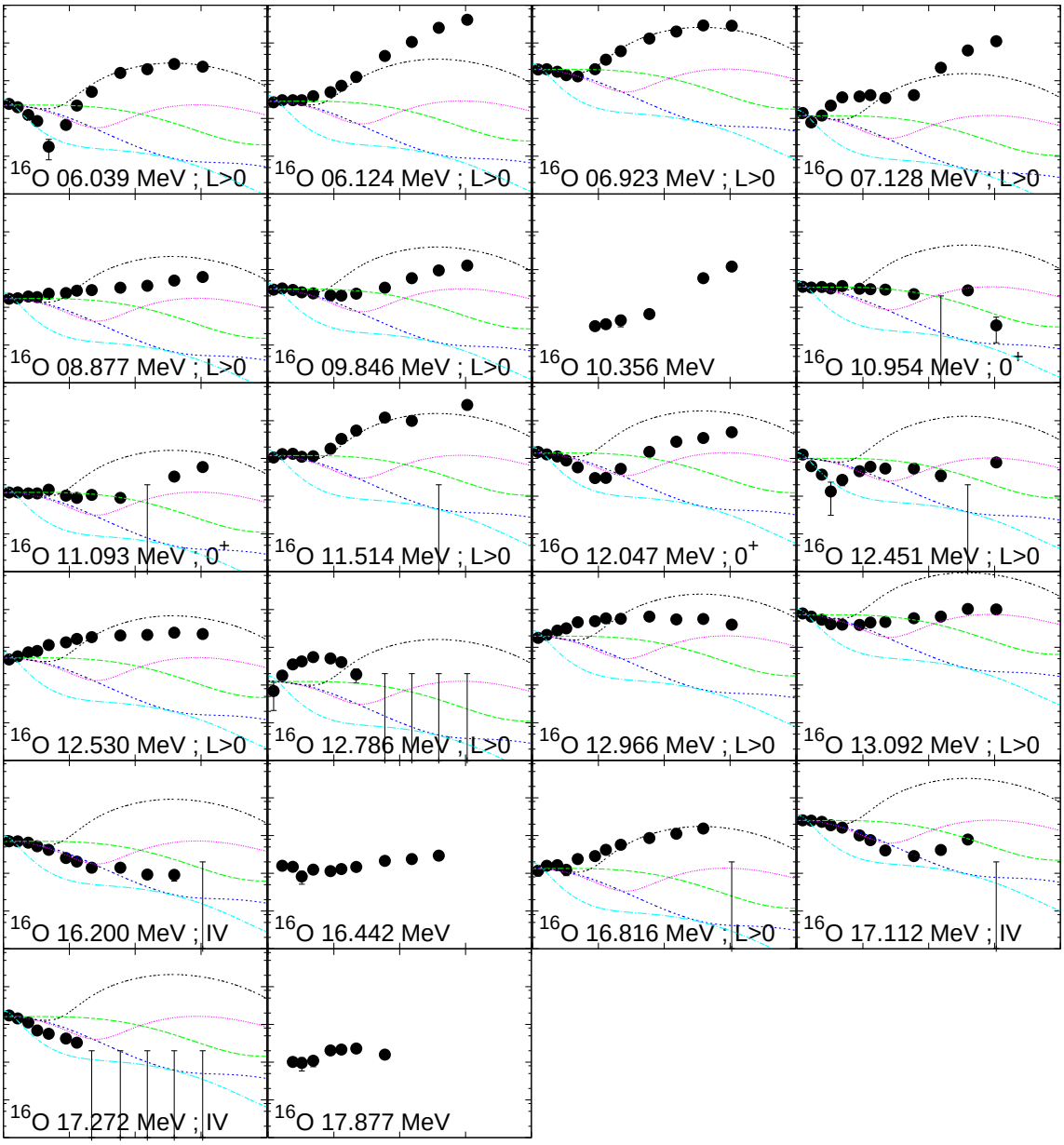

Figure C.2: Same as Fig. C.1, but for ^{16}O. See the text for the axes.

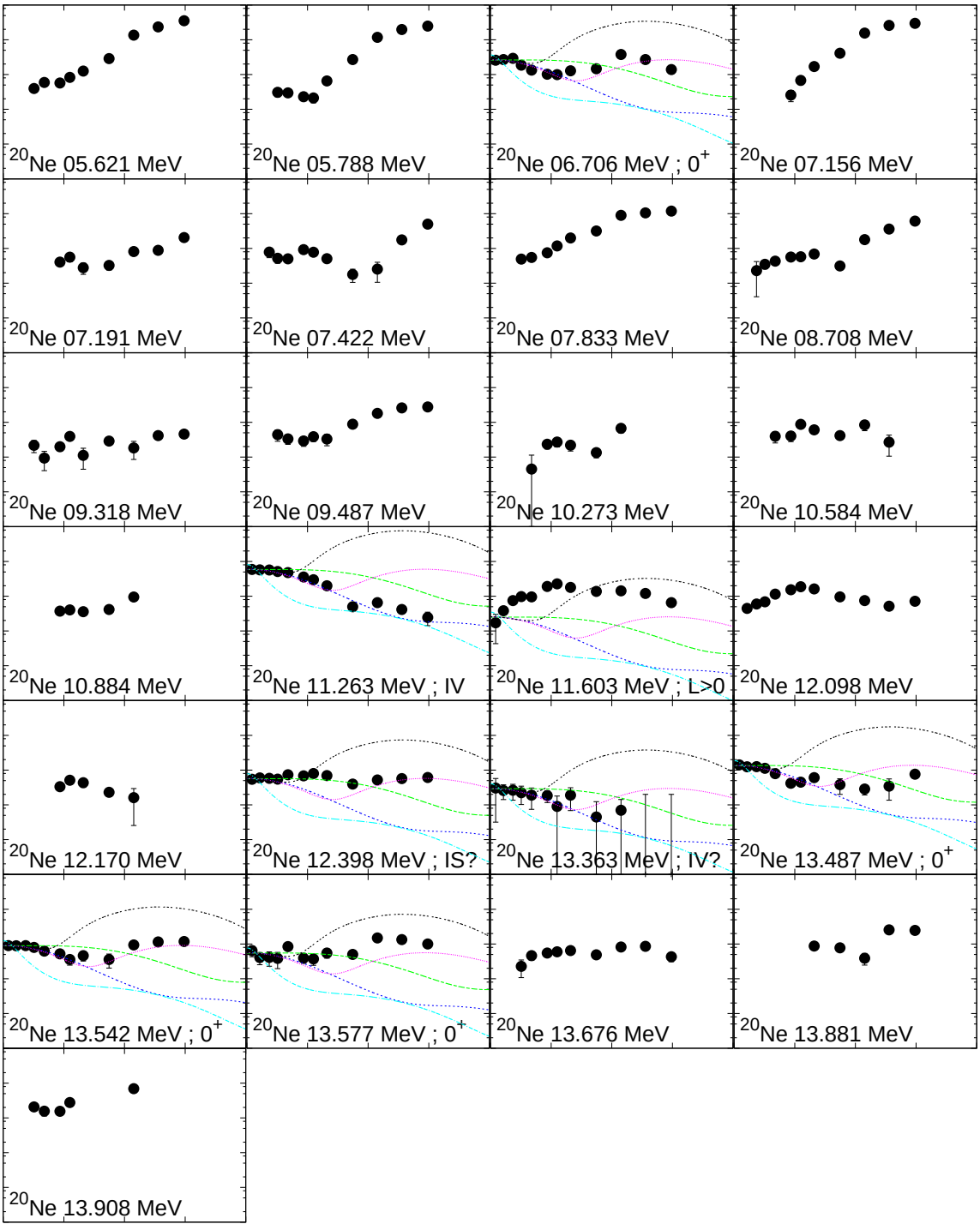

Figure C.3: Same as Fig. C.1, but for ^{20}Ne. See the text for the axes.

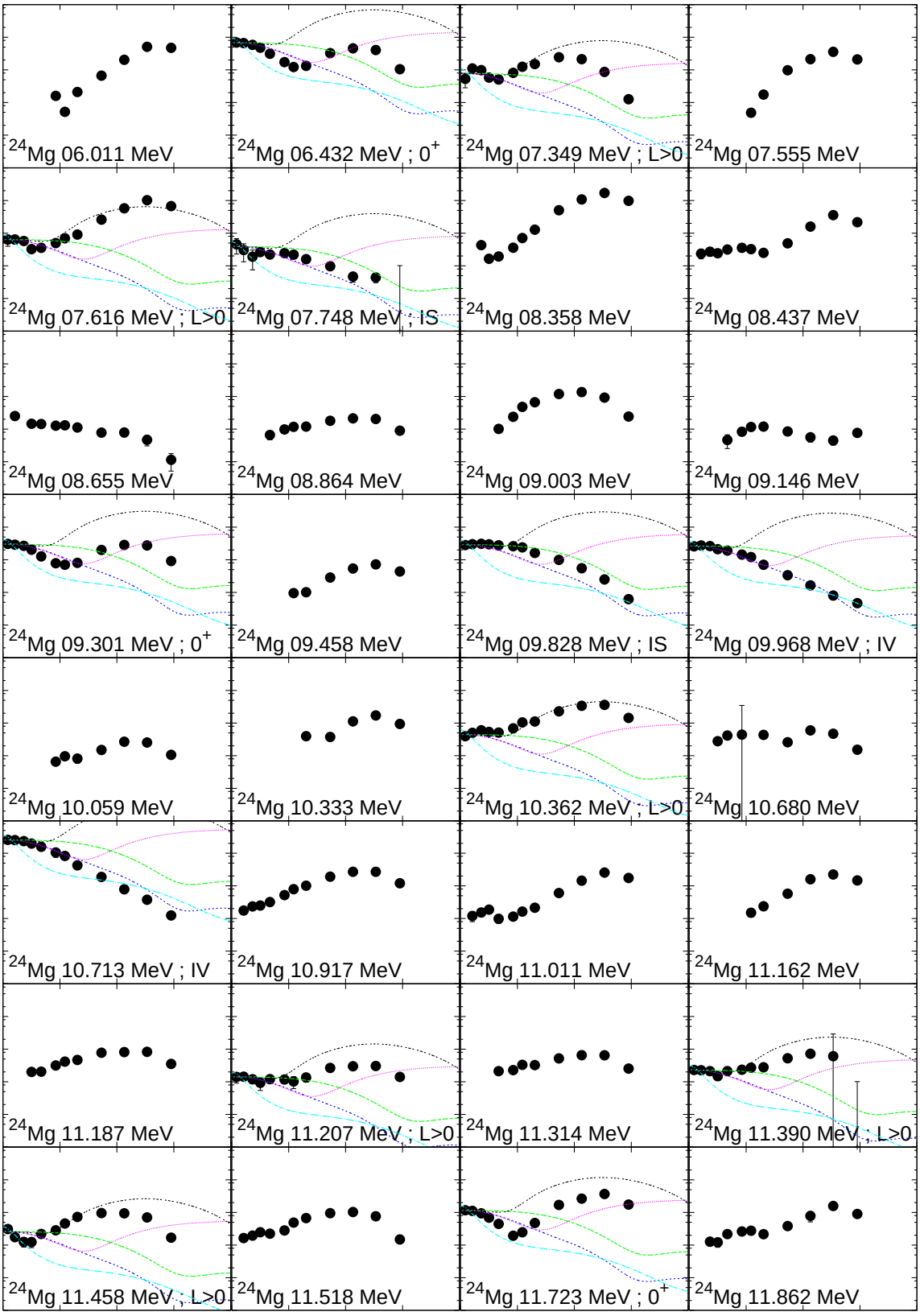

Figure C.4: Same as Fig. C.1, but for ^{24}Mg. See the text for the axes.

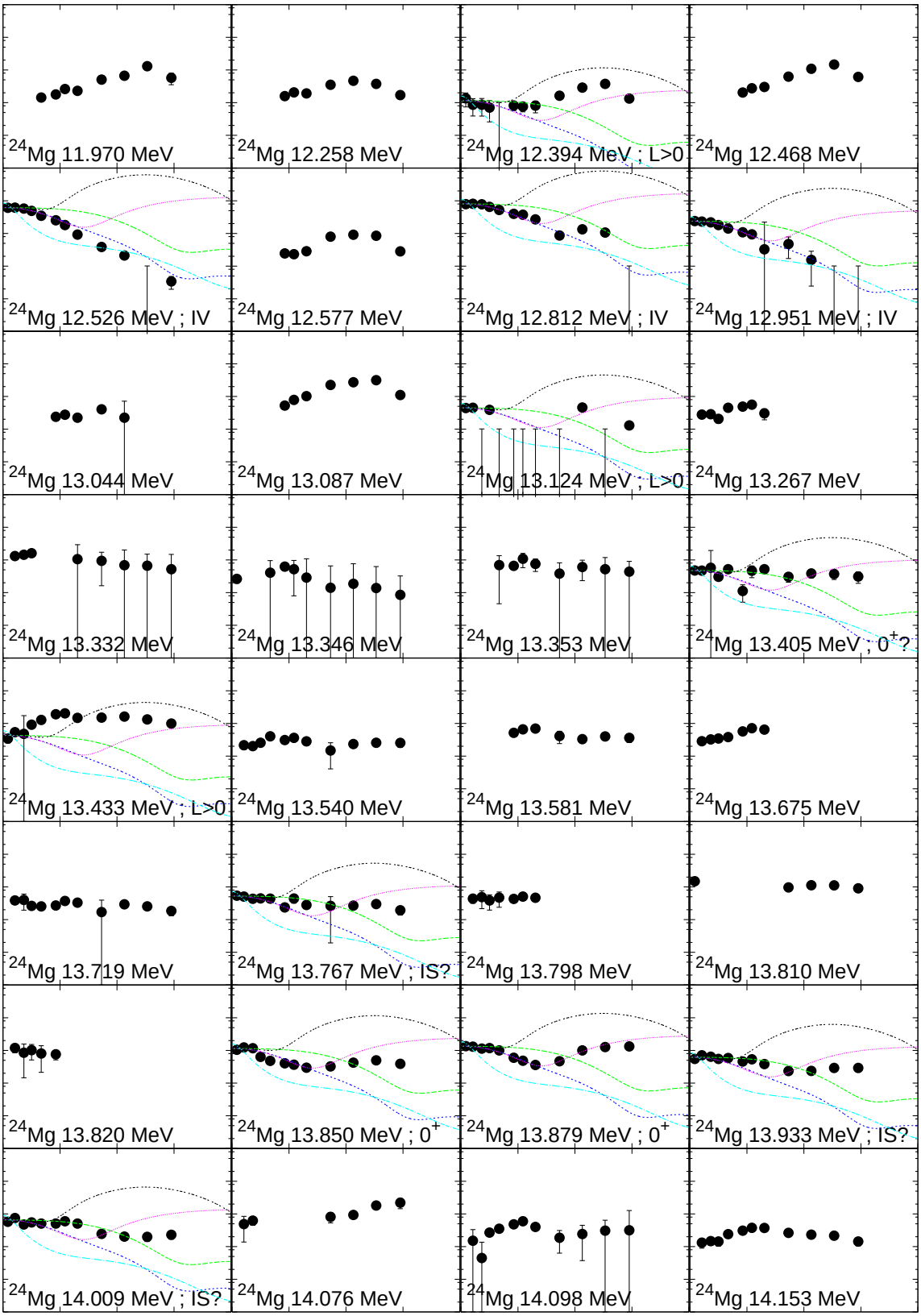

Figure C.5: Same as Fig. C.4 (continue).

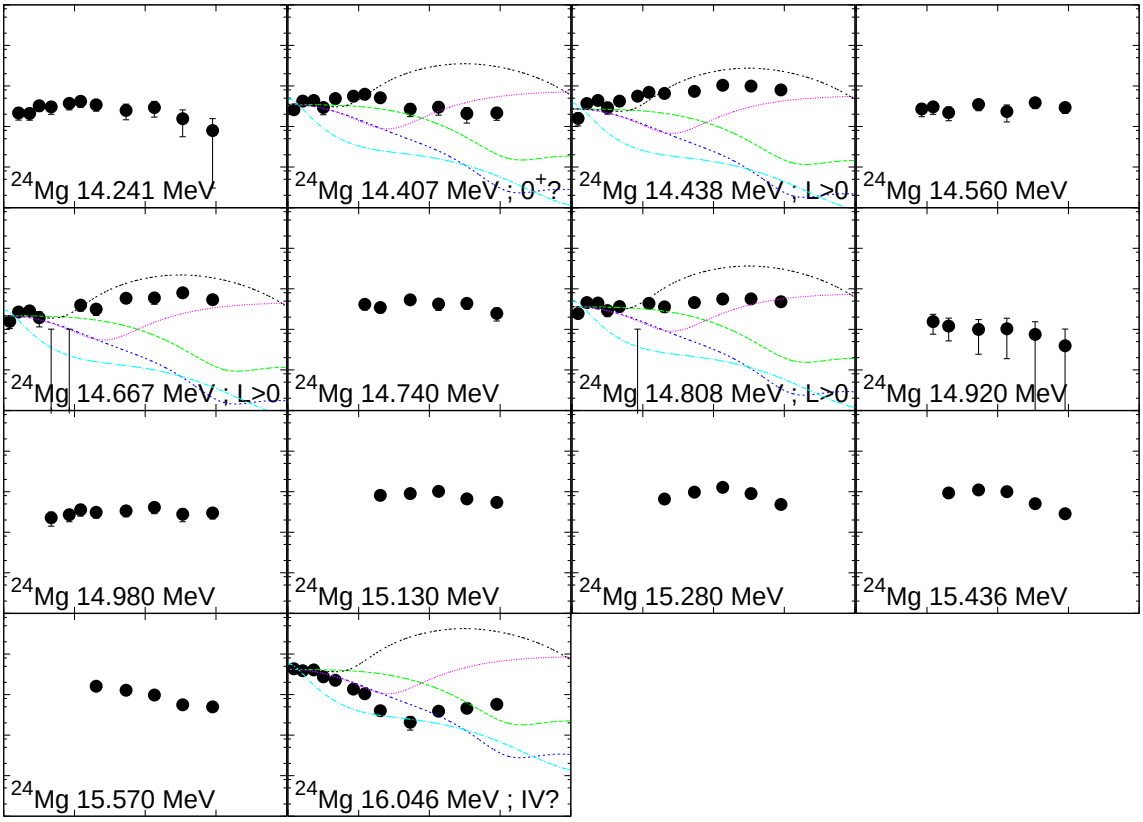

Figure C.6: Same as Fig. C.5 (continue).

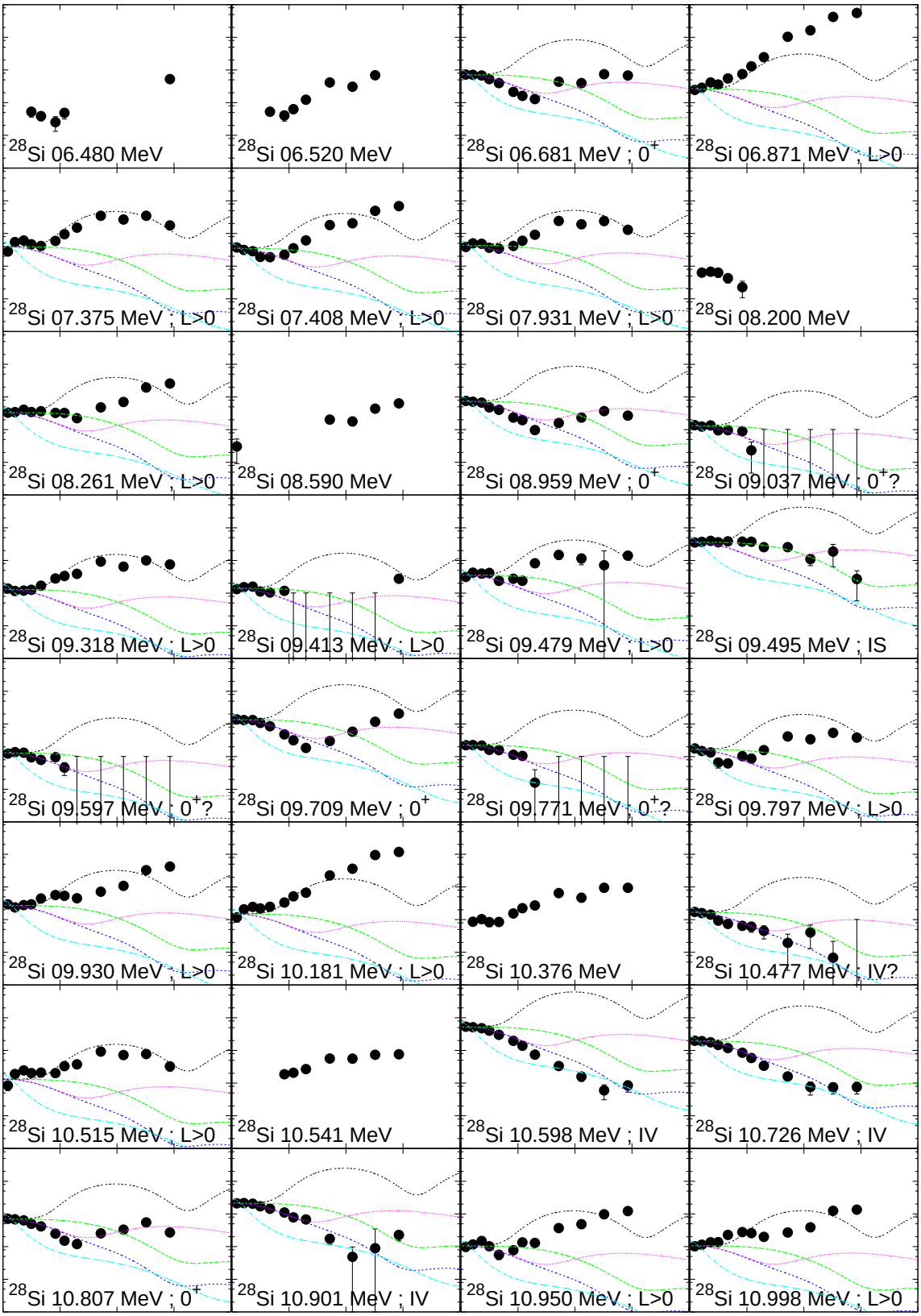

Figure C.7: Same as Fig. C.1, but for ^{28}Si. See the text for the axes.

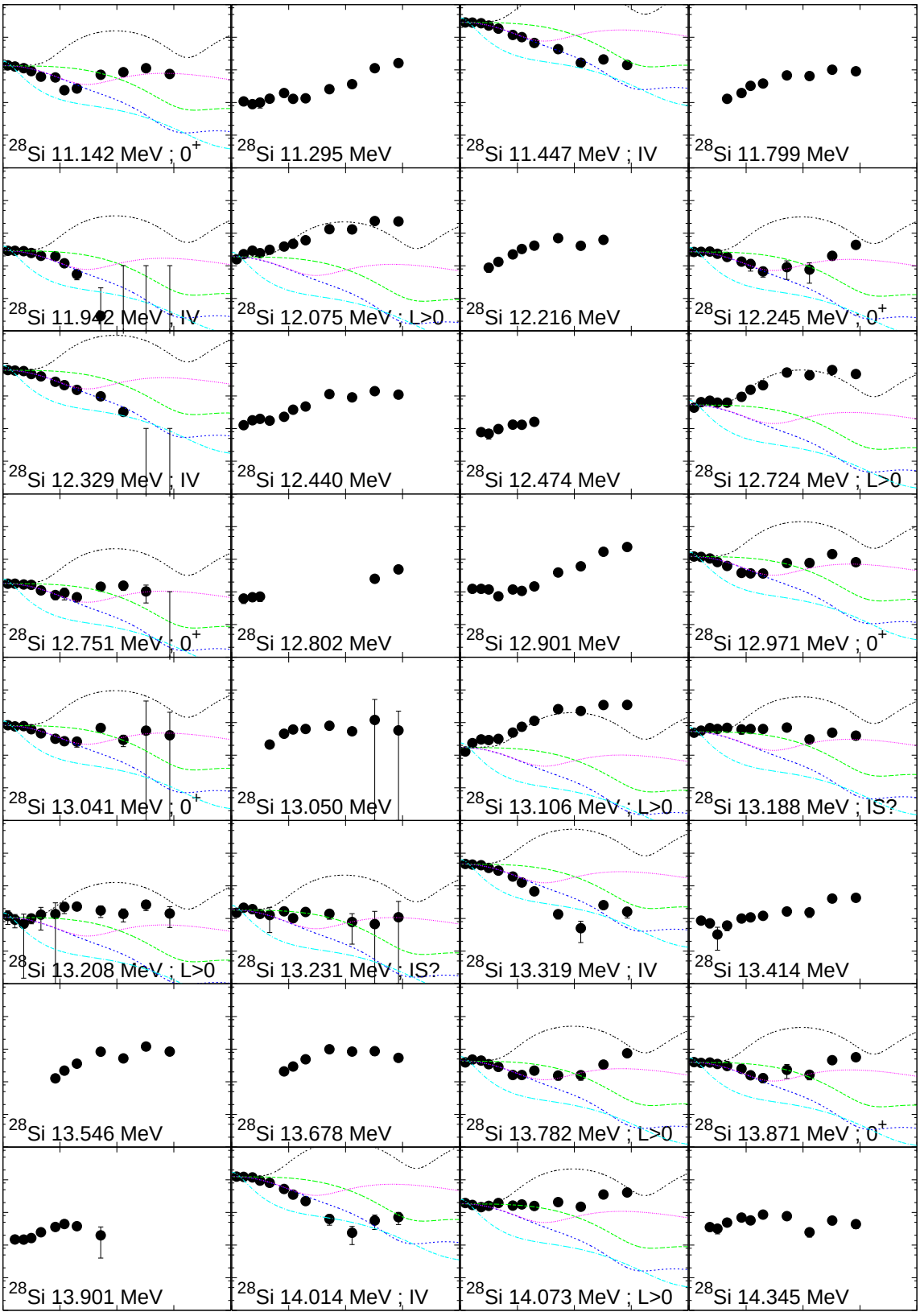

Figure C.8: Same as Fig. C.7 (continue).

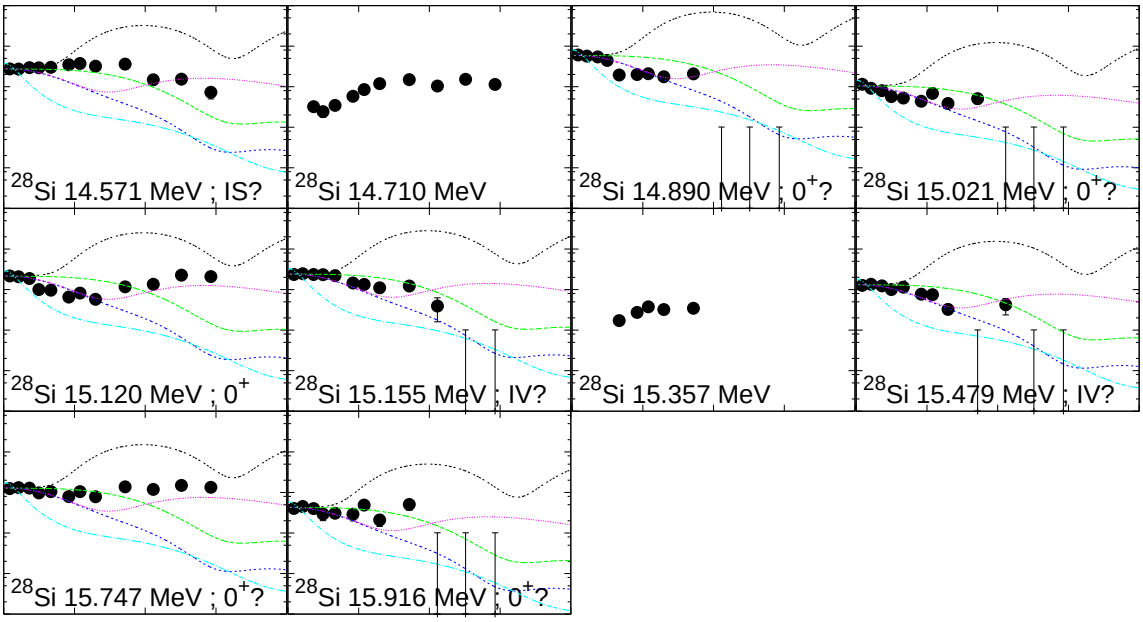

Figure C.9: Same as Fig. C.8 (continue).

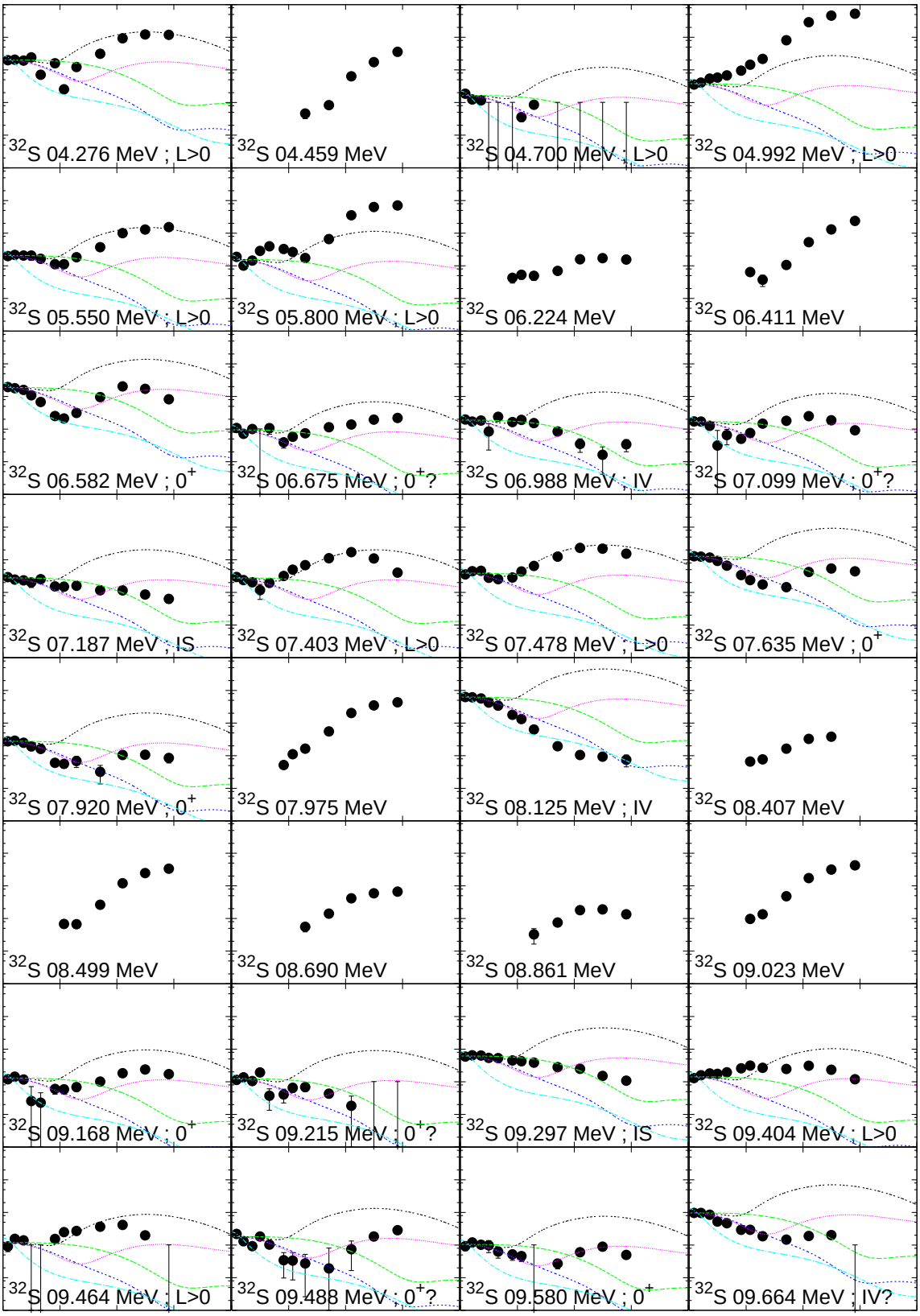

Figure C.10: Same as Fig. C.1, but for ^{32}S. See the text for the axes.

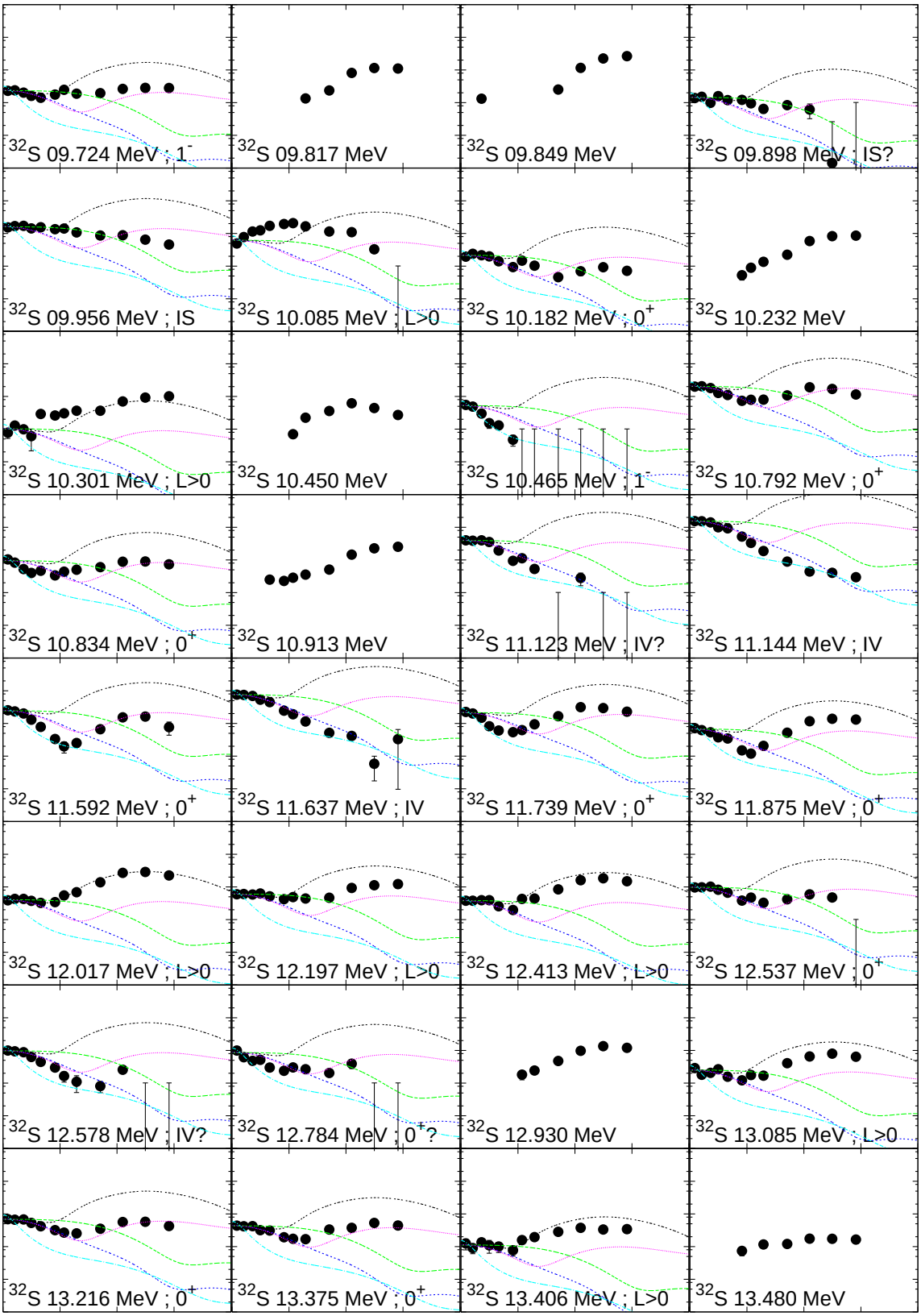

Figure C.11: Same as Fig. C.10 (continue).

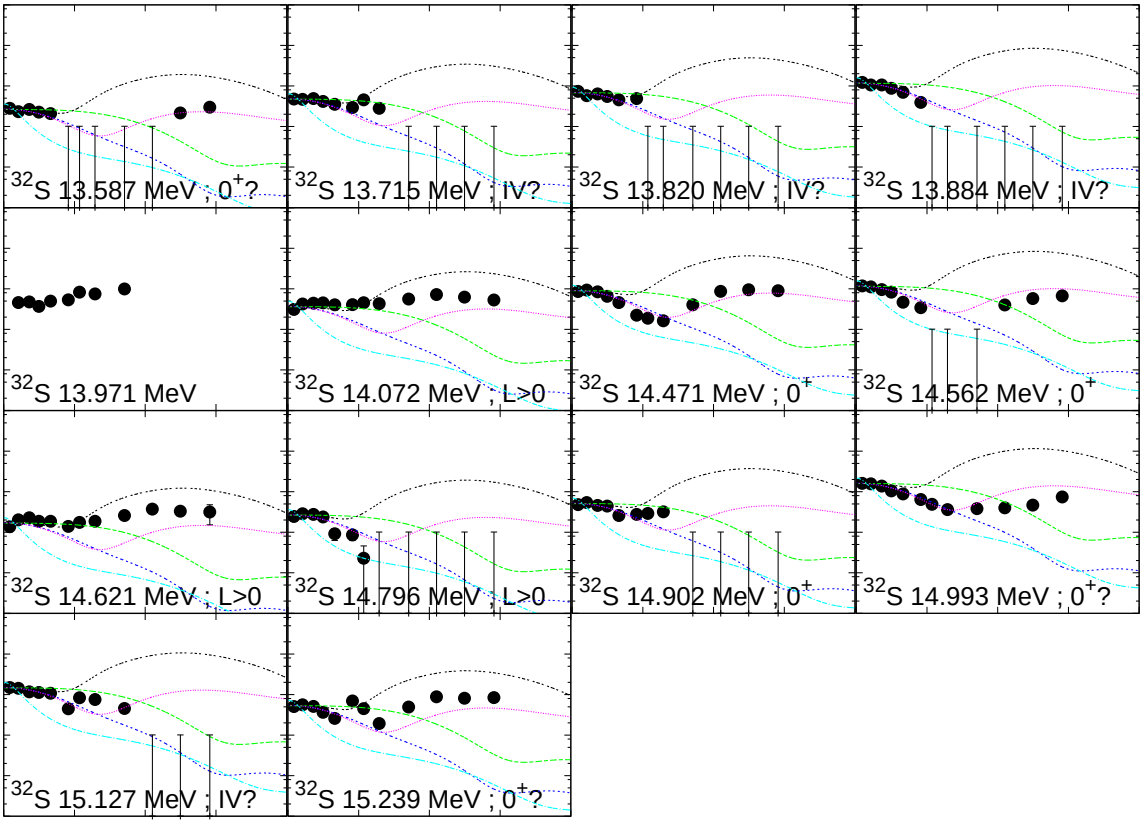

Figure C.12: Same as Fig. C.11 (continue).

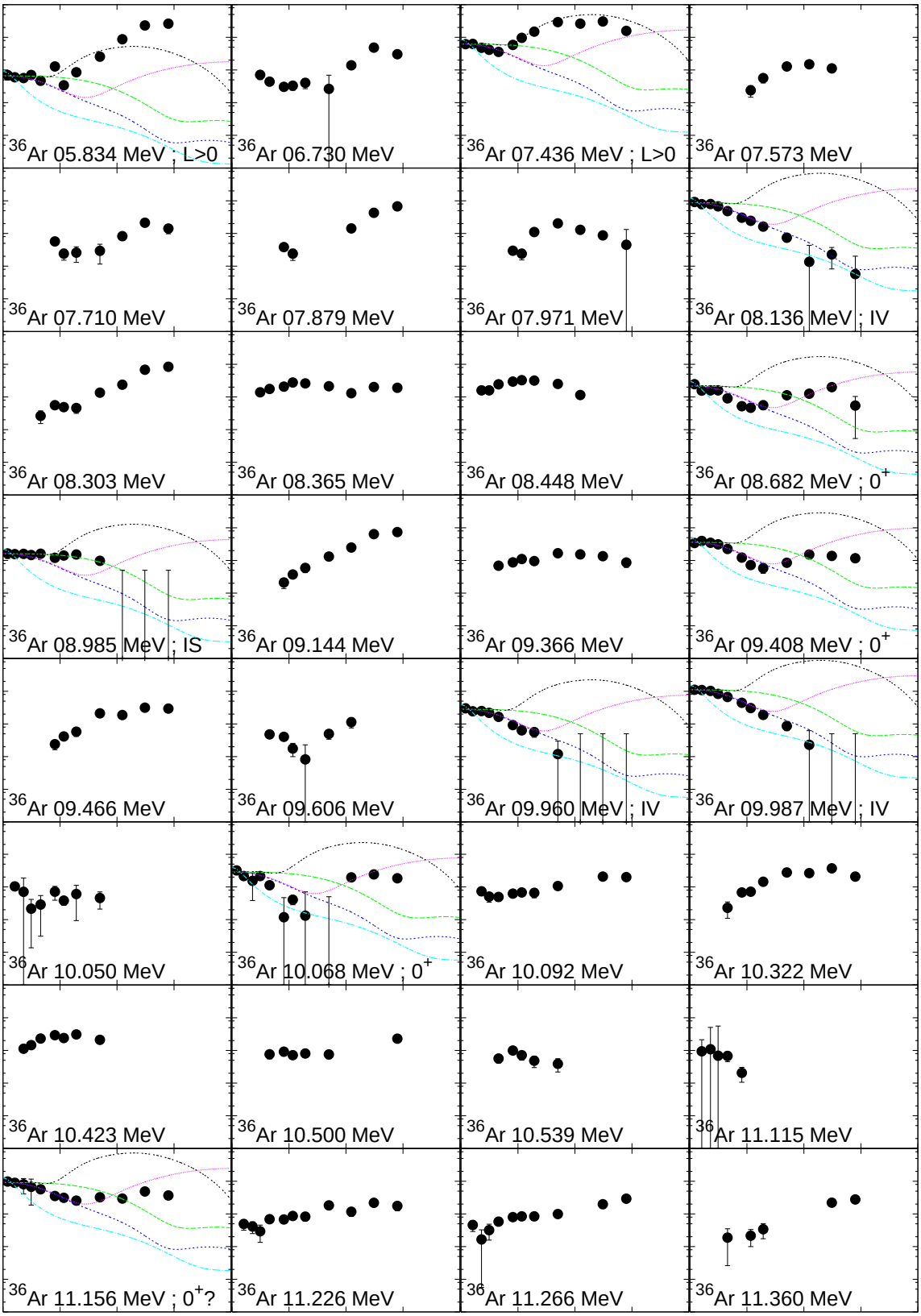

Figure C.13: Same as Fig. C.1, but for ^{36}Ar. See the text for the axes.

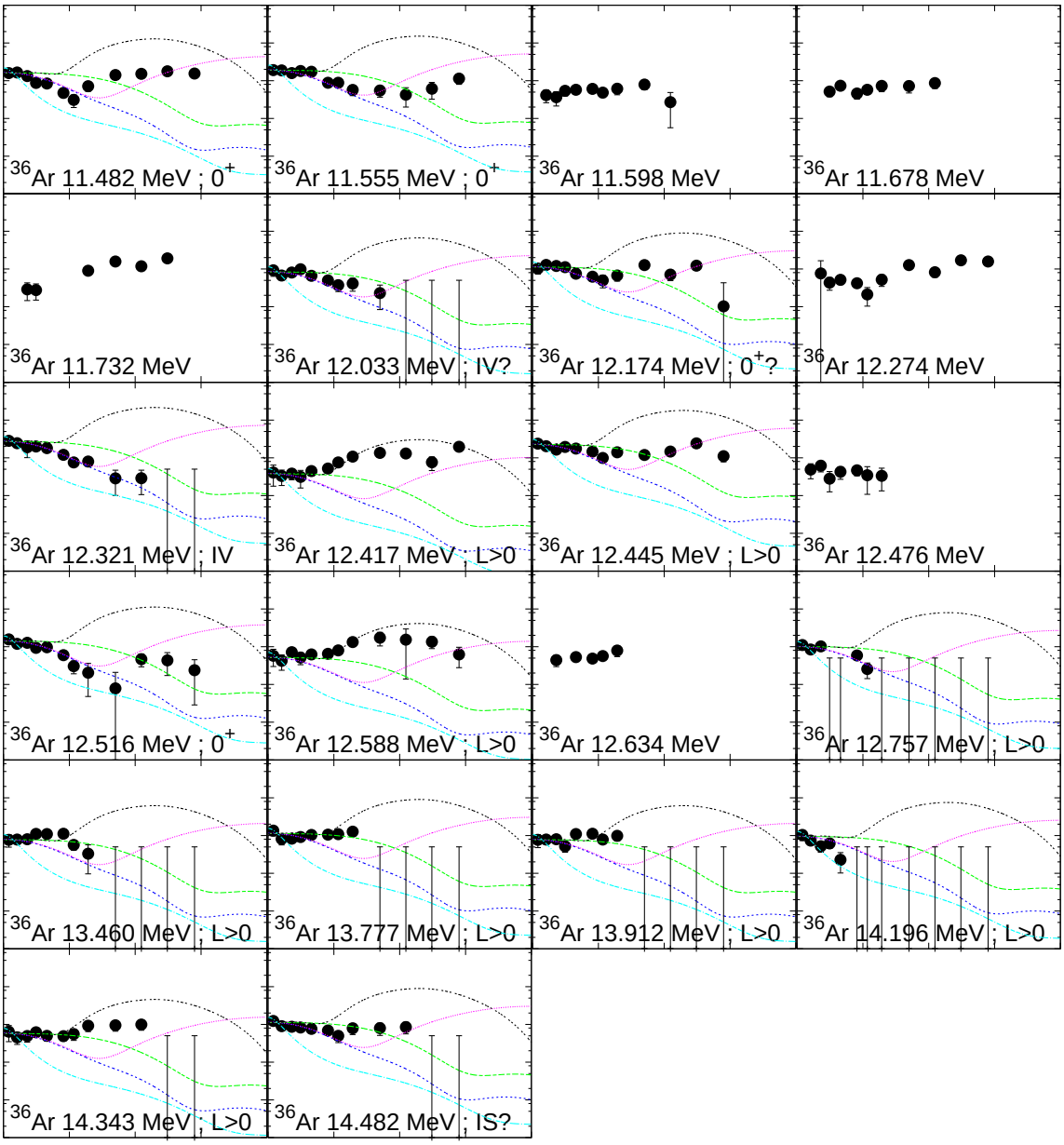

Figure C.14: Same as Fig. C.13 (continue).

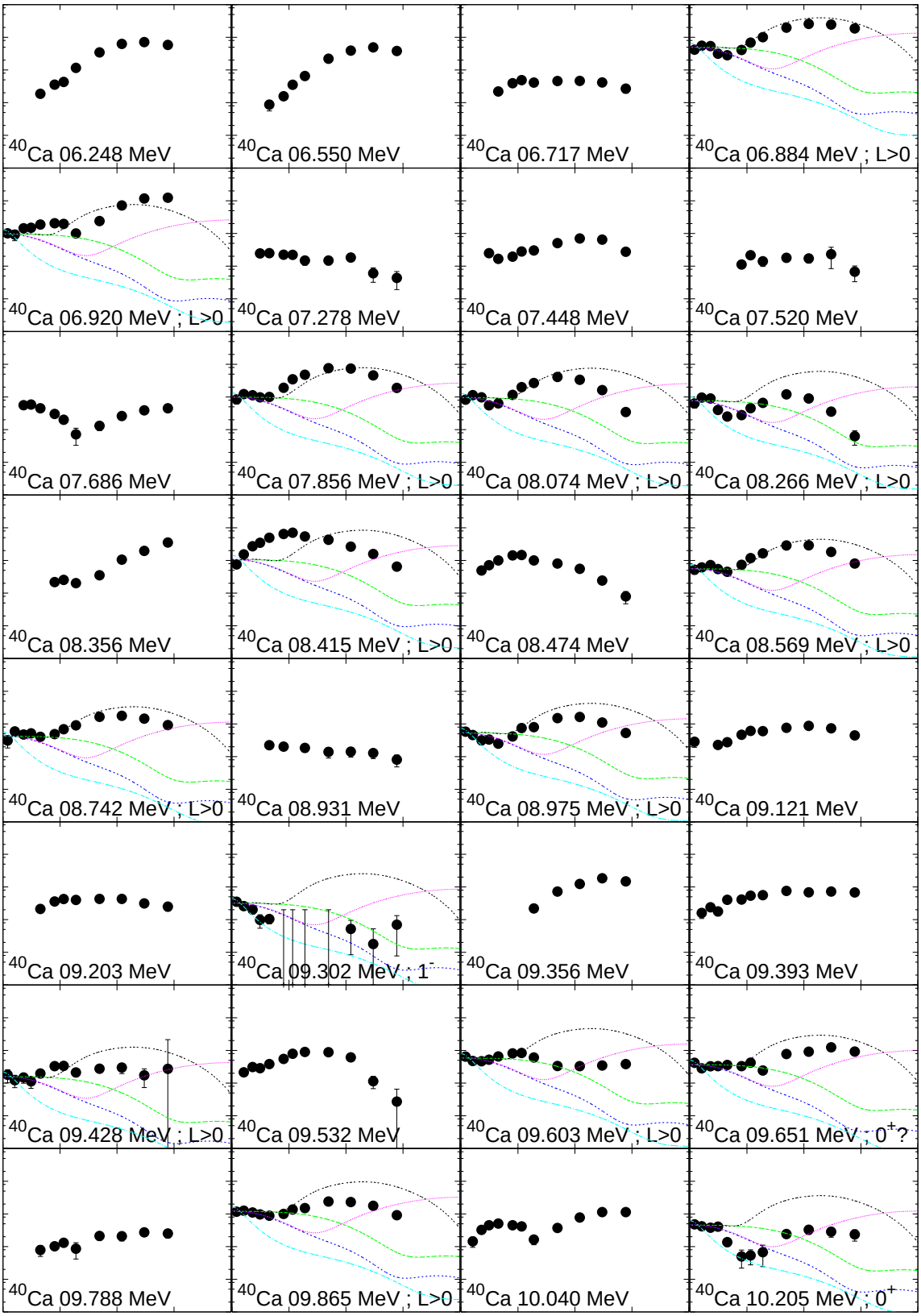

Figure C.15: Same as Fig. C.1, but for ^{40}Ca. See the text for the axes.

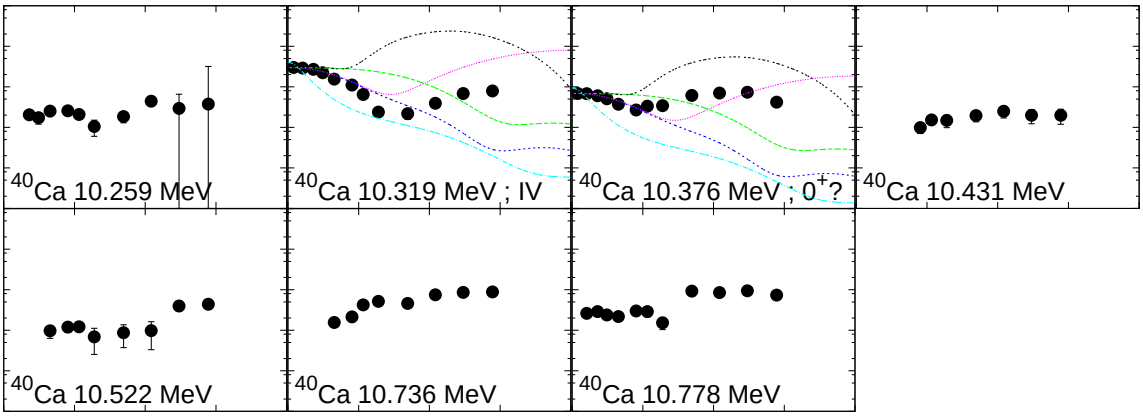

Figure C.16: Same as Fig. C.15 (continue).

Appendix D

Data table of elastics scattering

Observed cross sections and analyzing powers of elastic scattering at $E_p = 295$ MeV are summarized in the following.

Table D.1: Proton elastic scattering cross sections and analyzing powers on ^{12}C at $E_p = 295$ MeV.

θ_{cm} (degree)	dσ/dΩ (mb/sr)	A$_y$
6.65	424.408 ± 6.100	0.499 ± 0.010
9.97	239.140 ± 3.409	0.659 ± 0.008
13.29	110.960 ± 1.595	0.748 ± 0.007
16.60	41.305 ± 0.603	0.685 ± 0.008
19.91	11.406 ± 0.179	0.362 ± 0.010
23.22	2.053 ± 0.032	-0.392 ± 0.010
26.51	0.534 ± 0.009	-0.249 ± 0.011
29.80	0.614 ± 0.012	0.906 ± 0.008
33.09	0.652 ± 0.012	0.798 ± 0.008
36.36	0.455 ± 0.008	0.561 ± 0.010
39.62	0.239 ± 0.004	0.284 ± 0.012

Table D.2: Same as Table D.1, but for ^{20}Ne.

θ_{cm} (degree)	dσ/dΩ (mb/sr)	A$_y$
9.59	239.740 ± 11.084	0.651 ± 0.043
12.78	85.605 ± 4.037	0.736 ± 0.041
15.97	18.834 ± 0.932	0.412 ± 0.048
19.16	2.452 ± 0.162	-0.525 ± 0.061
22.34	1.343 ± 0.097	0.573 ± 0.067
25.52	1.106 ± 0.098	0.846 ± 0.074
28.70	0.492 ± 0.058	0.751 ± 0.104
31.87	0.170 ± 0.022	0.281 ± 0.128

Table D.3: Same as Table D.1, but for ^{24}Mg.

θ_{cm} (degree)	dσ/dΩ (mb/sr)	A_y
6.33	984.963 ± 14.044	0.483 ± 0.012
9.49	407.426 ± 5.853	0.753 ± 0.013
12.65	96.908 ± 1.415	0.665 ± 0.011
15.81	14.132 ± 0.205	0.243 ± 0.013
18.97	2.273 ± 0.038	-0.131 ± 0.015
22.12	3.242 ± 0.050	0.926 ± 0.010
25.27	2.401 ± 0.041	0.836 ± 0.012
28.42	0.914 ± 0.018	0.477 ± 0.016
31.56	0.170 ± 0.005	-0.301 ± 0.025
34.70	0.033 ± 0.002	-0.382 ± 0.051

Table D.4: Same as Table D.1, but for ^{28}Si.

θ_{cm} (degree)	dσ/dΩ (mb/sr)	A_y
6.28	1518.251 ± 22.316	0.438 ± 0.009
9.42	574.082 ± 8.697	0.628 ± 0.009
12.56	131.245 ± 2.362	0.655 ± 0.010
15.69	13.480 ± 0.255	-0.015 ± 0.013
18.83	4.592 ± 0.071	0.416 ± 0.010
21.96	6.213 ± 0.077	0.953 ± 0.005
25.09	3.674 ± 0.045	0.708 ± 0.006
28.22	1.090 ± 0.017	0.161 ± 0.011
31.34	0.168 ± 0.003	-0.747 ± 0.009
34.46	0.115 ± 0.002	0.594 ± 0.010
37.58	0.121 ± 0.003	0.788 ± 0.010

Table D.5: Same as Table D.1, but for ^{32}S.

θ_{cm} (degree)	dσ/dΩ (mb/sr)	A_y
6.25	1787.256 ± 44.971	0.438 ± 0.020
9.37	504.827 ± 12.694	0.626 ± 0.019
12.49	100.851 ± 2.564	0.610 ± 0.020
15.61	7.737 ± 0.203	-0.371 ± 0.021
18.73	7.110 ± 0.191	0.818 ± 0.019
21.84	6.879 ± 0.085	0.938 ± 0.008
24.96	2.769 ± 0.039	0.554 ± 0.011
28.07	0.466 ± 0.011	-0.342 ± 0.019
31.18	0.147 ± 0.005	0.222 ± 0.027
34.28	0.197 ± 0.006	0.903 ± 0.021

Table D.6: Same as Table D.1, but for ^{36}Ar.

θ_{cm} (degree)	dσ/dΩ (mb/sr)	A_y
9.33	578.319 ± 26.797	0.632 ± 0.039
12.44	75.157 ± 3.567	0.572 ± 0.042
15.54	5.815 ± 0.355	-0.538 ± 0.052
18.65	11.310 ± 0.591	0.936 ± 0.038
21.75	6.395 ± 0.366	0.843 ± 0.044
24.85	1.351 ± 0.107	0.116 ± 0.078
27.95	0.237 ± 0.044	-0.806 ± 0.154

Appendix E

Data table of differential cross sections at 0° and $B(M1)_\sigma$ and $B(M1)_{\sigma\tau}$ values

The excitation energies, differential cross sections at 0.40° in laboratory flame for the 0^+ and 1^+ transitions measured at $E_p = 295$ MeV are tabulated in the followings. The $B(M1)_\sigma$ and $B(M1)_{\sigma\tau}$ values in the IS and IV spin-$M1$ transitions, respectively, are also summarized. The uncertainties for excitation energy were ±10 keV in the region of 7−15 MeV. The error in the differential cross section originates from the quadric sum of the statistical, the systematic, and the fitting uncertainties. The uncertainty in the $B(M1)_{\sigma,\sigma\tau}$ values is arising from the quadric sum of the error in the cross section and that in the unit cross section. See the text in Sec. 6.6 for the details of the error.

For the comparison, the previous $B(M1)_\sigma$ and $B(M1)_{\sigma\tau}$ values from (p,p') experiments [12,83,84] are written in the tables of ^{16}O, ^{20}Ne, ^{24}Mg, ^{28}Si, ^{32}S. The $B(M1)$ values from (e,e') experiments [81,82,85,86] are shown in the tables of ^{12}C, ^{36}Ar, ^{40}Ca since the previous $B(M1)_\sigma$ and $B(M1)_{\sigma\tau}$ values were not found in the literature.

Table E.1: The excitation energies, cross sections at 0.40° in laboratory frame, and the $B(M1)_\sigma$ and $B(M1)_{\sigma\tau}$values assigned as IS and IV states, respectively, in ^{12}C.

Present (p,p')				$(e,e')^a$	
E_x (MeV)	J^π, T	$d\sigma/d\Omega_{\ 0.40^\circ}$ (mb/sr)	$B(M1)_{\sigma,\sigma\tau}$ ($\mu_N{}^2$)	E_x (MeV)	$B(M1)^b$ ($\mu_N{}^2$)
7.657	0^+	0.690 ± 0.026			
12.708	1^+IS	0.298 ± 0.016	0.147 ± 0.039	12.71	0.04 ± 0.00
15.113	1^+IV	3.429 ± 0.076	2.523 ± 0.552	15.11	2.63 ± 0.08

[a]From Ref. [81].

[b]The values are taken from Ref. [82].

Table E.2: Same as Table E.1, but for ^{16}O.

Present (p,p')				Previous $(p,p')^a$	
E_x (MeV)	J^π, T	$\mathrm{d}\sigma/\mathrm{d}\Omega$ $_{0.40^\circ}$ (mb/sr)	$B(M1)_{\sigma,\sigma\tau}$ ($\mu_N{}^2$)	E_x (MeV)	$B(M1)_{\sigma,\sigma\tau}$ ($\mu_N{}^2$)
10.954	0^+	0.035 ± 0.003			
11.093	0^+	0.013 ± 0.002			
12.047	0^+	0.148 ± 0.011			
				14.00	0.54 ± 0.04^b
16.200	1^+IV	0.070 ± 0.006	0.058 ± 0.014	16.22	0.08 ± 0.01
17.112	1^+IV	0.253 ± 0.019	0.208 ± 0.050	17.14	0.30 ± 0.03
17.272	1^+IV	0.173 ± 0.014	0.132 ± 0.032		
				18.77	0.17 ± 0.02^b

[a]From Ref. [83].

[b]Assigned as the IV 1^+ transition in Ref. [83].

Table E.3: Same as Table E.1, but for ^{20}Ne.

Present (p,p')				Previous $(p,p')^a$	
E_x (MeV)	J^π, T	$\mathrm{d}\sigma/\mathrm{d}\Omega$ $_{0.40^\circ}$ (mb/sr)	$B(M1)_{\sigma,\sigma\tau}$ ($\mu_N{}^2$)	E_x (MeV)	$B(M1)_{\sigma,\sigma\tau}$ ($\mu_N{}^2$)
6.706	0^+	0.258 ± 0.047			
11.263	1^+IV	0.592 ± 0.027	0.488 ± 0.117	11.25	0.49 ± 0.06
12.398	(1^+IS)	0.054 ± 0.013	0.018 ± 0.007^b		
13.363	(1^+IV)	0.030 ± 0.027	0.024 ± 0.022		
13.487	0^+	0.142 ± 0.019		13.51	0.25 ± 0.03
13.542	0^+	0.090 ± 0.017			
13.577	0^+	0.065 ± 0.022			
				15.72	0.14 ± 0.02^c

[a]From Ref. [84].

[b]Assumed as a mixed state with 0^+ (Sec. 6.3.4).

[c]Assigned as the IV 1^+ transition in Ref. [84].

Table E.4: Same as Table E.1, but for ^{24}Mg.

Present (p,p')				Previous $(p,p')^a$	
E_x (MeV)	J^π, T	$\mathrm{d}\sigma/\mathrm{d}\Omega$ $_{0.40^\circ}$ (mb/sr)	$B(M1)_{\sigma,\sigma\tau}$ ($\mu_N{}^2$)	E_x (MeV)	$B(M1)_{\sigma,\sigma\tau}$ ($\mu_N{}^2$)
6.432	0^+	0.688 ± 0.023			
7.748	1^+IS[b]	0.045 ± 0.023	0.023 ± 0.013	7.75	0.02 ± 0.01
9.301	0^+	0.306 ± 0.013			
9.828	1^+IS	0.282 ± 0.012	0.180 ± 0.051	9.83	0.29 ± 0.02
9.968	1^+IV	0.258 ± 0.011	0.238 ± 0.059	9.97	0.38 ± 0.03
10.713	1^+IV	2.558 ± 0.048	2.266 ± 0.549	10.72	2.75 ± 0.20
11.723	0^+	0.117 ± 0.010			
12.526	1^+IV	0.612 ± 0.020	0.559 ± 0.136	12.53	0.60 ± 0.03
12.812	1^+IV	0.794 ± 0.022	0.732 ± 0.178	12.82	0.85 ± 0.03
12.951	1^+IV	0.238 ± 0.012	0.215 ± 0.053	12.96	0.37 ± 0.02
13.405	(0^+)	0.048 ± 0.010			
13.767	$(1^+$IS)	0.054 ± 0.008	0.017 ± 0.006[c]		
13.850	0^+	0.105 ± 0.009			
13.879	0^+	0.135 ± 0.010		13.90	0.56 ± 0.09[d]
13.933	$(1^+$IS)	0.055 ± 0.008	0.021 ± 0.007[c]		
14.009	$(1^+$IS)	0.058 ± 0.009	0.023 ± 0.008[c]		
14.407	(0^+)	0.026 ± 0.006			
				14.87	0.02 ± 0.01[e]
				15.22	0.03 ± 0.01[e]
16.046	$(1^+$IV)	0.430 ± 0.038	0.385 ± 0.099	16.12	0.31 ± 0.06

[a]From Ref. [12].

[b]Assigned as not IV but IS although the shape of the angular distribution is close to that of IV. An IV state should be at higher than $E_x = 9.52$ MeV in ^{24}Mg owing to the isospin symmetry structure [102].

[c]Assumed as a mixed state with 0^+ (Sec. 6.3.4).

[d]Assigned as the IV 1^+ transition in Ref. [12].

[e]Assigned as the IS 1^+ transition in Ref. [12].

Table E.5: Same as Table E.1, but for ^{28}Si.

Present (p, p')				Previous $(p, p')^a$	
E_x (MeV)	J^π, T	$d\sigma/d\Omega$ $_{0.40^\circ}$ (mb/sr)	$B(M1)_{\sigma,\sigma\tau}$ ($\mu_N{}^2$)	E_x (MeV)	$B(M1)_{\sigma,\sigma\tau}$ ($\mu_N{}^2$)
6.681	0^+	0.072 ± 0.004			
8.959	0^+	0.075 ± 0.004			
9.037	(0^+)	0.014 ± 0.002			
9.495[b]	1^+IS	0.356 ± 0.009	0.237 ± 0.068	9.50	0.09 ± 0.01
9.597	(0^+)	0.012 ± 0.002			
9.709	0^+	0.138 ± 0.005		9.72	0.39 ± 0.06
9.771	(0^+)	0.022 ± 0.003			
10.477	$(1^+$IV)	0.017 ± 0.003	0.016 ± 0.005		
10.598	1^+IV	0.531 ± 0.012	0.493 ± 0.123	10.59	0.83 ± 0.12
10.726	1^+IV	0.198 ± 0.007	0.184 ± 0.046	10.73	0.32 ± 0.04
10.807	0^+	0.071 ± 0.004		10.82	0.21 ± 0.04
10.901	1^+IV	0.212 ± 0.007	0.203 ± 0.051	10.90	0.35 ± 0.05
11.142	0^+	0.137 ± 0.007		11.16	0.31 ± 0.07
11.447	1^+IV	2.844 ± 0.044	2.706 ± 0.673	11.45	3.32 ± 0.24
11.942	1^+IV	0.029 ± 0.004	0.028 ± 0.008		
12.245	0^+	0.027 ± 0.003			
12.329	1^+IV	0.623 ± 0.013	0.588 ± 0.147	12.33	0.73 ± 0.14
12.751	0^+	0.018 ± 0.003			
12.971	0^+	0.121 ± 0.006		12.99	0.23 ± 0.05
13.041	0^+	0.083 ± 0.005			
13.188	$(1^+$IS)	0.049 ± 0.006	0.019 ± 0.006[c]	13.22	0.03 ± 0.01
13.231	$(1^+$IS)	0.015 ± 0.004	0.012 ± 0.005		
13.319	1^+IV	0.468 ± 0.011	0.447 ± 0.112	13.35	0.81 ± 0.14
13.871	0^+	0.040 ± 0.004			
14.014	1^+IV	1.247 ± 0.026	1.222 ± 0.304	14.03	1.31 ± 0.12
14.571	$(1^+$IS)	0.275 ± 0.015	0.096 ± 0.030[c]		
14.890	(0^+)	0.604 ± 0.040			
15.021	(0^+)	0.115 ± 0.011			
15.120	0^+	0.217 ± 0.024			
15.155	$(1^+$IV)	0.236 ± 0.023	0.244 ± 0.065	15.15	0.42 ± 0.04
15.479	$(1^+$IV)	0.127 ± 0.012	0.133 ± 0.035	15.50	0.12 ± 0.08
15.747	(0^+)	0.125 ± 0.011		15.80	0.22 ± 0.02
15.916	(0^+)	0.040 ± 0.010			

[a] From Ref. [12].

[b] Decomposed from the state at 9.479 MeV (2^+; 0.031(4) mb/sr at 0.40°).

[c] Assumed as a mixed state with 0^+ (Sec. 6.3.4).

Table E.6: Same as Table E.1, but for ^{32}S.

Present (p, p')				Previous $(p, p')^a$	
E_x (MeV)	J^π, T	$d\sigma/d\Omega$ $_{0.40^\circ}$ (mb/sr)	$B(M1)_{\sigma,\sigma\tau}$ ($\mu_N{}^2$)	E_x (MeV)	$B(M1)_{\sigma,\sigma\tau}$ ($\mu_N{}^2$)
6.582	0^+	0.194 ± 0.007			
6.675	(0^+)	0.011 ± 0.003			
6.988	1^+IV[b]	0.020 ± 0.003	0.018 ± 0.005	6.98	0.02 ± 0.01
7.099	(0^+)	0.017 ± 0.003			
7.187	1^+IS[b]	0.029 ± 0.003	0.018 ± 0.006	7.19	0.02 ± 0.01
7.635	0^+	0.128 ± 0.005			
7.920	0^+	0.027 ± 0.003			
8.125	1^+IV	0.627 ± 0.018	0.608 ± 0.156	8.13	1.46 ± 0.19
9.168	0^+	0.012 ± 0.003			
9.215	(0^+)	0.011 ± 0.003			
9.297	1^+IS	0.059 ± 0.004	0.043 ± 0.013	9.28	0.05 ± 0.01
9.488	(0^+)	0.022 ± 0.003			
9.580	0^+	0.009 ± 0.003			
9.664	$(1^+$IV)	0.096 ± 0.005	0.096 ± 0.025	9.66	0.17 ± 0.02
9.898	$(1^+$IS)	0.014 ± 0.003	0.010 ± 0.004		
9.956	1^+IS	0.154 ± 0.006	0.111 ± 0.033	9.93	0.10 ± 0.02
10.182	0^+	0.019 ± 0.003			
10.792	0^+	0.200 ± 0.007			
10.834	0^+	0.104 ± 0.005			
11.123[c]	$(1^+$IV)	0.400 ± 0.023	0.398 ± 0.104		
11.144[c]	1^+IV	1.550 ± 0.042	1.553 ± 0.398	11.13	4.08 ± 0.53
11.592	0^+	0.253 ± 0.012			
11.637	1^+IV	0.761 ± 0.022	0.765 ± 0.196	11.63	2.38 ± 0.35
11.739	0^+	0.225 ± 0.014			
11.875	0^+	0.071 ± 0.007		11.88	0.37 ± 0.06
12.537	0^+	0.097 ± 0.009			
12.578	$(1^+$IV)	0.099 ± 0.009	0.098 ± 0.027	12.56	0.33 ± 0.06
12.784	(0^+)	0.099 ± 0.011			

[a]From Ref. [12].

[b]Followed to the assignment in Ref. [42].

[c]In the (p, p') spectrum, the peak was decomposed to be the two states.

Table E.7: Same as Table E.1, but for ^{32}S (continued).

Present (p,p')				Previous $(p,p')^a$	
E_x (MeV)	J^π, T	$\mathrm{d}\sigma/\mathrm{d}\Omega$ $_{0.40^\circ}$ (mb/sr)	$B(M1)_{\sigma,\sigma\tau}$ ($\mu_N{}^2$)	E_x (MeV)	$B(M1)_{\sigma,\sigma\tau}$ ($\mu_N{}^2$)
13.216	0^+	0.069 ± 0.005		13.23	0.04 ± 0.01
13.375	0^+	0.044 ± 0.005			
13.587	(0^+)	0.028 ± 0.005			
13.715	$(1^+\mathrm{IV})$	0.048 ± 0.006	0.049 ± 0.014		
13.820	$(1^+\mathrm{IV})$	0.074 ± 0.010	0.068 ± 0.020	13.77	0.03 ± 0.01
13.884	$(1^+\mathrm{IV})$	0.123 ± 0.008	0.118 ± 0.031	13.90	0.24 ± 0.03
14.471	0^+	0.086 ± 0.006			
14.562	0^+	0.118 ± 0.007			
14.902	0^+	0.048 ± 0.006		14.88	0.20 ± 0.04
14.993	(0^+)	0.160 ± 0.009		15.04	0.04 ± 0.01
15.127	$(1^+\mathrm{IV})$	0.149 ± 0.009	0.155 ± 0.040		
15.239	(0^+)	0.051 ± 0.005			
				15.58	0.28 ± 0.05[b]
				15.70	0.16 ± 0.04[b]
				15.84	0.26 ± 0.06[b]

[a] From Ref. [12].

[b] Assigned as the IV 1^+ transition in Ref. [12].

Table E.8: Same as Table E.1, but for ^{36}Ar.

Present (p,p')				$(e,e')^a$	
E_x (MeV)	J^π, T	$d\sigma/d\Omega$ $_{0.40^\circ}$ (mb/sr)	$B(M1)_{\sigma,\sigma\tau}$ ($\mu_N{}^2$)	E_x (MeV)	$B(M1)$ ($\mu_N{}^2$)
				7.440	0.13 ± 0.02^e
8.136	1^+IV	0.917 ± 0.086	0.864 ± 0.239	8.158	0.21 ± 0.06
				8.482	0.12 ± 0.03^e
8.682	0^+	0.247 ± 0.059			
8.985[b]	1^+IS	0.163 ± 0.049	0.114 ± 0.048		
9.408	0^+	0.341 ± 0.051			
9.960[c]	1^+IV	0.301 ± 0.045	0.281 ± 0.084		
9.987[c]	1^+IV	1.116 ± 0.063	1.158 ± 0.308	9.995	0.53 ± 0.06
10.068	0^+	0.321 ± 0.044			
				10.276	0.12 ± 0.03^e
				10.615	0.12 ± 0.05^e
				10.719	0.14 ± 0.03^e
				10.764	0.12 ± 0.03^e
11.156	(0^+)	0.979 ± 0.053		11.177	0.45 ± 0.05
				11.384	0.11 ± 0.02^e
11.482	0^+	0.158 ± 0.030			
11.555	0^+	0.191 ± 0.031			
12.033	$(1^+$IV)	0.093 ± 0.029	0.084 ± 0.034	12.066	0.16 ± 0.03
12.174	(0^+)	0.103 ± 0.029			
12.321	1^+IV	0.283 ± 0.034	0.281 ± 0.080		
12.516	0^+	0.156 ± 0.032			
				12.801	0.29 ± 0.08^e
				13.201	0.17 ± 0.08^e
				13.481	0.13 ± 0.03^e
				13.740	0.12 ± 0.04^e
				13.800	0.17 ± 0.03^e
14.482	$(1^+$IS)	0.124 ± 0.031	0.040 ± 0.016^d		

[a] From Ref. [85].

[b] The isoscalar 1^+ transition that was found in ^{36}Ar for the first time.

[c] In the (p,p') spectrum, the peak was decomposed to be the two states.

[d] Assumed as a mixed state with 0^+ (Sec. 6.3.4).

[e] Assigned as the $\Delta L \geq 1$ transition in the present work.

Table E.9: Same as Table E.1, but for ^{40}Ca.

Present (p, p')				$(e, e')^a$	
E_x (MeV)	J^π, T	$d\sigma/d\Omega$ $_{0.40^\circ}$ (mb/sr)	$B(M1)_{\sigma,\sigma\tau}$ ($\mu_N{}^2$)	E_x (MeV)	$B(M1)$ ($\mu_N{}^2$)
9.651	(0^+)	0.042 ± 0.008			
10.205	0^+	0.048 ± 0.007			
10.319	1^+IV	0.300 ± 0.012	0.325 ± 0.087	10.32	1.12 ± 0.27
10.376	(0^+)	0.069 ± 0.008			

[a]From Ref. [86].

Appendix F

Stability of analyzer target for the BLP

Several experiments using polarized beams have been performed at the RCNP. The polarizations of the beams have been measured by using the beam line polarimeter BLP which measures the asymmetry of the $p + p$ scattering. In the BLP, two pairs of plastic scintillation counters are used to detect elastically scattered protons and the recoil protons from the analyzer target in coincidence. The analyzing power of the scattering on the analyzer target used for the BLP should be known with enough accuracy to deduce the polarization of the beam. Since the analyzing power of a polyethylene (CH_2) sheet in the region of intermediate energies have been reported in Ref. [27], CH_2 sheets have been usually used for the analyzer target.

We studied the performance of CH_2 and aramid ($C_{14}O_2N_2H_3$, made by Asahi-kase CO. Ltd.)[1] films for the analyzer target using the 295 MeV proton beam. There are two BLP's (BLP1 and BLP2) in the WS beam line. An aramid film of 5.0 mg/cm^2 was placed at the target position of BLP1 and a CH_2 film of 8.4 mg/cm^2 was used in the BLP2. A typical beam intensity was 10 nA. Figure F.1 shows the relative time evolution of the scattering rates per unit beam charges, observed for the two BLP's during the beam irradiation. The beam charges were measured by using the Faraday cup in the scattering chamber. The relative hydrogen ratios at the beginning are normalized to unity. A generally decreasing tendency may be seen in the rate for the CH_2 target. The discontinuous rises in the figure were observed to occur at the times of fine adjustment of the beam line, which probably caused the slight changes in the beam position on the target. These observations most plausibly suggest that the hydrogen atoms were released from the target into vacuum by the proton bombardment. The event rate for the aramid foil target, on the other hand, was observed to be stable up to the accumulated beam charges of up to 100 μC.

[1]It is to be noted that the aramid film used as windows for the gas target cell was made by To-re CO. Ltd., $C_{14}O_2N_2Cl_2H_8$.

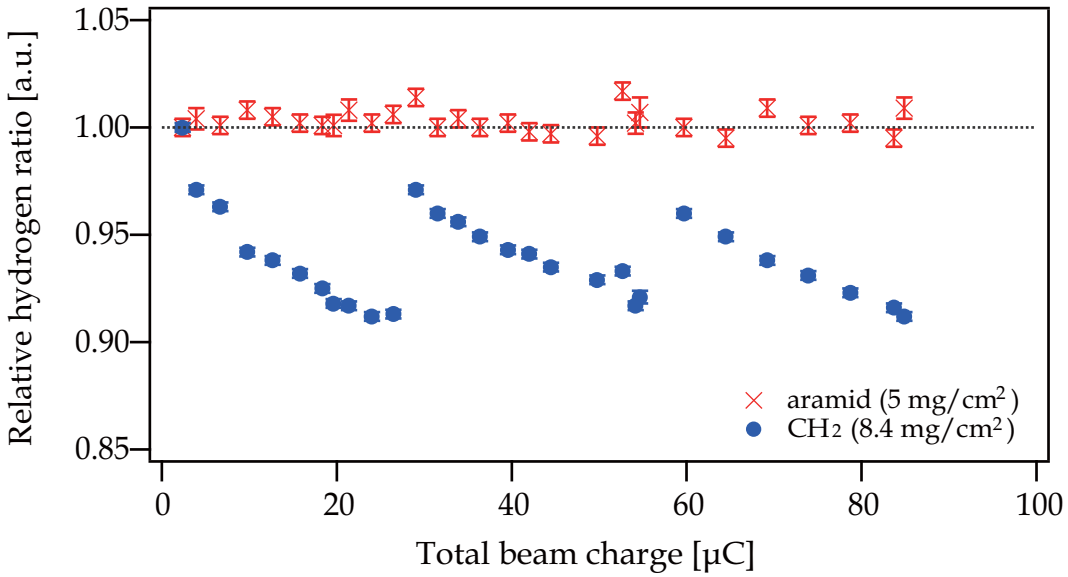

Figure F.1: The charge dependence of the relative hydrogen ratio in the aramid (5 mg/cm^2) and the CH_2 (8.4 mg/cm^2).

Assuming the analyzing power for the CH_2 target to be 0.40 $\pm$ 0.01 for 300 MeV proton beam [27], that of the aramid film was determined in absolute value to be

$$A_y^{aramid} = 0.38 \pm 0.01,$$

where the error originates from statistics. The A_y^{aramid} was used to evaluate the beam polarization in the analysis described in Chap. 5.

Bibliography

[1] C. Gaarde, Nucl. Phys. **A396**, 127c (1983).

[2] K. Ikeda, S. Fujii, and J.I. Fujita, Phys. Lett. **3**, 271 (1963).

[3] M. Ichimura, H. Sakai, T. Wakasa, Prog. Part. Nucl. Phys., **56**, 446 (2006).

[4] A.R. Edmonds, *Angular Momentum in Quantum Mechanics* (Princeton University, Princeton, NJ, 1960).

[5] W.G. Love and M.A. Franey, Phys. Rev. C **24**, 1073 (1981).

[6] M.A. Franey and W.G. Love, Phys. Rev. C **31**, 488 (1985).

[7] Toru Suzuki, Nucl. Phys. **A577**, 167c (1994), and references therein.

[8] A. Tamii, H. Akimune, I. Daito, Y. Fujita, M. Fujiwara, K. Hatanaka, K. Hosono, F. Ihara, T. Inomata, T. Ishikawa, M. Itoh, M. Kawabata,T. Kawabata, M. Nakamura, T. Noro, E. Obayashi, H. Sakaguchi, H. Takeda, T. Taki, H. Toyokawa, H.P. Yoshida, M. Yoshimura, M. Yosoi, Phys. Let. B **451**, 61 (1999).

[9] T. Kawabata, T. Ishikawa, M. Itoh, M. Nakamura, H. Sakaguchi, H. Takeda, T. Taki, M. Uchida, Y. Yasuda, M. Yosoi, H. Akimune, K. Yamasaki, G.P.A. Berg, H. Fujimura, K. Hara, K. Hatanaka, J. Kamiya, T. Noro, E. Obayashi, T. Wakasa, H.P. Yoshida, B.A. Brown, H. Fujita, Y. Fujita, Y. Shimbara, H. Ueno, M. Fujiwara, K. Hosono, A. Tamii, H. Toyokawa, Phys. Rev. C. **65**, 064316 (2002).

[10] A. Willis, M. Morlet, N. Marty, C. Djalali, J. Guillot, H. Langevin-Joliot, J. Van de Wiele, A. Mack, B. Bonin, R. Fergerson, E. Tomasi-Gustafsson, J.C. Lugol, J.C. Duchazeaubeneix, and H. Sakaguchi, Phys. Rev. C. **43**, 2177 (1991).

[11] N. Anantaraman, B.A. Brown, G.M. Crawley, A. Galonsky, B.H. Wildenthal, C. Djalali, N. Marty, M. Morlet, A. Willis, and J.C. Jourdain, Phys. Rev. Lett. **31**, 1409 (1984).

[12] G.M. Crawley, C. Djalali, N. Marty, M. Morlet, A. Willis, N. Anantaraman, B.A. Brown, and A. Galonsky, Phys. Rev. C. **39**, 311 (1989).

[13] B.H. Wildenthal, Prog. Part. Nucl. Phys **11**, 5 (1984).

[14] F. Petrovitch and W.G. Love Nucl. Phys. **A354**, 499c (1981).

[15] B.D. Anderson, T. Chittrakarn, A.R. Baldwin, C. Lebo, R. Madey, P.C. Tandy, J.W. Watson, C.C. Foster, B.A. Brown, and B.H. Wildenthal, Phys. Rev. C **36**, 2195 (1987).

[16] B.D. Anderson, N. Tamimi, A.R. Baldwin, M. Elaasar, R. Madey, D.M. Manley, M. Mostajabodda'vati, J.W. Watson, W.M. Zhang, and C.C. Foster, Phys. Rev. C **43**, 50 (1991).

[17] A. Arima, K. Shimizu, W. Bentz, and H. Hyuga, Adv. Nucl. Phys. **18**, 1 (1987).

[18] I.S. Towner, Phys. Rep. **155**, 263 (1987).

[19] Y. Sakemi, H. Sakaguchi, M. Yosoi, H. Akimune, T. Takahashi, A. Yamagoshi, A. Tamii, M. Fujiwara, K. Hatanaka, K. Hosono, T. Noro, H. Togawa, I. Daito, Y. Fujita, and T. Inomata, Phys. Rev. C. **51**, 3162 (1995).

[20] A. Tamii, Y. Fujita, H. Matsubara, T. Adachi, J. Carter, M. Dozono, H. Fujita, K. Fujita, H. Hashimoto, K. Hatanaka, T. Itahashi, M. Itoh, T. Kawabata, K. Nakanishi, S. Ninomiya, A.B. Perez-Cerdan, L. Popescu, B. Rubio, T. Saito, H. Sakaguchi, Y. Sakemi, Y. Sasamoto, Y. Shimbara, Y. Shimizu, F.D. Smit, Y. Tameshige, M. Yosoi and J. Zenhiro, Nucl. Instr. Meth. A **605**, 326-338 (2009).

[21] Y. Fujita, K. Hatanaka, G.P.A. Berg, K. Hosono, N. Matsuoka, S. Morinobu, T. Noro, M. Sato, K. Tamura, and H. Ueno, Nucl. Instr. Meth. B **126**, 274 (1997).

[22] H. Fujita, Y. Fujita, G.P.A. Berg, A.D. Bacher, C.C. Foster, K. Hara, K. Hatanaka, T. Kawabata, T. Noro, H. Sakaguchi, Y. Shimbara, T. Shinada, E.J. Stephenson, H. Uenoa, and M. Yosoi, Nucl. Instr. Meth. A **484**, 17 (2002).

[23] T. Wakasa, K. Hatanaka, Y. Fujita, G.P.A. Berg, H. Fujimura, H. Fujita, M. Itoh, J. Kamiya, T. Kawabata, K. Nagayama, T. Noro, H. Sakaguchi, Y. Shimbara, H. Takeda, K. Tamura, H. Uenob, M. Uchida, M. Uraki, and M. Yosoi, Nucl. Instr. Meth. A **482**, 79 (2002).

[24] M. Fujiwara, H. Akimune, I. Daito, H. Fujimura, Y. Fujita, K. Hatanaka, H. Ikegami, I. Katayama, K. Nagayama, N. Matsuoka, S. Morinobu, T. Noro, M. Yoshimura, H. Sakaguchi, Y. Sakemi, A. Tamii, and M. Yosoi, Nucl. Instr. Meth. A **422**, 484 (1999).

[25] P. Ludwig, R. Geller and G. Melin, Review of Scientific Instruments, **63**, p.2892 (1992).

[26] K. Hatanaka, K. Takahisa, H. Tamura, M. Sato, and I. Miura, Nucl. Instr. Meth. A **384**, 1575 (1997).

[27] H. Takeda, Memoirs of the Faculty of Science, Kyoto University, Vol. $XXXXIV$. No.1, Article 1, (2003).

[28] T. Noro et al., RCNP Annual Report, Osaka University, 1991, *pp.* 177.

[29] N. Fujita, Masters Thesis, Miyazaki University, 2009, (unpublished).

[30] N. Matsuoka and T. Noro, RCNP Annual Report, Osaka University, 1987, *pp.* 176; N. Matsuoka *et al.*, RCNP Annual Report, Osaka University, 1991, *pp.* 186.

[31] N. Matsuoka *et al.*, RCNP Annual Report, Osaka University, 1991, *pp.* 161.

[32] M. Itoh, H. Sakaguchi, M. Uchida, T. Ishikawa, T. Kawabata, T. Murakami, H. Takeda, T. Taki, S. Terashima, N. Tsukahara, Y. Yasuda, M. Yosoi, U. Garg, M. Hedden, B. Kharraja, M. Koss, B.K. Nayak, S. Zhu, H. Fujimura, M. Fujiwara, K. Hara, H.P. Yoshida, H. Akimune, M.N. Harakeh, and M. Volkerts, Phys. Rev. C. **68**, 064602 (2003).

[33] K. Sagara, private communication.

[34] H.P. Yoshida *et al.*, RCNP Annual Report, Osaka University, 1996, *pp.* 164.

[35] A. Tamii, H. Sakaguchi, H. Takeda, M. Yosoi, H. Akimune, M. Fujiwara, H. Ogata, M. Tanaka, H. Togawa, IEEE Trans. on Nucl. Sci. 43 (1996) 2488.

[36] T. Kawabata *et al.*, RCNP Annual Report, Osaka University, 1996, *pp.* 161.

[37] http://www.nndc.bnl.gov/nudat2.

[38] H. Fujita, G.P.A. Berg, Y. Fujita, K. Hatanaka, T. Noro, E.J. Stephenson, C.C. Foster, H. Sakaguchi, M. Itoh, T. Taki, K. Tamura, H. Ueno, Nucl. Instr. Meth. A **469**, 55 (2001).

[39] T. Kawabata, H. Akimune, H. Fujimura, H. Fujita, Y. Fujita, M. Fujiwara, K. Hara, K. Hatanaka, K. Hosono, T. Ishikawa, M. Itoh, J. Kamiya, M. Nakamura, T. Noro, E. Obayashi, H. Sakaguchi, Y. Shimbara, H. Takeda, T. Taki, A. Tamii, H. Toyokawa, N. Tsukahara, M. Uchida, H. Ueno, T. Wakasa, K. Yamasaki, Y. Yasuda, H.P. Yoshida and M. Yosoi, Nucl. Instr. and Meth. A **459**, 171 (2001).

[40] H. Matsubara, H. Sakaguchi, T. Kishi, and A. Tamii, Nucl. Instr. and Meth. B **267**, 3682-3687 (2009).

[41] B. Reitz, F. Hofmann, P. von Neumann-Cosel, F. Neumeyer, C. Rangacharyulu, A. Richter, G. Schrieder, D.I. Sober, and B.A. Brown, Phys. Rev. Lett. **82**, 291 (1999).

[42] F. Hofmann, P. von Neumann-Cosel, F. Neumeyer, C. Rangacharyulu, B. Reitz, A. Richter, G. Schrieder, D.I. Sober, L.W. Fagg, and B.A. Brown, Phys. Rev. C **65**, 024311 (2002).

[43] A. Tamii, Doctral Dissertation, Kyoto Univ. (1999), private communication.

[44] For example, G.F. Knoll, *Radiation Detection and Measurement, 3rd ed.*, John Wiley & Sons, Inc., New York (2000).

[45] J. Raynal, program code ECIS-88 NEA-0850/08.

[46] E.D. Cooper, S. Hama, B.C. Clark, and R.L. Mercer, Phys. Rev. C **47**, 297 (1993).

[47] J. Zenihiro, H. Sakaguchi, T. Murakami, H. Takeda, S. Terashima, Y. Matsuba, M. Yosoi, Y. Yasuda, and M. Itoh, Nucl. Phys. **A805**, 281 (2008), and private communication.

[48] E.D. Cooper, S. Hama, and B.C. Clark, Phys. Rev. C **80**, 034605 (2009).

[49] B.A. Brown and W.D.M. Rae, MSU-NSCL report (2007).

[50] B.A. Brown, and B.H. Wildenthal, Nucl. Phys. **A474**, 290 (1987).

[51] S. Cohen and D. Kurath, Nucl. Phys. **73**, 1-24 (1965).

[52] B.A. Brown and B.H. Wildenthal, Annu. Rev. Nucl. Part. Sci. **38**, 29 (1988).

[53] B.A. Brown and W.A. Richter, Phys. Rev. C **74**, 034315 (2006).

[54] J. Raynal, program code DWBA07 NEA-1209/008.

[55] K. Yagi, *Genshikaku butsuri gaku* (Asakura syotenn, Tokyo, 1971), in Japanese.

[56] Michael W. Kirson, Nucl. Phys. **A781**, 350 (2007).

[57] M. Lacombe, B. Loiseau, J.M. Richard, R. Vinh Mau, J. Côté, P. Pirès, and R. de Tourreil, Phys. Rev. C **21**, 861 (1980).

[58] H.V. von Geramb, in *The Interaction Between Medium Energy Nucleons in Nuclei−1982*, edited by H.O. Meyer, AIP Conf. Proc. No. 97 (AIP, New York, 1983), p. 44.

[59] T. Kawabata, Master Thesis, Kyoto University, 1998, (unpublished).

[60] Y. Fujita, H. Fujita, and Y. Shimbara, private communication.

[61] T.N. Taddeucci, C.A. Goulding, T.A. Carey, R.C. Byrd, C.D. Goodman, C. Gaarde, J. Larsen, D.J. Horen, J. Rapaport and E. Sugarbaker, Nucl. Phys. **A469**, 125 (1987).

[62] R.G.T. Zegers, T. Adachi, H. Akimune, Sam M. Austin, A.M. van den Berg, B.A. Brown, Y. Fujita, M. Fujiwara, S. Galès, C.J. Guess, M.N. Harakeh, H. Hashimoto, K. Hatanaka, R. Hayami, G.W. Hitt, M.E. Howard, M. Itoh, T. Kawabata, K. Kawase, M. Kinoshita, M. Matsubara, K. Nakanishi, S. Nakayama, S. Okumura, T. Ohta, Y. Sakemi, Y. Shimbara, Y. Shimizu, C. Scholl, C. Simenel, Y. Tameshige, A. Tamii, M. Uchida, T. Yamagata, and M. Yosoi, Phys. Rev. Lett. C **99**, 202501 (2007), and pravate communication.

[63] M. Sasano, H. Sakai, K. Yako, T. Wakasa, S. Asaji, K. Fujita, Y. Fujita, M.B. Greenfield, Y. Hagihara, K. Hatanaka, T. Kawabata, H. Kuboki, Y. Maeda, H. Okamura, T. Saito, Y. Sakemi, K. Sekiguchi, Y. Shimizu, Y. Takahashi, Y. Tameshige, and A. Tamii, Phys. Rev. C **79**, 024602 (2009).

[64] I.S. Towner and J.C. Hardy, Phys. Rev. C **77**, 025501 (2008).

[65] W.M. Yao *et al.* (Particle Data Group), J. Phys. G **33**, 1 (2006).

[66] Y. Fujita, B.A. Brown, H. Ejiri, K. Katori, S. Mizutori, and H. Ueno, Phys. Rev. C **62**, 044314 (2000).

[67] D.E. Alburger and A.M. Nathan, Phys. Rev. C **17**, 280 (1978).

[68] K. Minamisono, K. Matsuta, T. Minamisono, T. Yamaguchi, T. Sumikama, T. Nagatomo, M. Ogura, T. Iwakoshi, M. Fukuda, M. Mihara, K. Koshigiri, and M. Morita, Phys. Rev. C **65**, 015501 (2001); K. Minamisono, K. Matsuta, T. Minamisono, T. Yamaguchi, T. Sumikama, T. Nagatomo, M. Ogura, T. Iwakoshi, M. Fukuda, M. Mihara, and K. Koshigiri, Phys. Rev. C **65**, 015209 (2001).

[69] H.S. Wilson, R.W. Kavanagh, and F.M. Mann, Phys. Rev. C **22**, 1696 (1980).

[70] Y. Fujita, Y. Shimbara, A.F. Lisetskiy, T. Adachi, G.P.A. Berg, P. von Brentano, H. Fujimura, H. Fujita, K. Hatanaka, J. Kamiya, T. Kawabata, H. Nakada, K. Nakanishi, Y. Shimizu, M. Uchida, and M. Yosoi, Phys. Rev. C **67**, 064312 (2003).

[71] R.G.T. Zegers, H. Akimune, Sam M. Austin, D. Bazin, A.M. van den Berg, G.P.A. Berg, B.A. Brown, J. Brown, A.L. Cole, I. Daito, Y. Fujita, M. Fujiwara, S. Galès, M.N. Harakeh, H. Hashimoto, R. Hayami, G.W. Hitt, M.E. Howard, M. Itoh, J. Jänecke, T. Kawabata, K. Kawase, M. Kinoshita, T. Nakamura, K. Nakanishi,

S. Nakayama, S. Okumura, W.A. Richter, D.A. Roberts, B.M. Sherrill, Y. Shimbara, M. Steiner, M. Uchida, H. Ueno, T. Yamagata, and M. Yosoi, Phys. Rev. C **74**, 024309 (2006).

[72] Z. Janas, M. Karny, Y. Fujita, L. Batist, D. Cano-Ott, R. Collatz, P. Dendooven, A. Gadea, M. Gierlik, M. Hellström, Z. Hu, A. Jokinen, R. Kirchner, O. Klepper, F. Moroz, M. Oinonen, H. Penttilä, A. Plochocki, E. Roeckl, B. Rubio, M. Shibata, J.L. Tain, and V. Wittman, Eur. Phys. J. A **12**, 143 (2001).

[73] Y. Fujita, H. Fujita, T. Adachi, G.P.A. Berg, E. Caurier, H. Fujimura, K. Hara, K. Hatanaka, Z. Janas, J. Kamiya, T. Kawabata, K. Langanke, G. Martinez-Pinedo, T. Noro, E. Roeckl, Y. Shimbara, T. Shinada, S.Y. van der Werf, M. Yoshifuku, M. Yosoi, and R.G.T. Zegers, Eur. Phys. J. A **13**, 411 (2002).

[74] H. Fujita, Y. Fujita, T. Adachi, A.D. Bacher, G.P.A. Berg, T. Black, E. Caurier, C.C. Foster, H. Fujimura, K. Hara, K. Harada, K. Hatanaka J. Jänecke, J. Kamiya, Y. Kanzaki, K. Katori, T. Kawabata, K. Langanke, G. Martinez-Pinedo, T. Noro, D.A. Roberts, H. Sakaguchi, Y. Shimbara, T. Shinada, E.J. Stephenson, H. Ueno, T. Yamanaka, M. Yoshifuku, and M. Yosoi, Phys. Rev. C **75**, 034310 (2007).

[75] M. Sasano, Masters Thesis, the university of Tokyo, 2005, (unpublished).

[76] J. Bernabéu, T. Ericson, E. Hernández, and J. Ros, Nucl. Phys. **B378**, 131 (1992).

[77] T. Kawabata, H. Akimune, H. Fujimura, H. Fujita, Y. Fujita, M. Fujiwara, K. Hara, K.Y. Hara, K. Hatanaka, T. Ishikawa, M. Itoh, J. Kamiya, S. Kishi, M. Nakmura, K. Nakanishi, T. Noro, H. Sakaguchi, Y. Shimbara, H. Takeda, A. Tamii, S. Terashima, H. Toyokawa, M. Uchida, H. Ueno, T. Wakasa, Y. Yasuda, H.P. Yoshida, and M. Yosoi, Phys. Rev. C **70**, 034318 (2004).

[78] S. Raman, C.A. Houser, T.A. Walkiewicz and I.S. Towner, Atomic Data Nucl. Data Tables **21**, 567 (1978).

[79] T.N. Taddeucci, R.C. Byrd, T.A. Carey, D.E. Ciskowski, C.C. Foster, C. Gaarde, C.D. Goodman, E. Gülmez, W. Huang, D.J. Horen, J. Larsen, D. Marchlenski, J.B. McClelland, D. Prout, J. Rapaport, L.J. Rybarcyk, E. Sugarbaker, I.J. Van Heerden, and C.A. Whitten, Jr., Phys. Rev. C **42**, 935 (1990).

[80] F. Ajzenberg-Selove, Nucl. Phys. **A506**, 1 (1990).

[81] P. von Neumann-Cosel, H.-D. Gräf, U. Krämer, A. Richter, E. Spamer, Nucl. Phys. **A669**, 3 (2000).

[82] M.S. Fayache, P. von Neumann-Cosel, A. Richter, Y.Y. Sharon and L. Zamick, Nucl. Phys. **A627**, 14 (1997).

[83] C. Djalali, G.M. Crawley, B.A. Brown, V. Rotberg, G. Caskey, A. Galonsky, N. Marty, M. Morlet, and A. Willis, Phys. Rev. C **35**, 1201 (1987).

[84] A. Willis, M. Morlet, N. Marty, C. Djalali, G.M. Crawley, A. Galonsky, V. Rotberg and, B.A. Brown, Nucl. Phys. **A464**, 315 (1987).

[85] C.W. Foltz, D.I. Sober, L.W. Fagg, H.D. Gräf, A. Richter, E. Spamer, and B. Alex Brown, Phys. Rev. C **49**, 1359 (1994).

[86] W. Steffen, H.-D. Gräf, W. Gross, D. Meuer, A. Richter, E. Spamer, O. Titze, W. Knüpfer, Phys. Lett. B **95**, 23 (1980).

[87] I.S. Towner and F.C. Khanna, Nucl. Phys. **A399**, 334 (1983).

[88] Y. Utsuno, T. Otsuka, T. Mizusaki, and M. Honma, Phys. Rev. C **60**, 0543158 (1999), and Y. Utsuno, private communication.

[89] R. Machleidt, K. Holide and Ch. Elster, Phys. Rep, **149**, 1 (1987).

[90] M.S. Fayache, L. Zamick, Y.Y. Sharon, and Y. Durga Dwvi, Phys. Rev. C **61**, 024308 (2000).

[91] L.W. Fagg, Rev. Mod. **47**, 683 (1975).

[92] U.E.P. Berg, K. Ackermann, K. Bangert, C. Bläsing, W. Naatz, R. Stock, K. Wienhard, M.K. Brussel and, T.E. Chapuran, B.H. Wildenthal, Phys. Lett. **140B**, 191 (1984).

[93] E. Kuhlmann, Phys. Rev. C **20**, 415 (1979).

[94] E. Kuhlmann, Z Phys. A **332**, 527 (1985).

[95] A. Bohr and B. Mottelson, *Nuclear Structure*, (Benjamin, Inc., MA, 1969), Vol. 1.

[96] A. Richter, A. Weiss, O. Häusser, and B.A. Brown, Phys. Rev. Lett. **65**, 2519 (1990).

[97] C. Lüttge, P. von Neumann-Cosel, F. Neumeyer, C. Rangacharyulu, A. Richter, G. Schrieder, E. Spamer, D.I. Sober, S.K. Matthews, and B.A. Brown, Phys. Rev. C **53**, 127 (1996).

[98] P. von Neumann-Cosel, A. Richter, Y. Fujita, and B.D. Anderson, Phys. Rev. C **55**, 532 (1997).

[99] Y. Fujita, H. Akimune, I. Daito, M. Fujiwara, M.N. Harakeh, T. Inomata, J. Jänecke, K. Katori, C. Lüttge, S. Nakayama, P. von Neumann-Cosel, A. Richter, A. Tamii, M. Tanaka, H. Toyokawa, H. Ueno, and M. Yosoi, Phys. Rev. C **55**, 1137 (1997).

[100] Y. Fujita, H. Akimune, I. Daito, M. Fujiwara, M.N. Harakeh, T. Inomata, J. Jänecke, K. Katori, C. Lüttge, S. Nakayama, P. von Neumann-Cosel, A. Richter, A. Tamii, M. Tanaka, H. Ueno, and M. Yosoi, Nucl. Instr. and Meth. A **402**, 371 (1998).

[101] Y. Fujita, H. Akimune, I. Daito, H. Fujimura, M. Fujiwara, M.N. Harakeh, T. Inomata, J. Jänecke, K. Katori, A. Tamii, M. Tanaka, H. Ueno, and M. Yosoi, Phys. Rev. C **59**, 90 (1999).

[102] S. Rakers, C. Baümer, D. Frekers, R. Schmidt, A.M. van den Berg, V.M. Hannen, M.N. Harakeh, M.A. de Huu, H.J. Wo̎rtche, D.De Frenne, M. Hagemann, J. Heyse, E. Jacobs, and Y. Fujita, Phys. Rev. C **65**, 044323 (2002).

Acknowledgments

I would like to express a lot of thanks to many people for their help and hearty support in the course of the present work.

I am greatly indebted to my supervisor, Prof. Atsushi Tamii, who kindly gave me an opportunity to study this interesting subject. He gave me enlightening advices and continuous encouragements, and supported me in all the phases of my study.

I would like to express my gratitude to Prof. Yoshitaka Fujita for his enlightening guidance to nuclear physics. He also gave me many chances to see and discuss with physicists in the world.

I wish to thank Profs. Harutaka Sakaguch, Takahiro Kawabata, Drs. Youhei Shimizu, Kenji Suda, Yuji Tameshige, and Mr. Juzo Zenihiro for their help to prepare and develop several types of the targets.

I would like to appreciate valuable discussions with Profs. Achim Richter and Peter von Neumann-Cosel during my stay at Darmstadt.

I would like to address my thanks to all the collaborators of the RCNP-E249 and E299 experiments; Profs. John Carter, Kichiji Hatanaka, Berta Rubio, Yasuhiro Sakemi, Ricky D. Smit, Masaru Yosoi, and Drs. Tatsuya Adachi, Masanori Dozono, Hirohiko Fujita, Kunihiro Fujita, Masatoshi Itoh, Yukie Maeda, Kohsuke Nakanishi, Retief Neveling, Lucia-Ana Popescu, Satoshi Sakaguchi, Yoshihiro Shimbara, Yukiko Yamada, and Messrs. Noriyuki Fujita, Daisuke Ishikawa, Maiko Kato, Sho Kuroita, Atsushi Nonaka, Ana Belen Perez Cerdan, Iryna Poltoratska, Yoshiko Sasamoto, Hiroshi Tokieda, Ryosuke Yamada, for their great contributions and collaborations in completing this work successfully. I would like to thank Prof. Hiroyuki Okamura for his help, support and encouragement. I would like to mourn for him.

I deeply thank Prof. Hitoshi Nakada for his theoretical support and discussion. He gave me the quick and helpful responses to my email.

I specially thank Prof. Shumpei Morinobu for his critical reading of the manuscript.

I gratefully acknowledge the help and advices of all the staff members and engineers of RCNP. My special thanks are due to the members of the accelerator group for their efforts in providing beams with excellent quality during the experiment.

I would like to thank Profs. Susumu Simoura, Tomohiro Uesaka and the SHARAQ members at the CNS. This work was completed after my moving to the CNS.

Finally, I would like to express my great thanks to my parents, sister, brother, sister-in-law, and niece for their continuous supports.